THE UNIVERSITY OF CHICAGO

MEASUREMENTS OF DIRECT CP VIOLATION, CPT SYMMETRY, AND OTHER PARAMETERS IN THE NEUTRAL KAON SYSTEM

A DISSERTATION SUBMITTED TO
THE FACULTY OF THE DIVISION OF THE PHYSICAL SCIENCES
IN CANDIDACY FOR THE DEGREE OF
DOCTOR OF PHILOSOPHY

DEPARTMENT OF PHYSICS

BY
ELIZABETH TURNER WORCESTER

CHICAGO, ILLINOIS
DECEMBER 2007

Copyright © 2007 by Elizabeth T. Worcester
All rights reserved

To Moses

TABLE OF CONTENTS

LIST OF FIGURES viii

LIST OF TABLES xii

ABSTRACT xiv

ACKNOWLEDGEMENTS xv

1 INTRODUCTION 1
- 1.1 Background 1
- 1.2 Kaon Phenomenology 4
- 1.3 Calculating ϵ'/ϵ 9
- 1.4 Theory Status of ϵ'/ϵ 11
- 1.5 Measuring $Re(\epsilon'/\epsilon)$ 12
- 1.6 Experimental Status of $Re(\epsilon'/\epsilon)$ 13
- 1.7 Measuring Kaon Sector Parameters 14
- 1.8 Experimental Status of Kaon Sector Parameters 16
- 1.9 Personal Perspective 16

2 THE KTEV EXPERIMENT 20
- 2.1 Experimental Strategy 20
- 2.2 Beam 21
- 2.3 Detector 24
  - 2.3.1 Accidental Counters 26
  - 2.3.2 Regenerator 26
  - 2.3.3 Charged Spectrometer 30
  - 2.3.4 Calorimeter 30
  - 2.3.5 Vetos 35
  - 2.3.6 Trigger Hodoscopes 39
- 2.4 Data Acquisition 40
  - 2.4.1 Trigger 40
  - 2.4.2 Data Collection 46
- 2.5 Computing 47
- 2.6 Detector Calibration 48
  - 2.6.1 Charged Calibration 48

2.6.2 Neutral Calibration . . . 53
2.6.3 Veto Calibration . . . 59
2.7 Changes for 1999 . . . 62

3 DATA ANALYSIS . . . 65
3.1 $K \to \pi^+\pi^-$ Analysis . . . 65
3.1.1 Tracking . . . 65
3.1.2 Event Reconstruction . . . 68
3.1.3 Event Selection . . . 69
3.1.4 Updates since 2003 . . . 75
3.1.5 Yields . . . 78
3.2 $K \to \pi^0\pi^0$ Analysis . . . 78
3.2.1 Clustering . . . 79
3.2.2 Clustering Corrections . . . 82
3.2.3 Event Reconstruction . . . 96
3.2.4 Final Energy Scale . . . 99
3.2.5 Event Selection . . . 103
3.2.6 Updates Since 2003 . . . 109
3.2.7 Yields . . . 115

4 MONTE CARLO SIMULATION . . . 116
4.1 Kaon Propagation and Decay . . . 116
4.2 Tracing of Decay Products . . . 118
4.3 Simulation of the Drift Chambers . . . 118
4.4 Simulation of the CsI Calorimeter . . . 120
4.4.1 Electromagnetic Shower Simulation . . . 120
4.4.2 Simulation of Other Particles . . . 126
4.4.3 Digitization and Readout . . . 127
4.4.4 Monte Carlo Clustering and Corrections . . . 127
4.5 Accidental Overlays . . . 128
4.6 Simulation of the Trigger . . . 129
4.7 Updates Since 2003 . . . 129
4.7.1 Changes to Kaon Propagation and Decay . . . 129
4.7.2 Changes to Geometry and Tracing . . . 130
4.7.3 Changes to Detector Response . . . 132
4.7.4 Changes to Monte Carlo Analysis . . . 134
4.8 Monte Carlo Samples . . . 135

5 BACKGROUNDS . . . 138
5.1 Scattering Backgrounds . . . 138
5.1.1 Collimator Scattering . . . 138
5.1.2 Regenerator Scattering . . . 141

5.2 Non-$\pi\pi$ Background . . . 146
5.2.1 Backgrounds to $K \to \pi^+\pi^-$ Decays . . . 146
5.2.2 Backgrounds to $K \to \pi^0\pi^0$ Decays . . . 148
5.3 Updates Since 2003 . . . 150
5.4 Summary of Background Levels and Event Yields . . . 150

6 EXTRACTING PHYSICS PARAMETERS . . . 157
6.1 Acceptance Correction . . . 157
6.2 The Fitter . . . 158
6.3 Fits . . . 163
6.3.1 $Re(\epsilon'/\epsilon)$ Fit . . . 163
6.3.2 Δm and τ_S Fits . . . 164
6.3.3 CPT Fits . . . 166

7 SYSTEMATIC STUDIES . . . 169
7.1 Acceptance Correction . . . 169
7.2 $K \to \pi^+\pi^-$ Systematics . . . 172
7.2.1 Trigger . . . 172
7.2.2 Track and Momentum Reconstruction . . . 176
7.2.3 Cut Variations . . . 177
7.2.4 Drift Chamber Simulation . . . 177
7.2.5 Backgrounds . . . 179
7.2.6 Apertures . . . 179
7.2.7 Summary . . . 180
7.3 $K \to \pi^0\pi^0$ Systematics . . . 180
7.3.1 Trigger . . . 180
7.3.2 Cut Variations . . . 184
7.3.3 Energy Reconstruction . . . 190
7.3.4 Backgrounds . . . 197
7.3.5 Apertures . . . 200
7.3.6 Summary . . . 200
7.4 Fitter Systematics . . . 201
7.5 Changes Relative to 2003 Analysis . . . 202
7.6 Summary of Systematic Errors for $Re(\epsilon'/\epsilon)$ . . . 204
7.7 Systematic Errors for Kaon Sector Parameters . . . 204

8 RESULTS . . . 207
8.1 ϵ'/ϵ Results . . . 207
8.1.1 ϵ'/ϵ Crosschecks . . . 207
8.2 Kaon Sector Parameter Results . . . 209
8.2.1 Kaon Sector Parameter Crosschecks . . . 212
8.3 Comparison to Other Measurements . . . 213

8.4 Conclusions 215

A FIGURES FOR KAON SECTOR PARAMETER CROSSCHECKS 220

REFERENCES 233

LIST OF FIGURES

1.1 Diagram of the significance of the parameters ϵ and ϵ'. 10
1.2 Relative contributions to ϵ'/ϵ of the effective operators 12
1.3 History of published measurements of $Re(\epsilon'/\epsilon)$ prior to this result . . 15
1.4 Measurements of Δm used in the PDG average prior to this result . 17
1.5 Measurements of τ_S used in the PDG average prior to this result . . 18
1.6 Measurements of ϕ_{+-} used in the PDG average prior to this result . 19

2.1 Schematic of the KTeV beamline 22
2.2 Schematic of the KTeV detector 25
2.3 Diagram of the regenerator 27
2.4 Drift chamber hexagonal cell geometry 31
2.5 Diagram of the KTeV CsI calorimeter 32
2.6 Diagram of the Mask Anti and Ring Counter 35
2.7 Diagram of the Collar Anti 37
2.8 Schematic of the Downstream Vetos and Walls 38
2.9 Diagram of the trigger hodoscopes 39
2.10 Data taking periods for KTeV 46
2.11 Beam intensity distribution for 1999 run. 47
2.12 Sample drift chamber TDC distribution 49
2.13 Typical drift chamber Sum-of-Distance distribution 51
2.14 Schematic of laser system 54
2.15 Average CsI gain drift measured using laser 55
2.16 Electron calibration plots for sample calibration period 58
2.17 RC calibration plots for sample calibration period 61
2.18 Regenerator lead module MIP peak in hadronic conditions 62

3.1 True bend of tracks through the magnet 68
3.2 Angle used to define p_T^2 70
3.3 Event display for a $K \to \pi^+\pi^-$ event 71
3.4 Invariant mass distributions for $\pi^+\pi^-$ data. 73
3.5 p_T^2 distributions for $\pi^+\pi^-$ data. 74
3.6 Kaon energy distributions for $\pi^+\pi^-$ data. 76
3.7 Vertex z distributions for $\pi^+\pi^-$ data. 77
3.8 Definition of clusters near a beam hole. 80
3.9 Distribution of energy ratios and the corresponding position map. . 82
3.10 55 position bins for transverse energy maps 84

3.11 Measured longitudinal response for sample CsI crystals in 1999 . . . 87
3.12 Sample longitudinal energy profiles from GEANT. 88
3.13 Intrablock correction for the central region of the CsI. 90
3.14 Transverse variation across three sample CsI blocks. 91
3.15 E/P linearity for K_{e3} electrons before channel-by-channel correction. 92
3.16 E/P vs spill for K_{e3} electrons in 1999. 93
3.17 E/p and energy resolution for K_{e3} electrons after all corrections. . . 94
3.18 Photon correction in nine regions for 1999. 95
3.19 Three ways to pair four photons to make 2 π^0s. 98
3.20 Event display for a sample $K \to \pi^0\pi^0$ decay. 100
3.21 $K_S \to \pi^0\pi^0$ z vertex distributions used for regenerator edge matching in 1999. 101
3.22 Final energy scales applied to data in 1996, 1997, and 1999. 102
3.23 $K \to \pi^0\pi^0$ minimum cluster energy distributions for 1999. 104
3.24 $K \to \pi^0\pi^0$ minimum cluster separation distributions for 1999. 105
3.25 $K \to \pi^0\pi^0$ $\chi^2_{\pi^0}$ distributions for 1999. 106
3.26 $K \to \pi^0\pi^0$ χ^2_{γ} distributions for 1999. 107
3.27 $K \to \pi^0\pi^0$ $\mathrm{m}_{\pi^0\pi^0}$ distributions for 1999. 108
3.28 $K \to \pi^0\pi^0$ RING distributions for 1999. 110
3.29 $K \to \pi^0\pi^0$ z vertex distributions for 1999. 111
3.30 $K \to \pi^0\pi^0$ kaon energy distributions for 1999. 112
3.31 Change in the final energy scale adjustment relative to the 2003 analysis. 114

4.1 Position bins used for shower library generation. 121
4.2 E/p resolutions for K_{e3} electrons in 1999 data and Monte Carlo. . . 123
4.3 Cartoon of position shift to correct for differing incident angles. . . . 124
4.4 Cartoon of extra wrapping in the simulation of large blocks. 126
4.5 Data-MC comparison of fraction of energy in the seed block. 135
4.6 Data-MC comparison of fraction of energy in each of the 49 blocks in a small block cluster. 136

5.1 Identification of collimator scattering background using high p_T^2 $K \to \pi^+\pi^-$ decays. 140
5.2 p_K dependent factors in the regenerator scattering p_T^2 fit. 143
5.3 p_K dependent normalization factor for the regenerator scattering p_T^2 fit. 144
5.4 RING distributions for $K \to \pi^0\pi^0$ data and inelastic regenerator scattering MC. 145
5.5 Distributions used to normalize the background contributions in the vacuum beam $\pi^+\pi^-$ sample. 147

5.6 Invariant mass distributions for $K \to \pi^0\pi^0$ data and $3\pi^0$ background MC. 149
5.7 z vertex distributions for mass sidebands in $K \to \pi^0\pi^0$ data and $K_L \to \pi^0\pi^0\pi^0$ background MC. 149
5.8 p_T^2 distributions for $K \to \pi^+\pi^-$ and all backgrounds. 151
5.9 Invariant mass distributions for $K \to \pi^+\pi^-$ and all backgrounds. . . 152
5.10 RING distributions for $K \to \pi^0\pi^0$ and all backgrounds. 154
5.11 Invariant mass distributions for $K \to \pi^0\pi^0$ and all backgrounds. . . 155

6.1 MC acceptance as a function of z vertex for $K \to \pi^+\pi^-$ and $K \to \pi^0\pi^0$.158
6.2 K_L-K_S interference downstream of the regenerator. 160
6.3 Power law fit to f_- using KTeV $K \to \pi^+\pi^-$ data. 162

7.1 Data/MC ratio of z distributions for $K \to \pi^+\pi^-$ decays from 1997 and 1999. 170
7.2 Data/MC ratio of z distribution for $K \to \pi^+\pi^-$ decays from the full dataset. 171
7.3 Data/MC ratio of z distribution for $K_L \to \pi^0\pi^0\pi^0$ decays from 1996, 1997, and 1999. 173
7.4 Data-MC comparison of z distribution for $K_L \to \pi^0\pi^0\pi^0$ decays from the full dataset. 174
7.5 Data/MC ratio of z distribution for $K \to \pi^0\pi^0$ decays from 1996, 1997, and 1999. 175
7.6 Data-MC comparison of z distribution for $K \to \pi^0\pi^0$ decays from the full dataset. 176
7.7 Change in $Re(\epsilon'/\epsilon)$ with variation of p_T^2 cut. 178
7.8 L2 inefficiency as a function of minimum cluster energy. 183
7.9 Changes in $Re(\epsilon'/\epsilon)$ with variations of selection criteria. 185
7.10 Minimum cluster separation for vacuum beam $K \to \pi^0\pi^0$ data and MC. 186
7.11 χ^2_γ for vacuum beam $K \to \pi^0\pi^0$ data and MC. 186
7.12 $\chi^2_{\pi^0}$ for vacuum beam $K \to \pi^0\pi^0$ data and MC. 187
7.13 RING variable for vacuum beam $K \to \pi^0\pi^0$ data and MC. 188
7.14 Minimum cluster energy for vacuum beam $K \to \pi^0\pi^0$ data and MC. 189
7.15 Cluster and seed block energy for vacuum beam $K \to \pi^0\pi^0$ data and MC. 189
7.16 Data-MC comparisons of M_K vs z_K, E_K, minimum cluster separation, and photon angle. 191
7.17 Effect of 0.1%/100 GeV distortion on M_K vs E_K for 1999 data. . . . 192
7.18 z vertex distributions of $\pi^0\pi^0$ pairs produced hadronically in the regenerator. 194

7.19 z vertex distributions of $\pi^0\pi^0$ pairs produced hadronically in the vacuum window. 195
7.20 Energy scale tests at the regenerator and vacuum window. 196

8.1 $Re(\epsilon'/\epsilon)$ in subsets of the data sample. 208
8.2 $Re(\epsilon'/\epsilon)$ crosschecks. 210
8.3 $Re(\epsilon'/\epsilon)$ and $|f_-(70\ \mathrm{GeV}/c)|$ in 10 GeV/c momentum bins. 211
8.4 New world average for $Re(\epsilon'/\epsilon)$. 214
8.5 New world average for Δm. 216
8.6 New world average for τ_S. 217
8.7 Comparison of ϕ_{+-} to previous results. 218
8.8 Comparison of $\Delta\phi$ to previous results. 219

A.1 Δm in subsets of the $K \to \pi^+\pi^-$ data sample. 220
A.2 τ_S in subsets of the $K \to \pi^+\pi^-$ data sample. 221
A.3 Δm in subsets of the $K \to \pi^0\pi^0$ data sample. 221
A.4 τ_S in subsets of the $K \to \pi^0\pi^0$ data sample. 222
A.5 ϕ_{+-} in subsets of the $K \to \pi^+\pi^-$ data sample. 222
A.6 $\Delta\phi$ in subsets of the data sample. 223
A.7 Δm crosschecks using the $K \to \pi^+\pi^-$ sample. 224
A.8 τ_S crosschecks using the $K \to \pi^+\pi^-$ sample. 225
A.9 Δm crosschecks using the $K \to \pi^0\pi^0$ sample. 226
A.10 τ_S crosschecks using the $K \to \pi^0\pi^0$ sample. 227
A.11 ϕ_{+-} crosschecks. 228
A.12 $\Delta\phi$ crosschecks. 229
A.13 Δm in 10 GeV/c momentum bins using the $K \to \pi^+\pi^-$ sample. . . 230
A.14 τ_S in 10 GeV/c momentum bins using the $K \to \pi^+\pi^-$ sample. . . . 230
A.15 Δm in momentum bins using the $K \to \pi^0\pi^0$ sample. 231
A.16 τ_S in momentum bins using the $K \to \pi^0\pi^0$ sample. 231
A.17 ϕ_{+-} in 10 GeV/c momentum bins. 232
A.18 $\Delta\phi$ in 10 GeV/c momentum bins. 232

LIST OF TABLES

1.1 Some calculations of $Re(\epsilon'/\epsilon)$ within the Standard Model. 13

2.1 Typical charge and energy ranges covered by each QIE exponent . . 34
2.2 $K \to \pi^+\pi^-$ trigger requirements 43
2.3 $K \to \pi^0\pi^0$ trigger requirements 44

3.1 Summary of veto cuts for $K \to \pi^+\pi^-$ decays 72
3.2 Summary of selection criteria for $K \to \pi^+\pi^-$ decays 75
3.3 $\pi^+\pi^-$ event yields before background subtraction 78
3.4 Parameters for out-of-cone correction 89
3.5 Summary of veto cuts for $K \to \pi^0\pi^0$ decays 109
3.6 Summary of selection criteria for $K \to \pi^0\pi^0$ decays 113
3.7 $\pi^0\pi^0$ event yields before background subtraction 115

4.1 Veto detector thresholds 132
4.2 $K \to \pi^+\pi^-$ and $K \to \pi^0\pi^0$ MC event yields. 137

5.1 Summary of $K \to \pi^+\pi^-$ background levels 153
5.2 $\pi^+\pi^-$ event yields after background subtraction 153
5.3 Summary of $K \to \pi^0\pi^0$ background levels 153
5.4 $\pi^0\pi^0$ event yields after background subtraction 156

7.1 Summary of systematic errors due to acceptance upstream of the MA 172
7.2 Level 3 bias in $K \to \pi^+\pi^-$ trigger 177
7.3 Change in $Re(\epsilon'/\epsilon)$ with changes to DC efficiency simulation 178
7.4 Summary of systematic uncertainties in $Re(\epsilon'/\epsilon)$ from the $K \to \pi^+\pi^-$ analysis. 181
7.5 Level 1 inefficiencies in $K \to \pi^0\pi^0$ trigger 181
7.6 Level 2 inefficiencies in $K \to \pi^0\pi^0$ trigger 183
7.7 Level 3 inefficiencies in $K \to \pi^0\pi^0$ trigger 184
7.8 Summary of energy non-linearity systematic studies 192
7.9 Data-MC z shifts for hadronic $\pi^0\pi^0$ production in the regenerator and vacuum window. 197
7.10 Systematic errors due to backgrounds in the $K \to \pi^0\pi^0$ analysis. . . 199
7.11 Summary of systematic uncertainties in $Re(\epsilon'/\epsilon)$ from the $K \to \pi^0\pi^0$ analysis. 201

7.12 Summary of systematic uncertainties in $Re(\epsilon'/\epsilon)$ from the fitting procedure. 202
7.13 Summary of systematic uncertainties in $Re(\epsilon'/\epsilon)$. 205
7.14 Systematic uncertainties in kaon parameters 206

8.1 $Re(\epsilon'/\epsilon)$ results by year. 208
8.2 Summary of kaon sector parameter results. 213

ABSTRACT

We present precision measurements of the direct CP violation parameter, $Re(\epsilon'/\epsilon)$, the kaon parameters, Δm and τ_S, and the CPT tests, ϕ_{+-} and $\Delta\phi$, in neutral kaon decays. These results are based on the full dataset collected by the KTeV experiment at Fermi National Accelerator Laboratory during 1996, 1997, and 1999. This dataset contains $\sim$15 million $K \to \pi^0\pi^0$ decays and $\sim$69 million $K \to \pi^+\pi^-$ decays. We describe significant improvements to the precision of these measurements relative to previous KTeV analyses. We find $Re(\epsilon'/\epsilon) = [19.2 \pm 1.1(stat) \pm 1.8(syst)] \times 10^{-4}$, $\Delta m = (5265 \pm 10)\times 10^6\ \hbar s^{-1}$, and $\tau_S = (89.62 \pm 0.05)\times 10^{-12}$ s. We measure $\phi_{+-} = (44.09 \pm 1.00)^\circ$ and $\Delta\phi = (0.29 \pm 0.31)^\circ$; these results are consistent with CPT symmetry.

ACKNOWLEDGEMENTS

Thank you to my advisor, Ed Blucher, for choosing me to work on such a challenging and interesting analysis, and for making me run the marathon. Thank you also to the University of Chicago for taking me in under unusual circumstances and to everyone, especially Ed, who navigated all the beaurocracy required to make that possible. The intellectual environment here is very special and I am lucky to have been a part of it for so long.

Thank you to my collaborators on KTeV, especially Rick Kessler and Sasha Glazov, for all of your hard work on this analysis and everything you taught me. Thank you to the KTeV students who came before me, especially Val Prasad and Jim Graham, whose dissertations[1, 2] have proven invaluable.

Thank you to Fermilab, not only for providing the facility that made this experiment possible, but for creating such a pleasant atmosphere in which to live and work.

Thank you to UCLA for giving me an excellent foundation in physics during my first year graduate courses. Thank you to my friends and study partners from UCLA, Dave, Paul, Geno, Erik, and Kyle, with whom I learned so much and had so much fun. Thank you especially to Dave for being such a great friend against your will.

Thank you to my parents, John and Shirley Turner, who have always supported me in every way possible. I am grateful to have such loving and inspiring parents. I know that the confidence and curiousity required to take on this analysis comes from you.

Thank you to my husband, Matt, who gets me in ways that no one else can. I know how hard you worked to give me the time I needed to finish this analysis. I am grateful that your ultimate game was "so close" to my place and that Gleevec

is doing its job so well. I love you and the life we've made together. I'm looking forward to all the years we have ahead of us.

Thank you to my sons, Jack and Ellis, for being the amazing little boys that you are. You bring so much joy to our lives. Being your mother is my greatest privilege and first priority. I am taking a break from physics to be your Mommy full time but I know that when the time is right you will be proud of me for the work that I love as well as the time I've given to you.

Thank you to my dear sweet Moses who was my constant companion for eight years. You are probably the best thing that ever happened to me because loving you made so much that is beautiful about my life possible. I am so sorry that I couldn't protect you better. I wish that you were here with me to celebrate this accomplishment with the complete enthusiasm that you brought to everything you did. I love you and miss you so much. This dissertation is dedicated to the memory of your very special life.

CHAPTER 1
INTRODUCTION

The fourth definition of symmetry in my dictionary[3] is the one that we will be using for most of this dissertation.

> *4. the property of remaining invariant under certain changes – used of physical phenomena and of equations describing them*

The first definition,

> *1. beauty of form arising from balanced proportions*,

is often used to explain our attraction as physicists to the fourth, but I wonder if perhaps the truth is found in the reverse. Rather than seeking beauty in nature, I believe we see nature in that which we call beautiful.

1.1 Background

Noether's theorem[4] tells us that symmetries imply conservation laws, so symmetry is central to many of the most important ideas in physics. The discovery of a new symmetry, or of symmetry breaking, often leads to new understanding. In particle physics, the current belief is that, when combined, the three discrete symmetries of charge conjugation (C), parity (P), and time reversal (T) are a fundamental symmetry. Any local field theory that is invariant under Lorentz transformations is also invariant under CPT[5–8]. Since the Standard Model of particle physics and most extensions beyond the Standard Model are based on local field theories, there is strong evidence that CPT should be conserved.

The strong and electromagnetic interactions appear to be invariant under the individual operators C, P, and T, so it was once believed that the weak interaction

would be as well. The first hint of parity violation came in 1953 when Dalitz showed that the 2π and 3π decay modes of the K^+ required that the parent particles have opposite intrinsic parity even though they appeared to be (and in fact are) the same particle[9]. In 1956, Lee and Yang [10] suggested that parity violation could explain this so-called τ-θ puzzle and also proposed an experiment which could confirm parity violation. The experiment they suggested, the observation of angular asymmetry in the β-decay of spin-oriented nuclei, was first accomplished by Wu and collaborators[11] in 1957 using the decay electron from the β-decay of ^{60}Co. Their result was confirmed by several pion decay experiments the same year[12, 13]. It was immediately realized that these experiments demonstrated that charge conjugation was also violated. At the time, both experiment and theory pointed to the combination CP as the true symmetry.

CP violation was discovered in 1964 when Christenson, Cronin, Fitch, and Turlay [14] observed the decay of a long lived neutral kaon (believed to be K_2 which is CP odd) to $\pi^+\pi^-$ which is CP even. A year later it was confirmed that both K_S and K_L could decay to $\pi^+\pi^-$ when interference between the two states was observed using a regenerator[15]. Decays to the neutral final state $\pi^0\pi^0$ were shown to behave similarly [16, 17] which showed that the CP-violating asymmetry in K^0-$\bar{K}^0$ mixing is the primary source of CP violation in the kaon system.

The Standard Model of particle physics describes the strong interaction, the electroweak interaction, and the generational model of quarks and leptons. The coupling of quarks by the weak interaction can be described by the 3×3 unitary Cabibbo-Kobayashi-Maskawa (CKM) matrix[18]:

$$V = \begin{pmatrix} V_{ud} & V_{us} & V_{ub} \\ V_{cd} & V_{cs} & V_{cb} \\ V_{td} & V_{ts} & V_{tb} \end{pmatrix} \approx \begin{pmatrix} 1-\lambda^2/2 & \lambda & A\lambda^3(\rho - i\eta) \\ -\lambda & 1-\lambda^2/2 & A\lambda^2 \\ A\lambda^3(1-\rho-i\eta) & -A\lambda^2 & 1 \end{pmatrix} \tag{1.1}$$

In the Wolfenstein parameterization [19] given in Equation 1.1, $\lambda = sin\theta_C$ (the sine of the Cabibbo angle) and η parameterizes the level of CP violation. The unitarity condition means that the parameters in V can be written as three angles and a

complex phase. It is this complex phase which is responsible for all CP violation in the Standard Model; it can accommodate both indirect CP violation in K^0-$\bar{K}^0$ mixing and direct CP violation in the decays of neutral kaons.

While both direct and indirect CP violation are allowed by the Standard Model, direct CP violation was not observed until the 1990s. The first set of experiments in Europe and the United States did not agree well; the European experiment saw evidence for direct CP violation[20] while the US experiment was consistent with both direct CP violation and with no effect[21]. This led to a second round of experiments which, in 1999, definitively established the existence of direct CP violation[22, 23]. KTeV, the US experiment upon which this dissertation is based, announced the first definitive result.

The existence of CP violation is also of interest in astrophysics. The universe began with equal numbers of baryons and antibaryons, but in our current universe the matter-antimatter asymmetry appears to be large. In 1967 Sakharov proposed that a small baryon asymmetry may have been created in the early universe and that the three conditions needed for this to occur are[24]:

- baryon number violation
- C violation and CP violation
- interactions out of thermal equilibrium.

CP violation in the kaon system is a proof of concept for CP violation in that it confirms the existence of some level of CP violation in nature. However, CP violation which arises from a phase in the CKM matrix is not likely to be responsible for the baryon asymmetry of the universe as the effects of this phase in the early universe are small.[25]. So, the existence of non-Standard Model CP violation is suggested by astrophysics.

While Standard Model (and beyond the Standard Model) calculations of ϵ'/ϵ are not currently precise enough to detect any new physics in the level of CP violation in the kaon system, there may come a time when this measurement could be compared to calculations and used to support or rule out theories beyond the Standard Model.

1.2 Kaon Phenomenology

The neutral kaon $K^0(\bar{s}\mathrm{d})$ and its antiparticle $\bar{K}^0(\mathrm{s}\bar{d})$ are distinguishable only by strangeness quantum number. The strangeness quantum number is conserved in the strong interaction but violated in the weak interaction; therefore $K^0 \leftrightarrow \bar{K}^0$ transitions are allowed in weak interactions. This property of the kaon system leads to quantum mechanical mixing effects such as strangeness oscillation and regeneration.

In the absence of the weak interaction, K^0 and $\bar{K}^0$ are degenerate. Treating the weak Hamiltonian as a perturbation using standard perturbation theory shifts the degenerate levels by a small amount.

$$\Delta m_k \equiv |m_1 - m_2| = \langle K^0 \mid \hat{H}_w \mid \bar{K}^0 \rangle \tag{1.2}$$

The particles K_1 and K_2 are linear superpositions of K^0 and $\bar{K}^0$ which diagonalize the perturbation; they have masses m_1 and m_2.

$$\begin{aligned} \mid K_1 \rangle &= \frac{1}{\sqrt{2}}[\mid K^0\rangle + \mid \bar{K}^0\rangle] \\ \mid K_2 \rangle &= \frac{1}{\sqrt{2}}[\mid K^0\rangle - \mid \bar{K}^0\rangle] \end{aligned} \tag{1.3}$$

The two states have opposite eigenvalues under CP transformation; therefore one can decay to a CP even final state while the other is forced to decay to a CP odd final state. The difference in phase space available to the CP even 2π and CP odd semileptonic or 3π final states means that K_1 and K_2 have very different lifetimes.

Strangeness oscillation, the phenomenon in which an initially pure $\mid K^0\rangle$ or $\mid \bar{K}^0\rangle$ beam evolves over time into a state of mixed strangeness, is described in terms of the states $\mid K_1\rangle$ and $\mid K_2\rangle$ which have different masses and lifetimes. Regeneration occurs when a beam of long lived kaons passes through matter. The long lived kaon is a linear combination of K^0 and $\bar{K}^0$; because K^0 and $\bar{K}^0$ have opposite strangeness they interact differently which matter so passing through matter changes their admixture in the beam leading to a regeneration of short lived kaons[26]. For example, strong

and electromagnetic interactions dominate the scattering of a K_L beam on matter nuclei. Since strangeness is conserved by the strong interaction, processes such as $\bar{K}^0 p \to \Lambda\pi^+$ have no K^0 corollary. Therefore, the total cross-section of $\bar{K}^0$ on the nuclei is greater than the total cross-section of K^0 and the admixture of K^0 and $\bar{K}^0$ in the beam changes.

To further analyze kaon mixing and CP violation, we must be more explicit. The following discussion follows Belusevic[26] and Sachs[27]. Spacial inversion, or parity transformation (P), is maximally violated in the weak interaction. Particle-antiparticle exchange, or charge conjugation (C) is also violated by the weak interaction. It was once believed that the combination of these operators (CP) was a symmetry of nature and would be conserved by the weak interaction. K_1 and K_2 are CP eigenstates with eigenvalues CP=+1 and CP=-1 respectively. In the absence of CP violation, these would also be the weak eigenstates. Since K_1 is CP even, it would decay to the two-pion final states $\pi^+\pi^-$ and $\pi^0\pi^0$. The CP odd K_2 would have to decay semileptonically or to the three-pion final states $\pi^+\pi^-\pi^0$ and $\pi^0\pi^0\pi^0$. In this scenario, K_1 would be the short lived kaon and K_2 would be the long lived kaon because of the reduction in phase space associated with the semileptonic and three-pion final states. The true situation is not so far from this scenario; the weak interaction may be treated as a small perturbation, so the weak eigenstates are small perturbations away from the CP eigenstates. To find the weak eigenstates, we must solve the Schr$\ddot{o}$edinger-like equation

$$i\frac{d}{dt}\begin{pmatrix} a_1 \\ a_2 \end{pmatrix} = \mathcal{H}_{eff}\begin{pmatrix} a_1 \\ a_2 \end{pmatrix} \tag{1.4}$$

where the effective Hamiltonian $\mathcal{H}_{eff}$ can be written as two matrices:

$$\mathcal{H}_{eff} = \mathbf{M} - \frac{i}{2}\mathbf{\Gamma} \tag{1.5}$$

$$= \left[\begin{pmatrix} M_{11} & M_{12} \\ M_{12}^* & M_{22} \end{pmatrix} - \frac{i}{2}\begin{pmatrix} \Gamma_{11} & \Gamma_{12} \\ \Gamma_{12}^* & \Gamma_{22} \end{pmatrix}\right]. \tag{1.6}$$

Here $\mathbf{M}$ is the mass matrix and $\mathbf{\Gamma}$ is the decay matrix. The eigenvalue equation is

$$\mathcal{H}_{eff} \mid K_{S,L}\rangle = \lambda_{S,L} \mid K_{S,L}\rangle. \tag{1.7}$$

$\mathbf{M}$ and $\mathbf{\Gamma}$ are both Hermitian, but $\mathcal{H}_{eff}$ is not, so the eigenvalues $\lambda_{S,L}$ are complex and may be written as

$$\lambda_{S,L} = m_{S,L} - \frac{i}{2}\Gamma_{S,L}. \tag{1.8}$$

Solving

$$\mathcal{H}_{eff} \mid K_{S,L}\rangle = (m_{S,L} - \frac{i}{2}\Gamma_{S,L}) \mid K_{S,L}\rangle \tag{1.9}$$

we find that the weak eigenstates are

$$\begin{aligned} \mid K_S\rangle &= \frac{1}{\sqrt{1+|\epsilon-\Delta|^2}}(\mid K_1\rangle + (\epsilon-\Delta) \mid K_2\rangle) \\ \mid K_L\rangle &= \frac{1}{\sqrt{1+|\epsilon+\Delta|^2}}(\mid K_2\rangle + (\epsilon+\Delta) \mid K_1\rangle) \end{aligned} \tag{1.10}$$

where ϵ and Δ are small and defined by

$$\epsilon = \frac{\langle \bar{K}^0 \mid \mathcal{H}_{eff} \mid K^0\rangle - \langle K^0 \mid \mathcal{H}_{eff} \mid \bar{K}^0\rangle}{2\Delta m + i\Delta\Gamma} \tag{1.11}$$

and

$$\Delta = \frac{\langle K^0 \mid \mathcal{H}_{eff} \mid K^0\rangle - \langle \bar{K}^0 \mid \mathcal{H}_{eff} \mid \bar{K}^0\rangle}{2\Delta m + i\Delta\Gamma}. \tag{1.12}$$

Note that Δm and $\Delta\Gamma$ are defined such that both are positive: $\Delta m = m_L - m_S$ and $\Delta\Gamma = \Gamma_S - \Gamma_L$.

To understand the physical meaning of ϵ we apply the CP transformation to Equation 1.11 by realizing that this is equivalent to substituting $K^0 \leftrightarrow \bar{K}^0$. We find that $\epsilon \rightarrow -\epsilon$, so ϵ is a measure of CP violation. The short lived eigenstate is mostly CP even K_1 with a small admixture of CP odd K_2 while the long lived eigenstate is mostly CP odd with a little bit (ϵ) of CP even. We state that ϵ parameterizes CP violation in the mixing. The physical significance of Δ is derived from the fact that CPT conservation requires the same lifetimes and total decay amplitudes for

particles and anti-particles. Therefore, assuming CPT conservation yields

$$\langle K^0 \mid \mathcal{H}_{eff} \mid K^0 \rangle = \langle \bar{K}^0 \mid \mathcal{H}_{eff} \mid \bar{K}^0 \rangle, \tag{1.13}$$

so $\Delta = 0$ in the absence of CPT violation.

We can now express the weak eigenstates in terms of the states of definite strangeness, K^0 and $\bar{K}^0$.

$$\begin{aligned} \mid K_S \rangle &= \frac{1}{\sqrt{2(1+|\epsilon-\Delta|^2)}} \left[(1+\epsilon-\Delta) \mid K^0 \rangle + (1-\epsilon+\Delta) \mid \bar{K}^0 \rangle \right] \quad (1.14) \\ \mid K_L \rangle &= \frac{1}{\sqrt{2(1+|\epsilon+\Delta|^2)}} \left[(1+\epsilon+\Delta) \mid K^0 \rangle - (1-\epsilon-\Delta) \mid \bar{K}^0 \rangle \right] \end{aligned}$$

We now consider the K_L and K_S decay amplitudes to the $\pi\pi$ final states. For a state described by

$$\mid 0 \rangle = c_S \mid K_S \rangle + c_L \mid K_L \rangle \tag{1.15}$$

at t=0, the state at later time, t, is given by

$$\mid t \rangle = c_S e^{-im_S t} e^{-\Gamma_S t/2} \mid K_S \rangle + c_L e^{-im_L t} e^{-\Gamma_L t/2} \mid K_L \rangle. \tag{1.16}$$

The decay rate at time t is

$$|A_f(t)|^2 = |c_S A_{fS}|^2 \left\{ e^{-\Gamma_S t} + 2Re \left[\frac{c_L}{c_S} \frac{A_{fL}}{A_{fS}} e^{-i\Delta m t} \right] e^{-(\Gamma_S+\Gamma_L)t/2} + \left| \frac{c_L}{c_S} \right|^2 \left| \frac{A_{fL}}{A_{fS}} \right|^2 e^{-\Gamma_L t} \right\}. \tag{1.17}$$

The $K \to \pi\pi$ decay rate will contain an interference term proportional to

$$\eta_{\pi\pi} = A_{\pi\pi,L}/A_{\pi\pi,S}. \tag{1.18}$$

Using Equation 1.14 we find

$$\eta_{\pi\pi} = \epsilon + \Delta + \epsilon_{\pi\pi} \tag{1.19}$$

where

$$\epsilon_{\pi\pi} = \frac{A_{\pi\pi} - \bar{A}_{\pi\pi}}{A_{\pi\pi} + \bar{A}_{\pi\pi}}. \tag{1.20}$$

For a CP invariant system $A_{\pi\pi} = \bar{A}_{\pi\pi}$, so $\epsilon_{\pi\pi}$ is a measure of direct CP violation in $K \to \pi\pi$ decays.

The possible $\pi\pi$ final states are $\pi^+\pi^-$ and $\pi^0\pi^0$. In order to calculate the decay amplitudes we must consider final state interactions, which requires an isospin analysis. Only the symmetric isospin states $I = 0$ and $I = 2$ are allowed as final states for the two pions. Using the Clebsch-Gordan coefficients we find

$$\begin{aligned} A_{+-} &= \frac{1}{\sqrt{3}}(\sqrt{2}A_0 + A_2) \\ A_{00} &= \frac{1}{\sqrt{3}}(A_0 - \sqrt{2}A_2) \end{aligned} \tag{1.21}$$

We now write the decay amplitudes in terms of their reduced amplitudes and phases and use Equation 1.21 to rewrite Equation 1.20. Ultimately, [1] we find that

$$\begin{aligned} \epsilon_{+-} &= \frac{\epsilon'}{1+\omega} \\ \epsilon_{00} &= \frac{-2\epsilon'}{1-2\omega} \end{aligned} \tag{1.22}$$

where

$$\epsilon' = \frac{i}{\sqrt{2}} \frac{Im(a_2)}{a_0} e^{i\delta}, \tag{1.23}$$

$$\omega = \frac{1}{\sqrt{2}} \frac{Re(a_2)}{a_0} e^{i\delta}, \tag{1.24}$$

$\delta = \delta_2 - \delta_0$, and we have chosen the convention that a_0 is real.

We can now calculate

$$\langle \pi^+\pi^- \mid \mathcal{H}_{eff} \mid K_2 \rangle = A_0 \frac{2}{\sqrt{3}} \frac{e^{i\delta_2}}{e^{i(\delta_2 - \delta_0)}} \epsilon'. \tag{1.25}$$

[1] See Sachs[27] page 209-211 for a full treatment.

This means that the CP odd K_2 can decay into a CP even two-pion final state and that this will occur at a rate proportional to ϵ'. So, ϵ is a measure of CP violation in the mixing and ϵ' is a measure of direct CP violation in the the decay amplitudes. The significance of these parameters is illustrated in Figure 1.1.

Plugging Equations 1.22 in to Equation 1.19 and assuming CPT conservation, we find the ratios of decay amplitudes to be

$$\begin{aligned} \eta_{+-} &= \epsilon + \frac{\epsilon'}{1+\omega} \\ \eta_{00} &= \epsilon - \frac{2\epsilon'}{1-2\omega}. \end{aligned} \tag{1.26}$$

The ΔI $= 1/2$ rule implies that ω is small, so we can make the approximation

$$\begin{aligned} \eta_{+-} &= \epsilon + \epsilon' \\ \eta_{00} &= \epsilon - 2\epsilon' \end{aligned} \tag{1.27}$$

which shows that η_{+-} and η_{00} can be different, that the difference is parameterized by ϵ', and that any difference between η_{+-} and η_{00} is evidence of direct CP violation.

1.3 Calculating ϵ'/ϵ

The following discussion closely follows the review by Bertolini, Eeg, and Fabbrichesi [28] and is intended to give the reader a flavor of what is involved in the calculations rather than a rigorous treatment. To calculate ϵ'/ϵ one must calculate the decay amplitudes

$$\epsilon'/\epsilon = \frac{1}{\sqrt{2}} \left(\frac{\langle (\pi\pi)_{(I=2)} \mid \mathcal{L}_W \mid K_L \rangle}{\langle (\pi\pi)_{(I=0)} \mid \mathcal{L}_W \mid K_L \rangle} - \frac{\langle (\pi\pi)_{(I=2)} \mid \mathcal{L}_W \mid K_S \rangle}{\langle (\pi\pi)_{(I=0)} \mid \mathcal{L}_W \mid K_S \rangle} \right) \tag{1.28}$$

The framework for calculating these amplitudes is an effective theory in which the higher scales are integrated out retaining only effective operators made of lighter degrees of freedom. The short distance physics (consisting of the the lighter degrees of freedom) is encoded in Wilson coefficients which multiply the effective operators.

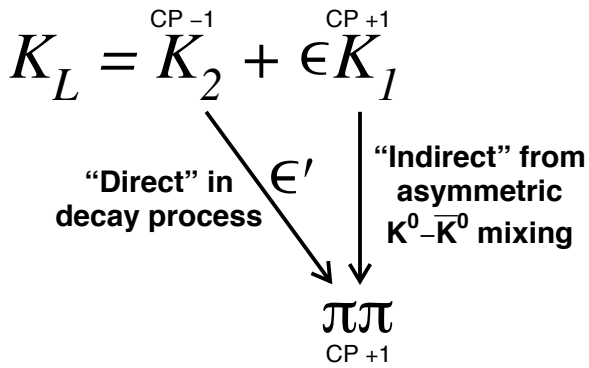

Figure 1.1: Diagram of the significance of the parameters ϵ and ϵ'.

The $\Delta S = 1$ quark effective Lagrangian used for calculating ϵ'/ϵ is

$$\mathcal{L}_W = -\sum_i C_i(\mu) Q_i(\mu) \tag{1.29}$$

where the $C_i(\mu)$ depend on the Fermi coupling (G_F), the CKM matrix elements, and the Wilson coefficients. In turn, the Wilson coefficients depend on the masses m_t, m_W, m_B, and m_c, the intrinsic QCD scale (Λ_{QCD}), and the renormalization scale (μ). The Q_i are the effective four quark-operators. The following ten operators are standard.

$$\left.\begin{aligned} Q_1 &= (\bar{s}_\alpha u_\beta)_{V-A}(\bar{u}_\beta d_\alpha)_{V-A} \\ Q_2 &= (\bar{s}u)_{V-A}(\bar{u}d)_{V-A} \end{aligned}\right\} \quad \text{W exchange}$$

$$\left.\begin{aligned} Q_{3,5} &= (\bar{s}d)_{V-A}\sum_q (\bar{q}q)_{V\mp A} \\ Q_{4,6} &= (\bar{s}_\alpha d_\beta)_{V-A}\sum_q (\bar{q}_\beta q_\alpha)_{V\mp A} \end{aligned}\right\} \quad \text{QCD penguin loops}$$

$$\left.\begin{aligned} Q_{7,9} &= \frac{3}{2}(\bar{s}d)_{V-A}\sum_q \hat{e}_q(\bar{q}q)_{V\pm A} \\ Q_{8,10} &= \frac{3}{2}(\bar{s}_\alpha d_\beta)_{V-A}\sum_q \hat{e}_q(\bar{q}_\beta q_\alpha)_{V\pm A} \end{aligned}\right\} \quad \text{electroweak penguin loops} \tag{1.30}$$

Here α and β are color indices, $\hat{e}_q$ are the quark charges, and (V $\pm$ A) are the Dirac structure $\gamma_\mu(1 \pm \gamma_5)$. As noted, the operators arise from different diagrams of the theory. CP violation involves the loop induced operators Q_3 - Q_{10}.

The calculation of ϵ'/ϵ is divided into a short-distance (perturbative) part and a long-distance (non-perturbative) part. The short-distance calculation of the Wilson coefficients of all the relevant operators is well understood at next-to-leading-order[29–34]. The long-distance part is more uncertain and is being approached using lattice QCD, phenomenological estimates, and QCD-like models combined with chiral perturbation theory. The pie chart in Figure 1.2 shows the relative contributions of these operators to ϵ'/ϵ in one approximation.[2] The destructive interference between the gluonic and electroweak loops makes it difficult to calculate ϵ'/ϵ with the desired accuracy.

1.4 Theory Status of ϵ'/ϵ

Table 1.1 lists some theoretical predictions of $Re(\epsilon'/\epsilon)$ within the Standard Model. As described in Section 1.3, the difficulty with these calculations is the determination of the long-distance matrix elements. Cancellations between the QCD and electroweak contributions to the value of ϵ'/ϵ increase the uncertainty on these calculations. The largest source of difference in the predictions of ϵ'/ϵ is the size of the hadronic matrix element of the gluonic penguin Q_6 in the various techniques. This is because this matrix element contains significant higher order chiral contributions to the I=0 amplitudes[35].

[2]The approximation used in 1.2 is the Vacuum Saturation Approximation.

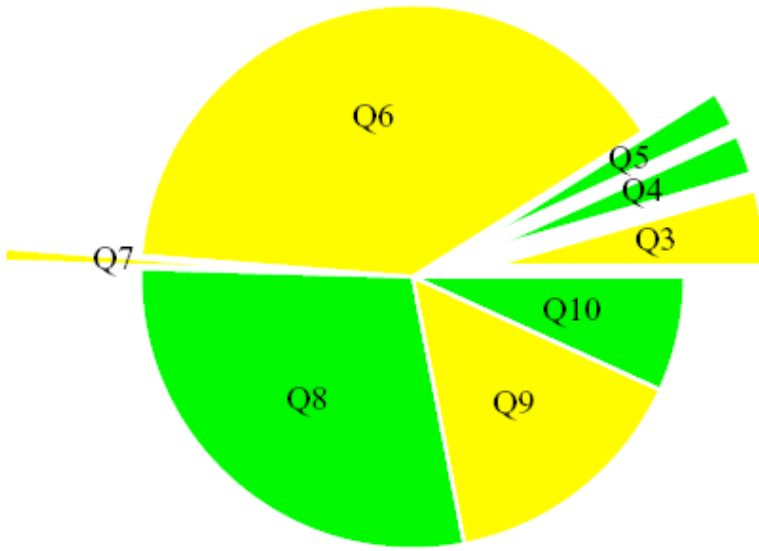

Figure 1.2: Relative contributions to ϵ'/ϵ of the effective operators. Operators giving a positive (negative) contribution are colored light (dark) gray. Figure courtesy of S. Bertolini [35].

1.5 Measuring $Re(\epsilon'/\epsilon)$

In Section 1.2 we determined that η_{+-} and η_{00}, the ratios of K_L to K_S decay amplitudes to the $\pi^+\pi^-$ and $\pi^0\pi^0$ final states, are related to ϵ and and ϵ' by:

$$\eta_{+-} = \frac{A(K_L \to \pi^+\pi^-)}{A(K_S \to \pi^+\pi^-)} = \epsilon + \epsilon' \tag{1.31}$$
$$\eta_{00} = \frac{A(K_L \to \pi^0\pi^0)}{A(K_S \to \pi^0\pi^0)} = \epsilon - 2\epsilon'.$$

Measurements of $\pi\pi$ phase shifts [48] show that the phases of ϵ and ϵ' are approximately equal in the absence of CPT violation. Therefore, $Re(\epsilon'/\epsilon)$ is a measure of direct CP violation and $Im(\epsilon'/\epsilon)$ is a measure of CPT violation. Experimentally, this means that we may measure $Re(\epsilon'/\epsilon)$ from the double ratio of the pion decay rates of K_L and K_S:

$$1 + 6Re(\epsilon'/\epsilon) \approx \left|\frac{\eta_{+-}}{\eta_{00}}\right|^2 = \frac{\Gamma(K_L \to \pi^+\pi^-)/\Gamma(K_S \to \pi^+\pi^-)}{\Gamma(K_L \to \pi^0\pi^0)/\Gamma(K_S \to \pi^0\pi^0)} \tag{1.32}$$

Method	$Re(\epsilon'/\epsilon)$ ($\times 10^{-4}$)	Year	Reference
Lattice Gauge	4.6 ± 3.0	1997	Ciuchini [36]
Chiral Quark Model	17^{+14}_{-10}	1998	Bertolini *et al.* [37]
Phenomenological	8.5 ± 5.9	1999	Buras[38]
Lattice Gauge	4 ± 7	1999	Ciuchini *et al.* [39]
Chiral Quark Model	< 3.3	1999	Bel'kov *et al.* [40]
Chiral Quark Model	34 ± 18	2000	Bijnens and Prades [41]
$1/N_C$ expansion	7-24.7	2000	Hambye *et al.* [42]
$1/N_C$ expansion	17 ± 9	2001	Pallante, Pich, and Scimeni [43]
Chiral Quark Model	20 ± 9	2001	Wu [44]
Phenomenological	$\leq (22 \pm 9)$	2001	Narison [45]
$1/N_C$ expansion	45 ± 30	2003	Sánchez [46]
$1/N_C$ expansion	19^{+11}_{-9}	2004	Pich [47]

Table 1.1: Some calculations of $Re(\epsilon'/\epsilon)$ within the Standard Model. "Method" refers to the approach used to calculate the long-distance (non-perturbative) part of the matrix elements. The largest source of difference among these predictions is the size of the matrix element of the gluonic penguin, Q_6.

1.6 Experimental Status of $Re(\epsilon'/\epsilon)$

Since the early 1990s, a series of measurements of $Re(\epsilon'/\epsilon)$ have been made by experiments at the European Center for Nuclear Research (CERN) and the Fermi National Accelerator Laboratory (FNAL). The CERN experiments are NA31 and NA48; the FNAL experiments are E731 and KTeV. While all four experiments measure $Re(\epsilon'/\epsilon)$ using the double ratio of $K \to \pi\pi$ decay rates, there are differences in experimental technique. The primary difference between KTeV and NA48 is that KTeV uses a Monte Carlo simulation to correct for acceptance differences while NA48 relies on a reweighting technique. Figure 1.3 depicts the history of experimental results over the last 15 years[3]. The measurements in 1999 established that $Re(\epsilon'/\epsilon)$ is greater than zero and therefore that direct CP violation occurs in $K \to \pi\pi$ decays. The goal of the later measurements is to reduce the uncertainty on the value of $Re(\epsilon'/\epsilon)$ by analyzing all available data and to make full use of the available statistics by reducing

[3]Later reanalysis of the the KTeV 96/97a data changed this result from $(28.0 \pm 4.1)\times 10^{-4}$ (the value published in 1999) to $(23.2 \pm 4.4)\times 10^{-4}$.

the systematic errors associated with these measurements. The final measurement from NA48[49] was released in 2002 and is

$$Re(\epsilon'/\epsilon) = [14.7 \pm 2.2] \times 10^{-4}. \tag{1.33}$$

The most recent measurement from KTeV[50] was published in 2003 and is

$$\begin{aligned} Re(\epsilon'/\epsilon) &= [20.7 \pm 1.48(stat) \pm 2.39(syst)] \times 10^{-4} \\ &= [20.7 \pm 2.8] \times 10^{-4}. \end{aligned} \tag{1.34}$$

These results supercede earlier NA48 and KTeV measurements. The current value quoted by the PDG[51] is

$$Re(\epsilon'/\epsilon) = [16.5 \pm 2.6] \times 10^{-4}, \tag{1.35}$$

where the error has been scaled by 1.6 according to the PDG procedure for combining results. The measurement described in this dissertation is the final KTeV measurement of $Re(\epsilon'/\epsilon)$. It includes all KTeV data and supercedes previous KTeV measurements.

1.7 Measuring Kaon Sector Parameters

In Equation 1.17 we see that the kaon decay rate for a superposition of K_L and K_S states at time t has a term proportional to e^{-t/τ_S} and an interference term proportional to $\cos(\Delta m t + \phi_\eta)$. The z-vertex distributions of $K_S \to \pi^+\pi^-$ and $K_S \to \pi^0\pi^0$ decays are sensitive to the K_S lifetime. The $K \to \pi^+\pi^-$ and $K \to \pi^0\pi^0$ decay distributions from a beam containing a K_S and a K_L component are sensitive to the interference term and thus Δm. KTeV fits for Δm and τ_S simultaneously using decays from a beam containing a mixture of K_L and K_S. We perform these fits separately for the charged and neutral final states and report a weighted average; the charged final state has the better statistical precision. We use $K \to \pi^+\pi^-$ decays to fit for ϕ_{+-}. $\Delta\phi$ is defined as the difference $\phi_{00} - \phi_{+-}$ and for small $|\epsilon'/\epsilon|$ is related

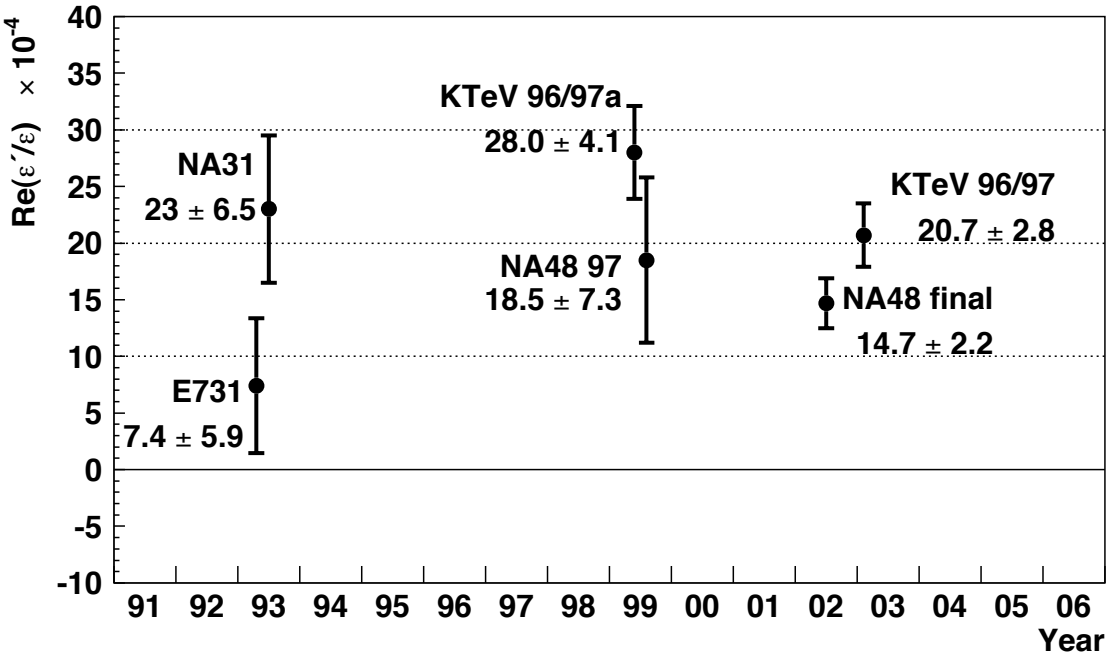

Figure 1.3: History of published measurements of $Re(\epsilon'/\epsilon)$ prior to this result. References are [20–23, 49, 50].

to $Im(\epsilon'/\epsilon)$ by

$$\Delta\phi \approx -3Im(\epsilon'/\epsilon) \tag{1.36}$$

We measure $\Delta\phi$ by fitting for both $Re(\epsilon'/\epsilon)$ and $Im(\epsilon'/\epsilon)$ simultaneously. The phases ϕ_{+-} and ϕ_{00} are expected to be equal to the superweak phase in the absence of CPT violation, so these measurements are CPT tests. The details of all of these fits are described in Chapter 6.

1.8 Experimental Status of Kaon Sector Parameters

The current PDG average values for the kaon sector parameters are[51]

$$\begin{aligned} \Delta m &= (5290 \pm 16)\times 10^{6}\ \hbar \mathrm{s}^{-1} \\ \tau_S &= (89.53 \pm 0.05)\times 10^{-12}\ \mathrm{s} \\ \phi_{+-} &= (43.4 \pm 0.7)^{\circ} \\ \Delta\phi &= (0.2 \pm 0.4)^{\circ} \end{aligned} \tag{1.37}$$

Here the fits for Δm and τ_S assume CPT is conserved, but the fits for the phases do not. Figures 1.4, 1.5, and 1.6 show the experimental results that go into the PDG averages for the kaon sector parameters Δm, τ_S, and ϕ_{+-}. The PDG value for $\Delta\phi$ includes only the KTeV result from 2003 ($\Delta\phi = (0.39 \pm 0.50)^{\circ}$)[50] and a combined result from E731 and E773 ($\Delta\phi = -0.30 \pm 0.88)^{\circ}$)[52].

1.9 Personal Perspective

The results presented in this dissertation are the culmination of work beginning many years ago and involving many collaborators. The measurement of $Re(\epsilon'/\epsilon)$ using the KTeV detector has been the subject of three previous dissertations from the University of Chicago: Peter Shawhan[60], James Graham[2], and Valmiki Prasad[1]. The previous KTeV measurement using data collected in 1996 and 1997 was described in detail in a 2003 PRD[50]. The current result builds on the work that came before it by adding data taken during 1999 and by making significant improvements to the Monte Carlo simulation and the data analysis. This dissertation will present a complete summary of the detector and the analysis, but will emphasize those parts of the detector and analysis that I worked on personally or that have changed significantly since the 2003 PRD. During 1999 data collection I was responsible for the maintenance and calibration of the regenerator and the photon veto detectors. My analysis efforts have focused on $K \to \pi^0\pi^0$ including the calibra-

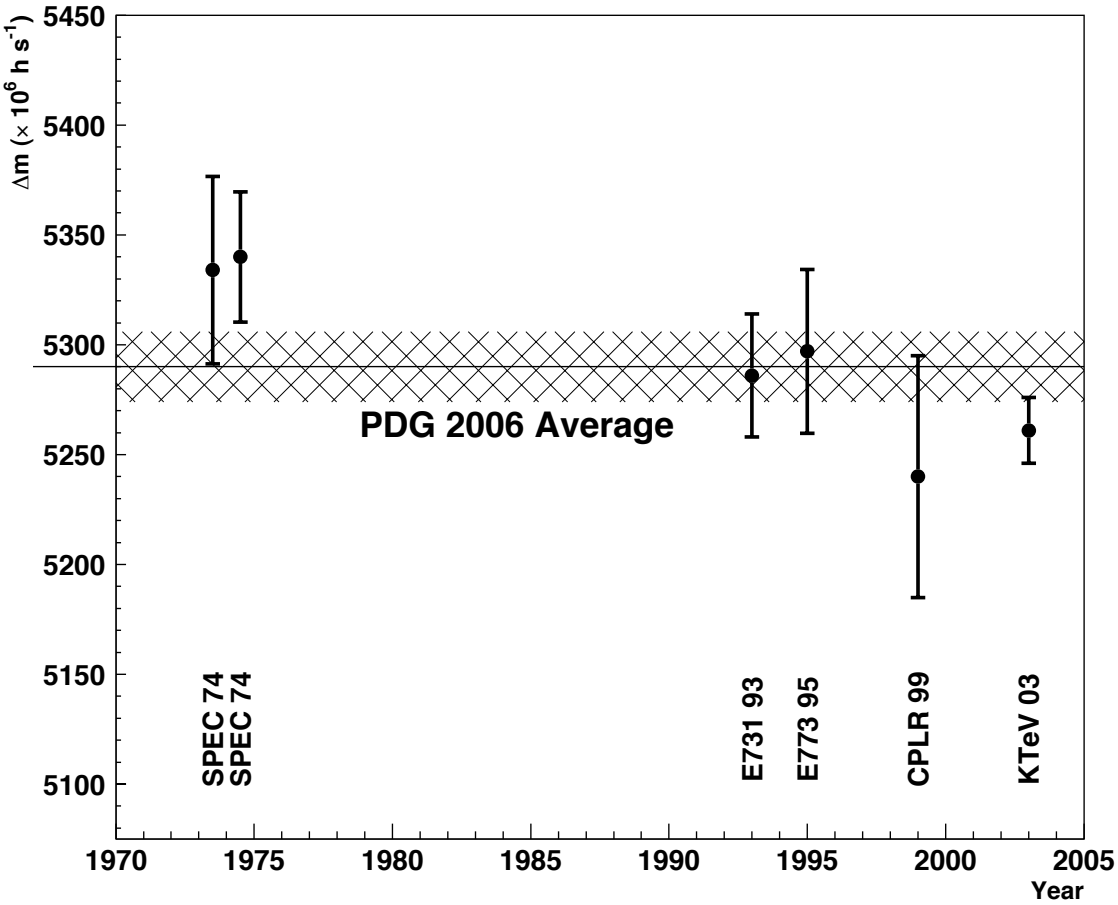

Figure 1.4: Measurements of Δm used in the PDG average prior to this result. References are [50, 52–56].

tion of the CsI calorimeter, the simulation of electromagnetic showers in the Monte Carlo, and the reconstruction and analysis of $K \to \pi^0\pi^0$ decays.

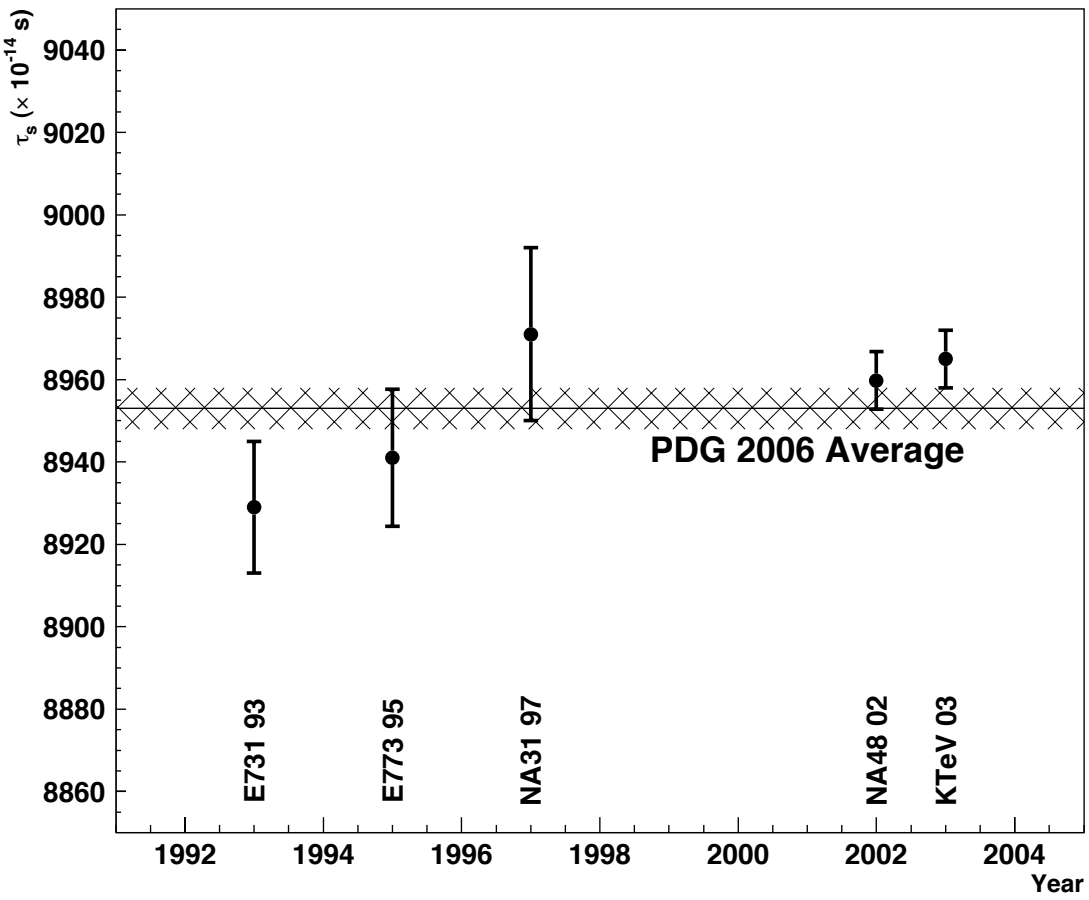

Figure 1.5: Measurements of τ_S used in the PDG average prior to this result. References are [50, 52, 55, 57, 58].

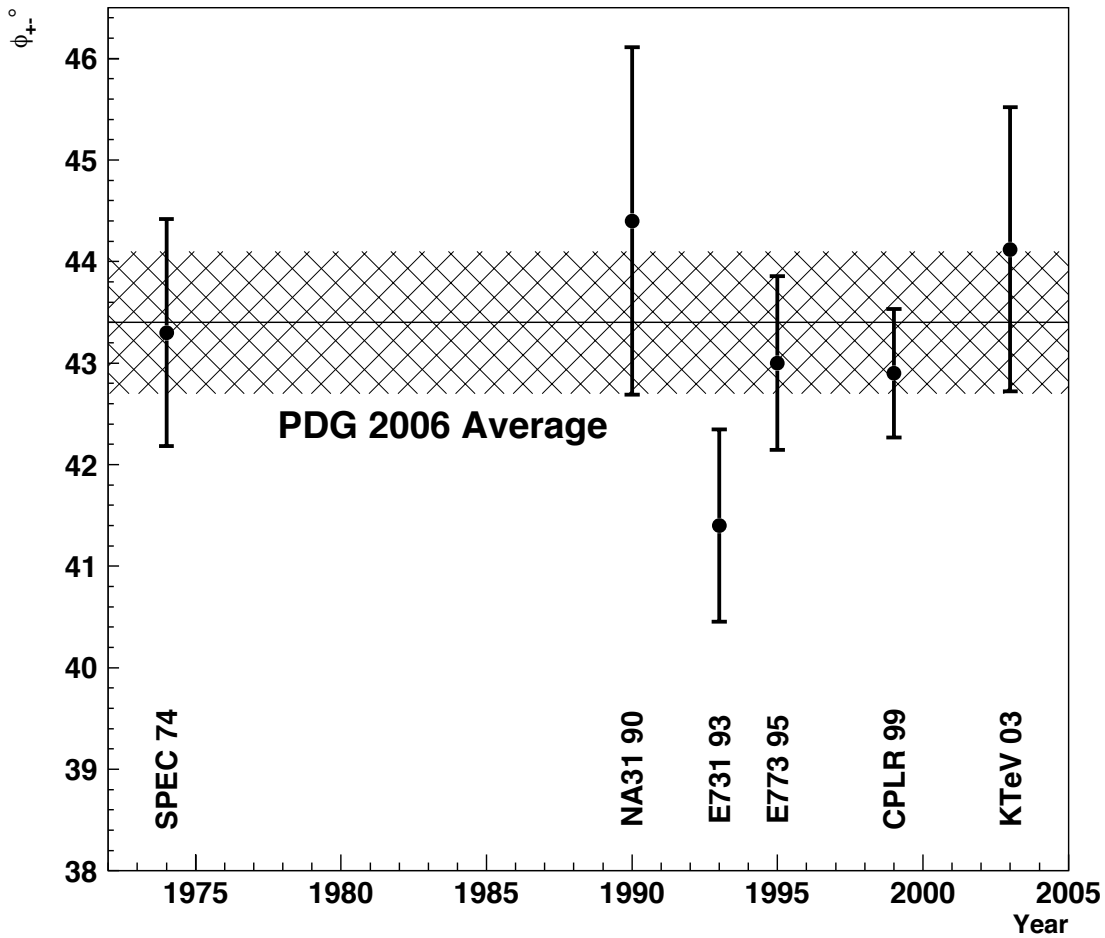

Figure 1.6: Measurements of ϕ_{+-} used in the PDG average prior to this result. References are [50, 52, 54–56, 59].

CHAPTER 2
THE KTEV EXPERIMENT

2.1 Experimental Strategy

We measure $Re(\epsilon'/\epsilon)$ by measuring the decay rates of K_L and K_S to the two-pion final states $\pi^+\pi^-$ and $\pi^0\pi^0$:

$$\frac{\Gamma(K_L \to \pi^+\pi^-)/\Gamma(K_S \to \pi^+\pi^-)}{\Gamma(K_L \to \pi^0\pi^0)/\Gamma(K_S \to \pi^0\pi^0)} = \left|\frac{\eta_{+-}}{\eta_{00}}\right|^2 \approx 1 + 6Re(\epsilon'/\epsilon) \tag{2.1}$$

This measurement requires a source of K_S and K_L decays and a detector capable of reconstructing both the charged and neutral final states. KTeV uses protons from the Fermilab Tevatron incident on a fixed target to produce two identical K_L beams and then takes advantage of the regeneration phenomenon by placing a regenerator in one of the beams to create a coherent $\mid K_L\rangle + \rho \mid K_S\rangle$ state. Here ρ is the regeneration amplitude; its value is determined by the properties of the regenerator and is such that most of the $K \to \pi\pi$ decays collected in the regenerator beam are K_S decays. We collect $K \to \pi^+\pi^-$ and $K \to \pi^0\pi^0$ decays in each beam simultaneously in an evacuated decay volume. Downstream of the vacuum region, charged pions from $K \to \pi^+\pi^-$ decays are detected in a spectrometer consisting of four drift chambers, two of which are located on each side of a dipole magnet. The drift chambers measure the positions of the charged particles; the momentum of each particle is determined from the bend angle in the magnet and is calibrated using the kaon mass. Photons from the electromagnetic decay of the neutral pions from $K \to \pi^0\pi^0$ decays are detected in a pure Cesium Iodide (CsI) calorimeter. The calorimeter is segmented to allow reconstruction of the photon positions; the energy deposit is calibrated using electrons from $K_L \to \pi^\pm e^\mp \nu$ decays. The decay and detector regions are surrounded by a veto system to reduce backgrounds from

scattered kaons, interactions in the detector, and other kaon decay modes. We use a Monte Carlo simulation to correct for the acceptance difference between $K \to \pi\pi$ decays in the vacuum and regenerator beams; this acceptance difference is due to the different decay vertex distributions resulting from the large difference in K_L and K_S lifetimes. The simulation includes geometric effects, detector efficiencies, and the effects of accidental activity. The simulation is checked using distributions from high statistics samples of $K_L \to \pi^{\pm}e^{\mp}\nu$ and $K_L \to \pi^0\pi^0\pi^0$ decays as well as the signal decay modes. Backgrounds to the signal modes are simulated using the Monte Carlo, normalized to the data, and subtracted. The $Re(\epsilon'/\epsilon)$ measurement is made by inputting the background subtracted numbers of $K \to \pi^+\pi^-$ and $K \to \pi^0\pi^0$ decays collected in each beam along with their acceptances from the Monte Carlo to a fitting program which accounts for the effect of $K_L - K_S$ interference in the regenerator beam. By adjusting the binning and CPT assumptions, we can also use the fitter to extract measurements of the other kaon parameters Δm, τ_S, ϕ_{+-}, and $\Delta\phi$.

2.2 Beam

The KTeV kaon beams are produced by a beamline of magnets, absorbers, and collimators which clean and collimate the products of a proton beam incident on a fixed target. Figure 2.1 is a top view of the KTeV beamline.

The protons are provided by the Fermilab Tevatron which delivers $\sim 3 \times 10^{12}$ 800 GeV/c protons in a 20 second spill once every minute.[1] The proton beam has a 53 MHz RF structure so that the protons are clumped in 1 ns wide buckets arriving every 19 ns. The protons are incident on a beryllium oxide (BeO) target which is 3×3 mm^2 transverse to the beam and 30 cm long. The length corresponds to about one proton interaction length. The angle of incidence on the target is 4.8 mrad with respect to a line from the target to the center of the detector; this targeting angle is chosen as a compromise between increasing kaon flux at small angles and reducing the neutron-to-kaon ratio at large angles.

[1]The spill duty cycle for 1999 data improved to 40 second spills every 80 seconds.

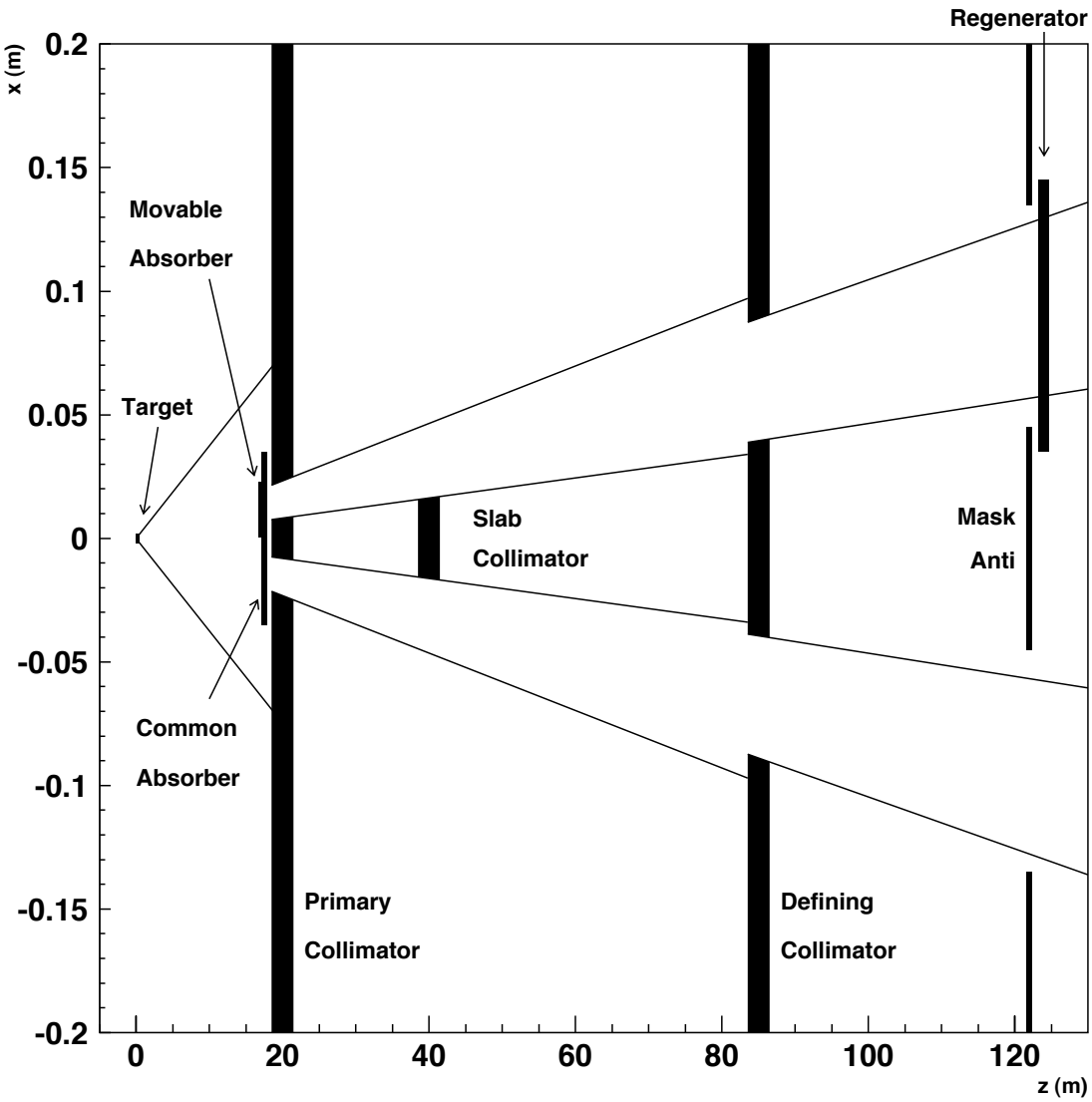

Figure 2.1: Schematic of the KTeV beamline. Figure courtesy of P. Shawhan [60].

The KTeV coordinate system is defined relative to the center of the BeO target. The positive z-axis points from the target to the center of the detector and the positive y-axis points up. The positive x-axis points to the left if the observer is facing downstream. The z-axis points roughly north and the x-axis points roughly west.

Immediately downstream of the target, the beam consists of protons, muons, and other charged particles, neutral kaons, neutrons, photons, and hyperons. This beam is cleaned and collimated into two kaon beams in a beamline which is about 100 m long.

A series of four sweeping magnets located from $z = 2$-90 m remove the remaining primary photons and muons produced in the target, absorbers, and collimators. The common absorber, located at $z = 18.5$ m, consists of a 7.62 cm thick slab of lead followed by a 52.3 cm slab of beryllium. The lead absorbs photons from the beam and the beryllium increases the kaon-to-neutron ratio by transmitting a higher fraction of kaons than neutrons. The common absorbers transmit about 19% of the incident kaons and about 10% of the incident neutrons. It is important to further reduce the neutron-to-kaon ratio in the regenerator beam to reduce the rate of hadronic interactions in the regenerator. The movable absorber at $z = 19$ m is made of 45.7 cm of beryllium, covers only one beam at a time, and alternates between the beams synchronously with the regenerator. It provides an additional attenuation factor of 3.8 for neutrons and 2.3 for kaons in the regenerator beam. The kaon-to-neutron ratio is about 0.77 in the vacuum beam and about 1.25 in the regenerator beam after the absorbers. Most hyperons in the secondary beam decay near the target.

The neutral kaon beams are shaped by a system of collimators. The primary collimator is located at z = 20 m and is a 1.5 m long brass and steel block with square tapered holes. It provides the initial collimation and helps to reduce the beam halo. The tapered holes reduce backgrounds from kaon scatters in the collimators. The slab collimator is a 2 m thick iron slab located at $z = 38$ m which sits between the beams and prevents particles that scatter in the primary collimator from crossing between the beams. The defining collimator is a tungsten block with tapered square

holes located at $z = 85$ m. It defines the size and solid angle of each beam. At the defining collimator, each beam is 4.4×4.4 cm^2 and subtends solid angle 0.24 μstr. The beam centers are separated by 14.2 cm and the horizontal angle between the two beams is 1.6 mrad.

Most of the K_S component of the two beams decays near the target. Downstream of the defining collimator, the residual K_S component of the vacuum beam increases the $K \to \pi\pi$ decay rate by 0.4% compared with a pure K_L beam of equal intensity. This contribution to the decay rate varies with energy; it is negligible for kaons with momenta less than 100 GeV/c and increases to 15% at 160 GeV/c. The final beam composition before the regenerator is the following: the vacuum beam has a 2.0 MHz flux of kaons with a neutron-to-kaon ratio of 1.3 and an average kaon momentum of 70 GeV/c while the regenerator beam has a 0.9 MHz kaon flux with a neutron-to-kaon ratio of 0.8. The hyperon flux is about 1 kHz in the vacuum beam and the total muon flux is about 200 kHz.

The beamline and decay region are evacuated to reduce the level of scattering. The vacuum is held at about 10^{-6} Torr and extends from $z = 28$-159 m, covering the most of the beamline and the entire decay region of $z = 110$-158 m used in the analysis. The downstream end of the vacuum region is sealed with a 0.14% radiation length vacuum window made of kevlar and mylar. The vacuum window is 7.6 mm thick and supports a force of 222 KN. The vacuum tank is 243.84 cm in diameter at the vacuum window; the window deflects by almost 15 cm from the edge of the vacuum tank to the center of the window. Scattering and hadronic interactions in the vacuum window are both important to the analysis.

2.3 Detector

Kaon decays that occur downstream of the defining collimator may be reconstructed by the KTeV detector. Figure 2.2 is a schematic view of the detector. The accidental counters are located near the target and the regenerator and some of the vetos are located in the evacuated decay region, but most of the detector elements lie downstream of the decay volume which ends with the vacuum window at $z = 159$ m.

Downstream of the vacuum window, the space between the detector elements is filled with helium to reduce interactions from the neutral beams and to reduce scattering and photon conversions of the decay products. The total amount of matter traversed by the neutral beams upstream of the CsI calorimeter is about 4% of a radiation length. The regenerator is active and is used as part of the trigger and veto systems as well as to provide K_S regeneration. The charged spectrometer is the primary detector for reconstructing $K \to \pi^+\pi^-$ decays while the CsI calorimeter is used to reconstruct $K \to \pi^0\pi^0$ decays. The veto system consists of a number of lead-scintillator detectors in and around the primary detectors. The trigger uses signals from all of the detectors to select desired events. The following is a detailed description of each of the relevant detector elements.

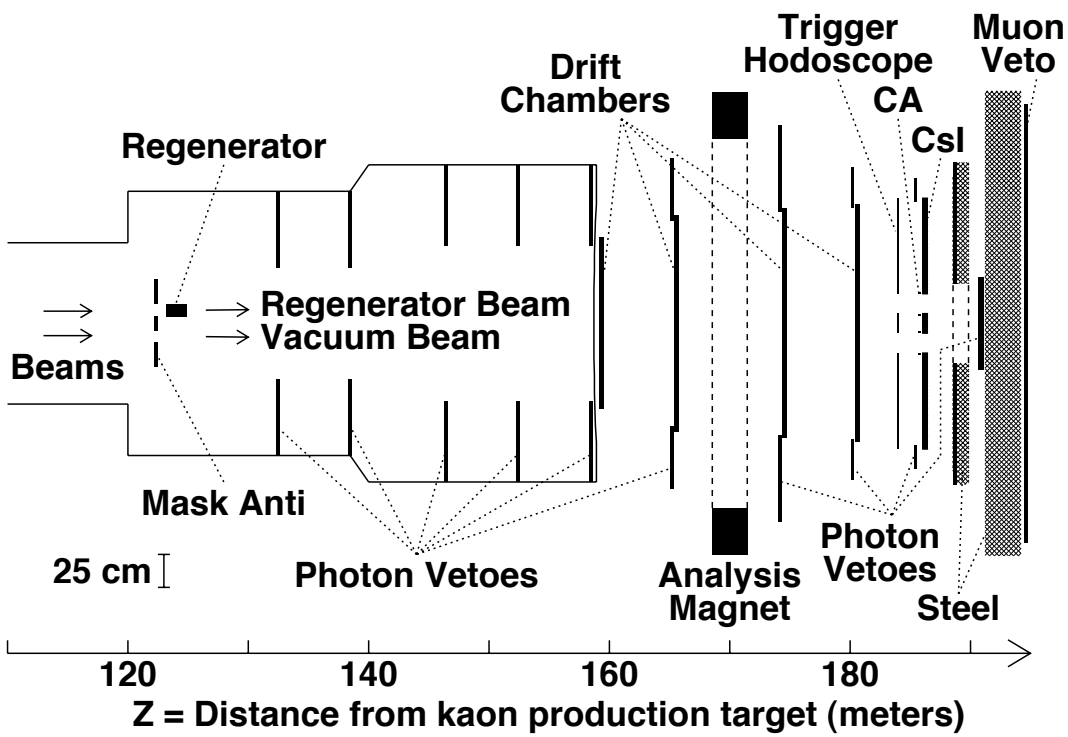

Figure 2.2: Schematic of the KTeV detector. Figure courtesy of P. Shawhan [60].

2.3.1 Accidental Counters

We use a set of three counters near the target to trigger on primary beam activity uncorrelated with activity in the detector. These events are used in the Monte Carlo simulation to model accidental activity in the detector which is proportional to the instantaneous intensity of the proton beam. The three scintillation counters are each viewed by a photomulitplier tube, are located 1.8 m from the target, and are oriented at an angle of 90° with respect to the beam axis. The target is viewed by the counters through a 6.4 × 6.4 mm^2 hole in the shielding surrounding the target.

2.3.2 Regenerator

To create a source of K_S decays, we place a 1.7 m long regenerator in one of the beams at z = 123.8-125.5 m. We alternate the position of the regenerator between the two beams once per minute to reduce systematic uncertainties related to left-right asymmetries in the detector and beamline. The regenerator is made of 84 10×10×2 cm^3 scintillator modules followed by a lead-scintillator module which is 10×10 cm^2 in the transverse direction and consists of 5.6 mm of lead, 4 mm of scintillator, 5.6 mm of lead, and 4 mm of scintillator. A schematic of the regenerator is shown in Figure 2.3a. The regeneration amplitude at the average kaon momentum of 70 GeV/c is $|\rho| \sim 0.03$. This value of the regeneration amplitude is sufficient to ensure that most of the $K \to \pi\pi$ decays in the regenerator beam are from the regenerated K_S component. About 20% of $K \to \pi\pi$ decays in the regenerator beam come from the K_L component or from $K_S - K_L$ interference. This contribution ranges from 5% near the regenerator to 90% at the vacuum window. The isoscalar carbon in the regenerator accounts for about 95% of the regeneration amplitude which simplifies the model used to describe ρ in the fitter. Downstream of the regenerator, the flux of unscattered kaons in 0.15 MHz.

K_S regeneration occurs when a K_L beam interacts with matter because the $K^0 - \bar{K}^0$ admixture in the beam changes as the strangeness eigenstates interact differently with matter. This interaction can happen in three ways: coherent regeneration, diffractive regeneration, and elastic regeneration. Coherent regeneration occurs in

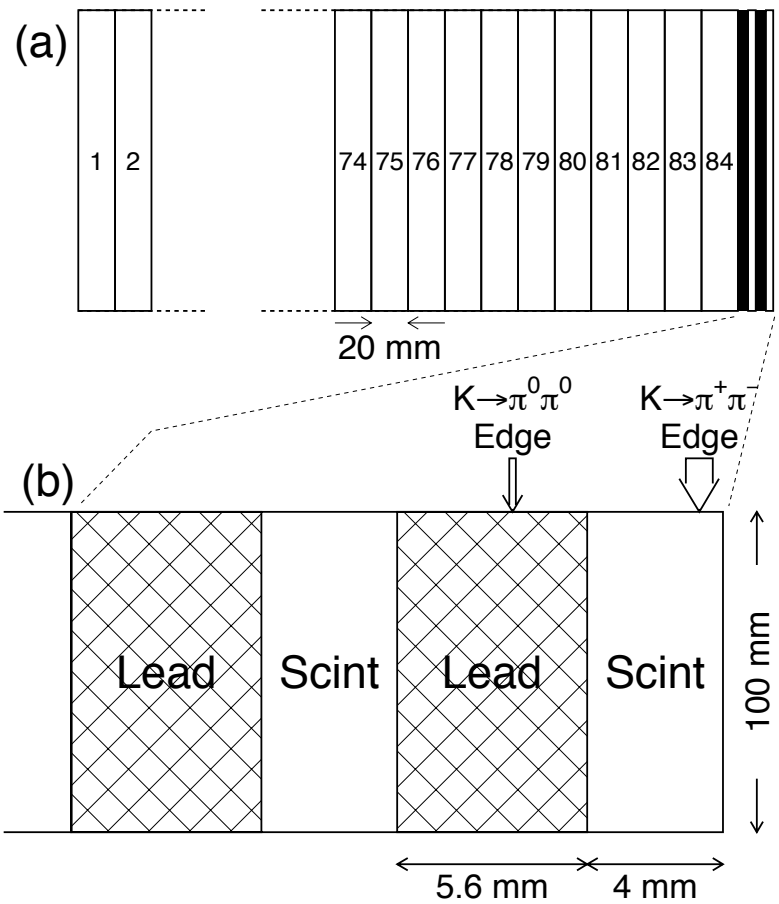

Figure 2.3: (a) Diagram of the regenerator and (b) magnified view of the downstream end of the regenerator. Vertical arrows above the lead and scintillator show the effective edge locations for $K \to \pi^0\pi^0$ and $K \to \pi^+\pi^-$ decays. The width of each arrow indicates the uncertainty.

the forward direction. Diffractive regeneration occurs when the kaon scatters off the target nucleus at a finite angle but does not break up the nucleus. Inelastic regeneration occurs when the target nucleus is destroyed; secondary particles are often produced. We use only decays from coherently regenerated kaons for this analysis; diffractive and inelastic scatters are treated as background. We choose not to accept scattered kaons because of the difficulty in accurately reconstructing large angle scatters in the $K \to \pi^0\pi^0$ decay mode. Misreconstructed scattering angles could lead to the assignment of a kaon decay to the wrong beam leading to a bias in $Re(\epsilon'/\epsilon)$. Scattered events have non-zero angles with respect to the beam direction; as there are more regenerator scatters in the regenerator beam than the vacuum beam, this leads to different distributions of kaon angles in the two beams. Since the acceptance of the detector depends on kaon angle, accepting scattered kaons would create an acceptance difference between the vacuum and regenerator beams at the same energy and vertex position which could lead to additional systematic uncertainties. For forward scatters the acceptance is the same at a given energy and vertex position because the angular distribution of kaons is the same in the two beams.

The length of the regenerator corresponds to about two hadronic interaction lengths; this maximizes the level of coherent regeneration with respect to diffractive scattering. The diffractive-to-coherent ratio is 0.09 for $K \to \pi\pi$ decays downstream of the regenerator; we make analysis cuts which further reduce this ratio. There are many times more inelastic scatters than coherently regenerated kaons; we use an active regenerator to reduce the level of inelastic scatters. Each of the 85 modules is viewed by 2 photomultiplier tubes, one from above and one from below. Inelastic interactions typically deposit 1-100 MeV in the regenerator; we measure the energy deposit in the regenerator and reject events which deposit more than 8 MeV in any of the scintillator modules. Inelastic scatters which produce secondary particles may also be rejected by other veto detectors. After all veto requirements, the background from inelastic scattering is smaller than the contribution from diffractive scattering.

The downstream end of the regenerator defines the beginning of the decay region for $K \to \pi\pi$ decays in the regenerator beam. The lead in the last regenerator module

is intended to define a sharp upstream edge for the decay region. A small number of decays inside the regenerator may still be accepted because charged pions from $K \to \pi^+\pi^-$ decays can exit the last 4 mm piece of scintillator without depositing enough energy to be vetoed and photons from $K \to \pi^0\pi^0$ decays can pass through both the scintillator and the lead.

For $K \to \pi^0\pi^0$ decays, the effective regenerator edge is calculated using a model which includes K_L transmission, K_S regeneration, decays within the regenerator, the propagation of the 4 photon decay products through the regenerator, and the $2\pi^0$ z-vertex resolution. The z-vertex distribution of a model which does not allow decays in the regenerator is compared to the full model; the measured downstream regenerator edge in the model which allows decays is 6.2 ± 0.1 mm upstream of the edge in the model which does not allow decays.

For $K \to \pi^+\pi^-$ decays, the effective edge is determined by the veto threshold in the lead-scintillator module. To make sure this edge is well-defined, we make a tight offline cut on the energy deposit in the lead-scintillator module. We use a sample of muons in which one muon passed through the regenerator during nominal data-taking to calibrate the energy deposit of one minimum ionizing particle through the lead-scintillator module under hadronic conditions. Using this calibration, the known geometry of the phototube placement, and the offline cut, we can calculate the probability for two minimum ionizing pions to escape the last piece of scintillator as a function of position within the scintillator. We integrate this probability distribution to find the effective edge. We find that the effective regenerator edge for $K \to \pi^+\pi^-$ decays is (0.7 ± 0.4) mm upstream of the physical end of the regenerator for 1999. For 1997 data, the offline cut is not as tight and the edge is (1.65 ± 0.4) mm upstream of the physical end of the regenerator.

The location of the effective edges for 1999 are illustrated in Figure 2.3b. These effective edges are inputs to the fitter. Decays within the regenerator are simulated by the Monte Carlo.

2.3.3 Charged Spectrometer

$K \to \pi^+\pi^-$ decays are reconstructed by a charged spectrometer which includes four drift chambers and a dipole magnet. The two upstream drift chambers are located at $z = 159$ m and $z = 166$ m. They are followed by the magnet at $z = 170$ m and the two downstream drift chambers at $z = 175$ m and $z = 181$ m. The magnet has a 3×2 m^2 aperture, produces a field that is uniform to better than 1%, and imparts a kick of $\sim$412 MeV/c in the horizontal plane. During data taking, the polarity of the magnet was reversed every few days. The size of the drift chambers increases with distance from the target; the smallest chamber is 1.26×1.26 m^2 and the largest chamber is 1.77×1.77 m^2.

Each drift chamber consists of 2 planes of horizontal wires to measure y positions and 2 planes of vertical wires to measure x positions. The planes have a hexagonal cell geometry formed by six field-shaping wires which surround each sense wire. The cells are 6.35 mm wide. Figure 2.4 illustrates the drift chamber cell geometry. The two x planes and the two y planes are offset by one half-cell to resolve the left-right ambiguity.

The drift chambers are filled with a 50-50 argon-ethane gas mixture. The drift velocity is about 50 μm/ns for a maximum drift time across a cell of 150 ns. We therefore define the in-time window to be 150 ns. Lecroy 3373 multi-hit Time-to-Digital Converters (TDCs) are used to measure the drift times relative to the trigger. The total TDC time window is 2.5 times longer than the in-time window and is centered on the intime window. The single-hit position resolution of the drift chambers is typically 110 μm. The final momentum resolution is $\sigma_p/p \simeq [1.7 \oplus (p/14)] \times 10^{-3}$, where p is the track momentum in GeV/c. The calibration of the charged spectrometer is described in Section 2.6.1.

2.3.4 Calorimeter

$K \to \pi^0\pi^0$ decays are reconstructed using the Cesium Iodide electromagnetic calorimeter located at $z = 185$ m. It consists of 3100 pure CsI crystals of 2 different sizes. There are 2232 2.5×2.5 cm^2 crystals in the center region, each of which is viewed

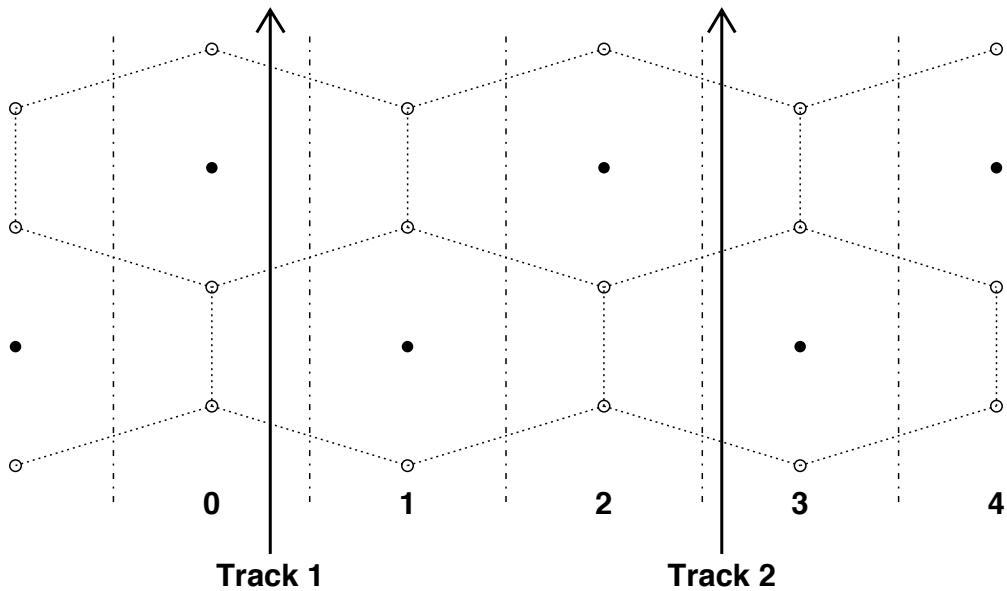

Figure 2.4: Drift chamber hexagonal cell geometry showing six field wires (open circles) around each sense wire (solid dots).

by a 1.9 cm Hamamatsu R5364 PMT, and 868 5×5 cm^2 crystals each viewed by a 3.8 cm Hamamatsu R5330 PMT. The total transverse size of the calorimeter is 1.9×1.9 m^2. Each crystal is 50 cm (27 radiation lengths) long. There are two 15×15 cm^2 carbon fiber beam pipes whose centers are separated by 30 cm to allow the two beams to pass through. Figure 2.5 shows the layout of the CsI crystals.

CsI has a radiation length of 1.85 cm and a nuclear interaction length of 36.5 cm. This means that electromagnetic showers produced by photons and electrons deposit most of their energy in the 50 cm long crystals, while hadronic showers produced by pions do not. The Moliere radius of CsI is 3.8 cm which reduces the number of overlapping showers and allows the 2.5×2.5 cm^2 crystals to provide good position resolution. The calorimeter is housed inside a light-tight steel blockhouse. The humidity and temperature inside the blockhouse is strictly controlled since CsI

tends to absorb moisture and its light output decreases ∼1.5% per degree Celsius temperature increase.

The CsI crystals were tested in the lab before installation in the calorimeter. The light output and longitudinal response were measured using a ^{137}Cs source. The crystals were wrapped in mylar that is black on one side and aluminized on half of the other. The fraction of wrapping that was reflective varied from crystal to crystal. This was done to make the longitudinal response of the crystals as uniform as possible to improve energy resolution and linearity. We achieved a longitudinal response that is uniform to within 5%. The wrapping is ∼12 μm thick; the fraction of dead material in the calorimeter is ∼0.06% and the energy lost in the wrapping per shower is ∼0.015% for showers in the small blocks.

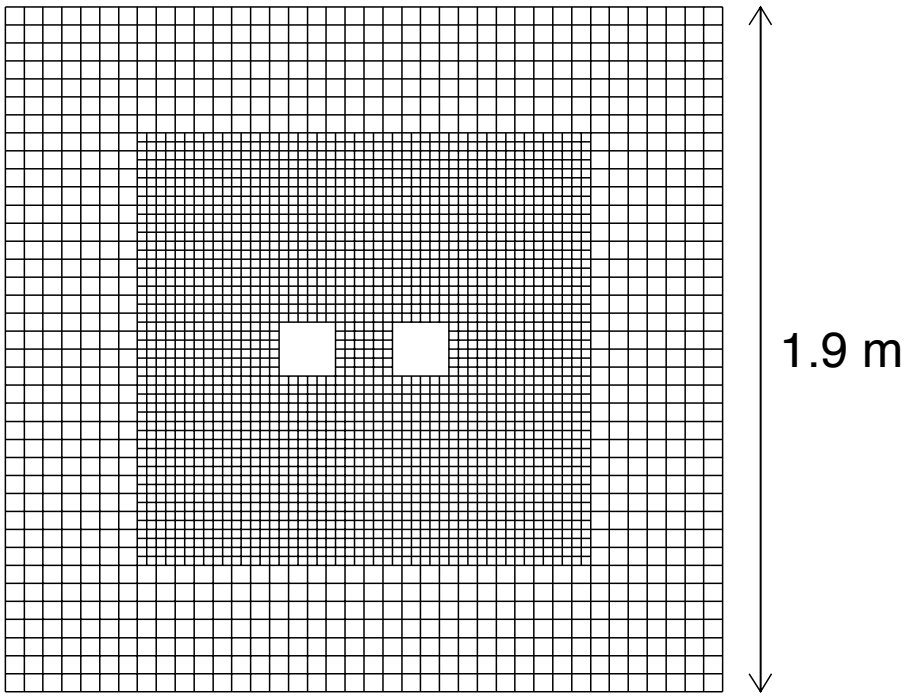

Figure 2.5: Transverse view of the KTeV CsI calorimeter, showing the small inner crystals, the large outer crystals, and the beam pipes.

The scintillation light produced by the CsI has a fast component and a slow component. The fast component has decay times of 10 ns and 36 ns and maximum light output at a wavelength of 315 nm while the slow component has a decay time of $\sim$1 μs and maximum light output at 480 nm. We reduce the fraction of light from the slow component using a Schott UV filter placed between the crystal and the PMT; this reduces the total light output by $\sim$20% but increases the fast component fraction from 80% to 90%. We want to minimize the contribution from the slow output to reduce accidental pile-up effects. The average light yield of the CsI with the filter in place is 20 photo-electrons per MeV of energy deposit. Operating at higher gains improves the linearity of response of the PMTs, so those crystals with high light output were partially masked to reduce light output when run at high gain. Typical phototube gains are 2500-5000.

Each channel in the calorimeter consists of a CsI crystal, a PMT, and a custom digitizer which integrates the charge delivered by the PMT. The digitizing electronics for the calorimeter are located inside the blockhouse directly behind the PMTs. We call the digitizer a "digital PMT" (DPMT); it has 16 bits of dynamic range with 8-bit resolution which allows us to measure energy deposits from a few MeV to 100 GeV. The DPMT consists of a Flash ADC and two custom integrated circuits: the Charge-Integrator and Encoder (QIE) and the Driver/Buffer/Clock (DBC).

The QIE divides the PMT current into 8 ranges (1/2, 1/4, 1/8, 1/16, 1/32, 1/64, 1/128, 1/256 of the input current), accumulates charge on capacitors over a single clock cycle or "slice", and uses a series of fast comparators to select the appropriate range of sensitivity given the voltage accumulated on each capacitor. The selected range is indicated by a binary code called the QIE "exponent" which is recorded by the flash ADC. The charge and corresponding energy ranges covered by each QIE exponent are shown in Table 2.1. The QIE actually uses four circuits in a rotating sequence so that the system has no dead time; each circuit is identified by a "phase" which runs from 0 to 3. The digital output of the QIE is a 3-bit range exponent and a 2-bit phase. The analog output of the QIE is the signal and a reference voltage.

The output of the QIE is digitized by an 8-bit Harris Flash ADC; we call the digitized signal from the ADC the "mantissa." The DBC contains a FIFO to store

QIE Exponent	Charge (pC)	Energy (GeV)
0	0 - 2.35	0 - 0.226
1	2.35 - 6.8	0.226 - 0.654
2	6.8 - 16.0	0.654 - 1.541
3	16.0 - 34.0	1.541 - 3.276
4	34.0 - 71.0	3.276 - 6.84
5	71.0 - 145.0	6.84 - 14.00
6	145.0 - 270.0	14.00 - 26.01
7	> 270.0	> 26.01

Table 2.1: Typical charge and energy ranges covered by each QIE exponent

the digital output of the QIE and the flash ADC on each clock cycle; the FIFO can store up to 40 slices of data. When the level 1 trigger requirement is met, 32 slices are loaded into a second FIFO. If the level 2 trigger requirement is also met, the data are transferred to a readout buffer called the "pipeline." Details of the multi-level trigger system are discussed in Section 2.4.1. It takes 4.9 μs to transfer a 32 slice event.

In 1997 and 1999, the digitization and readout of the calorimeter operated at the Tevatron RF frequency of 53 MHz and the signal integration time was 114 ns or 6 RF buckets. In 1996, the readout frequency was 18 MHz (RF/3) and the integration time was twice as long.

The calibration to covert integrated charge to energy is accomplished using an in-situ laser system and an offline calibration using momentum-analyzed electrons from $K_L \to \pi^{\pm} e^{\mp} \nu$ decays. The laser system consists of a pulsed Nd:YAG laser, a fluorescent dye, and a variable filter to span the full dynamic range of the readout system. The laser light has wavelength 360 nm and is distributed to each CsI crystal using quartz fibers. The laser system is described in more detail in Section 2.6.2. The final energy resolution of the calorimeter is $\sigma_E/E \simeq 2\%/\sqrt{E} \oplus 0.3\%$, where E is in GeV. The position resolution of the calorimeter is 1.2 mm for showers in the small blocks and 2.4 mm for showers in the large blocks. The calibration of the calorimeter is described in Section 2.6.2.

2.3.5 Vetos

The KTeV detector uses a system of lead-scintillator veto elements to define edges and apertures, to reduce trigger rates, and to reduce backgrounds.

Mask Anti

The Mask Anti (MA) defines the upstream acceptance of the detector. It is located just upstream of the regenerator at $z = 123$ m. It is a 16 radiation length (X_0) lead-scintillator sandwich with two 9×9 cm^2 holes to allow the beams to pass through. A diagram of the MA is shown in Figure 2.6a. The MA is read out by fibers embedded in the scintillator. Each fiber is viewed by a PMT which is digitized by an ADC. The MA output is also discriminated to form a trigger source which may be used to veto events at trigger level. The primary purpose of the MA is to veto K_L decays which occur upstream of the regenerator in the regenerator beam.

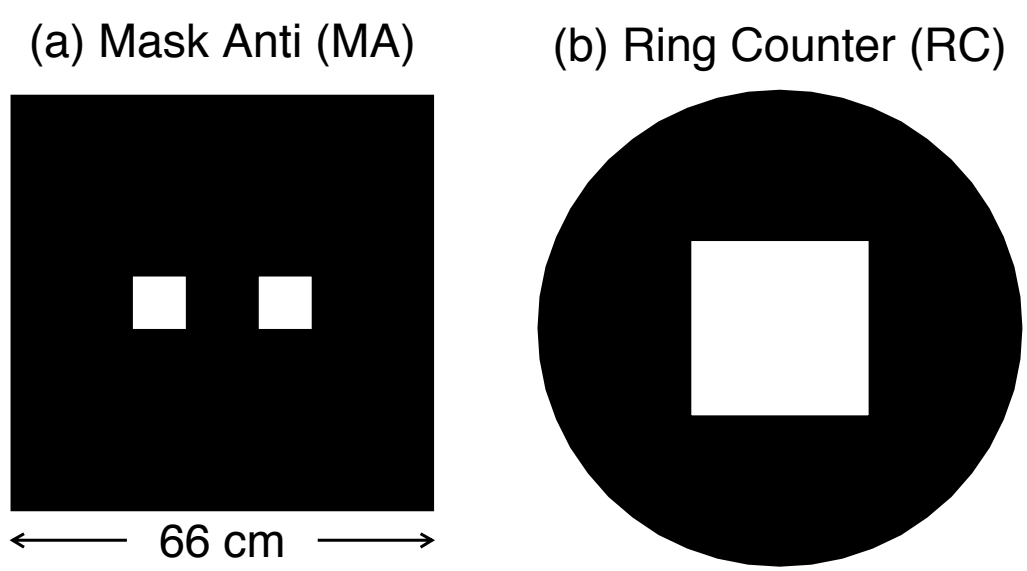

Figure 2.6: (a) Transverse view of mask anti. (b) Transverse view of ring counter. The square aperture size varies for the five RCs but is ∼1 m.

Ring Counters

The ring counters (RCs) are five 16 X_0 lead-scintillator veto detectors which are positioned around the outer edge of the decay region to veto events in which a particle escapes the detector. They are made of 24 layers of lead-scintillator sandwich and have a square inner aperture and a circular outer aperture. The size of the inner aperture is different for each of the five detectors such that a particle which misses the inner edge of a RC will hit the CsI calorimeter. A transverse view of a generic RC is shown in Figure 2.6b. The RCs are bolted into the vacuum tank at points where the tank segments are joined: $z = 132.6$ m, $z = 138.6$ m, $z = 146.6$ m, $z = 152.6$ m, and $z = 158.6$ m. They are read out by fibers viewed by PMTs; the output is digitized by ADCs and discriminated to form a trigger source. The RCs are particularly useful in vetoing background from $K_L \to \pi^0\pi^0\pi^0$ decays.

Spectrometer Antis and CsI Anti

The spectrometer antis (SAs) and the CsI Anti (CIA) provide veto coverage for the region downstream of the vacuum decay region. They are also 16 X_0 lead-scintillator sandwiches. The three SAs are located just upstream of the three downstream drift chambers at $z = 165.1$, $z = 174.0$, and $z = 180.0$. They are square annular detectors with inner apertures sized such that a particle missing the SA would hit the calorimeter. The CIA has the same design as the SAs and is located just upstream of the CsI at $z = 185.1$ m. Its inner aperture is small enough to occlude 1/2 of the outer ring of crystals in the calorimeter to veto events that are so close to the edge of the CsI that they would be poorly reconstructed. Like the other vetos, the SAs and CIA are read out by ADCs and used to form a trigger source.

Collar Anti

The collar anti (CA) is designed to define the inner aperture of the CsI. It consists of two identical 8.7 X_0 tungsten-scintillator detectors which sit directly on the beam hole pipes of the CsI. The CA covers $\sim$1.5 cm of the inner ring of crystals surrounding

the beam holes to veto events that would be poorly reconstructed due to energy lost down the beam holes. A diagram of the transverse view of the CA is shown in Figure 2.7. The CA is read out by long fibers which are viewed by PMTs located at the edge of the calorimeter. As with the other vetos, the CA is digitized by an ADC and is used as a trigger source.

Downstream Vetos and Walls

Figure 2.8 shows the layout of the walls and vetos downstream of the CsI calorimeter. Like the other veto detectors, the downstream vetos are digitized by ADCs and may be used as trigger sources.

Immediately downstream of the CsI at $z = 188.5$ is a lead wall to absorb electromagnetic showers that leak out the back of the calorimeter and to cause hadrons to shower. The hadron anti (HA) is a veto detector consisting of scintillation counters

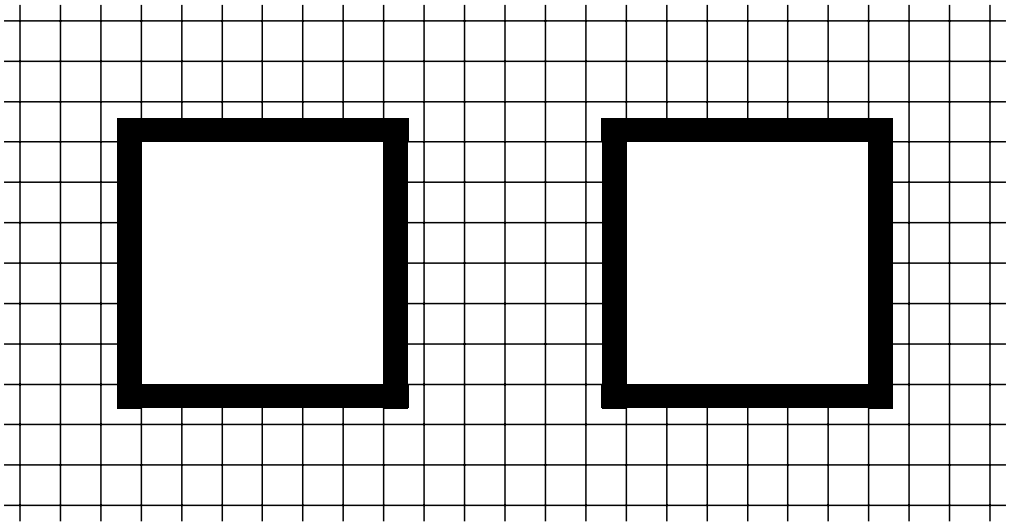

Figure 2.7: (a) Transverse view of collar anti. Some of the small blocks at the center of the CsI calorimeter are shown. The CA is shown as the two shaded "picture-frame" regions that cover the inner 60% of the CsI crystals surrounding the beam holes.

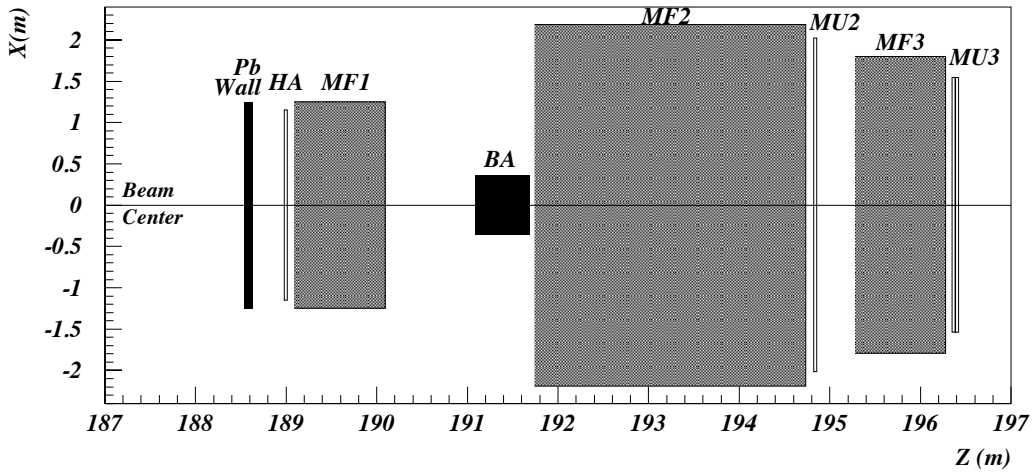

Figure 2.8: Schematic showing the positions of the lead wall, the HA, MF1-3, the BA, and MU2-3. Figure courtesy of B. Quinn [61].

located downstream of the lead wall at $z = 189.0$. It is designed to veto charged pions from $K_L \to \pi^{\pm} e^{\mp} \nu$ decays.

The back anti (BA) is designed to catch particles that go down the beam holes and also serves as a dump for the neutral beams. It is located in the beamline behind a block of steel downstream of the CsI at $z = 191.1$ m. The steel block (MF1) is present to reduce backsplash from the BA. The BA is segmented longitudinally to attempt to distinguish electromagnetic and hadronic showers. It is 30 X_0 long, but only BA1 (the first 10 X_0 of the BA) is used as a veto.

Downstream of the BA are two more blocks of steel (MF2 and MF3) located at $z = 191.7$ m and $z = 195.3$ m, each of which is followed by a plane of muon counters (MU2 and MU3) located at $z = 194.8$ and $z = 196.4$ m. The muon vetos are scintillation counters. They are particularly useful for reducing background to the charged signal mode from $K_L \to \pi^{\pm} \mu^{\mp} \nu$ decays. The lead wall and the three steel blocks sum to 31 interaction lengths.

2.3.6 Trigger Hodoscopes

The trigger hodoscopes (VV′ or V0 and V1) are two back-to-back banks of scintillator counters used in by the trigger to identify the presence of charged particles. They are located at $z = 183$ m. The banks are 0.95×0.95 m^2 and contain 30 and 32 counters which are 11 cm wide and 88 cm or 110 cm long. The counters are oriented such that the they are split just above or below the beam holes and they are offset from each other by one half counter to reduce the effect of gaps between the counters. The layout of the trigger hodoscopes is shown in Figure 2.9.

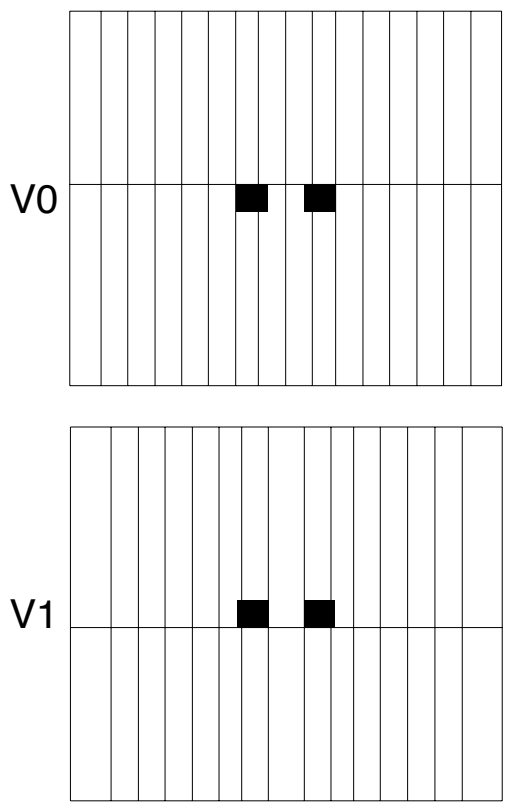

Figure 2.9: Transverse view of the trigger hodoscopes VV*prime*

2.4 Data Acquisition

2.4.1 Trigger

Three level trigger

KTeV uses a three level trigger to reduce the rate of stored events to ∼2 kHz. There are 16 different physics triggers that may have independent level 1, level 2, and level 3 requirements. They may also have individual prescales applied.

The level 1 trigger has no deadtime and makes a decision every 19 ns synchronously with the beam RF structure. The level 1 trigger is based on fast signals from the detector; most of the signals are discriminated combinations of signals from PMTs. The primary information used in the charged level 1 trigger comes from the drift chamber ORs (DCORs) and the trigger hodoscope (VV′). The DCORs provide information about activity in the two drift chambers upstream of the magnet while VV′ provides information about charged particles downstream of the spectrometer. The most important level 1 source for neutral triggers is E-total (ET) which is the analog sum of the in-time dynode signals of all 3100 PMTs in the CsI calorimeter. These signals are transported from the detector on "hardline" cables which are coaxial cables that transmit signals at ∼0.9c rather than the ∼0.6c that is achieved by conventional coaxial cables. The signals are synchronized such that the signal from a particle moving through the detector at velocity c would arrive at the level 1 logic modules simultaneously. This means that signals from the upstream detectors pass through longer delay cables than signals from downstream detectors. Copies of the level 1 trigger sources are sent to trigger TDCs and latches which may be used by the offline analysis. The level 1 trigger decision is made by memory lookup modules and may be inhibited by veto signals. The raw level 1 rate is ∼40 KHz.

The level 2 trigger consists of custom electronics which do more sophisticated processing than level 1 and introduce a deadtime of 2-3 μs. The primary level 2 processors for the charged mode triggers are custom hit counting modules called "bananas" and "kumquats" and a track finding system called the "y-Track Finder" (YTF). For all of these processors, only signals from the y views of the drift chambers

are used so that hits from the same wires are used for both regenerator and vacuum beam events. For the purposes of this analysis, the bananas and kumquats are functionally equivalent; they count the number of adjacent wires with in-time hits (hits which arrive within the 200-250 ns gate) and the trigger decision is based on the total hit count from each chamber view. The hit counting system makes its decision in ∼800 ns. The YTF determines whether or not the DC hits are consistent with two straight tracks in the y view. It is specifically designed to select $K \to \pi^+\pi^-$ decays, so it looks for one up-going and one down-going track with an overlap region in the center of the spectrometer which counts as both up- and down-going. It uses the logical OR of groups of wires from the hit-counting system as inputs and is implemented using commercial programmable logic and memory lookup modules. Its decision time is a few hundred nanoseconds faster than the hit-counting system, so it does not contribute any additional deadtime to the level 2 trigger.

The level 2 decision for neutral mode triggers is based on the Hardware Cluster Counter (HCC) which counts isolated clusters of energy in the CsI calorimeter. The HCC counts a cluster as a set of contiguous channels with energies exceeding a threshold of 1 GeV. The inputs to the HCC are the digital bits from the ET boards which are on if the channel is above threshold. The cluster finding algorithm is based on a series of 2×2 grids so that several operations can be performed in parallel and the process takes an amount of time independent of the calorimeter illumination. The HCC energy thresholds are adjusted during data taking such that the thresholds are approximately the same for all channels. This is done by setting all the comparator thresholds to the same value and adjusting the gains for each channel by changing the voltages on the PMTs. The HCC processing time is about 1.5 μs; this is the longest processing time of any of the level 2 trigger elements.

If an event is rejected by level 2 the detector front-end modules are cleared and the trigger system is re-enabled. When an event is accepted by level 2, the entire detector is read out into VME computer memories which takes about 15 μs. The total rate of events accepted at level 2 is about 10 kHz.

The level 3 trigger decision is made by one of 24 200-MHz SGI processors running a software filter. The memories are able to store data from the entire spill, so the

processors have a full minute to process the data without deadtime. At level 3, tracks and clusters are reconstructed using code similar to the offline analysis code and cuts on kinematic and particle identification quantities are made. These calculations rely on online calibrations, so the cuts must be rather loose. Prescales for individual physics triggers may be applied at this stage, and a fraction of events for each trigger are accepted at random to allow for studies of any level 3 inefficiencies. The rate of events accepted by the level 3 trigger is about 2 kHz.

Events selected by the trigger are written to Digital Linear Tape (DLT) for storage. We typically write about 40,000 events per minute to tape. In 1996 and 1997 the events were written out to nine tape drives, three for each of the processing "planes," in the order in which they were processed. In 1999 a more sophisticated online split was introduced which separates the individual triggers into sets of related triggers. Each set is then directed to one of the three tape drives available for each plane. Additionally, some of the smaller datasets are written to disks which are later spooled to tape. The online split is discussed further in Section 2.7.

Charged Mode Trigger

Trigger 1 is the physics trigger which selects $K \to \pi^+\pi^-$ events for this analysis. This trigger is designed to identify kaon decays consistent with an unscattered $K \to \pi^+\pi^-$ decay with an emphasis on efficiency rather than the purity of the sample. The trigger 1 requirements are summarized in Table 2.2.

The level 1 sources used by this trigger are VV′, DCOR, and the veto counters. We require at least two hits in the V bank and one hit in the V′ bank, or vice versa. We also require that the pattern of hits in VV′ be consistent with an unscattered kaon decay, which means that the sum of the transverse momenta of the decay products is zero. This is accomplished by requiring one hit to be in the east part of the detector and one to be in the west while also requiring that one of the hits be in the top part of the detector while the other is in the bottom part. The definitions of "east" and "west" each include the center of the detector so there is overlap between the regions. Overlap between the "up" and "down" regions comes from the

Trigger Element	Requirement
Level 1	
Spill	Beam delivered from Tevatron
VV′ hit counting	2 hits in V, 1 hit in V′ OR
	1 hit in V, 2 hits in V′
VV′ East-West-Up-Down	1 hit in V-East or V′-East
	1 hit in V-West or V′-West
	1 hit in V-Up or V′-Up
	1 hit in V-Down or V′-Down
DCOR	3 DCOR hits
Vetos	Veto on regenerator, SAs,
	CIA, MU2
Level 2	
Hit Counting	2 in-time DC hits in at least 3 y views
	and 1 hit in the 4th view
YTF	1 upward and 1 downward-going y track
Level 3	
Reconstructed mass	$m_{\pi^+\pi^-} > 450$ MeV/c^2
Energy/Momentum	E/p < 0.9

Table 2.2: $K \to \pi^+\pi^-$ trigger requirements

overlapping geometry of the two banks; see Figure 2.9. The DCORs are signals from the 4 planes of the two upstream drift chambers DC1 and DC2. Groups of 16 DC wires from the x and y view of each chamber are "OR"ed together by electronics; we require hits in 3 of the 4 views. This requirement removes decays which occur downstream of DC1. Events are vetoed when significant energy is deposited in the regenerator, SAs, CIA, or MU2.

Level 2 requirements are designed to select events with drift chamber hits in the y-view which are consistent with two tracks from a common vertex. The decision is based on hit counting and the YTF. We require that the Bananas find at least two hits in three of the four drift chambers and at least one hit in the remaining chamber. Only the y views of the drift chambers are used. We also require that the YTF find 2 track candidates in the y view, one upward-going and one downward-

going. One of these two tracks is allowed to be of poor quality, missing a hit in DC1 or DC2.

The level 3 filter code reconstructs two charged tracks in the spectrometer. The reconstructed mass must be > 450 MeV/c^2. To identify the particles as pions, tracks are matched to clusters in the calorimeter and E/p must be < 0.9 for each track.

Neutral Mode Trigger

$K \to \pi^0\pi^0$ decays for this analysis are selected by trigger 4. As with the charged trigger, this trigger is designed to be as efficient as possible. The trigger 4 requirements are summarized in Table 2.3.

Trigger Element	Requirement
Level 1:	
Spill	Beam delivered from Tevatron
Etotal	Energy in CsI > 24 GeV
Vetos	Veto on Reg, SAs, CIA, CA, HA
Level 2:	
HCC	4 clusters
Level 3:	
Reconstructed mass	$m_{\pi^+\pi^-} > 450$ MeV/c^2
Pairing Chi Squared	$\chi^2_{\pi^0} > 500$

Table 2.3: $K \to \pi^0\pi^0$ trigger requirements

The level 1 trigger requirement is simply that the total energy deposit in the CsI be greater than 24 GeV. Events are vetoed if significant energy is deposited in the regenerator, SAs, CIA, CA, or HA. The level 2 trigger requirement is that the HCC find exactly 4 clusters[2]. The level 3 filter code performs a modified clustering algorithm which requires an HCC bit to be set and builds 5×5 clusters of small blocks and 3×3 clusters of large blocks. We require that level 3 find exactly 4 clusters. The code then calculates cluster energies and positions and applies only the "missing block", "out-of-cone", and "overlap" corrections to the cluster energies. The reconstruction algorithm calculates a reconstructed invariant mass assuming

[2]In 1996 and early 1997 data taking 4 or 5 clusters were accepted by level 2.

that the four clusters are photons and assigning each photon to one of the two π^0s from the kaon decay by testing which combination yields the best vertex agreement. We require the reconstructed invariant mass to be greater than 450 MeV/c^2 and we make a loose cut on a measure of the pairing quality, $\chi^2_{\pi^0}$. The event reconstruction is similar to the offline reconstruction which is described in detail in Section 3.2.

Other Triggers

In addition to the two triggers which collect events for the signal modes, there are many other physics triggers which are used to collect events for calibrations, systematic studies, and cross-checks. Trigger 2 has the same level 1 and level 2 requirements as the charged mode signal trigger but requires E/P > 0.9 for one of the tracks to select $K_L \to \pi^{\pm} e^{\mp} \nu$ decays which are used for calibration of the CsI and detector acceptance studies. This trigger is prescaled so that only $\sim$10% of these candidates are saved. Triggers 3 and 5 are "level-1-only" versions of the signal mode triggers; they have similar level 1 requirements to the signal mode triggers but make no requirements at level 2. These triggers are heavily prescaled and are used to study biases in the level 2 trigger. Trigger 6 is a neutral trigger which requires 6 clusters rather than 4. It is used to select $K_L \to \pi^0\pi^0\pi^0$ decays which are used for detector calibration and acceptance studies. Trigger 7 is a muon trigger which requires a hit in the muon vetos; for this analysis it is used only for regenerator calibration. Trigger 8 is an accidental trigger which collects events which will be overlaid on the Monte Carlo simulation to model the effects of intensity dependent accidental activity. Trigger 10 is a minimum bias trigger which requires only a Tevatron spill signal and at least 2 hits in one of the trigger hodoscopes. This trigger is heavily prescaled. There are also a number of calibration triggers including a "pedestal" trigger which reads out the entire CsI calorimeter a few times per spill and a laser trigger which monitors the CsI performance using the pulsed laser system.

2.4.2 Data Collection

This result is based on data taken during KTeV E832 runs in 1996, 1997, and 1999. KTeV took $K \to \pi\pi$ data for the measurement of $Re(\epsilon'/\epsilon)$ from October to December 1996, from April to July 1997, and from June to September 1999. These data taking periods along with the periods in which KTeV took data in E799 mode are depicted in Figure 2.10.

During 1999, we took data at two levels of beam intensity to allow us to check for any intensity dependence of the results. Beam intensities are measured using a Secondary Emission Monitor (SEM) which measures the number of protons per spill incident on the target. About 43% of the 1999 data was collected at low intensity (defined as SEM $< 5.0 \times 10^{12}$) while 57% was collected at high intensity (SEM $> 5.0 \times 10^{12}$). The average SEM at low intensity is $\sim 4 \times 10^{12}$ while the average SEM at high intensity is $\sim 6.5 \times 10^{12}$. Figure 2.11 shows the distribution

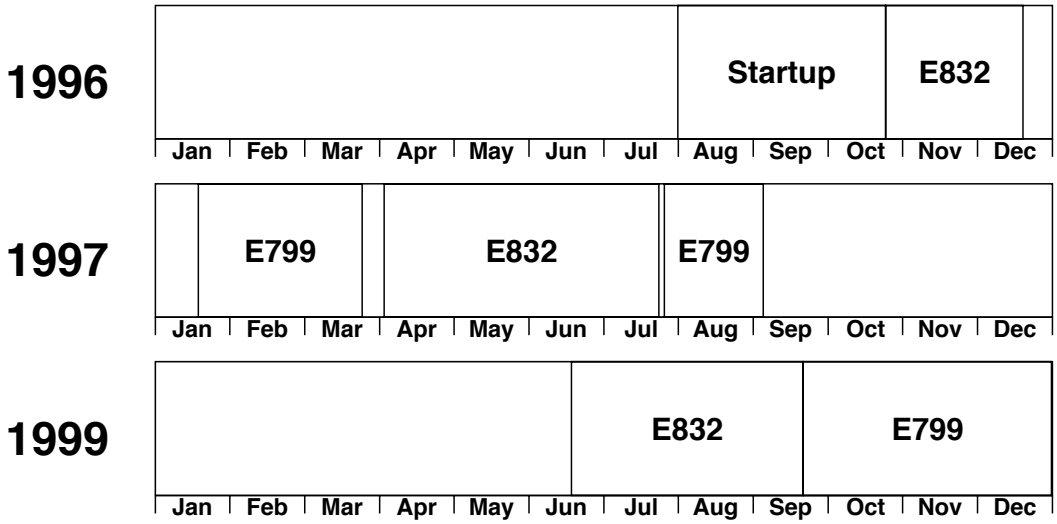

Figure 2.10: Data taking periods for KTeV

of intensities during the 1999 run. The average SEM for 1996 and 1997 data is $\sim 3 \times 10^{12}$.

The statistical precision of the $Re(\epsilon'/\epsilon)$ measurement is limited by the number of $K \to \pi^0\pi^0$ decays collected in the vacuum beam. This result is based on $\sim$0.8 million vacuum beam $K \to \pi^0\pi^0$ events in 1996, $\sim$2.1 million vacuum beam events in 1997, and $\sim$ 3.1 million vacuum beam events in 1999. In total, we have collected almost 6 million $K \to \pi^0\pi^0$ vacuum beam events.

2.5 Computing

The KTeV offline analysis is done on a cluster of 4 DEC machines which are located at FNAL: kpasa (a DEC 8400 server with 10 CPUs), ksera (a DEC 8400 server with 10 CPUs), klik (a DEC 4100 server with 4 CPUs), and klak(a DEC 4100 server with 4 CPUs). There are additional machines: kbella, which is used primarily as a disk server and kaos which is used as a disk server and a server for the farm. We

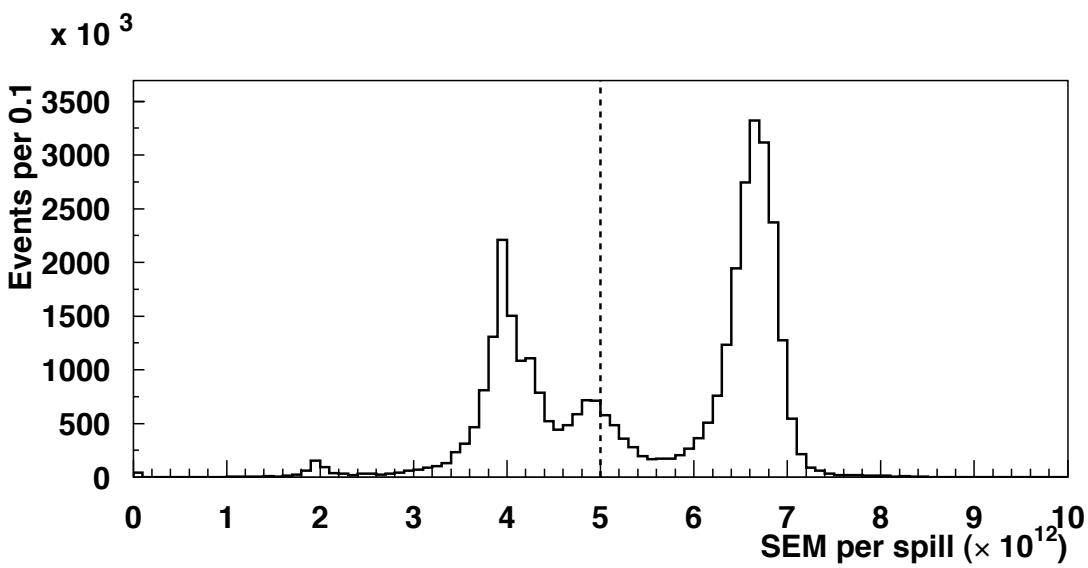

Figure 2.11: Beam intensity distribution for 1999 run. The dashed line indicates the boundary between "low" and "high" intensity for the purposes of our crosscheck.

have ∼8 TB of disk storage mounted on these 6 machines. Data were originally stored on DLT and accessed through operator mounted tape drives, but are now stored in the FNAL mass storage system, Enstore. Enstore is accessed through the dCache caching system. KTeV also makes extensive use of the FNAL farm which is a LINUX based distributed computing system with hundreds of nodes available. The farm is particularly useful for generation of large Monte Carlo datasets as our MC generation is well suited to distributed computing.

2.6 Detector Calibration

2.6.1 Charged Calibration

The calibration of the charged spectrometer requires the calibration of each of the drift chambers, the alignment of the drift chambers to each other and to the rest of the KTeV detectors, and the calibration of the transverse momentum kick from the analyzing magnet. The procedures for these calibrations are described briefly in this Section; see [2] for a more detailed discussion.

TDC Calibration

The drift chambers use TDCs operated in "common-stop" mode to measure drift times which means that the first hit in the drift chamber starts the TDC and the trigger signal stops it. Hits that are farthest from the wires have the longest drift times and thus the smallest TDC values. In order to convert the TDC information to a position, we must determine the relative timing of a given wire and then determine the precise relationship between time and distance. The timing offsets, t(0), measure the TDC value for each wire that corresponds to zero drift distance. The x(t) relations convert drift times to drift distances and thus position information. The TDC distributions for each wire will be used to measure these relations; a sample TDC distribution is shown in Figure 2.12.

The t(0) is defined as the TDC count at the 50% point between the zero event point and the "plateau" of the TDC distribution. As seen in 2.12, this corresponds

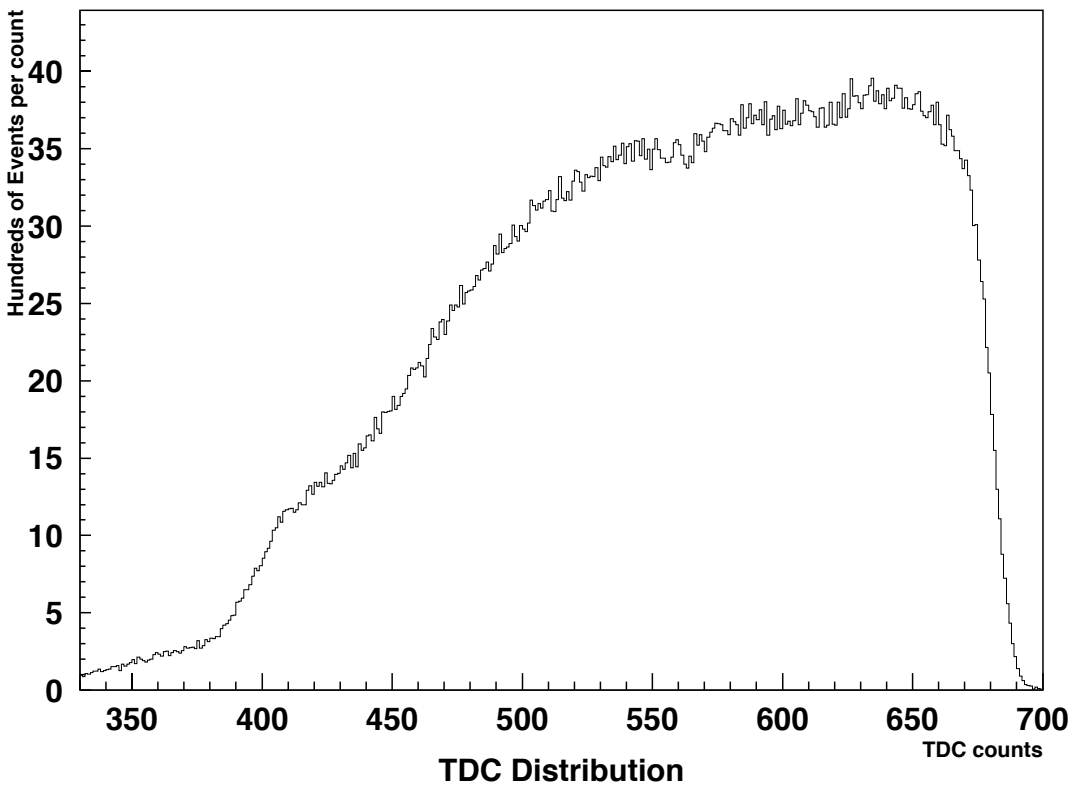

Figure 2.12: Sample drift chamber TDC distribution. The common-stop edge is seen at ∼680 TDC counts and the plateau of the distribution is seen from 550-680 counts. Figure courtesy of J. Graham[2].

to ∼680 TDC counts. Wire-to-wire variations in this value can be caused by varying cable lengths in the electronics, differing pulse heights, channel-to-channel or module-to-module variations in the amplifiers or TDCs, or in the common stop from the trigger. To map these variations, we group the 16 wires which are input to each TDC and assume that the TDC distribution of this group is representative of the true TDC distribution for each wire. We then compare the TDC distribution of the wire to the TDC distribution of the group by sliding the distributions past each other and using the Kolmogorov-Smirnov (KS) test. This calibration is an iterative

process which converges after two to three iterations. In 1996 data, typical shifts in the timing are 1-2 ns; the timing shifts in 1997 and 1999 are < 0.5 ns.

To measure the relationship between drift times and drift distances, we use a sample of $K_L \rightarrow \pi^{\pm} e^{\mp} \nu$ decays and collect the TDC distribution for hits on the reconstructed tracks grouping each of the 16 drift chamber planes together. We correct for missing hits using hit information from another drift chamber plane. The x(t) relationship is then given by

$$x(t) = d_{cell} \times \frac{\sum_{t_0}^{t} N(t)}{\sum_{t_0}^{t_m} N(t)} \tag{2.2}$$

where t_0 and t_m are the minimum and maximum drift times, d_{cell} is the maximum drift distance of 6.35 mm, and N(t) is the number of events in a 0.5 ns TDC bin. This calibration relies on the fact that the illumination of tracks across each drift cell is uniform and the reasonable assumptions that the earliest TDC hit comes from right next to the sense wire, the latest TDC hit comes from the edge of the cell, and that the distribution is ordered such that larger times correspond to larger distances. The drift chamber features which affect the x(t) relation are cell geometry, gas mixture, and voltage; these should be the same for each wire in a given chamber, so it is valid to group each drift chamber plane. The x(t) calibration process is iterative because the track-finding algorithm has some dependence on the x(t) maps. This calibration is performed in time periods corresponding to one to two days.

SODs

The sum-of-distances (SOD) for two hits from a good track should be equal to the sense wire separation, 6.35 mm. A typical SOD distribution before the final correction is shown in Figure 2.13. The Gaussian peak of this distribution is 6.32 mm and the mean of the distribution is 6.34 mm. A final correction is applied to the x(t) maps to move the mean SOD closer to the expected value of 6.35 mm. The correction is derived by assuming that the first drift electron does not correspond to zero drift distance so that a small offset should be applied to the x(t) maps such that

the mean SOD distribution is fixed to the cell width. This correction is determined iteratively and the final correction is ∼25 μm.

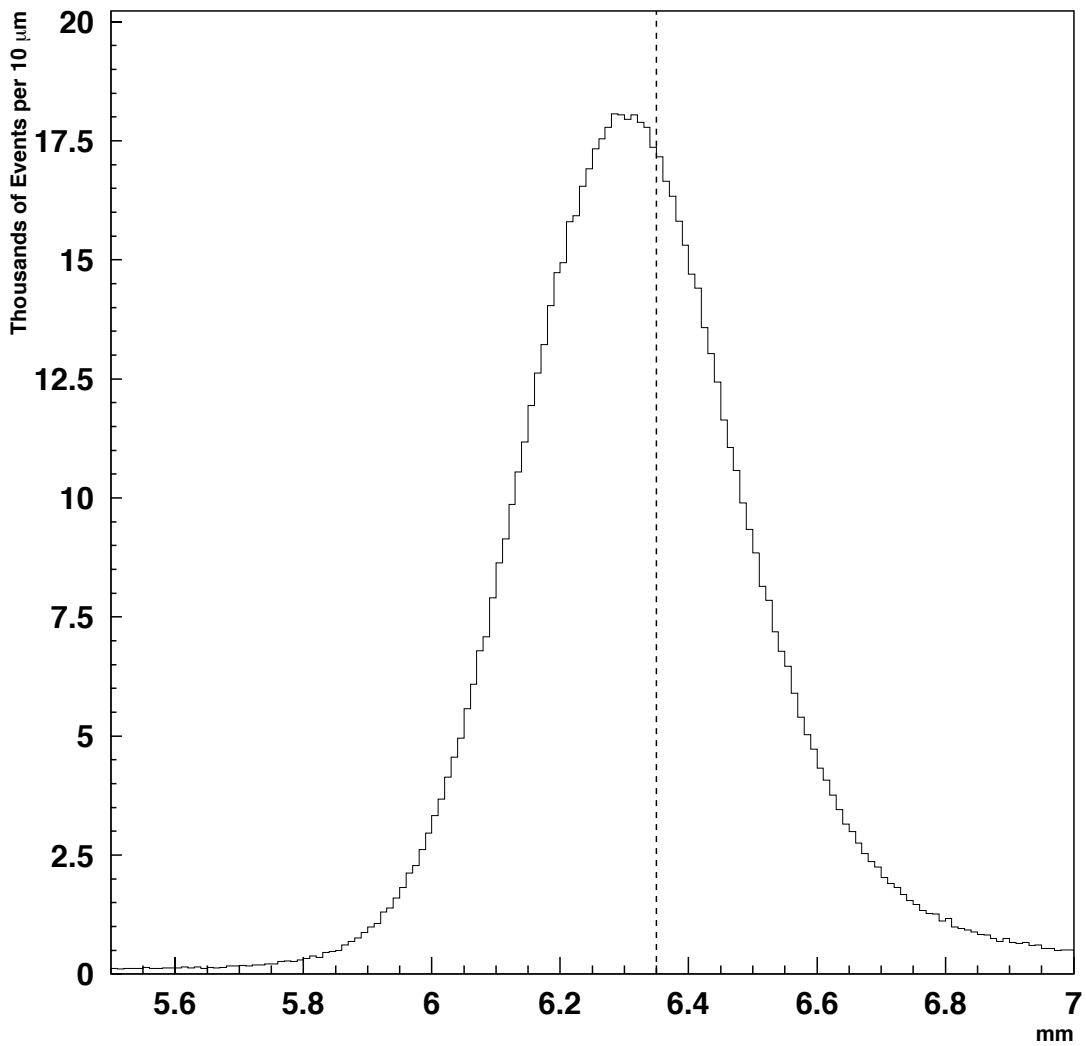

Figure 2.13: Typical drift chamber SOD distribution. The dotted line shows the mean cell size (6.35 mm) indicating that the peak is shifted low. Figure courtesy of J. Graham[2].

Alignment

The first step in the drift chamber alignment is to align DC2 and DC3 in a coordinate system defined by DC1 and DC4. For this calibration, we use straight muon tracks obtained from special muon-only runs taken once a day with the beam-stop in and the analysis magnet turned off. Using these muon tracks, we fit a straight line to the measured positions in DC1 and DC4 and compare the positions of the tracks in DC2 and DC3 to the expected positions based on the fitted line. This comparison yields both the offset and rotation of a plane.

The alignment of DC2 and DC3 with respect to DC1 and DC2 assumes that there is no rotation between DC1 and DC4. If there is a rotation between DC1 and DC4 it will introduce a rotation in DC2 and DC3 because their offsets and rotations are determined in a non-orthogonal reference frame. This rotation can be measured using two-track decays with a common vertex. Since the two tracks share a vertex, they define a plane. If they are reconstructed in DC1 and DC2 and determined to be nonplanar, we determine that there is a residual rotation between the two chambers. This angle is then applied to DC2, DC3, and DC4. We use $K_L \to \pi^{\pm} e^{\mp} \nu$ decays for this "corkscrew" alignment and the rotation we measure is $\sim$450 μrads.

The drift chambers are aligned to the external coordinate system by projecting tracks to the target and the CsI calorimeter. To measure the target position, we use $K \to \pi^+ \pi^-$ decays from the vacuum beam and project the reconstructed kaon momentum back to the z-position of the target. We use electrons from $K_L \to \pi^{\pm} e^{\mp} \nu$ decays to measure the calorimeter position by identifying their tracks with clusters in the calorimeter and comparing the reconstructed cluster positions with the extrapolated track positions.

Magnet Kick

The analyzing magnet imparts a kick of $\sim$412 MeV/c in the horizontal plane. The exact magnitude of this kick is determined from the data by reconstructing $K \to \pi^+ \pi^-$ decays and tuning the kick such that the reconstructed $\pi^+ \pi^-$ mass is equal to the kaon mass. This calibration is performed in run periods lasting two to

three days and corresponding to the periods in which the magnet was run with the same polarity.

2.6.2 Neutral Calibration

The calibration of the CsI calorimeter requires the conversion of integrated charge to energy. The DPMT calibration calibrates the response of the CsI readout electronics and the electron calibration fixes the energy scale using momentum analyzed electrons. Excellent energy linearity is very important in minimizing the systematic errors on $Re(\epsilon'/\epsilon)$ so attention is paid to linearity of response at every stage of the calibration and reconstruction. Many of the corrections that allow us to achieve such linear energy measurements are too intricately linked to the details of cluster reconstruction to be discussed here; they are described fully in Section 3.2.

DPMT Calibration

The laser system is used to deliver light at known intensities spanning the full dynamic range of the calorimeter readout. Figure 2.14 is a schematic of the laser system. Light from a Nd:YAG laser with frequency tripling optics passes through a filter wheel which allows us to vary the intensity. The light is then sent to four "bowling balls" which contain fluorescent dye. The fluorescent dye emits light with a peak wavelength of 380 nm when illuminated by the laser light. The light level emitted by the dye is monitored by a PIN diode that is read out by a 20-bit ADC. Each bowling ball supplies light to one quadrant of the calorimeter; light is transmitted from the balls to each crystal by a quartz fiber. The quartz fibers are attached to the back (DMPT end) of the CsI crystal.

The DPMT calibration is accomplished using special runs with 5 Hz laser pulses which scan the full dynamic range of the QIE. We compare the intensity of laser light measured by the PIN diodes to the integrated PMT current for each channel. We use a linear, least-squares fit to determine the slopes and intercepts for each QIE range and phase. The fit has 64 parameters: a slope and intercept for each of the 8 QIE ranges and phases. After the DPMT calibration, the deviation of the

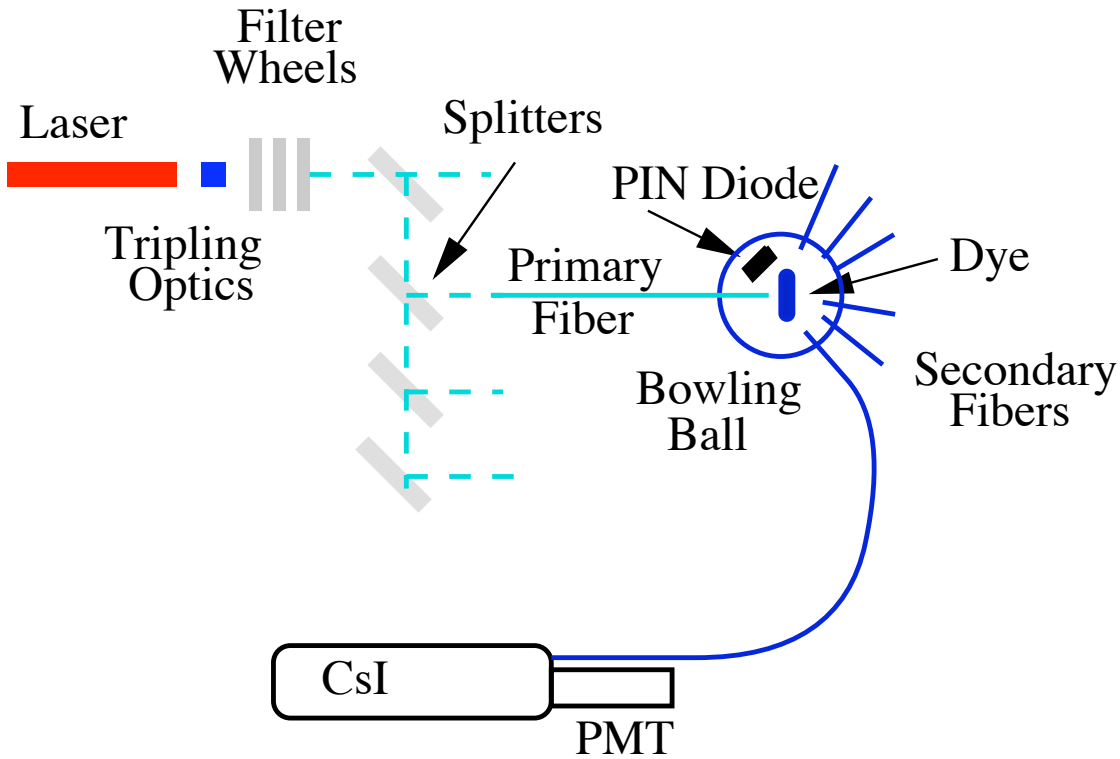

Figure 2.14: Schematic of laser system

measured response from a linear fit is less than 0.2%. This calibration is performed before data-taking begins and is stable throughout the run.

Laser Correction

A correction for fluctuations in the DPMT response is measured using the 1 Hz fixed-intensity laser flashes that are collected during nominal data taking. The mean response of each channel over a spill is determined by normalizing to the measured light level from the PIN diode readout. The change in response for each spill with respect to the first spill of the calibration period is applied as a correction to the channel's gain in offline reconstruction. The average gain drift measured by the laser during 1997 is shown in Figure 2.15.

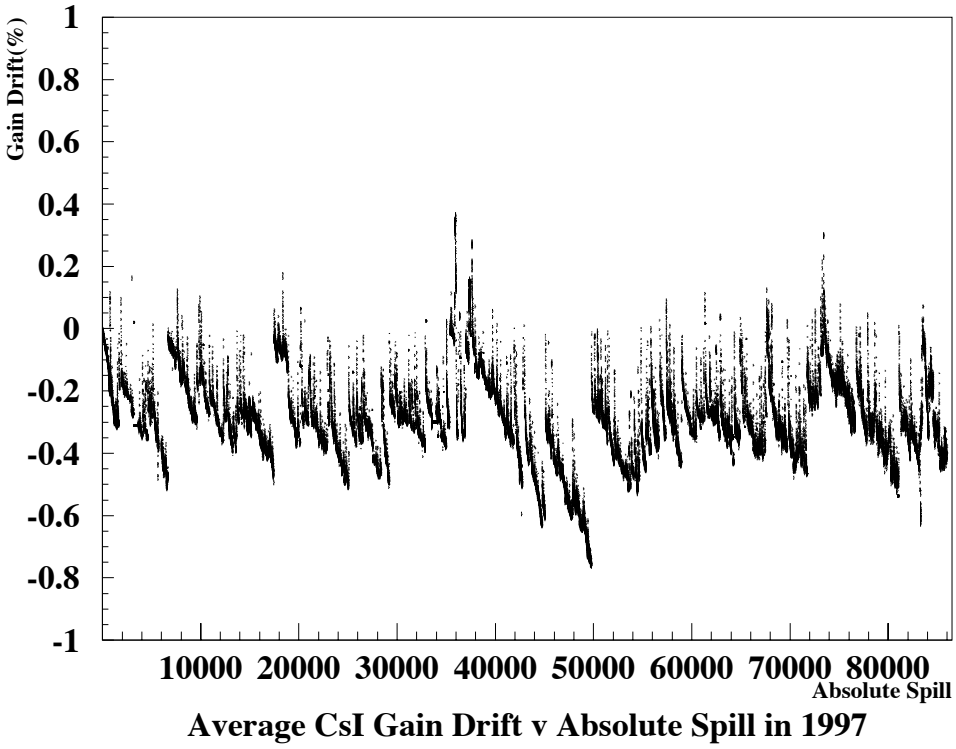

Figure 2.15: Average CsI gain drift measured using laser versus absolute spill in 1997. Figure courtesy of V. Prasad[1].

Electron Calibration

The calorimeter energy scale is calibrated using electrons and positrons from $K_L \rightarrow \pi^{\pm} e^{\mp} \nu$ decays collected during nominal data taking. We compare the reconstructed energy in the CsI for an electron cluster to the electron momentum measured by the charged spectrometer. We assume that the measurement of the electron momentum is accurate and that any non-linearity in the momentum measurement is small. We force the energy/momentum (E/p) distribution to be centered at 1.0 in each of the 3100 CsI channels by adjusting the "charge-to-energy" conversion constant (Q/E) for each channel. We associate each electron cluster with the CsI channel in the

cluster which contains the most energy. The calibration is performed iteratively and converges within four iterations.

The electron sample used for this calibration is chosen to minimize contamination to the electron clusters from nearby pion clusters or accidental activity. The analysis relies on the charged and neutral reconstruction which is described in detail in Chapter 3. We perform standard track and cluster reconstruction and select $K_L \rightarrow \pi^{\pm}e^{\mp}\nu$ events from trigger 2 which have two good tracks. One track must have E/p $>$ 0.8 to be consistent with an electron while the other must have E/p $<$ 0.8 to be consistent with a charged pion.

We make several cuts on the quality of the track reconstruction; we require both χ^2_{vtx} and χ^2_{offmag} be $<$ 20 as high values of these variables generally indicate that the track has been misreconstructed.

We make kinematic cuts to ensure that the decay is consistent with a $K_L \rightarrow \pi^{\pm}e^{\mp}\nu$ decay. We reconstruct the event assuming the two tracks are charged pions and require $m_{\pi\pi}$ $<$ 500 MeV to remove $K \rightarrow \pi\pi$ decays. We require the kinematic variable "pp0kine" which is designed to reject $K \rightarrow \pi^+\pi^-\pi^0$ decays be $>$ -0.02.

The electron cluster must be well separated from the pion cluster in the calorimeter to minimize any contamination from the pion cluster. We require that the reconstructed positions of the two clusters be separated by at least 30 cm and if the two cluster positions are within 50 cm of each other we require that the pion does not shower in the CsI.

We make several cuts against accidental activity in the CsI. We require that the sum of energy in any cluster more than 30 cm away from the pion cluster (not including the electron cluster) be $<$ 10 GeV. We also require that χ^2_{γ}, a measure of how well the transverse energy distribution of the electron cluster matches the expected distribution for an electromagnetic cluster, be $<$ 3.0. This is a tight cut for this variable. The cuts against accidental activity are so effective that the application of a cut on the timing of the energy deposit in the calorimeter makes no difference to the analysis so we do not apply any such cut.

Finally, we make several cuts on the energy deposit in the veto detectors near the CsI. We require that the energy deposit in the CA be $<$ 3 GeV to avoid events

in which the electron shower comes from an electron that scattered in the CA. We also require that the energy deposit in the CIA be < 1.4 GeV to remove events in which some of the electron shower splashed back to the CIA.

In reconstructing the electron cluster in the CsI calorimeter, we make a number of corrections to the reconstructed energy. These include the laser correction described earlier in this Section, corrections for energy missing from or mistakenly added to the reconstructed cluster energy (the missing block correction, the threshold correction, and the sneaky energy correction), and corrections for non-uniformity of crystal response (the intra-block correction and the longitudinal uniformity correction). The measurement of these corrections requires the calibration, so the entire calibration process is iterated several times adding new corrections with each iteration. The sample of calibration electrons is also used to generate several additional cluster energy corrections which are applied in the $K \to \pi^0\pi^0$ analysis. All of these corrections are described in detail in Section 3.2.2. Finally, we correct the measured momentum for energy lost as the electron traverses the small amount of matter between the magnet (where the momentum is measured) and the calorimeter (where the energy is measured). The total energy loss due to ionization downstream of the magnet is 3.42 MeV for 1996 and 1997 and 3.88 MeV for 1999.

The electron calibration is performed in run ranges corresponding to several days of data-taking. The calibration ranges are selected to correspond to the ranges used for the laser correction and to any potentially major change to the CsI such as extended downtimes or the replacement of hardware components. There are 33 calibration ranges for 1996, 36 calibration ranges for 1997, and 30 calibration ranges for 1999.

Figure 2.16 shows the E/p distribution, the E/p resolution as a function of momentum, and E/p as a function of momentum for a sample calibration period in 1999. The low-side tail in the E/p distribution is believed to come from hadronic photon interactions in the calorimeter. These interactions produce charged pions whose energy may not be reconstructed as part of the CsI cluster causing us to underestimate the energy of the incident particle. The resolution and linearity seen in Figure 2.16 are improved after final corrections are applied.

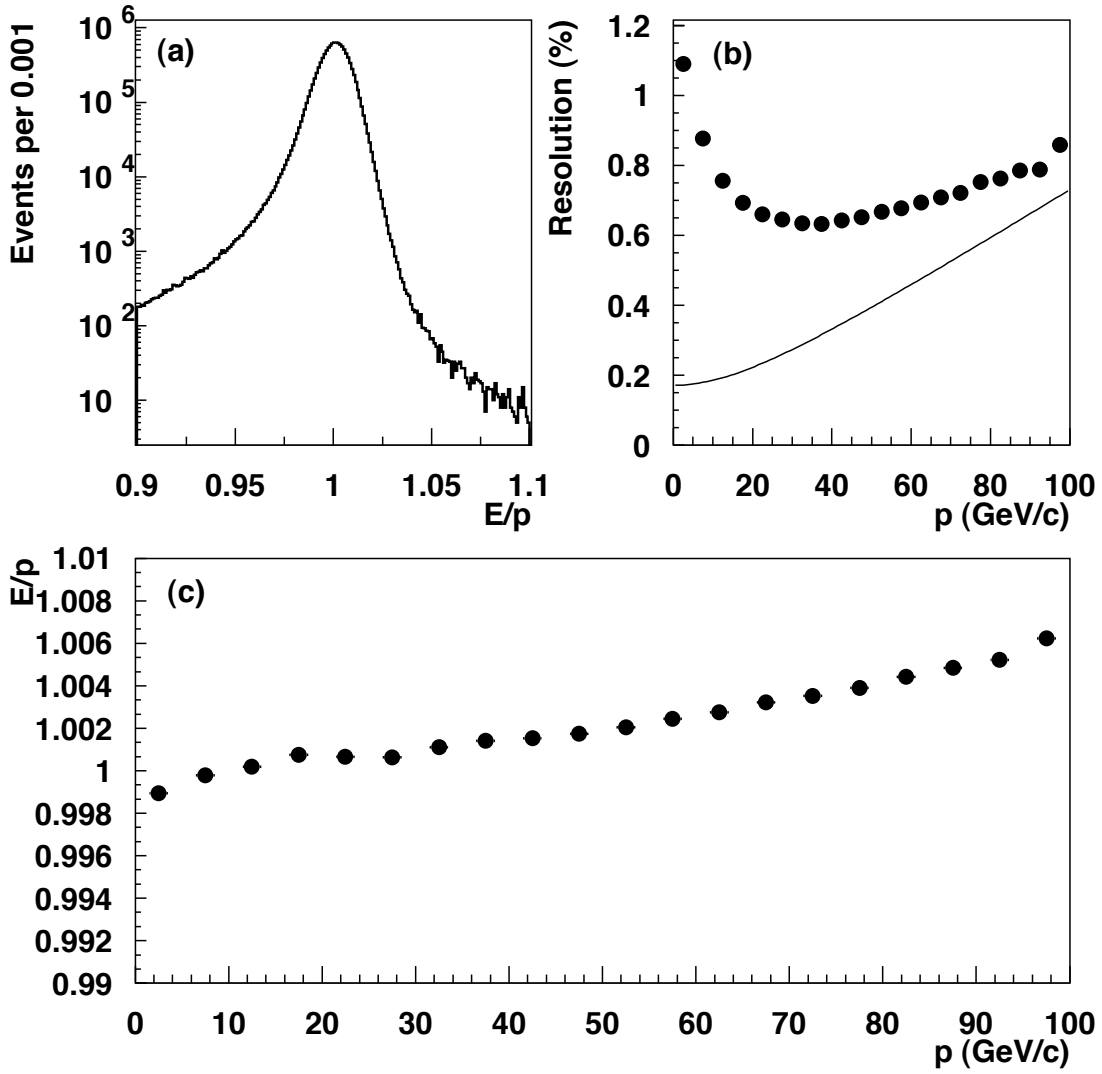

Figure 2.16: Electron calibration plots for all 3100 CsI channels for a sample calibration period from 1999. (a) E/p distribution. (b) E/p resolution as a function of momentum. The fine curve shows the contribution from momentum resolution. (c) E/p as a function of momentum.

2.6.3 Veto Calibration

In the calibration of the veto detectors, we find the number of ADC counts each detector channel reports when a single Minimum Ionizing Particle (MIP) passes through it. This is done channel-by-channel using muons from special muon-only runs taken with the beam-stop in and the analysis magnet turned off. This calibration is performed at the beginning of data-taking to match the channel-to-channel gains in each detector; the voltages applied to the PMTs are adjusted if necessary. This gain matching is important since many of the veto detectors are used in the trigger. The calibration is repeated offline in several run ranges to track any change in the gains during the data-taking period. The gain can then be converted to an energy deposit using a conversion factor which is specific to each detector.

The MA, the RCs, the SAs, the CIA, the CA, and the BA are all calibrated using the same technique. In each case, a trigger in the muon run selects events with a substantial energy deposit in the detector of interest. Selection criteria based on the geometry of the detector are imposed to select events in which a muon passes straight through the detector module. For example, in the RC calibration we require that the two nearest RC detectors also have a hit in the same channel and that the two neighboring channels do not have hits. In other words, when selecting events for RC7 channel 8, we require hits in RC6 channel 8 and RC8 channel 8 and no hits in RC7 channels 7 and 9. We plot the ADC distribution of the selected events for each channel to find the MIP peak and we fit the peak to a skewed Gaussian function given by Equation 2.3.

$$f(x) = p_1 \times exp\left[-\frac{1}{2}\left(\frac{x - p_2}{p_3 + p_4(x - p_2)}\right)^2\right] \tag{2.3}$$

The mean of this skewed Gaussian is the gain for each channel. Figure 2.17a shows a sample MIP peak from one muon run used for the RC calibration in 1999. Figure 2.17b shows the distribution of gains for all 80 RC channels for the same calibration run. Details of the selection criteria for each detector can be found in [62] with the

exception that the current CA calibration uses the same method as is used for the other veto detectors.

To convert the gains to energy deposits, we use $K \to \pi^+\pi^-\pi^0$ events in which one photon is missing and the other three particles are detected in the CsI calorimeter. We then use the kaon mass and the requirement that the total momentum transverse to the beam be zero as constraints to calculate the energy and position of the missing particle. When the missing particle hits a veto detector, we can compare the predicted energy of the missing particle to the number of MIPs reported by the detector to generate a conversion factor. This calibration is described in [62]. The conversion factor is of order 100 MeV/MIP and varies for each detector group.

Regenerator Calibration

The procedure for calibrating the regenerator ADCs is similar to that for the other vetos. We find the MIP peak for each channel and fit it to a Gaussian distribution. We do not perform a formal calibration of the conversion factor from MIPs to energy; our cuts on regenerator energy deposits are in units of MIPs. As with the other vetos, the regenerator gains are measured using special muon-only runs. The final step in the regenerator calibration is to determine the energy deposit of a minimum ionizing particle passing through the lead-scintillator module at the end of the regenerator under nominal data-taking conditions. We use trigger 7, a trigger which requires a hit in the muon vetos, and select events in which a single muon passes through the regenerator. We find the MIP peak and fit it to a Landau distribution. Figure 2.18 shows the lead-scintillator module MIP peak from 1999 in units of nominal MIPs.

It is also possible to measure the MIP peak using $\pi^+\pi^-$ junk events believed to come from K^* and Δ production in the last lead module. The muon sample and the $\pi\pi$ junk sample are measuring different quantities; the peak from the muon sample measures the energy deposit of a single minimum ionizing particle passing through both pieces of scintillator in the last regenerator module while the peak from the $\pi\pi$ junk sample measures the energy deposit of two minimum ionizing particles passing through the second piece of scintillator only. From the geometry of the phototube

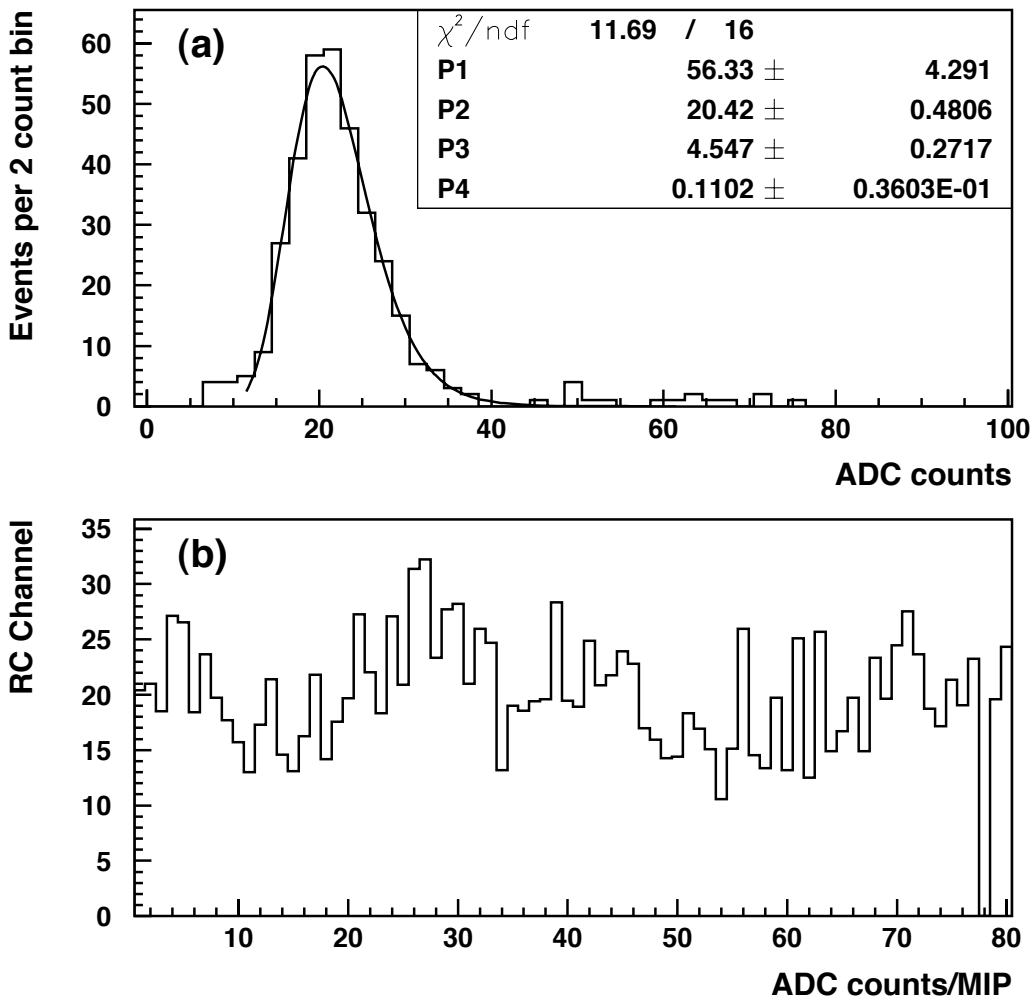

Figure 2.17: RC calibration plots for a sample calibration period from 1999. (a) MIP peak for a single RC channel. The function shows the skewed Gaussian fit with a mean of 20.42. (b) Mean of MIP peaks for all 80 RC channels. Each RC detector has 16 channels. The channel with zero gain was not functional during this period.

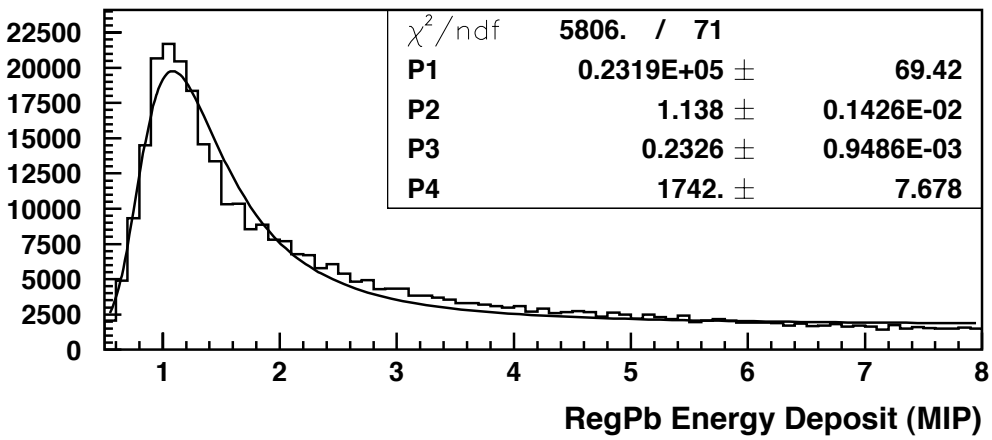

Figure 2.18: Regenerator lead module MIP peak in hadronic conditions. This distribution is made using the muon sample; the function shows the Landau fit with a mean of 1.14 MIPs.

placement we expect that $(43 \pm 7)\%$ of the light comes from the second piece of scintillator. We would therefore expect that the muon MIP peak is 14% higher than the $\pi\pi$ junk MIP peak, and that is exactly what we observe.

2.7 Changes for 1999

A number of changes were made to the KTeV experiment in preparation for data-taking in 1999. Most of these changes were designed to improve the efficiency of data collection for the 1999 run. The plans for all of these changes are detailed in a FNAL proposal[63].

Beam

The spill duty cycle of the Tevatron was improved from 20 second spills every 60 seconds in 1996 and 1997 to 40 second spills every 80 seconds in 1999. The average available beam intensity was higher in 1999 than in 1996 and 1997. The maximum

available intensity was $\sim$8 $\times 10^{12}$ protons per spill (2 $\times 10^{11}$ protons per second) in 1999 compared to $\sim$3.5 $\times 10^{12}$ protons per spill (1.75 $\times 10^{11}$ protons per second) in 1996 and 1997. As discussed in Section 2.4.2, KTeV chose to take about half of the data at high intensity and half at lower intensity as a systematic cross-check.

CsI Electronics

During 1996 and 1997 data-taking there were a large number of failures of the CsI custom electronics. These failures account for a full half of the data-taking inefficiency during 1996 and 1997. They also affect the data quality and complicate the calibration of the calorimeter. The cause of the failures was determined to be out-of-specification fabrication problems by the vendor. All of the DBC and QIE chips were re-fabricated and installed in the CsI in preparation for the 1999 run. The re-fabrication of the chips was successful; no DPMTs had to be replaced during the 1999 E832 run compared to 2-4 per day toward the end of the 1997 run.

Drift Chamber Repair and Helium Bags

Several of the drift chambers required repair due to radiation damage. About half of DC1 was restrung and a second chamber was cleaned. The helium bags placed between the chambers in 1996 and 1997 to minimize the matter seen by the neutral beams after leaving the vacuum decay region were leaky and contained mostly air by the end of the 1997 run. They were replaced with gas-tight bags for 1999.

ADC Change for Veto Detectors

We changed from 10 bit to 8 bit FERA ADCs for the veto detectors to reduce the readout time. The readout time for the ADCs in 1996 and 1997 was 8.7 μs for digitization; the reduction to 8 bit precision reduces that time by $\sim$3 μs. For the regenerator, MA, RC, SA, VV$'$, HA, MU2, and MU3 detectors, we moved to 8 bit precision and kept the same dynamic range. This reduced the number of counts per minimum ionizing particle for these detectors, but the MIP signals were still in the

range of ∼20 counts/MIP which is sufficient for calibration. For the CA and BA detectors we reduced the dynamic range by a factor of four when switching to 8 bit ADCs.

Additional Trigger Elements

Additional trigger sources were formed from the regenerator, MA, and RC signals and sent to TDCs. These extra trigger sources have different TDC thresholds from the nominal trigger sources which allows for tighter or looser cuts to be made offline on the trigger sources. It also turned out to be useful to have a redundancy of trigger source modules in case of failure of the nominal sources.

Online split

In 1996 and 1997, data was written out to nine DLTs simultaneously. Each tape contained the same mix of all trigger types which meant that a large offline effort was required to split these raw data tapes into samples of more manageable size prior to analysis. In 1999, physics triggers were divided into three subsets: charged mode triggers, neutral mode triggers, and K_{e3} triggers. The charged mode set includes trigger 1 ($K \to \pi^+\pi^-$ trigger) with its associated L1 only, random accept, and minimum bias triggers. The neutral mode set includes trigger 4 ($K \to \pi^0\pi^0$ trigger) and trigger 6 ($K_L \to \pi^0\pi^0\pi^0$ trigger) with the neutral L1 only and random accept triggers. The K_{e3} sample includes $K_L \to \pi^\pm e^\mp \nu$ triggers from trigger 1 for acceptance studies and trigger 2 for the electron calibration. There is also a set from the calibration plane which includes accidental triggers and calibration triggers such as the CsI pedestal and laser triggers. These subsets were each written to three DLTs simultaneously. Finally, small data samples were written to disk for immediate access; these disk files were later backed up on DLT. The switch to the online split required increased disk space and an upgrade to the network connection. It saved many months of effort associated with the offline split, made data available for analysis more quickly, and substantially reduced the number of tapes used during 1999.

CHAPTER 3
DATA ANALYSIS

This chapter describes the reconstruction and selection of $K \to \pi^+\pi^-$ and $K \to \pi^0\pi^0$ decays. The $K \to \pi^+\pi^-$ analysis consists primarily of the reconstruction of tracks in the spectrometer; the vertices and momenta of the tracks are used to calculate kinematic quantities describing the decay. The reconstruction of photon showers in the calorimeter is the basis for the $K \to \pi^0\pi^0$ analysis; the positions and energies of the reconstructed clusters are used to calculate the decay vertex and the kinematics of the decay. Event selection in both modes consists of a set of cuts designed to select events which are well reconstructed, to reduce backgrounds, and to select kinematic and fiducial regions appropriate to the KTeV detector.

3.1 $K \to \pi^+\pi^-$ Analysis

This section is intended to provide a brief overview of the $K \to \pi^+\pi^-$ analysis; see [2] for a more detailed discussion.

3.1.1 Tracking

The process of track finding begins by combining drift chamber hits into pairs and classifying those pairs. The pairs are then used to build track candidates in the x and y views separately. Next vertex candidates, which are combinations of x and y track candidates, are identified and matched to clusters in the calorimeter. A number of track corrections are applied at this stage and finally the best vertex from the list of candidates is selected.

A drift chamber "in-time hit" is defined as an analog signal above the TDC threshold for a given wire within the in-time window of 235 ns from the trigger

signal. As described in Section 2.3.3, the two planes of each drift chamber view are offset by one-half cell so that the two hits will form pairs that determine on which side of the wire the particle passed. The sum-of-distance (SOD) for a pair of hits should be equal to the cell size of 6.35 mm. Pairs of hits are classified based on their SOD; SODs are "good" if they are within ± 1 mm of the cell size, "low" if they are less than 5.35 mm, and "high" if they are greater than 7.35 mm. Quality values for the pairs are assigned based on SOD value and used to make decisions within the tracking algorithm. A pair receives a quality value of 4 for a good SOD and 2 for a low or high SOD. Isolated single hits receive a quality value of 1.

The procedures for finding track candidates in the x and y views are different because the y tracks are straight while the x tracks are bent by the magnet. Track candidates are found in the y view by forming a line between one hit pair in DC1 and one in DC4 and then searching for pairs in DC2 and DC3 that fall within 5 mm of the line. If hit pairs are found in DC2 and DC3 the quality values of the hit pairs in all four drift chambers are summed. A track candidate with four good SODs has a quality sum of 16; we keep track candidates with a quality sum of at least 11. Then the track is fit to a line and the candidate is kept if the fit χ^2 is acceptable. In general, track candidates are not allowed to share hits; we calculate the number of remaining y track candidates that can exist without sharing hits and require that at least two independent y tracks exist. Track candidates in the x view are found by forming track segments separately in the upstream and the downstream drift chambers and then matching the segments at the midplane of the analysis magnet. The quality sum for the upstream segments is required to be at least 4 and the quality sum of the downstream segments must be at least 5. For each combination of upstream and downstream segments, the distance between the projections of the two segments at the magnet must be less than 6 mm and the total quality sum must be at least 11. We require at least two x track candidates which do not share hits to proceed.

Vertex candidates are sets of x track candidates matched to sets of y track candidates consistent with originating at the same z position. We find the z position of the intersection of each pair of x track candidates and compare it to the intersection

of each pair of y track candidates to form a vertex candidate. The two x track candidates in a vertex candidate are required to bend in opposite directions in the magnet to be consistent with particles of opposite charge. We resolve the ambiguity of matching x track candidates with y track candidates by matching tracks to clusters of energy in the calorimeter. We combine each $x-y$ track candidate into a full track candidate and extrapolate it to the face of the calorimeter; the position of the extrapolated track must match the reconstructed cluster position to within 7 cm.

Track corrections are applied at this point because most of them require that both the x and y coordinate of a track at a given z position be known. We correct for the physical rotation of the drift chambers, individual wire positions, and the time-delay of the pulse propagating along the wire. We make corrections to the SOD value based on the angle of the track through the drift cell. We then correct the hits in DC2 and DC3 to account for the fact that the trajectories of particles through the magnet are not actually straight lines; we include the effect of a small residual magnetic field between the drift chambers. Figure 3.1 illustrates this correction. We make further corrections to the SODs to resolve issues of hit sharing and SODs that are classified as good but are more than 600 μm from the nominal cell size. We refit y track segments upstream and downstream of the magnet to allow for a slight y-bend at the magnet. After all corrections, we calculate χ^2_{offmag}, which is a measure of how well upstream and downstream track segments match at the magnet.

The best vertex is chosen from the vertex candidates by fitting the upstream track positions in x and y to the constraint that they come from a common (x,y,z) point in space. This fit has eight data points (two points on two tracks in x and y) and seven unknowns (the three coordinates of the vertex position and the slopes for two tracks in x and y) so the fit has one degree of freedom. The selection of the best vertex is based on the fit χ^2, the match between the upstream and downstream track segments at the magnet, and the number of good SOD pairs used in the vertex candidate.

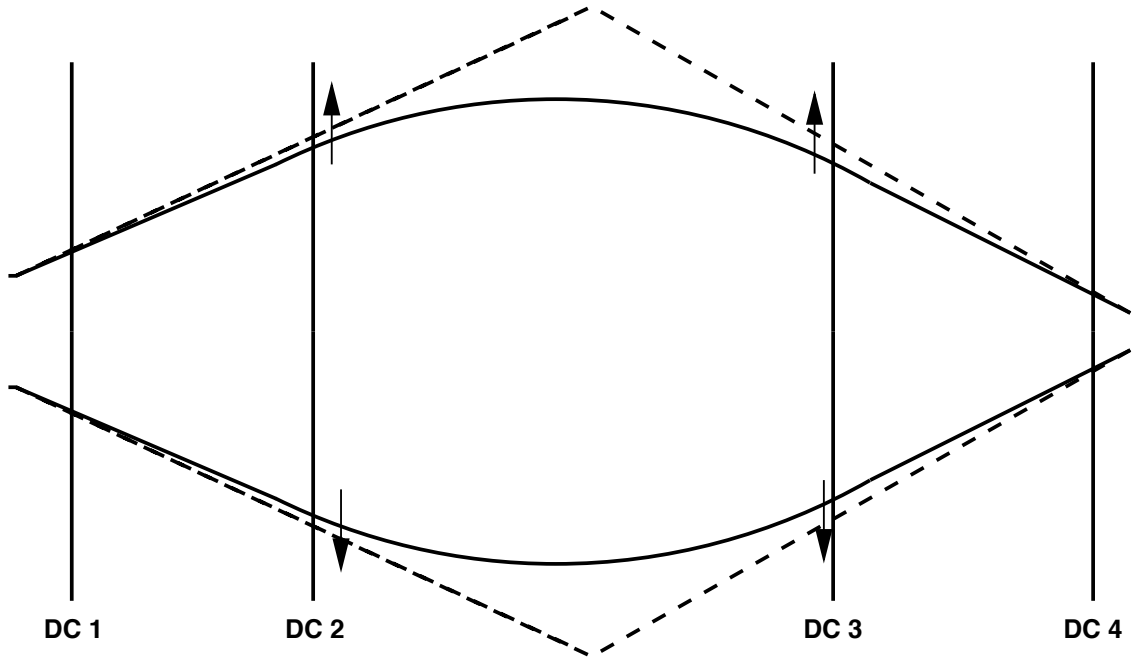

Figure 3.1: The true bend of tracks through the magnet (solid curves) and the assumed straight tracks (dotted lines). We correct the hit positions in DC2 and DC3 (shown as arrows) to line up the hit positions to straight lines. Figure courtesy of J. Graham[2].

3.1.2 Event Reconstruction

In the event reconstruction we use the vertex and the momenta of the two tracks forming that vertex to calculate the invariant mass of the two particles, their lab energy, and the sum of their momenta transverse to the beam direction. Assuming the two tracks come from pions, the invariant mass of the two-track system is

$$m^2_{\pi^+\pi^-} = 2m^2_\pi + 2\sqrt{m_\pi + p_1^2}\sqrt{m_\pi + p_2^2} - 2\vec{p_1}\cdot\vec{p_2} \tag{3.1}$$

$$\sim 2m^2_\pi + p_1 p_2 \theta^2 + m^2_\pi(R + 1/R), \tag{3.2}$$

where R = p1/p2 and θ is the opening angle of the two tracks. The energy is

$$E_{\pi^+\pi^-} = \sqrt{m^2_\pi + p_1^2} + \sqrt{m^2_\pi + p_2^2}. \tag{3.3}$$

As discussed in Section 2.3.2, this analysis accepts decays of unscattered kaons only. We reject scattered events using the sum of momenta transverse to the kaon direction of flight; unscattered events should have no net transverse momentum (p_T). Because it is particularly important to understand events that scatter in the regenerator, we calculate p_T^2 by assuming that the scattering occurred in the regenerator. In other words, in Figure 3.2 we use

$$p_T^2 = |\vec{p}|^2 sin^2\phi_R \tag{3.4}$$

rather than $|\vec{p}|^2 sin^2\phi_V$. This does not make any difference for coherent events and allows us to better characterize scattering in the regenerator which is important for understanding backgrounds in the $K \to \pi^0\pi^0$ analysis.

Figure 3.3 shows the KTeV event display for a reconstructed two track event including the tracks matched to clusters in the calorimeter, the two straight y tracks, the two bent x tracks, and the reconstructed invariant mass and p_T^2. In this particular event, the decay vertex is in the regenerator beam.

3.1.3 Event Selection

The $K \to \pi^+\pi^-$ event sample is chosen by applying a series of requirements that are designed to ensure data quality, suppress backgrounds, and select kinematic and fiducial regions appropriate for the KTeV detector.

We reject some runs or portions of runs because of hardware malfunctions during data-taking and verify the level 1 trigger in software by requiring that the two tracks alone satisfy the level 1 trigger requirement. We make loose cuts on the track quality variables χ^2_{vtx} and χ^2_{offmag}. The vertex χ^2 describes how consistent the two tracks are with coming from a common vertex; we require $\chi^2_{vtx} < 500$. The offmag χ^2 describes how well the upstream and downstream track segments match at the magnet; we require $\chi^2_{offmag} < 100$.

We make a number of cuts on the energy deposit in the veto detectors. The most important veto cuts are the muon veto cuts which suppress background from $K_L \to \pi^\pm\mu^\mp\nu_\mu$ decays and the regenerator cuts which reduce background from scat-

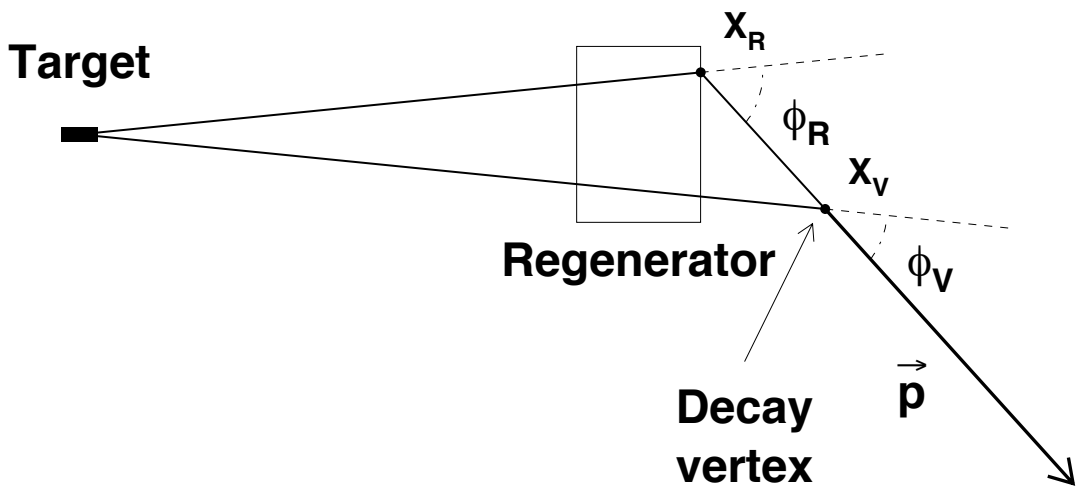

Figure 3.2: Cartoon of scattering in the regenerator showing the angle used to define p_T^2. The kaon scatters at point x_R and decays at point x_V. We use the angle ϕ_R to calculate p_T^2 for all events. Figure courtesy of J. Graham[2].

tered kaons. The remaining veto cuts are made for consistency with the $K \to \pi^0\pi^0$ analysis. The way in which the veto cuts are applied varies between the two years; in 1999 we rely more on the trigger sources which have thresholds set in hardware during data collection and less on the measured energy deposit in the veto detectors which comes from the ADC readout of the detectors. The veto cuts we apply for each year are summarized in Table 3.1. We use the spectrometer and the calorimeter as "veto detectors" also: we reject events with any tracks other than those from the vertex and we reject events with extra clusters having energy greater than 1.0 GeV. We avoid cutting on satellite clusters from pion interactions by requiring any extra cluster used to remove an event be at least 20 cm from the extrapolated track position at the CsI. We require E/p < 0.85 to identify the tracks as pions and require p > 8 GeV/c to ensure 100% efficiency for the muon veto detectors; these cuts suppress background from K_{e3} and $K_{\mu 3}$ decay modes.

We remove events with 1.112 GeV/c^2 $< m_{p\pi} <$ 1.119 GeV/c^2, where $m_{p\pi}$ is the invariant mass assuming the higher momentum particle is a proton. This removes

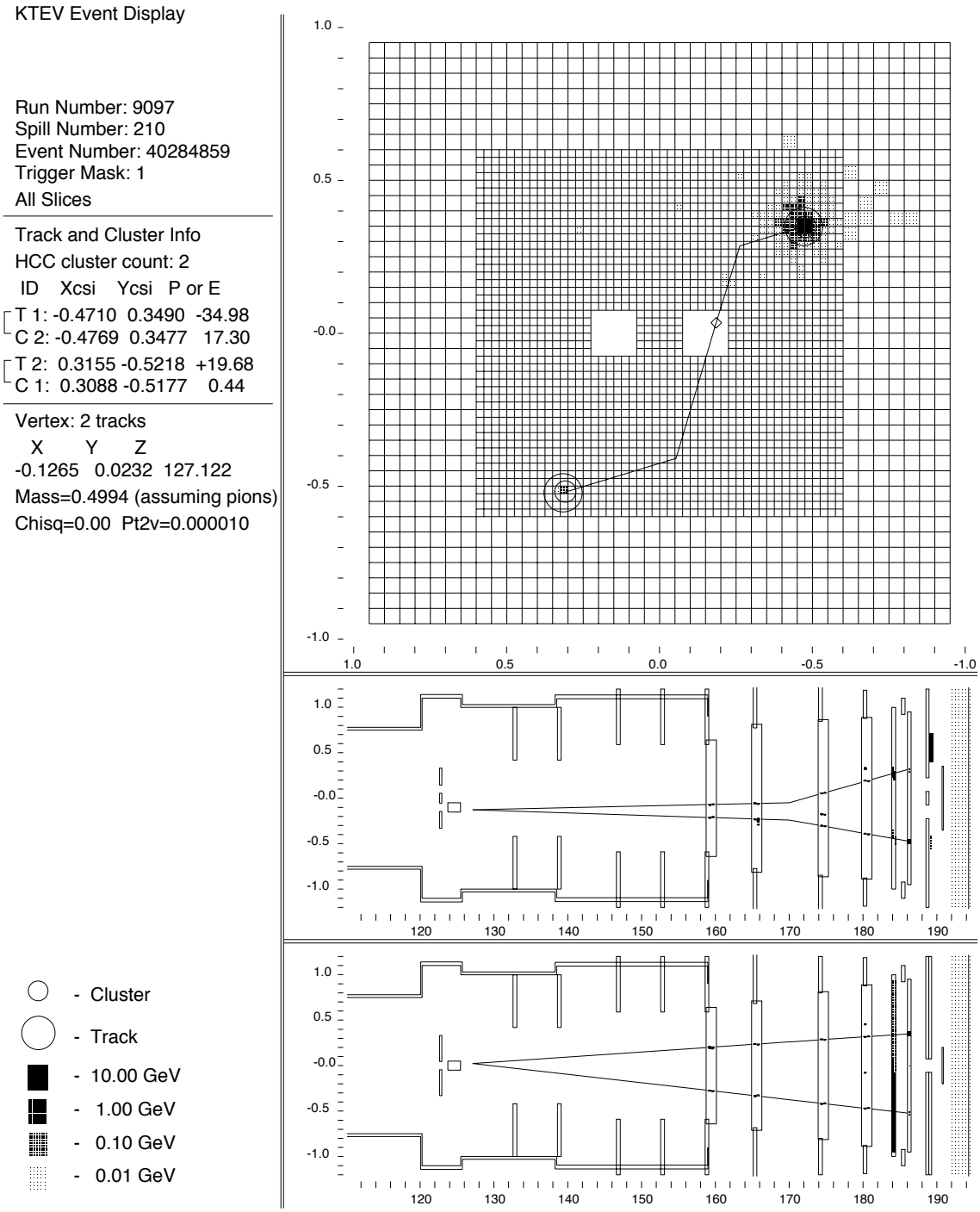

Figure 3.3: Event display for a $K \to \pi^+\pi^-$ event. The top panel shows the clusters of energy in the calorimeter with matching track projections. The middle panel shows the x view of the tracks with the bend at the analysis magnet. The bottom panel shows the straight y tracks. In the middle panel the decay vertex is seen to be within the regenerator beam. Figure courtesy of J. Graham[2].

Veto Detector	1997 Cut	1999 Cut
Regenerator	E < 2.0 mips	E < 1.75 mips
Regenerator Pb	E < 0.7 mips	E< 0.25 mips
MA	E < 0.1 GeV	L1 trigger source = F
RCs	L1 trigger source = F	L1 trigger source = F
SAs	E < 0.3 GeV and L1 trigger source = F	L1 trigger source = F
CIA	E < 0.3 GeV and L1 trigger source = F	E < 0.3 GeV and L1 trigger source = F
CA	no cut	no cut
BA1	no cut	no cut
HA	no cut	no cut
MU2/MU3	Nhit = 0	Nhit = 0

Table 3.1: Summary of veto cuts for $K \to \pi^+\pi^-$ decays. Some cuts are applied differently for 1997 and 1999. Compare to the requirements for $K \to \pi^0\pi^0$ decays in Table 3.5.

background from $\Lambda \to p\pi^-$ decays where the proton is mis-identified as a pion. Figure 3.4 shows the $\pi^+\pi^-$ invariant mass distributions for the two beams; we require 488 MeV/c^2 < $m_{\pi^+\pi^-}$ < 508 MeV/c^2. Figure 3.5 shows the p_T^2 distributions; we require $p_T^2 < 250$ MeV^2/c^2.

We cut away from a number of physical apertures to simplify the Monte Carlo simulation. We require the tracks to point at least 2 mm into the CsI away from the CA edges and to point at least 2.9 cm inside the outer edge of the CsI. If the vertex position is upstream of the MA, we require the track position at the MA be less than 4 cm from the nominal beam center. We cut away from wires at the edges of the drift chambers; this cut varies with each chamber. To reduce the possibility of x and y track candidate mismatches, we require that the projections of the tracks at the CsI be separated by 6 cm in x and in y. We also require a minimum separation between the tracks in the x and y views at each drift chamber. This cut is defined in terms of the cell to which each track is assigned; we require the tracks to be separated by at least 3 cells at each chamber. This cut removes events which are difficult to simulate. We remove beam halo events by requiring that the vertex (x,y)

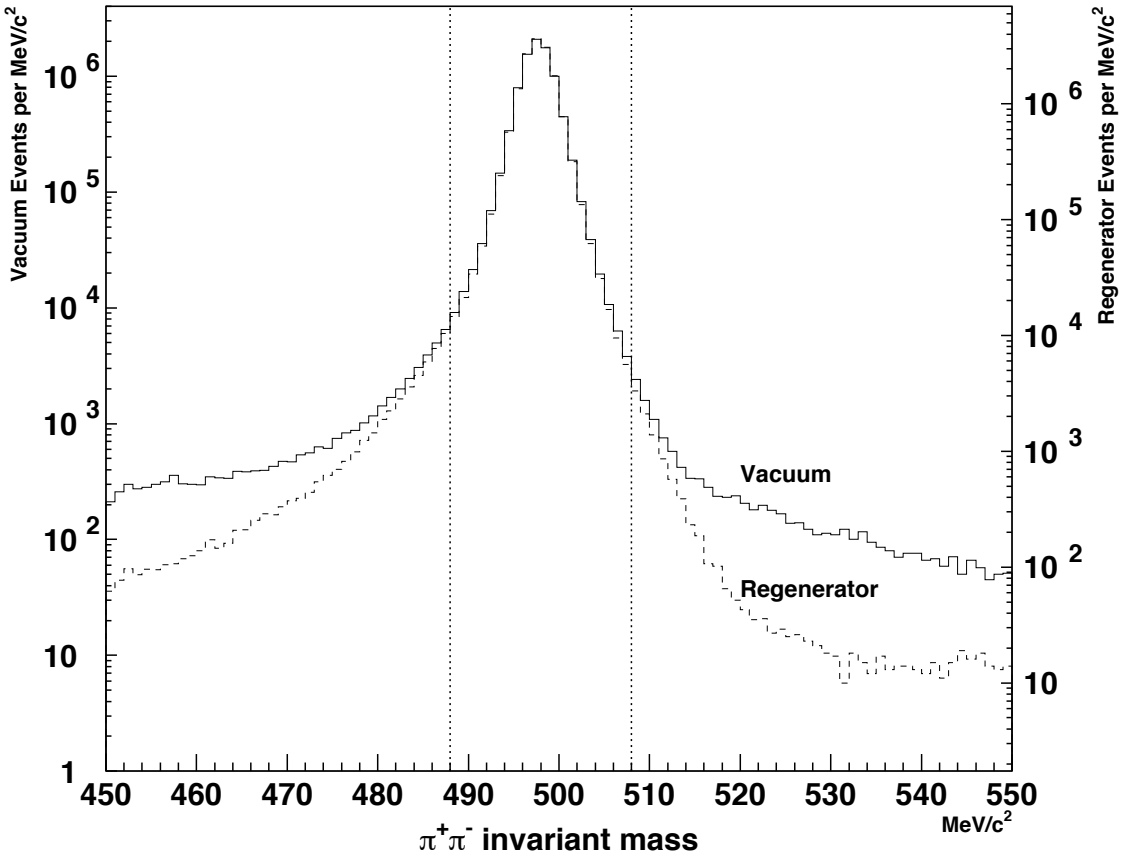

Figure 3.4: Invariant mass distributions for $\pi^+\pi^-$ data for both beams after all other analysis cuts are applied. The dotted lines show where our cuts are made. Figure courtesy of J. Graham[2].

position reconstruct within a 75 cm^2 square at the z of the downstream edge of the regenerator.

Finally we require the kaon energy to be between 40 and 160 GeV and the z vertex position to be 110 m $<$ z $<$ 158 m. The 40 GeV energy cut is chosen because of rapidly falling detector acceptance at lower kaon energies and the 160 GeV energy cut is chosen as a compromise between increased statistics and target-K$_S$ contamination. The upstream vertex cut is chosen to be well upstream of the MA. This requirement removes few events in the vacuum beam and none in the regener-

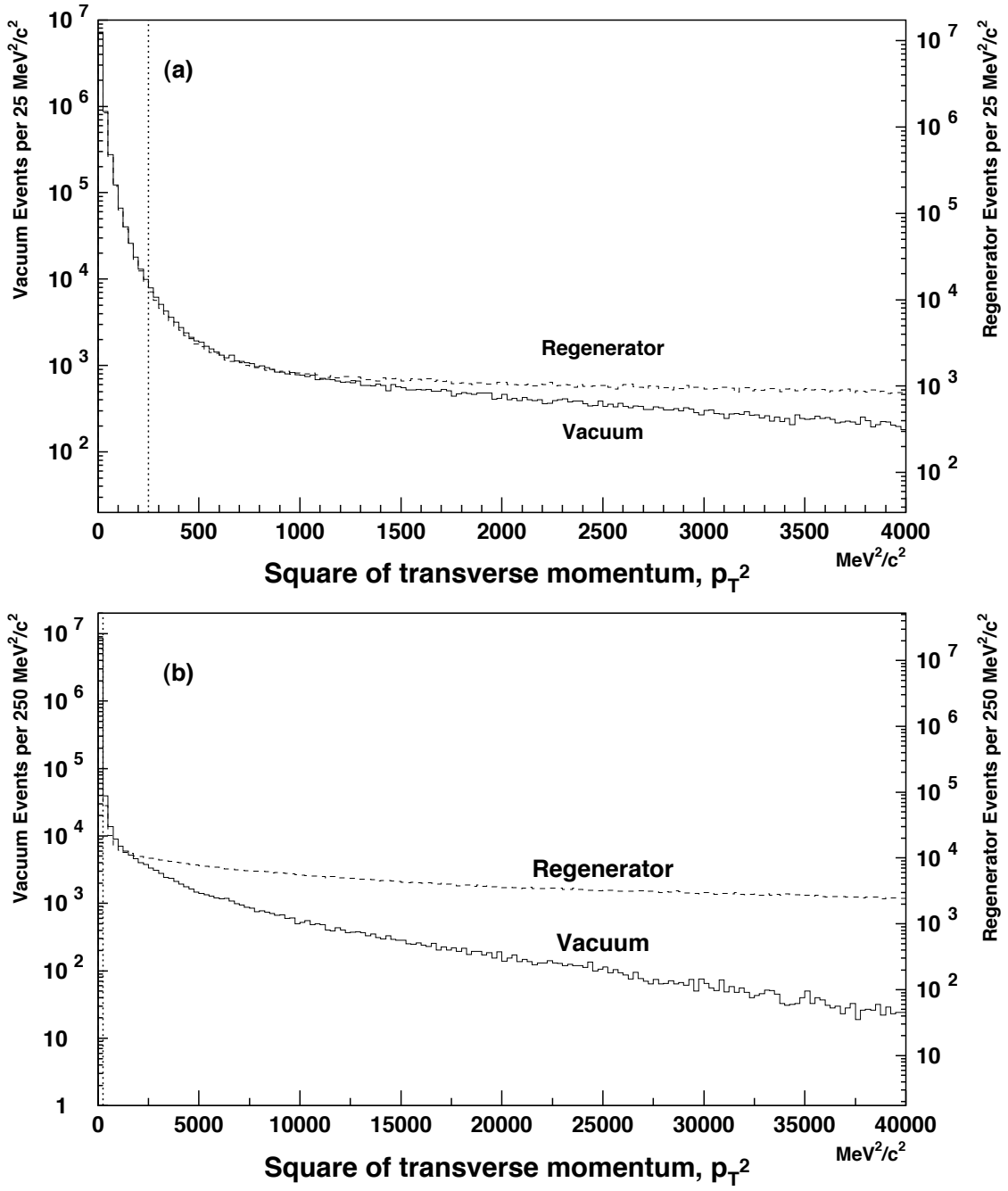

Figure 3.5: p_T^2 distributions for $\pi^+\pi^-$ data for both beams after all other analysis cuts are applied. The dotted lines show where our cut is made. (a) and (b) show the same data on two different horizontal scales. Figure courtesy of J. Graham[2].

ator beam. The downstream vertex cut is chosen to avoid backgrounds from beam interactions in the vacuum window. These cuts are identical for the $K \to \pi^+\pi^-$ and $K \to \pi^0\pi^0$ samples. Figures 3.6 and 3.7 show the kaon energy and vertex z distributions for the $\pi^+\pi^-$ sample.

Summary

The selection criteria for $K \to \pi^+\pi^-$ decays are summarized in Table 3.2.

Quantity	Cut Value
Veto cuts	See Table 3.1
Vertex chi-squared	$\chi^2_{vtx} < 500$
Offmag chi-squared	$\chi^2_{offmag} < 100$
Number of tracks	$N_{trk} = 2$
Extra clusters	$E_{extra} < 1.0$ GeV
E/p	E/p < 0.85
pπ invariant mass	$m_{p\pi} < 1.112$ GeV/c^2 or $m_{p\pi} > 1.119$ GeV/c^2
$\pi^+\pi^-$ invariant mass	488 MeV/c^2 $< m_{\pi^+\pi^-} <$ 508 MeV/c^2
Transverse momentum	$p_T^2 < 250$ MeV^2/c^2
CA aperture	> 2 mm
CsI outer aperture	> 2.9 cm
Distance from beam center at MA	< 4 cm
Track separation at CsI	> 6 cm
Cell separation	≥ 3 cells
Transverse vertex	< 75 cm^2
Kaon energy	40 GeV $< E_K <$ 160 GeV
z vertex	110 m $< Z_K <$ 158 m

Table 3.2: Summary of selection criteria for $K \to \pi^+\pi^-$ decays

3.1.4 Updates since 2003

There have been a few changes to the $K \to \pi^+\pi^-$ analysis since [2] and the 2003 PRD[50]. The drift chamber sizes have been updated based on a measurement done in the lab in 2002. See Section 4.7 for more details on the survey. The cut on minimum track separation at the CsI has been tightened from 3 cm to 6 cm. The MA clearance cut is now made in terms of distance of the track from the center

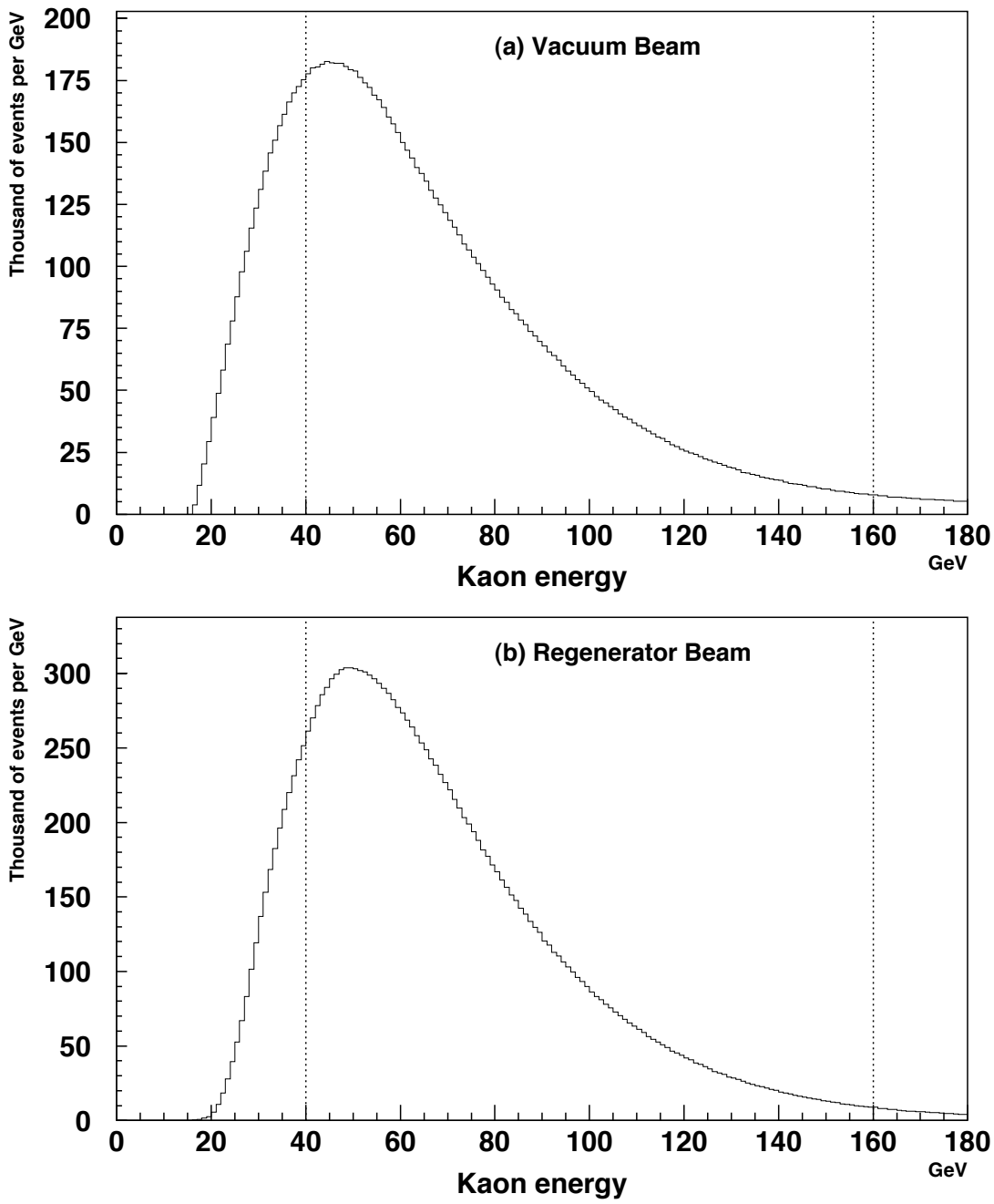

Figure 3.6: Kaon energy distributions for $\pi^+\pi^-$ data after all other analysis cuts are applied. The dotted lines show where our cuts are made. Figure courtesy of J. Graham[2].

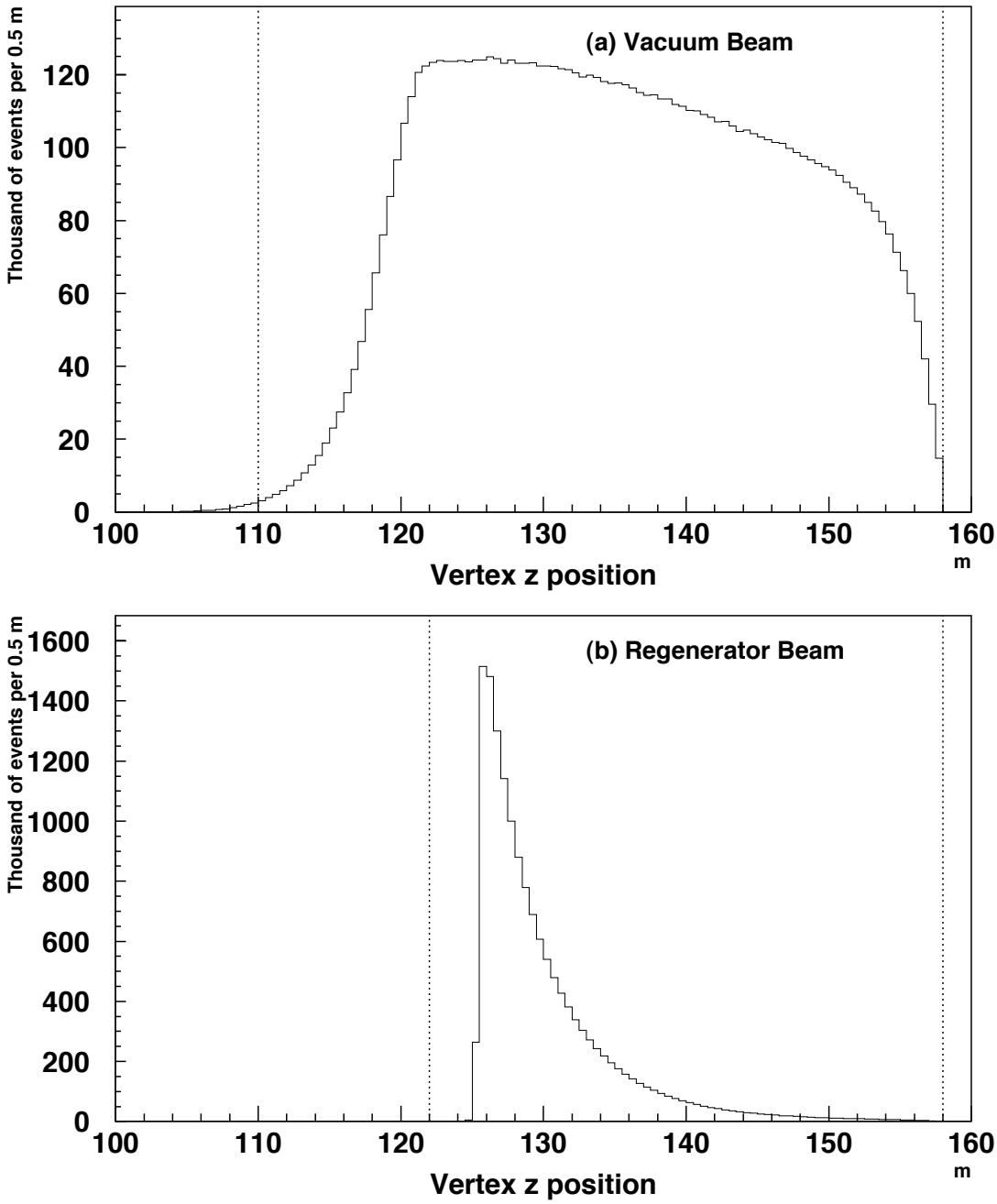

Figure 3.7: Vertex z distributions for $\pi^+\pi^-$ data after all other analysis cuts are applied. The dotted lines show where our cuts are made with the exception that the upstream vertex cut is made at 110 m in the regenerator beam; there is no effective difference between the actual cut and the cut shown by the dotted line. Figure courtesy of J. Graham[2].

of the beam rather than distance to the edge of the MA. Making the cut this way reduces systematics from simulation of the beam shape.

Regenerator Pb Cut for 1999

In 1999, the online threshold for the regenerator Pb module was higher than in 1997, and higher than our offline cut. This would have led to large uncertainties in the charged mode effective regenerator edge. The effect of making a tighter offline cut is studied using $\pi^+\pi^-$ junk events. We find that an offline cut on the energy deposit in the regenerator Pb module of 0.25 MIPs significantly reduces the junk background and allows more precise determination of the charged mode regenerator edge. We apply the cut of 0.25 MIPs to 1999 data only.

3.1.5 Yields

Table 3.3 contains the number of $K \to \pi^+\pi^-$ events selected before background subtraction.

Year	Vacuum Beam	Regenerator Beam
1997	10670688	18594207
1999	14447735	25115620
Total	25118423	43709827

Table 3.3: $\pi^+\pi^-$ event yields before background subtraction

3.2 $K \to \pi^0\pi^0$ Analysis

To reconstruct $K \to \pi^0\pi^0$ decays using the KTeV detector, we first identify clusters of energy in the calorimeter and reconstruct the energies and positions of the photons associated with each cluster. A number of corrections are made to both the block and cluster energies based on our knowledge of the CsI performance and the reconstruction algorithm. We use the cluster positions and energies along with the known π^0 mass to determine which pair of photons is associated with which neutral pion from the kaon decay and calculate the decay vertex, the center of energy,

and the $\pi^0\pi^0$ invariant mass. We make cuts to select $K \to \pi^0\pi^0$ decays, reduce backgrounds, and cut away from regions that are not well simulated by the Monte Carlo.

3.2.1 Clustering

The first step in reconstructing clusters is to determine the energy deposit in each block of the CsI which was read out. We unpack the digitized DPMT information in each slice and use the DPMT calibration (see Section 2.6.2) to convert it to a charge. This charge is integrated over 6 in-time slices or 114 ns.[1] The integrated charge is converted to an energy using the Q/E constants that are measured for each channel by the electron calibration (see Section 2.6.2). The laser correction, which corrects for spill-to-spill drifts in each channel's gain, is applied to each block energy.

To build clusters, we search for blocks that are local energy maxima by comparing the energy in each block to the energies in the 8 blocks around it. In the case of a large block which is adjacent to small blocks on the small-large boundary, we check the energies of the two small blocks which touch it but not of those diagonal to it. When a local maximum is found, it is called a "seed block" and we build a cluster with the seed block at its center. The clusters are 7×7 arrays of small blocks or 3×3 arrays of large blocks. If the seed block is near the small-large boundary so that its cluster contains both small and large blocks, the cluster is defined as a 3×3 array of large blocks where the small blocks are combined to form large-block equivalents. If the seed block is near the beam holes so that its cluster contains "blocks" that are in the beam hole, the cluster may not wrap around the beam hole unless the seed block is at the corner of the beam hole. The definitions of clusters for seed blocks near the beam holes are illustrated in Figure 3.8. We sum the energies of the blocks in the cluster to find a raw cluster energy; this raw energy must still be corrected for a number of geometric and detector effects.

[1] In 1996, the DPMTs were operated at RF/3, so the charge is integrated over 4 RF/3 slices or 228 ns.

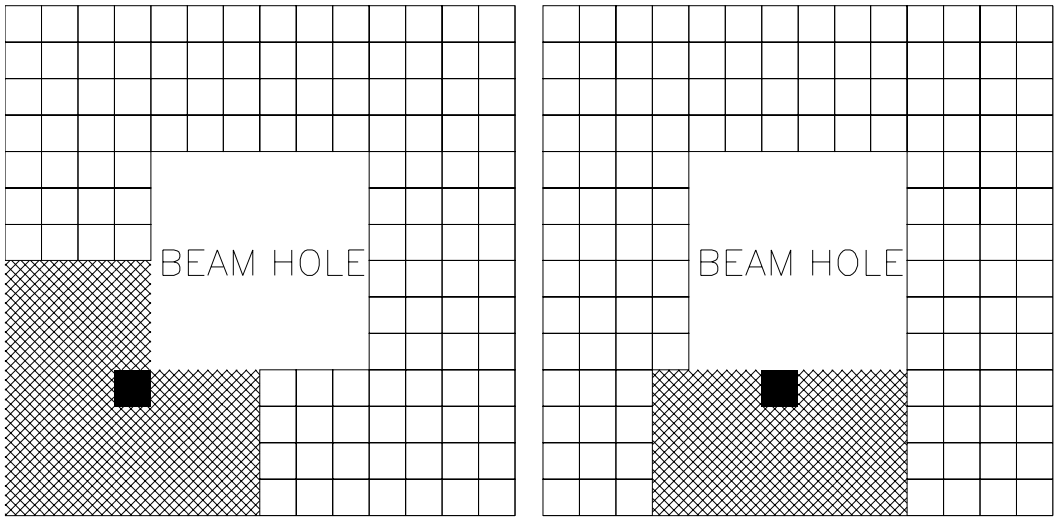

Figure 3.8: Definition of clusters near a beam hole. The seed block is in black and the blocks that are included in the cluster are shaded. Figure courtesy of V. Prasad[1].

Clustering may be done with or without an HCC requirement. "Hardware clustering" requires that the seed block for each cluster have its HCC bit on, meaning that its energy is greater than ∼1 GeV. We require that the offline energy of the seed block reconstruct to at least 100 MeV to exclude clusters which have very little energy but whose HCC bit is on due to a hardware error. "Software clustering" makes no requirement on the HCC; we require that the seed block contain at least 100 MeV and that the sum of the energies in the cluster be at least 250 MeV. For the $K \to \pi^0\pi^0$ analysis we first identify hardware clusters and then search for additional low-energy clusters using software clustering. For the electron calibration we

perform software clustering only, since there is no HCC requirement in the trigger which selects these events.

We define the transverse position of each cluster to be its center-of-energy. We reconstruct the position of a cluster by calculating the fraction of energy in neighboring columns and rows of the cluster. We use a map which is based on the uniform photon illumination across each crystal to convert these ratios to a position within the seed block.

The maps are generated using photons from $K \rightarrow \pi^0\pi^0$ decays with all nominal selection criteria with the exception that we remove the minimum cluster energy requirement so that the maps will be more accurate at low energies. We also require that the clusters be isolated, meaning there are no other clusters within 40 cm, so that there is no contamination from nearby clusters. To make the maps, we measure the ratio of energy in an adjacent row or column to the row or column containing the seed block. We then integrate the distribution of these ratios and, assuming that the distribution of photons is uniform across the face of the crystal, we rescale the resulting function from 0-N to -x-x. Figure 3.9 shows the energy ratio distribution and the corresponding position map for small blocks in one of the energy bins. There are separate maps for small and large blocks and the maps are binned in 6 logarithmic energy bins (2 GeV, 4 GeV, 8 GeV, 16 Gev, 32 GeV, and 64 GeV). Separate maps are generated for data and Monte Carlo.

The positions we measure are the x and y positions at the z position of the mean shower depth in the calorimeter. For particles with significant incident angles this means that the x and y positions determined by the position algorithm are not exactly comparable if the energy, incident angle, and particle type are not identical. We measure the position resolution using electrons from $K_L \rightarrow \pi^{\pm}e^{\mp}\nu$ decays by comparing the reconstructed cluster position to the position of the track extrapolated to the mean electron shower depth in the calorimeter. The average position resolution is 1.2 mm for small blocks and 2.4 mm for large blocks.

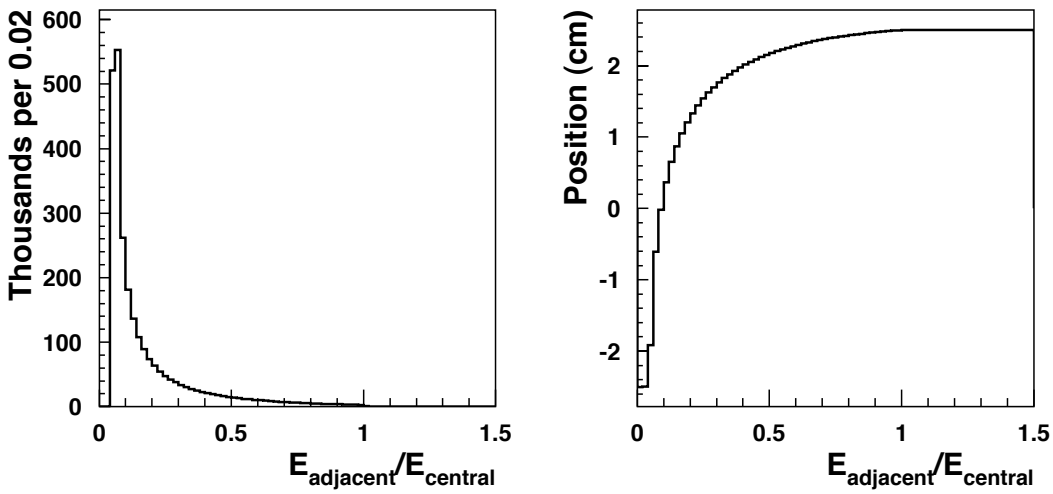

Figure 3.9: Distribution of the ratio of energy in an adjacent row or column to the energy in the central row or column (left) and the corresponding position map (right). These sample plots are for small blocks in the 32 GeV energy bin.

3.2.2 Clustering Corrections

We correct the cluster energies for a number of geometric and detector effects. For clusters that share blocks, we must partition the energy in the overlapping blocks. We correct for extra energy that comes from nearby clusters which do not share blocks and that leak energy across the beam holes. We correct for blocks that are missing from the cluster because their energies are below the readout threshold or because they are located in the beam holes or outside the calorimeter. We correct the energy in each block for the variation in longitudinal response of the CsI crystals. After these "block-level" corrections we re-sum the energies in the cluster and apply multiplicative "cluster-level" corrections to the new cluster energy. First we apply a correction to account for energy from the shower that is outside the 7×7 or 3×3 cluster. Then we correct for a number of detector effects including the transverse non-uniformity of energies across each block, the non-linearity of each channel with energy, and spill-to-spill variations in the CsI response. For 1996 data we also apply

a "phase correction" which accounts for different energy non-linearities in the 3 RF phases. Finally, for the $K \to \pi^0\pi^0$ analysis we apply a photon correction which is designed to correct any residual differences between photons and the electrons that are used to calibrate the calorimeter.

Overlap Correction

The overlap correction separates the energy deposited in two or more clusters that share blocks by using the transverse energy maps to predict how much energy each particle contributed to the shared blocks. The transverse energy maps are generated using photons from $K \to \pi^0\pi^0$ decays and the same selection criteria as the position maps. The maps are based on the position of the cluster within the seed block. There are 55 position bins, each of which contains the block energies for a 9×9 array surrounding the seed block. The 55 bins are distributed evenly in x and y in one octant of the crystal; the octant symmetry is used to find the correct map for positions in the rest of the block. Figure 3.10 shows the distribution of position bins used by the transverse energy maps. The maps are independent of energy; the predicted energy in each block is normalized to the energy of the cluster whose transverse distribution we are trying to predict. Separate maps are generated for data and Monte Carlo. For each shared block, the energy deposit predicted by the transverse energy maps for each cluster is assigned to that cluster and the cluster energy is re-summed. The process is iterated until the cluster energy changes by less than 5 MeV and the x and y positions change by less than 1 mm relative to the previous iteration.

Neighbor Correction

The neighbor correction estimates the amount of underlying energy in each block that comes from nearby clusters which are less than 50 cm away but outside the 3×3 or 7×7 cluster boundary. The correction uses a 13x13 transverse energy map to predict the energy contribution from neighboring clusters. This map is generated by GEANT[64] using electron showers and is the same for data and Monte Carlo. It is

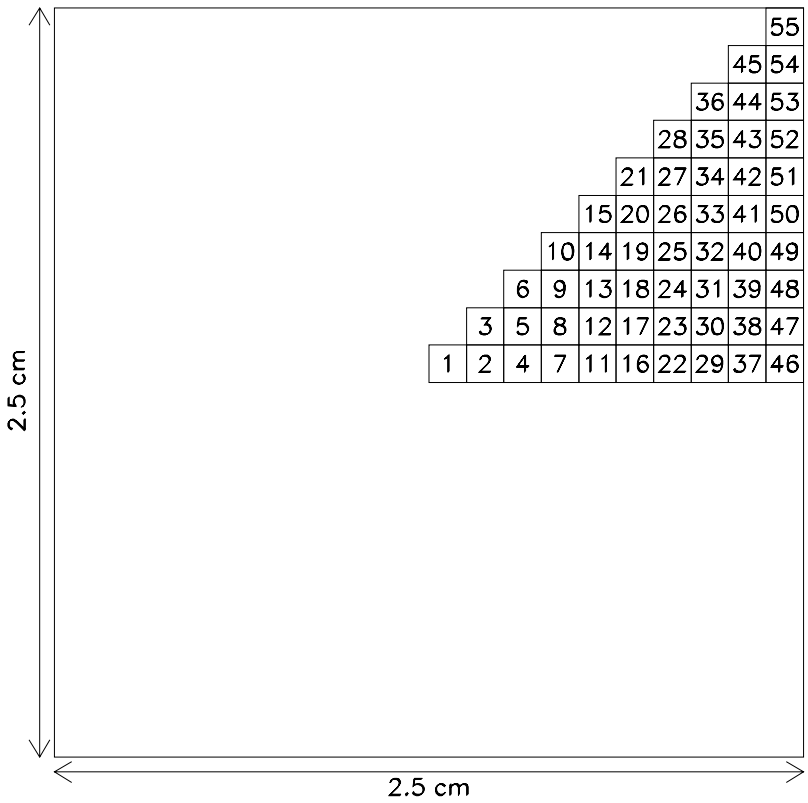

Figure 3.10: 55 position bins for transverse energy maps

not binned in position or energy and the predicted energy in each block is normalized to the measured cluster energy. Energy predicted to have come from neighboring clusters is subtracted from each block and the cluster energy is re-summed. The correction allows for block energies to be negative if the predicted energy from a neighbor is greater than the energy measured in a given block.

Missing Block Correction

The missing block correction estimates the amount of energy that would have been present in blocks which are missing from the cluster because they are inside the beam hole or outside the CsI array. The correction uses the same transverse energy

maps used by the overlap correction to predict the energy in each missing block. The cluster energy is re-summed.

Sneaky Energy Correction

The sneaky energy correction is applied when two or more clusters are near the beam holes. The overlap and neighbor corrections are not sufficient to separate the energies of clusters near beam holes because the maps they use to predict the fraction of energy contributed by each cluster are generated using showers that are away from the beam holes and thus assume that there is no empty space between clusters. When clusters are near the beam holes, more energy will "leak" across the beam holes and be deposited on the opposite side than if CsI crystals were present between the clusters. The sneaky energy correction uses $K_L \rightarrow \pi^{\pm}e^{\mp}\nu$ electron showers to generate a map of this energy leakage across the beam holes. The map is not binned in position or energy and is the same for data and Monte Carlo. The sneaky energy correction is made for clusters that are within four blocks of the beam hole in x and or y. The predicted energy contribution from leakage across the beam holes is subtracted and the cluster energy is re-summed.

Iteration of Overlap, Neighbor, Missing Block, and Sneaky Energy Corrections

The overlap, neighbor, missing block, and sneaky energy corrections all rely on the cluster energy to normalize the amount of energy in each block predicted by the various maps, so we must iterate these corrections. At the same time, care must be taken to avoid double counting corrections in the case where both the overlap or neighbor correction and the sneaky energy correction are applicable. This is accomplished by saving the original block energies before any corrections in a separate array. The overlap, neighbor, and missing block corrections are applied so that the sneaky energy correction will have the correct cluster energy to use for its calculations. The sneaky energy correction is then applied to the original block energies and the overlap, neighbor, and missing block corrections are repeated. It is also

important to note that a simple version of the out-of-cone correction is temporarily applied to the cluster energies used for normalization by these corrections. The full out-of-cone correction is applied at cluster level after all the block level corrections are applied.

Threshold Correction

The threshold correction estimates the amount of energy in blocks that were not read out because the energy deposit was below threshold. The ratio of the energy deposit in a block to the threshold energy is of the form a + bln(E) where the parameters a and b are fit separately for each block position in the cluster. The values of these parameters are such that the predicted fraction of threshold energy decreases with distance from the seed block and increases logarithmically with cluster energy. The readout threshold is known for each CsI channel, so the energy below threshold is calculated and added to the cluster energy sum.

Longitudinal Uniformity Correction

The longitudinal response of the CsI crystals is uniform to within ∼5%. To correct for this residual non-uniformity of response, we apply the longitudinal uniformity correction to each block in a cluster. The longitudinal response of each CsI crystal is measured in ten 5-cm z bins using cosmic ray muons that pass vertically through the CsI calorimeter. Typically the crystal response increases with z as the shower nears the PMT. Figure 3.11 shows the measured response of two sample crystals in 1999. This measured response is convoluted with the GEANT[64] prediction of a shower's longitudinal distribution to correct the energy in each block. The GEANT[64] shower profiles are generated separately for photons and electrons. There are individual profiles for each block position within the cluster and they are binned in local position relative to the center of the seed block and in the 6 logarithmic cluster energy bins that are used throughout the analysis (2 GeV, 4 GeV, 8 GeV, 16 GeV, 32 GeV, and 64 GeV). The mean shower depth for photons and electrons varies logarithmically with energy. Figure 3.12 shows sample photon shower profiles

for three energy bins. We use a logarithmically weighted average of the two energy bins surrounding the cluster energy to better simulate the actual longitudinal profile for a given cluster energy. Each block is corrected individually and the cluster energies are re-summed.

In Monte Carlo, we only simulate the longitudinal uniformity of the central 13 CsI crystals in a cluster. (See Chapter 4 for details on the simulation.) For this reason, when we apply the longitudinal uniformity correction to Monte Carlo events we must be careful to apply it only to those blocks in which the effect is simulated. It is possible that the cluster we reconstruct does not have the same seed block as the cluster we generated, so we store the generated seed block and use that information to decide which blocks in a cluster should receive the correction. We also use the shower's generated energy bin to select the block's shower profile rather than interpolating between energy bins.

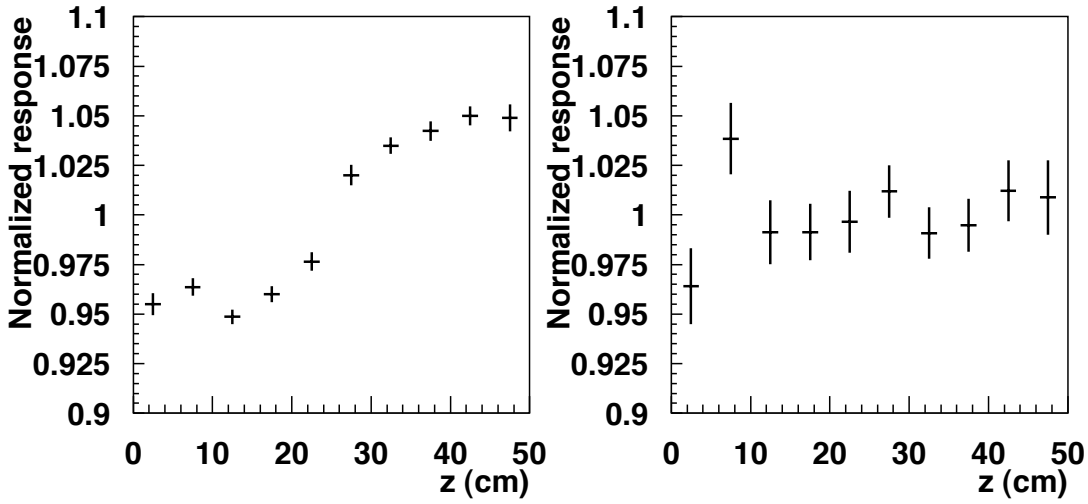

Figure 3.11: Measured longitudinal response for sample CsI crystals in 1999. Channel 1370 (left) is a small block and 435 (right) is a large block. The precision of the measurement varies depending on the position of a block within the calorimeter because the cosmic ray trigger rate is not constant across the calorimeter.

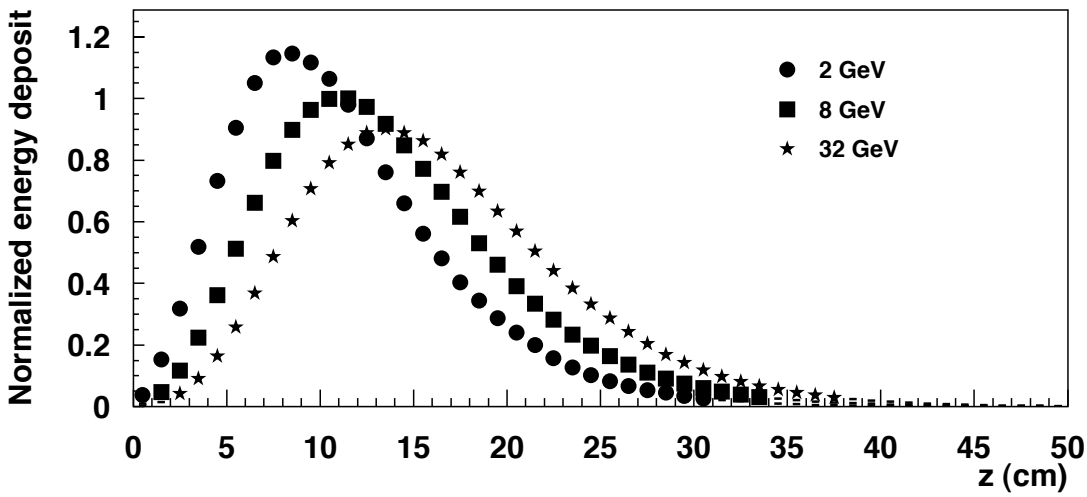

Figure 3.12: Sample longitudinal energy profiles from GEANT[64] for 2, 8, and 32 GeV photon showers. These profiles are for the central block in the cluster.

Out-of-cone Correction

The out-of-cone correction is applied because an EM shower is not fully contained by the 7×7 small block or 3×3 large block clusters we define in the calorimeter. Out-of-cone refers to the fraction of energy not included in the clusters. We measure the out-of-cone correction using the same GEANT[64] simulation used to generate the Monte Carlo shower library (see Chapter 4). The correction is parameterized by a quadratic function of the reconstructed distance from the cluster center and a linear function of the reconstructed energy. The correction is generated separately for photons and electrons and for small and large blocks; clusters containing both small and large blocks are treated as 3x3 clusters of large blocks. This means that for clusters containing both small and large blocks the correction does not include energy lost in the wrapping of the small blocks. We correct for this effect using a parametrization that is a function of position. The effect of incident angle on the out-of-cone correction was studied at length. We conclude that the method used for the position reconstruction is affected by incident angle in such a way that the angle

effect is included in our parameterization as a function of reconstructed position. The out-of-cone correction function is given by Equation 3.5 where x and y are the reconstructed distances from the center of the seed block in cm, E is the uncorrected cluster energy, and w is the wrapping correction.

$$\frac{1}{out-of-cone} = [p_1 + p_2(x^2 + y^2)][q_1 + q_2 E] - \frac{w}{E} \tag{3.5}$$

The values of the correction parameters are given in Table 3.4. The magnitude of the correction is roughly 5%.

	Small Blocks Photons	Large Blocks Photons	Small Blocks Electrons	Large Blocks Electrons
p_1	0.95830	0.94628	0.95865	0.94653
p_2	-0.00145	-0.00131	-0.00153	-0.001
q_1	1.00022	1.00033	1.00022	1.00019
q_2	-2.7E-5	-4.1E-5	-2.7E-5	-2.3E-5

Table 3.4: Parameters for out-of-cone correction

Intrablock Correction

The intrablock correction accounts for variations in the energy response across the face of the blocks. The source of this variation is not well understood. Differences due to the reconstruction are addressed by the out-of-cone correction, so there are either some residual shortcomings to the out-of-cone correction or the effect is physical. The variation in response is measured using K_{e3} electrons from the calibration sample. The correction is made by dividing each cluster seed block into a 5×5 grid and measuring the energy deposit of electrons in each of these position bins. A multiplicative correction is applied to the total cluster energy based on the cluster's reconstructed position within the seed block. The correction is normalized such that the average correction over each block (25 bins) is 1.0. Figure 3.13 shows the intrablock correction for the central region of the calorimeter. Figure 3.14 shows the variation across the faces of three sample blocks in x and y. Variations in transverse

response are not simulated by the Monte Carlo, so this correction is applied to data only.

Phase Correction

In 1996, the DPMTs were operated at RF/3 which meant that in-time events could be present in three separate "RF phases" within the DPMT integration slice. The phase correction is applicable only to 1996 data and corrects for differences in energy linearity between the three RF phases. The correction is measured using E/p of K_{e3} electrons from the calibration sample and is applied multiplicatively to the cluster energy.

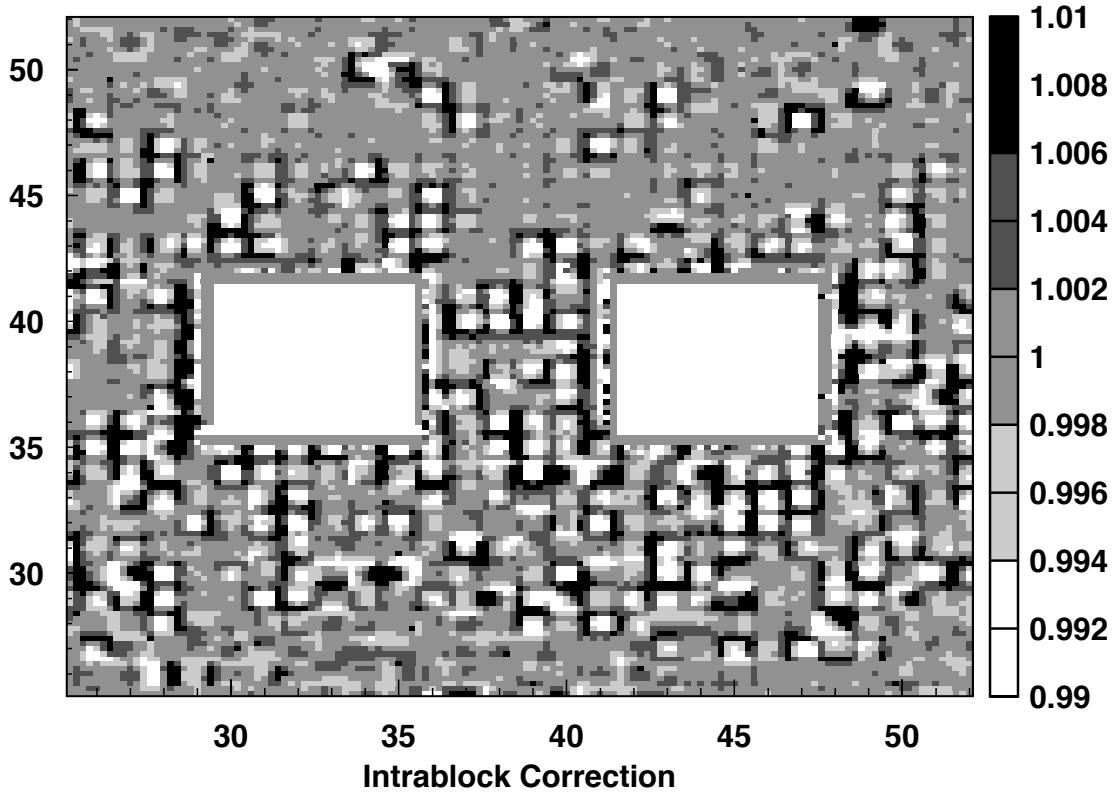

Figure 3.13: Intrablock correction for the central region of the CsI.

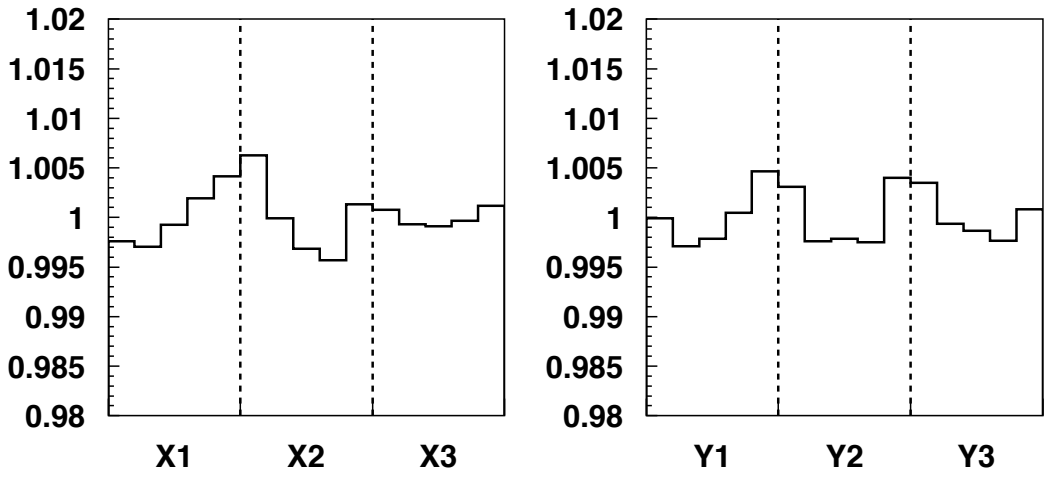

Figure 3.14: Transverse variation across three sample CsI blocks in x (left) and y (right). The dashed lines indicate the boundaries between blocks.

Channel-by-Channel Linearity Correction

The channel-by-channel linearity correction removes the residual energy non-linearity. It is measured separately for each CsI channel in data and Monte Carlo using E/p of K_{e3} electrons from the calibration sample. Figure 3.15 shows the global linearity for all channels before the correction and the linearities for four sample channels. The non-linearity is generally less than 1%. The channel-to-channel variation of the linearity is not great for most channels; this is because earlier corrections have accounted for many of the sources of variation of response among the channels. The correction is applied multiplicatively to the cluster energy based on the cluster energy and the seed block index.

Spill-by-Spill Correction

The spill-by-spill correction is applied to correct for time variations in the response of the calorimeter as a whole. These fluctuations could be due to small temperature

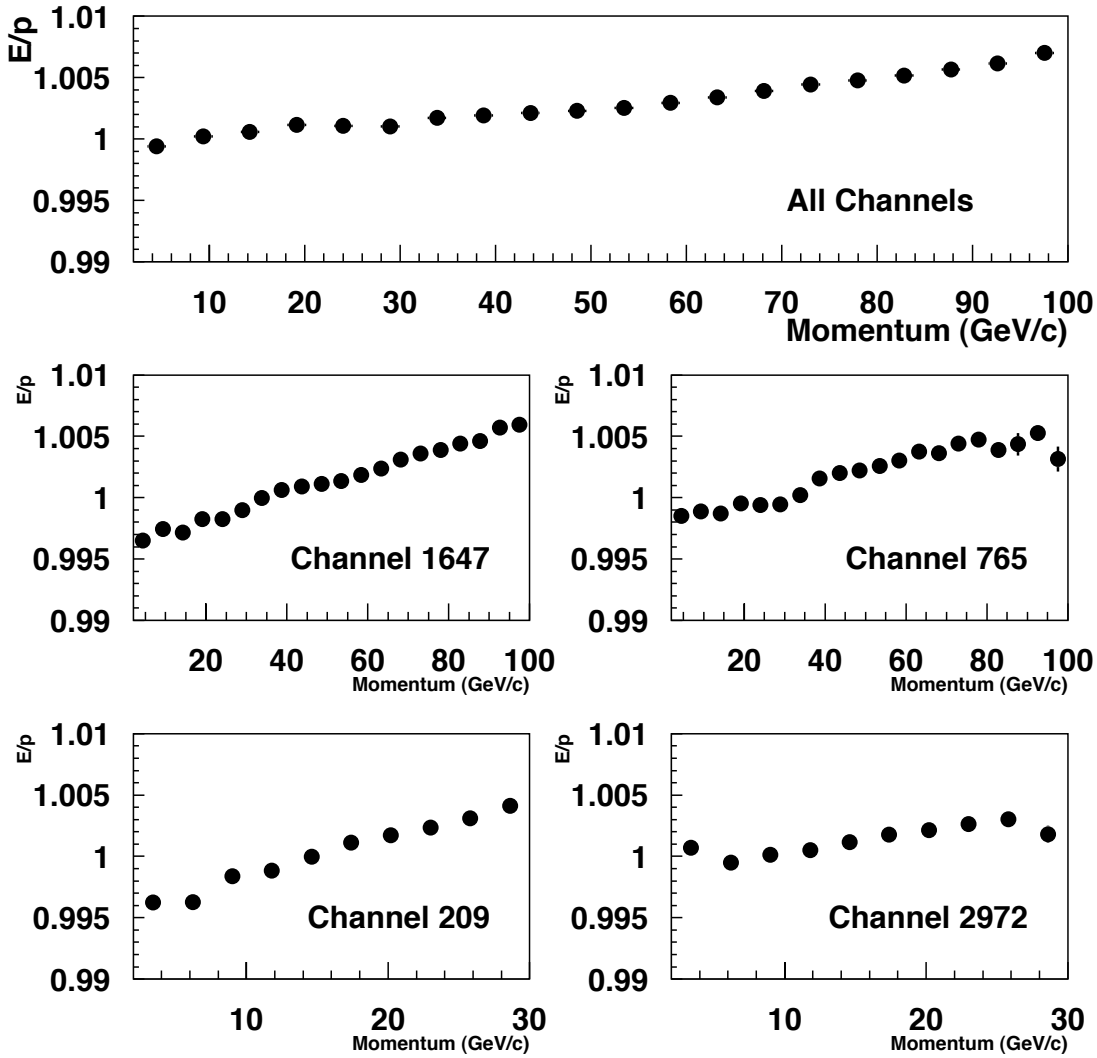

Figure 3.15: E/P linearity for K_{e3} electrons before channel-by-channel correction in 1999. The top panel shows the global linearity while the four bottom panels show linearities for four sample channels. Channels 1647 and 765 are small blocks and channels 209 and 2972 are large blocks.

changes in the blockhouse which cause changes in the scintillation response of the CsI crystals or other global effects. The correction is measured using E/p of K_{e3} electrons from the calibration sample as a function of spill. Figure 3.16 shows the spill by spill correction for the 1999 run. The spill-by-spill correction is applied to data only.

Final CsI Performance

The quality of the calibration and the CsI performance is evaluated by analzying K_{e3} electrons from the calibration sample with all corrections applied. The electron calibration for 1996, 1996, and 1999 is based on 1.5 billion total electrons. Figure 3.17 shows the E/p distribution and the energy resolution as a function of momentum after all corrections. The final energy resolution of the calorimeter is $\sigma_E/E \simeq 2\%/\sqrt{E} \oplus 0.3\%$, where E is in GeV.

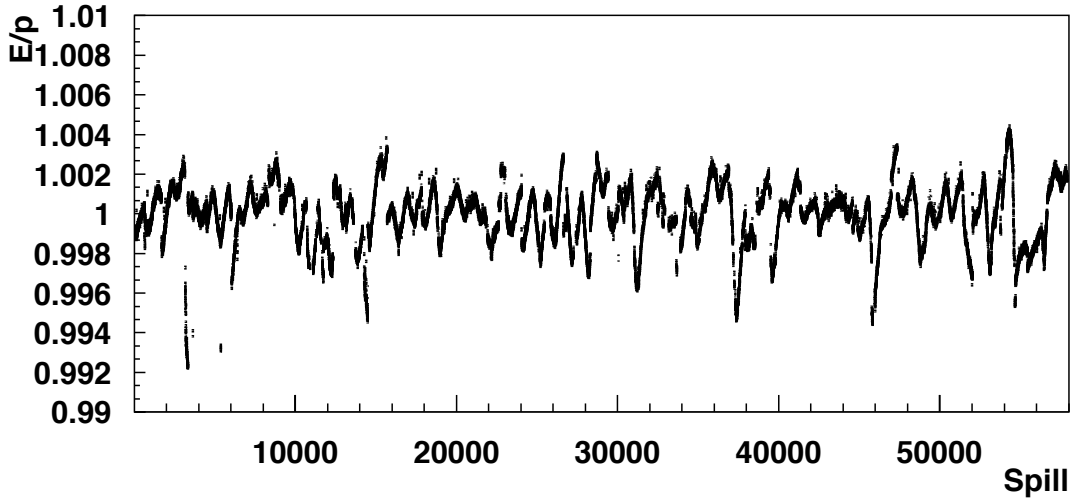

Figure 3.16: E/P vs spill for K_{e3} electrons in 1999.

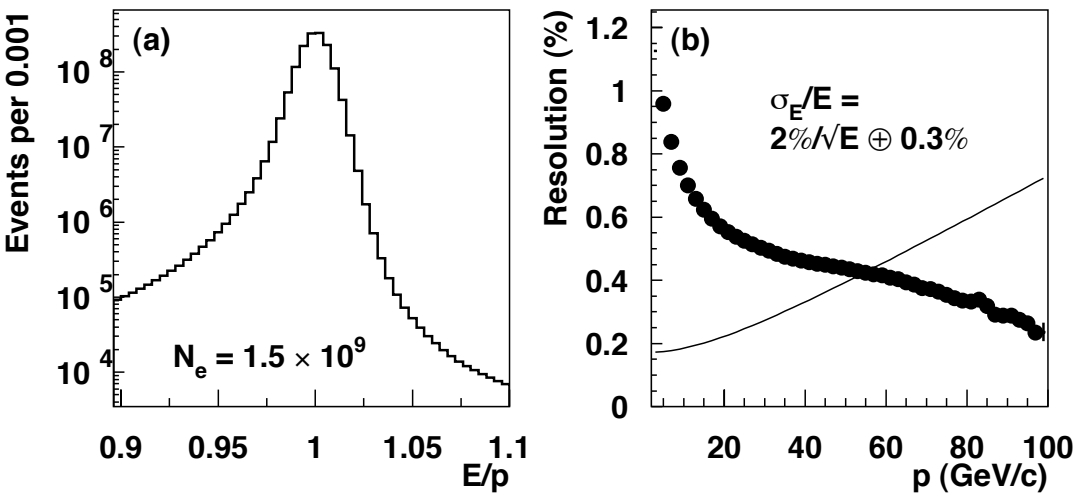

Figure 3.17: K_{e3} electrons after all corrections. (a) E/p for 1.5×10^9 electrons. (b) Energy resolution. The fine curve shows the momentum resolution function that has been subtracted from the E/p resolution to find the energy resolution.

Photon Correction

The photon correction is generated using $K \to \pi^0\pi^0$ and $K_L \to \pi^0\pi^0\pi^0$ events and is applied to neutral clusters to correct any difference between photons and electrons that are not included in the electron calibration and the preceding corrections. This correction is designed to match data to Monte Carlo and is therefore applied to data only.We fit each event for the photon energies applying 6 (4) kinematic constraints for $\pi^0\pi^0\pi^0$ ($\pi^0\pi^0$). The correction is generated in 9 separate regions of the calorimeter. We apply a correction which is a weighted average of corrections from $K \to \pi^0\pi^0$ and $K_L \to \pi^0\pi^0\pi^0$ events. We iterate three times[2] and add the corrections from each iteration to find the final correction. Figure 3.18 shows the correction as a function of photon energy for each of the nine calibration regions. The correction is less than 0.2% except in the region nearest the beam holes; we remove events in this region for the analysis. The correction becomes flat with

[2]Only one iteration is performed for 1996.

energy for energies above which we have too few events to measure the correction well.

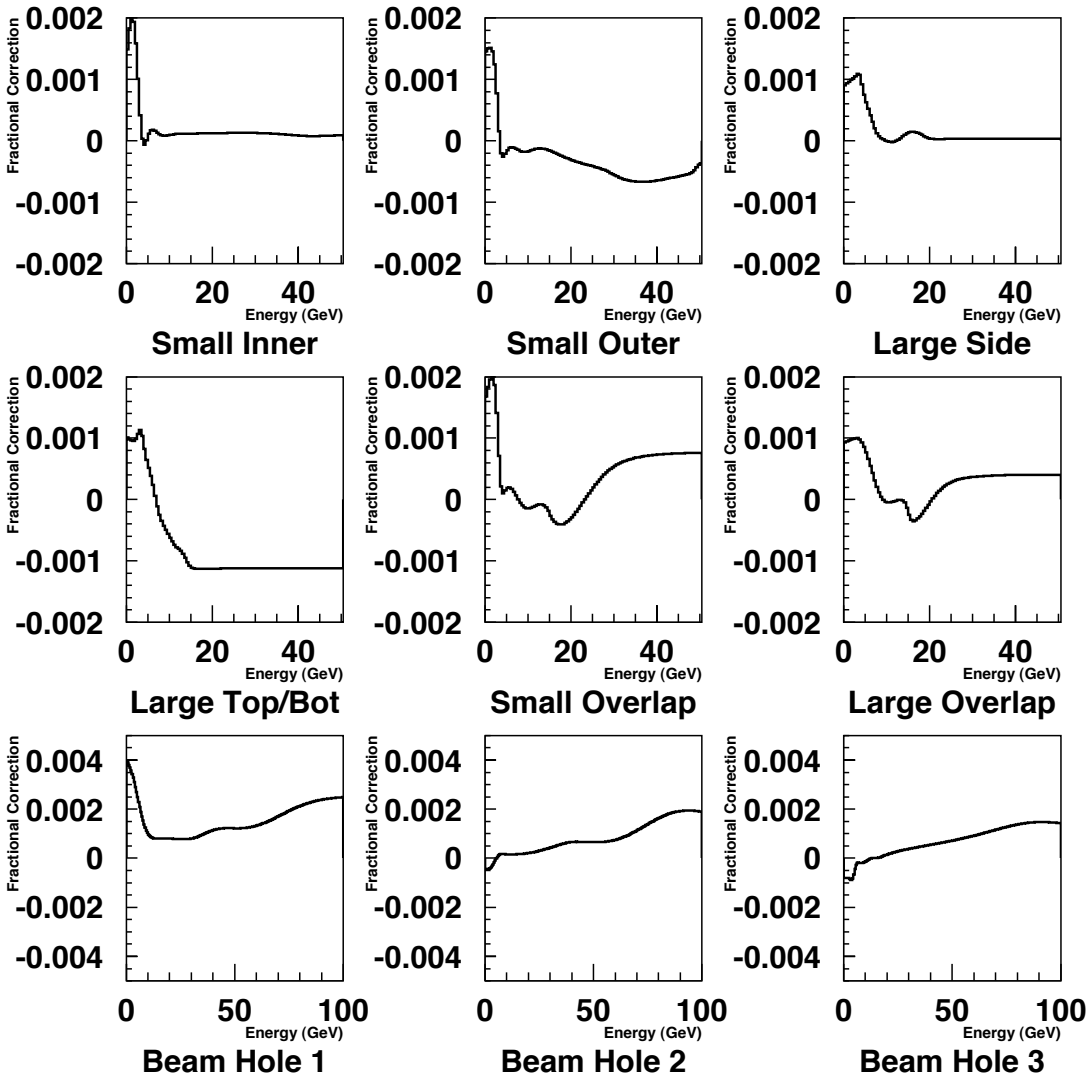

Figure 3.18: Photon correction in nine regions for 1999. The three beam hole regions correspond to rings of crystals around the beam holes, where "Beam Hole 1" is the first ring, "Beam Hole 2" is the second ring, and "Beam Hole 3" is the third ring. Note the different vertical scale for the beam hole regions.

3.2.3 Event Reconstruction

$K \to \pi^0\pi^0$ and $K_L \to \pi^0\pi^0\pi^0$ events are fully reconstructed using the positions and energies of the four or six photon clusters in the CsI calorimeter. The $K_L \to \pi^0\pi^0\pi^0$ reconstruction is almost identical to the $K \to \pi^0\pi^0$ reconstruction, but for simplicity this discussion will be in terms of the $\pi^0\pi^0$ reconstruction. We are able to reconstruct the z vertex of the kaon decay, the (x,y) components of the center-of-energy of the kaon, the kaon energy, and the $\pi^0\pi^0$ invariant mass, .

We must first determine which pair of photons is associated with which pion in the $K \to \pi^0\pi^0$ decay. For four photons, there are three possible pairings. For each pairing we calculate the distance in z between the π^0 decay vertex and the mean shower depth in the CsI for both pions. We calculate the $\gamma\gamma$ invariant mass and use the pion mass as a constraint:

$$\begin{aligned} m_{\gamma\gamma}^2 \equiv m_{\pi^0}^2 &= (E_1^2 + E_2^2) - |\vec{p_1} + \vec{p_2}|^2 \\ &= 2(E_1E_2 - \vec{p_1} \cdot \vec{p_2}) \\ &= 2E_1E_2(1 - cos\theta_{12}) \end{aligned} \tag{3.6}$$

Since the opening angle between the photons is small, we make the approximations $(1 - cos\theta_{12}) \approx \theta_{12}^2$ and $\theta_{12} \approx r_{12}/z_{12}$ where r_{12} is the transverse distance between the two photons at the CsI and z_{12} is the distance from the π^0 decay vertex to the mean shower depth in the CsI. Substituting these approximations into Equation 3.7 we find the distance, z_{12}, in terms of known quantities:

$$z_{12} \approx \frac{\sqrt{E_1E_2}}{m_{\pi^0}} r_{12}. \tag{3.7}$$

For each pairing, we compare the calculated z for each pion. In general, only the correct pairing will give a consistent z for both pions while the incorrect pairings will have mismatches between the two calculated distances. This is illustrated in Figure 3.19. The consistency of the measured z is quantified using the pairing chi-squared

variable, $\chi^2_{\pi^0}$.

$$\chi^2_{\pi^0} \equiv \sum_{i=1}^{N_{\pi^0}=2} \left(\frac{z_i - z_{avg}}{\sigma_i} \right)^2 \tag{3.8}$$

In Equation 3.8, z_i is the calculated z distance for each pion, z_{avg} is the weighted average of the distance z_i for both pions, and σ_i is the energy dependent vertex resolution for each pion. The resolution is based on a parameterization of the position resolution which is a function of energy and local position relative to the center of the seed block. The pairing which gives the minimum value of $\chi^2_{\pi^0}$ is chosen as the correct pairing. We measure the fraction of events in which we select the wrong pairing using Monte Carlo events; we choose the incorrect pairing for 0.007% of $K \to \pi^0\pi^0$ events. The z vertex of the kaon decay is taken to be Z_{CsI} - z_{avg} for the best pairing, where Z_{CsI} is the z position of the mean shower depth in the CsI.

We find the center-of-energy of the kaon decay by weighting the position of each photon by its energy. The x and y components of the center-of-energy are

$$\begin{aligned} x_{coe} &\equiv \frac{\sum x_i E_i}{\sum E_i} \\ y_{coe} &\equiv \frac{\sum y_i E_i}{\sum E_i} \end{aligned} \tag{3.9}$$

where the sums are over all the photons. The center-of-energy is the point at which the kaon would have intercepted the plane of the CsI if it had not decayed, so we can calculate the (x,y) position of the decay vertex by assuming it lies on the line between the target and the center-of-energy. The x coordinate of the kaon decay vertex is used to determine whether the kaon came from the regenerator or the vacuum beam.

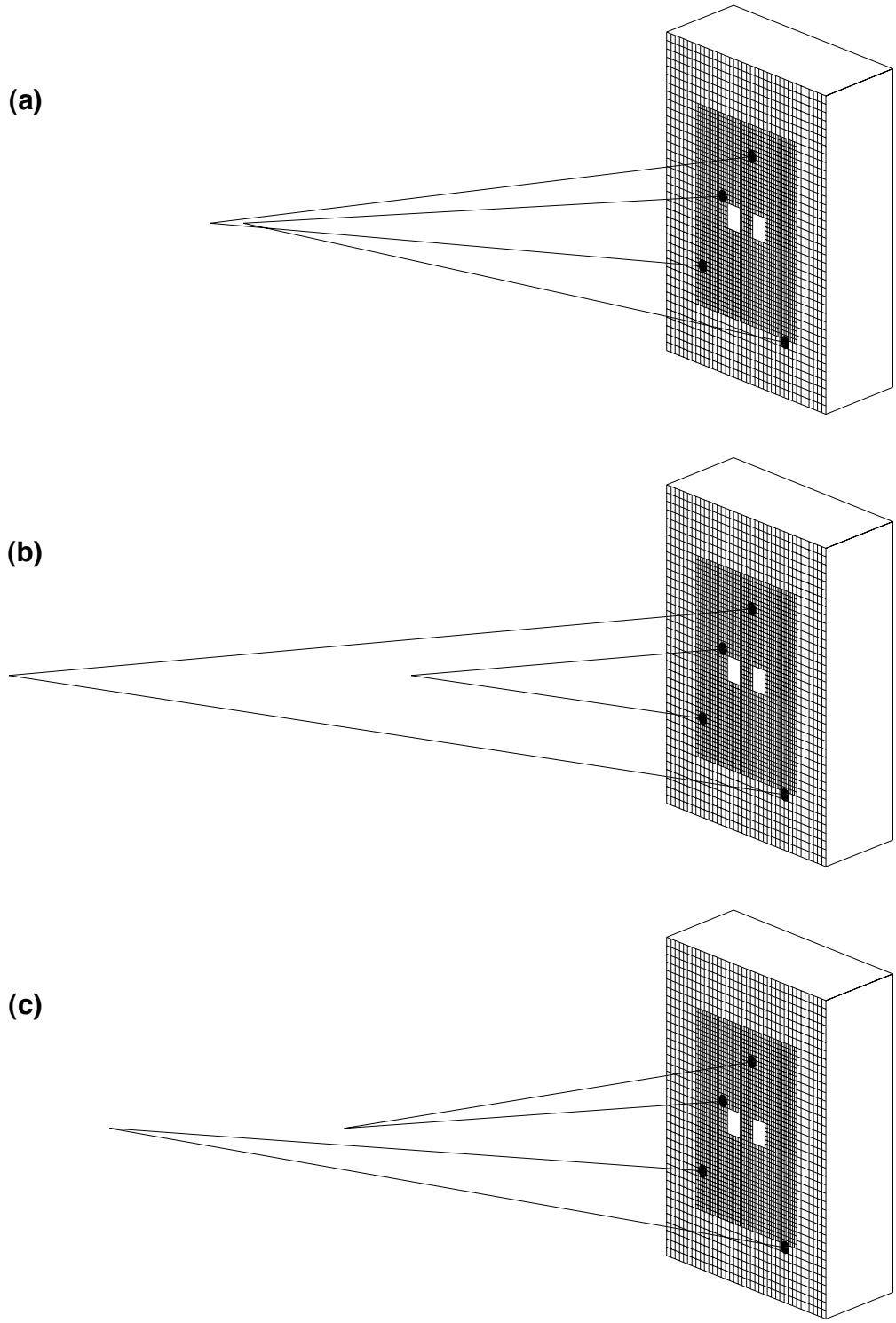

Figure 3.19: Three ways to pair four photons to make 2 π^0s. Pairing (a) gives a consistent vertex for the 2 π^0s and is therefore most consistent with a $K \to \pi^0\pi^0$ decay.

The kaon energy, E_K is simply the sum of the four photon energies. The $\pi^0\pi^0$ invariant mass is now calculated from the energy and momentum of the kaon:

$$m^2_{\pi^0\pi^0} = \left(\sum E_i\right)^2 - \left(\sum \frac{E_i(x_i - x_K)}{\sqrt{z^2_{avg} + (x_i - x_K)^2 + (y_i - y_K)^2}}\right)^2 - \left(\sum \frac{E_i(y_i - y_K)}{\sqrt{z^2_{avg} + (x_i - x_K)^2 + (y_i - y_K)^2}}\right)^2 - \left(\sum \frac{E_i z_{avg}}{\sqrt{z^2_{avg} + (x_i - x_K)^2 + (y_i - y_K)^2}}\right)^2 . \tag{3.10}$$

An event display for a sample $K \to \pi^0\pi^0$ decay is shown in Figure 3.20.

3.2.4 Final Energy Scale

The energy scale is set by the electron calibration and the photon correction. A small residual energy scale mismatch between data and Monte Carlo is removed by adjusting the energy scale in data such that the sharp edge in the z vertex distribution at the regenerator matches between data and Monte Carlo. The correction is measured by sliding finely binned $K \to \pi^0\pi^0$ data and Monte Carlo z vertex distributions in the regenerator beam past each other and using the KS test. The correction is applied to each cluster as a function of kaon energy in the same 10 GeV energy bins that are used by fitter. Figure 3.21 shows the data and Monte Carlo z distributions before and after the correction and the MC-data shift as a function of energy. The shift in vertex z position is converted to an energy scale using the distance from the regenerator edge to the z position of the CsI: f_{scale} = 1 - Δz/61.0. The average mismatch in z vertex between data and Monte Carlo in 1997 and 1999 is about 2.5 cm which corresponds to an energy scale adjustment of 0.04%. There is a larger adjustment of ~0.1% required for 1996. The final energy scales applied to data in each year are shown in Figure 3.22. After we apply the final energy scale, all kinematic quantities are recalculated prior to event selection.

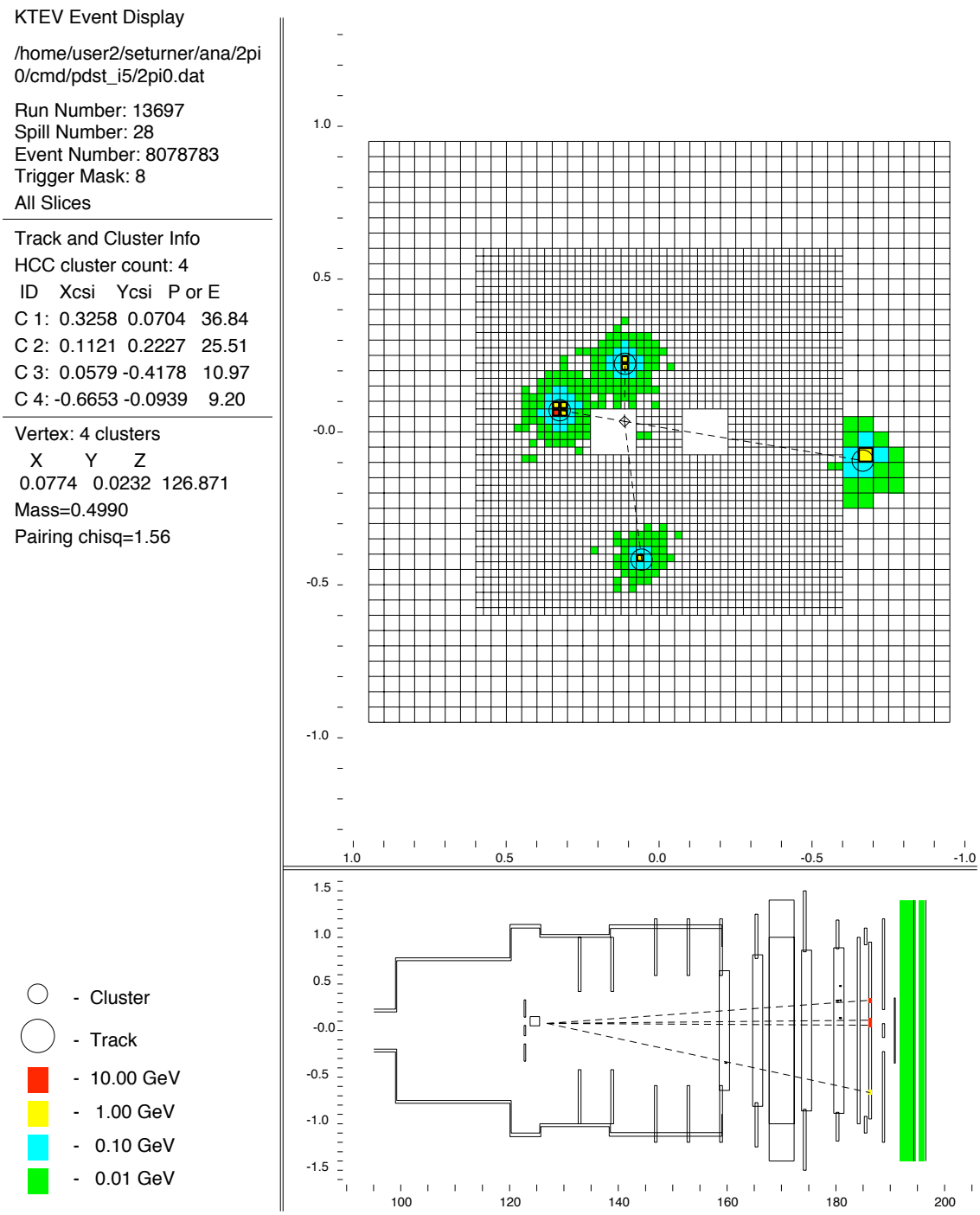

Figure 3.20: Event display for a sample $K \to \pi^0\pi^0$ decay. The four clusters of energy in the CsI are shown. The cluster energies, reconstructed decay vertex, reconstructed $m_{\pi^0\pi^0}$ invariant mass, and $\chi^2_{\pi^0}$ are shown on the left. The bottom panel shows the photon trajectories from the decay vertex to the CsI. The x-position of the vertex is in the same beam as the regenerator, so this event is consistent with a K_S decay.

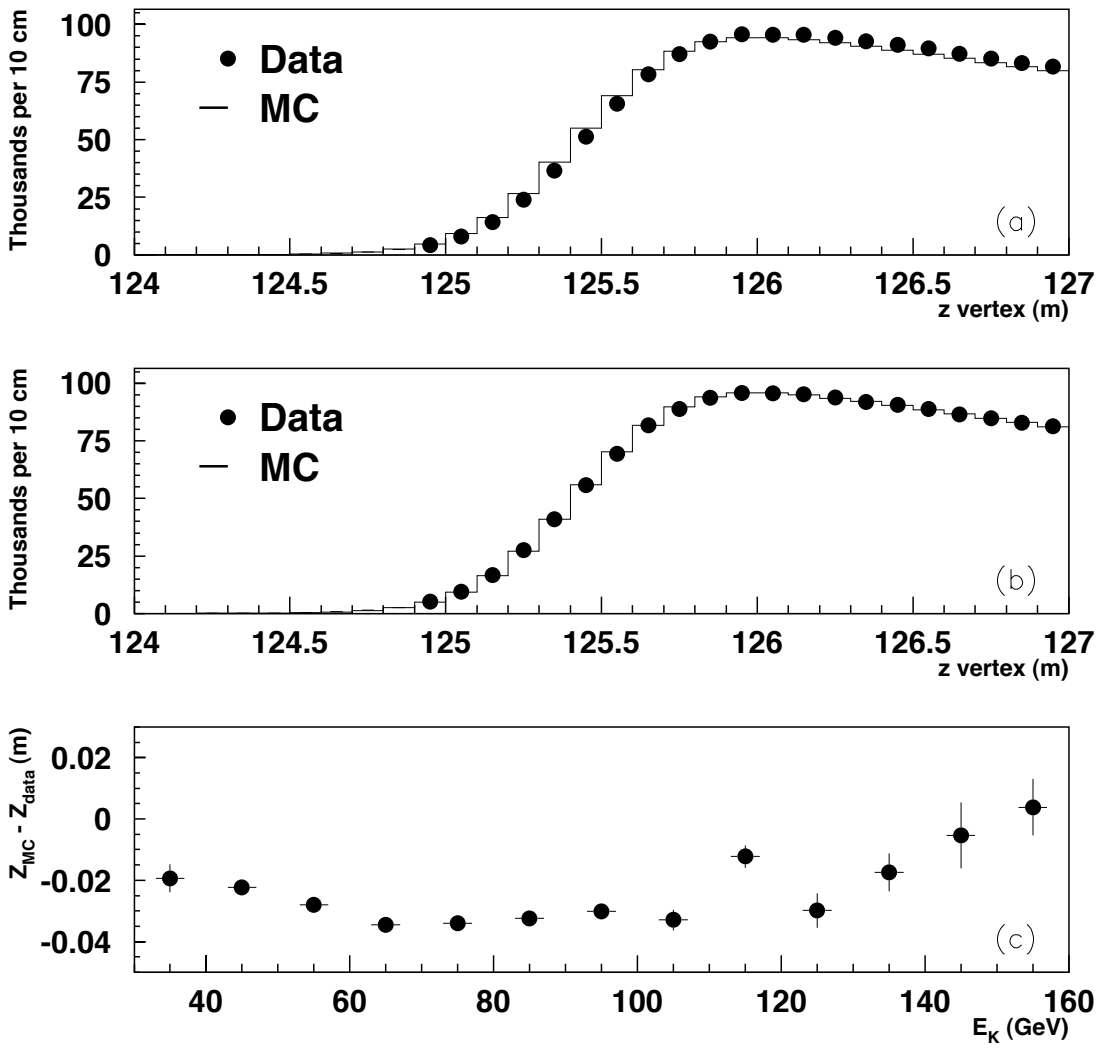

Figure 3.21: $K_S \to \pi^0\pi^0$ z vertex distributions used for regenerator edge matching in 1999. (a) Data and Monte Carlo before scale adjustment. (b) Data and Monte Carlo after scale adjustment. (c) Shift required to match data to Monte Carlo.

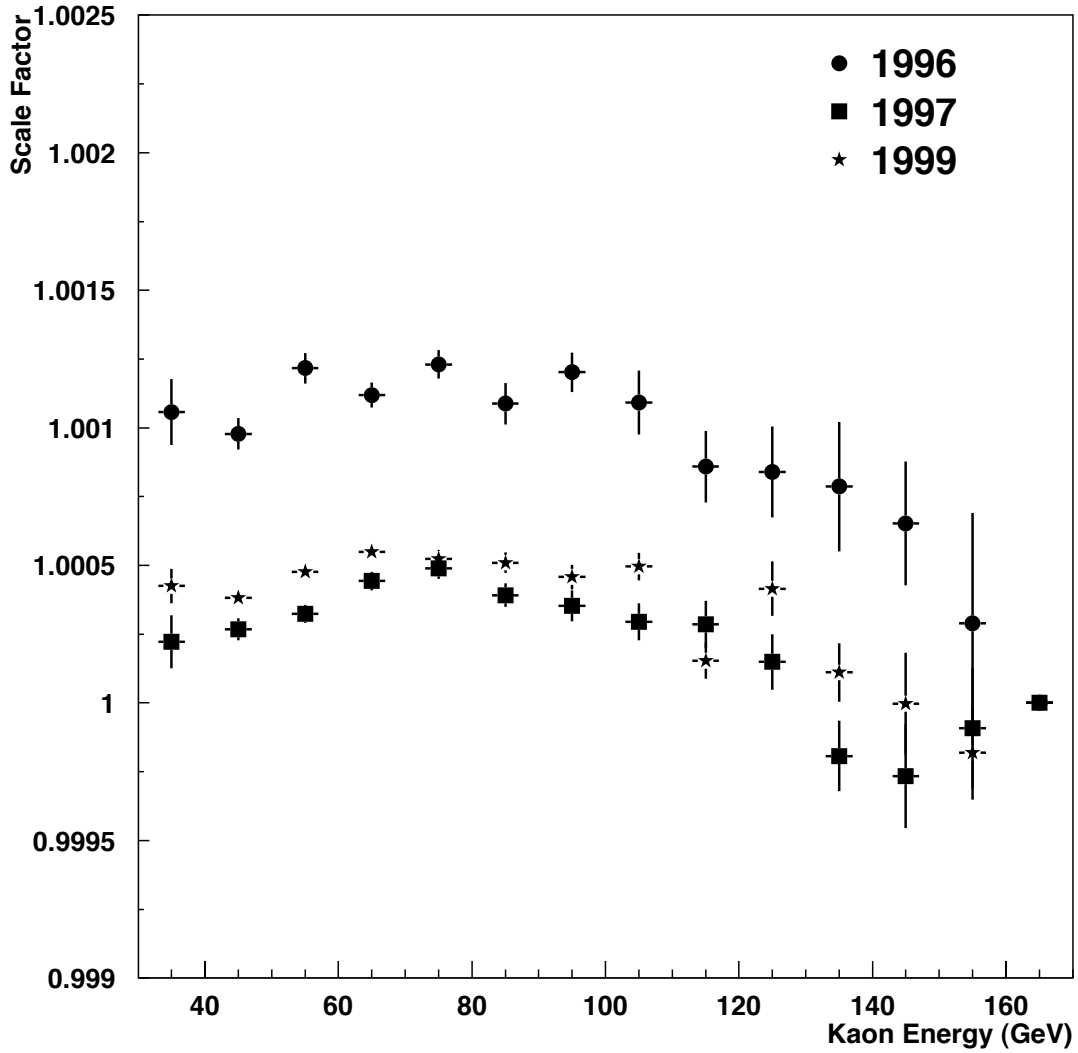

Figure 3.22: Final energy scales applied to data in 1996, 1997, and 1999.

3.2.5 Event Selection

The selection criteria for the $K \to \pi^0\pi^0$ sample are designed to ensure that the events are well reconstructed, to suppress backgrounds, and to select kinematic and fiducial regions appropriate for the KTeV detector.

We reject some runs or portions of runs because of hardware malfunctions during data-taking. We select events which are well reconstructed by removing events in which cluster energies are likely to be poorly reconstructed and by making cuts on the quality of the photon pairing and the transverse shape of the clusters.

The energy of each CsI cluster is required to be greater than 3 GeV. Figure 3.23 shows the minimum cluster energy distribution for both beams. Below 3 GeV, imperfect simulation of the HCC thresholds leads to disagreement between data and Monte Carlo. Also, there are not enough low energy electrons from $K_L \to \pi^\pm e^\mp \nu$ decays to measure the channel-by-channel linearity correction below about 4 GeV, so the correction is not reliable at very low energies. It is difficult to separate the energy deposit in two very close clusters so the minimum distance between the reconstructed positions of the CsI clusters is required to be greater than 7.5 cm. Figure 3.24 shows the minimum cluster separation distribution for both beams.

We remove events with clusters whose seed is in the first ring of blocks around the beam holes. Clusters in this region are not very well reconstructed because of energy leakage across the beam holes and multiple overlapping or nearby clusters. The "pipefrac" variable is a measure of the energy distribution of showers in which the seed block is adjacent to the beam hole. Pipefrac is the ratio of energy in the nearest neighbor which is not adjacent to a beam hole to the energy in the seed block and is required to be less than 4%. This cut is irrelevant in light of the pipe block cut which removes events with seed blocks which are adjacent to the beam holes.

$\chi^2_{\pi^0}$ is required to be less than 50. This is a rather loose cut; more than 99% of $K \to \pi^0\pi^0$ events passing all other cuts have $\chi^2_{\pi^0}$ values below 10. However there is a significant tail that extends well beyond the cut at 50. The primary purpose of this cut is to reduce background from $K_L \to \pi^0\pi^0\pi^0$ events in which two of the

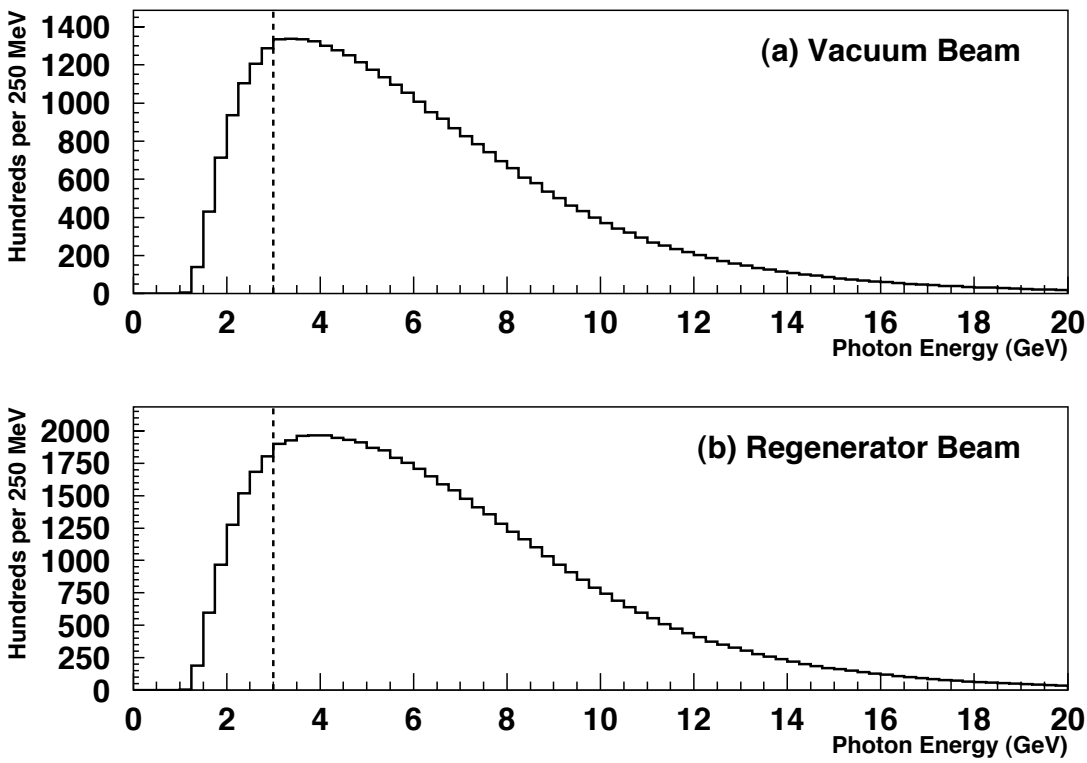

Figure 3.23: $K \to \pi^0\pi^0$ minimum cluster energy distributions for 1999. The dashed line indicates our cut.

photons escape the detector; in this case it is likely that the missing photons come from different pions so the remaining photons must be paired incorrectly. In 1997, the $K_L \to \pi^0\pi^0\pi^0$ background level is .22% in the vacuum beam. For comparison, cutting at $\chi^2_{\pi^0} < 12$ reduces the $K_L \to \pi^0\pi^0\pi^0$ background level for 1997 to .12%. Figure 3.25 shows the $\chi^2_{\pi^0}$ distribution for both beams.

χ^2_γ is a measure of how well the transverse energy distribution of each CsI cluster matches the expected distribution for a photon. This variable is calculated by comparing the transverse energy distribution of each cluster to the transverse energy map. Figure 3.26 shows the χ^2_γ distributions for both beams. The maximum value of χ^2_γ for each event is required to be less than 48.

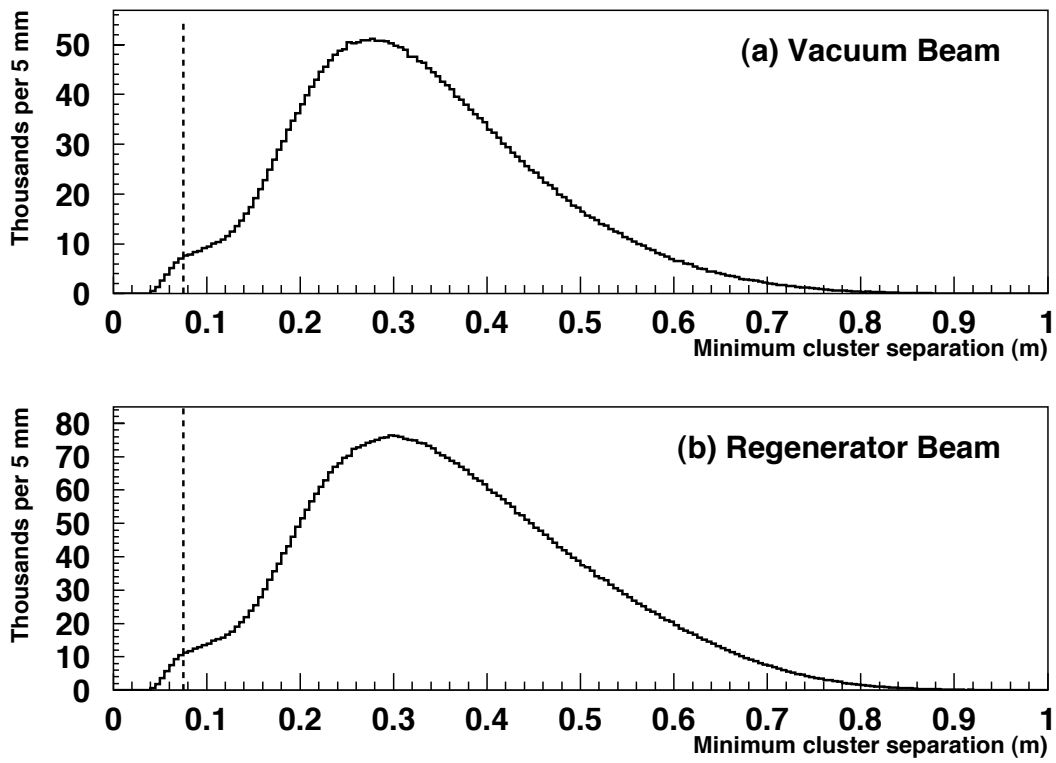

Figure 3.24: $K \rightarrow \pi^0\pi^0$ minimum cluster separation distributions for 1999. The dashed line indicates our cut.

The reconstructed kaon mass is required to be 490 MeV/c^2 $< \mathrm{m}_{\pi^0\pi^0} <$ 505 MeV/c^2. The sidebands of the $\mathrm{m}_{\pi^0\pi^0}$ distribution are almost exclusively $K_L \rightarrow \pi^0\pi^0\pi^0$ background with a small contribution from events in which the photons have been mispaired. Figure 3.27 shows the $\mathrm{m}_{\pi^0\pi^0}$ distributions for both beams.

We make a number of cuts on the veto detectors which are designed to reduce backgrounds. These cuts vary among the three years. For 1997 and 1999 data we cut events in which the RC, SA/CIA, MA, or BA1 L1 trigger sources fire; we do not use the trigger sources for 1996 data. For 1996 and 1997 data, the energy deposit in the SAs and CIA is required to be less than 300 MeV and the energy deposit in BA1 must be less than 500 MeV. The energy deposit in the CA must be less than 1 GeV

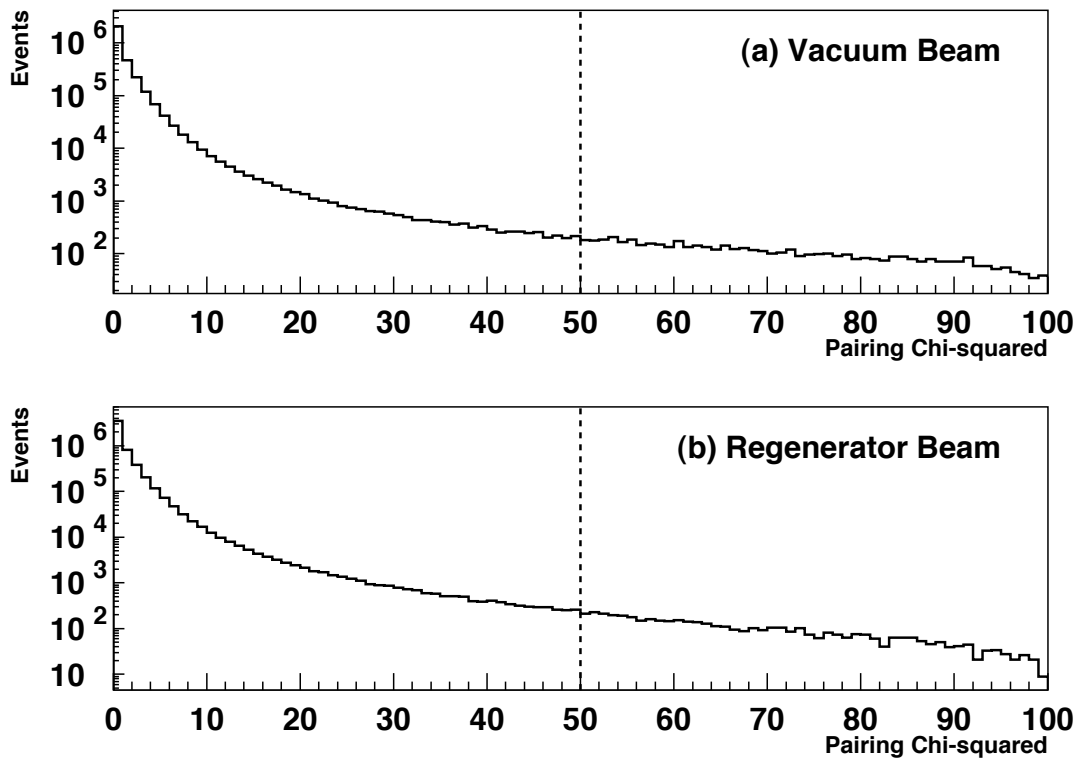

Figure 3.25: $K \to \pi^0\pi^0$ $\chi^2_{\pi^0}$ distributions for 1999. The dashed line indicates our cut.

and the energy in the MA must be less than 300 MeV for all years. In 1997 data we cut events in which the HA L1 trigger source fires. The maximum energy deposit in the regenerator must be less than 2 MIPs for 1996/1997 and less than 1.75 MIPs for 1999. The energy deposit in the lead modules at the end of the regenerator must be less than 0.7 MIPs for all years. These cuts are all summarized in Table 3.5. The variation among the years is due to differences in hardware; different trigger sources are available, the trigger source thresholds are different, or the detector efficiencies are different. The only exception is the MA energy cut in 1999; there is a problem with the simulation of the 1999 MA trigger source in the Monte Carlo so applying a cut on MA energy improves data-MC agreement.

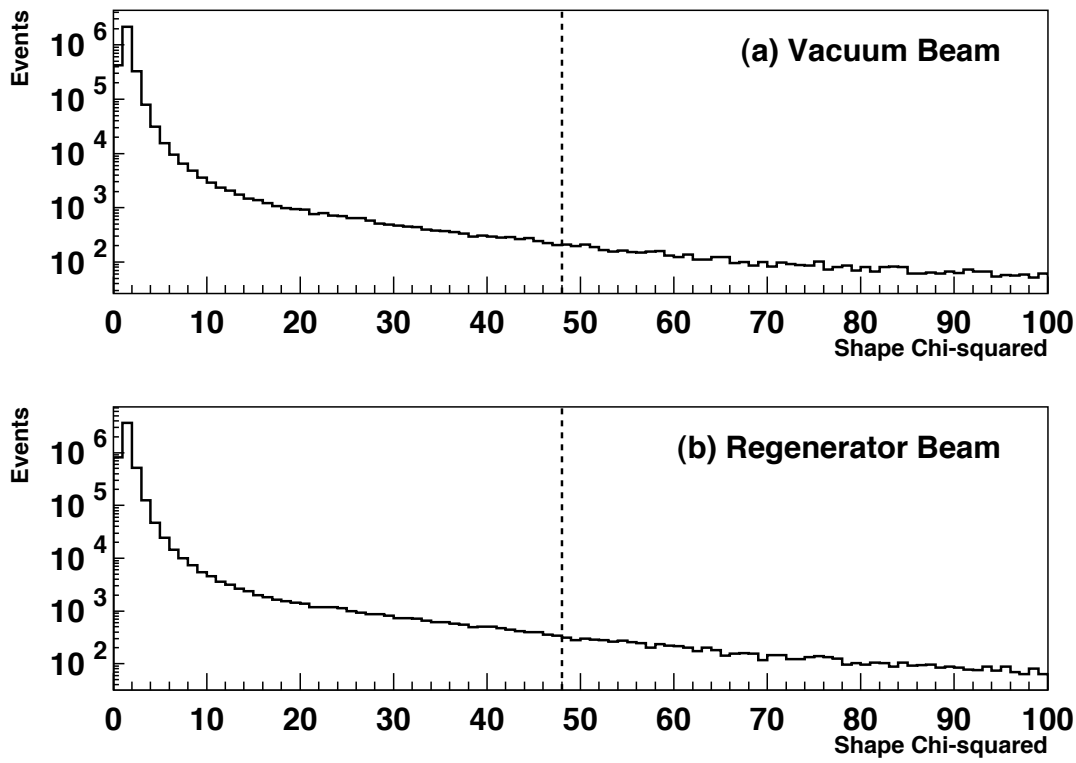

Figure 3.26: $K \to \pi^0\pi^0$ χ^2_γ distributions for 1999. The dashed line indicates our cut.

We use the calorimeter, spectrometer, and trigger hodoscope as "veto detectors" by cutting on extra clusters, tracks, and hits. The sum of energy in any extra clusters must be less than 600 MeV. The number of extra intime clusters must be less than 2. We require that the number of reconstructed tracks be exactly zero, the number of intime pairs in drift chambers 2, 3 and 4 be less than 6, and the number of TDC hits in VV′ be less than 4.

In the $K \to \pi^+\pi^-$ analysis we are able to use p_T^2 to remove events in which the kaon scatters in the collimator or the regenerator. This variable is not available for $K \to \pi^0\pi^0$ decays since we do not measure the photon angles, so we use the "ring number" variable to reject scattered kaon decays. Ring number is calculated using

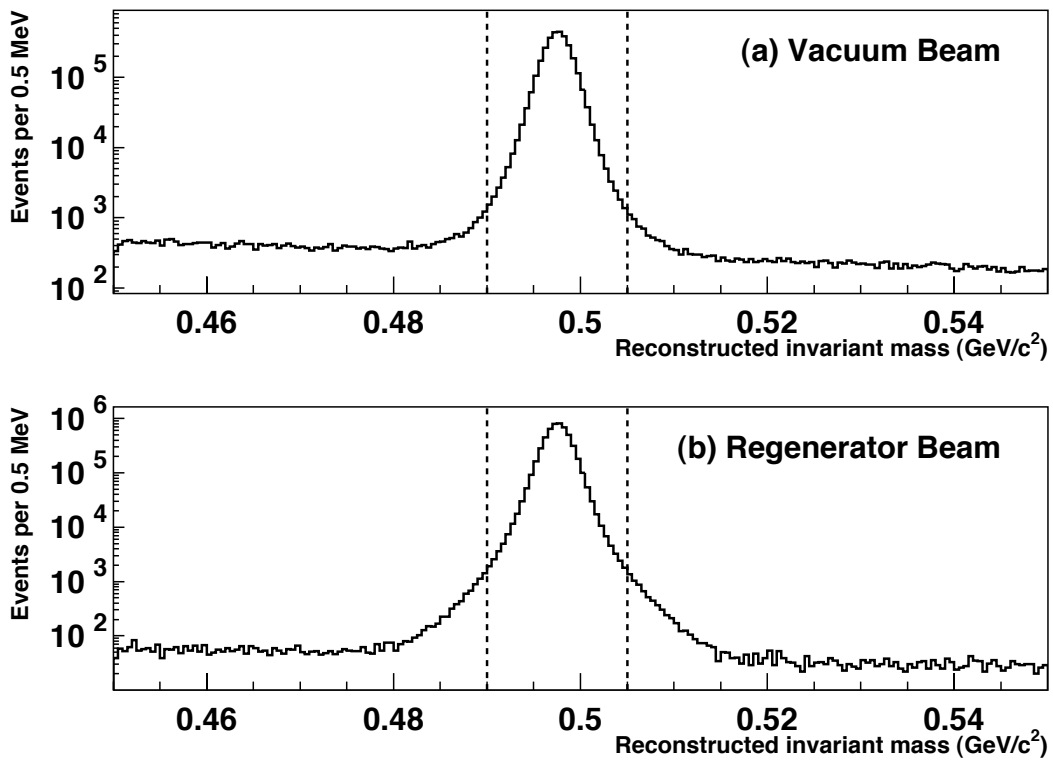

Figure 3.27: $K \to \pi^0\pi^0$ $\mathrm{m}_{\pi^0\pi^0}$ distributions for 1999. The dashed lines indicate our cuts.

the center-of-energy of the reconstructed clusters and is defined as

$$RING = 40000 \times Max(\Delta x_{coe}^2, \Delta y_{coe}^2) \tag{3.11}$$

where Δx_{coe} and Δy_{coe} are the distances from the center-of-energy to the center of the closest beam hole. Each ring has area 1 cm^2. Events with ring number less than 81 cm^2 should be kaon decays from inside one of the two beams. Figure 3.28 shows the ring number distributions for both beams. The ring number is required to be less than 110 cm^2.

Veto Detector	1996 Cut	1997 Cut	1999 Cut
Regenerator	E < 2.0 mips	E < 2.0 mips	E < 1.75 mips
Regenerator Pb	E < 0.7 mips	E < 0.7 mips	E < 0.7 mips
MA	E < 0.3 GeV	E < 0.3 GeV	E < 0.3 GeV and L1 trigger source = F
RCs	E < 0.3 GeV	L1 trigger source = F	L1 trigger source = F
SAs	E < 0.3 GeV	E < 0.3 GeV and L1 trigger source = F	L1 trigger source = F
CIA	E < 0.3 GeV	E < 0.3 GeV and L1 trigger source = F	E < 0.3 GeV and L1 trigger source = F
CA	E < 1.0 GeV	E < 1.0 GeV	E < 1.0 GeV
BA1	E < 5.0 GeV	E < 5.0 GeV and L1 trigger source = F	L1 trigger source = F
HA	no cut	L1 trigger source = F	no cut
MU2/MU3	no cut	no cut	no cut

Table 3.5: Summary of veto cuts for $K \to \pi^0\pi^0$ decays. Some cuts are applied differently for the three years. Compare to the requirements for $K \to \pi^+\pi^-$ decays in Table 3.1.

The reconstructed z vertex of the kaon decay is required to be 110-158 m downstream of the target and the total kaon energy is required to be between 40-160 GeV. These cuts are identical for the $K \to \pi^+\pi^-$ and $K \to \pi^0\pi^0$ samples. Figures 3.29 and 3.30 show the z vertex and kaon energy distributions, respectively.

The selection criteria for $K \to \pi^0\pi^0$ decays are summarized in Table 3.6.

3.2.6 Updates Since 2003

A number of changes have been made to the analysis since the most recent KTeV $Re(\epsilon'/\epsilon)$ result was published in 2003[50].

Cut Changes

For the current analysis we remove clusters whose seed is in the first ring of of CsI crystals around the beam holes. This cut is added because clusters in this region are not well reconstructed.

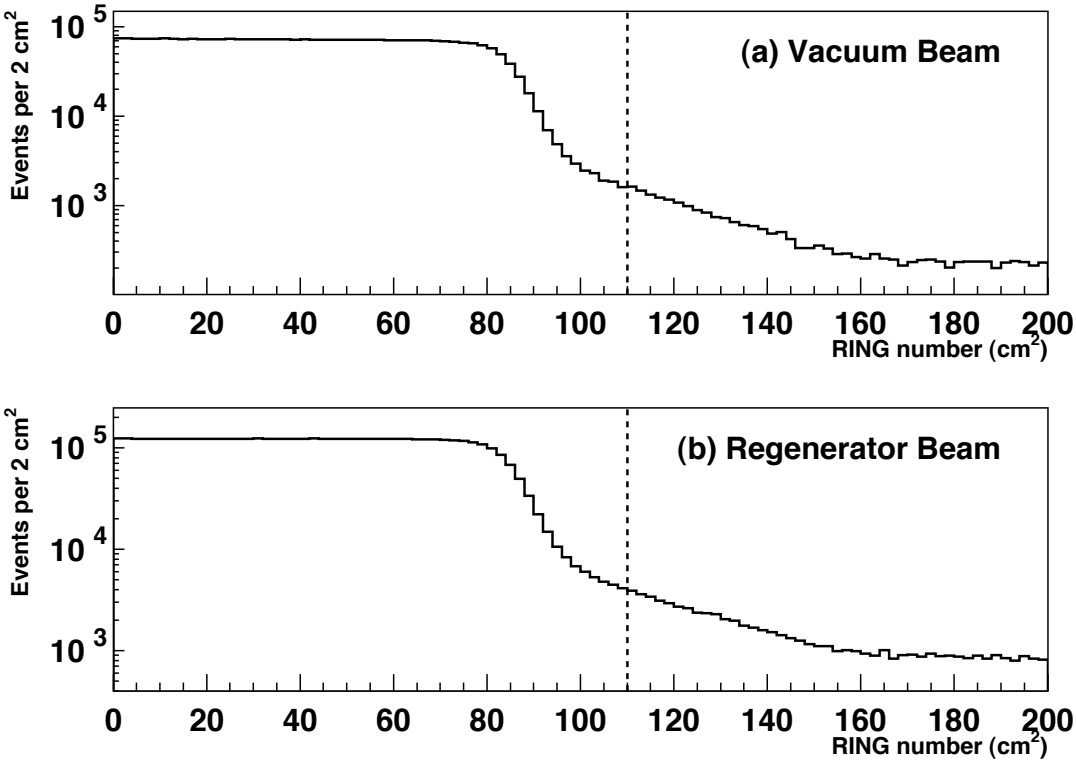

Figure 3.28: $K \to \pi^0\pi^0$ RING distributions for 1999. The dashed line indicates our cut.

We loosen the pairing chi-squared cut from 12 to 50. This is done primarily for consistency with the V_{us} analysis[65]. The V_{us} analysis uses this looser cut as well as the pipe block cut so when we decided to add the pipe block cut it made sense to move to a previously established set of cuts. Loosening this cut increases the $K_L \to \pi^0\pi^0\pi^0$ background level, but this background is well understood so the higher background level is acceptable.

We also add a cut on the energy distribution of showers in which the seed block is adjacent to a beam hole. We calculate the ratio of energy in the nearest neighbor which is not adjacent to a beam hole to the energy in the seed block. If the minimum value of this ratio in an event is less than 4%, the event is removed. This cut is

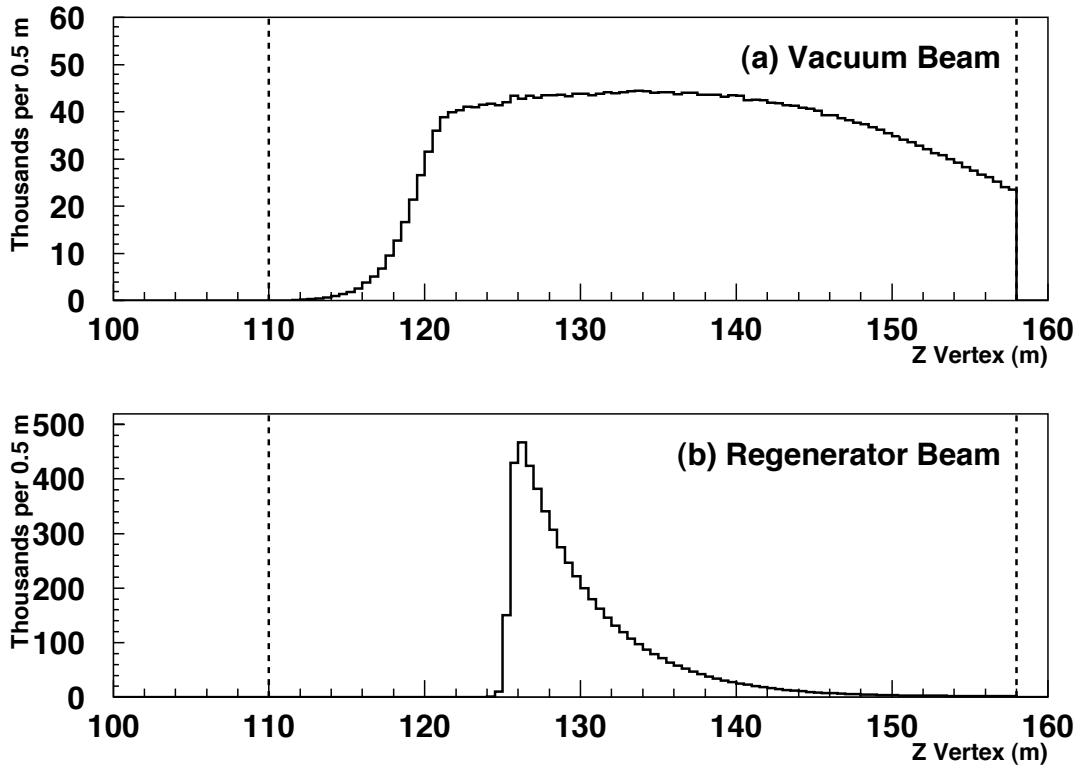

Figure 3.29: $K \to \pi^0\pi^0$ z vertex distributions for 1999. The dashed lines indicate our cuts.

added for for consistency with other analyses but given the cut on clusters with a seed in a pipe block, it is irrelevant.

Out-of-cone correction

In the previously published analysis, the out-of-cone correction was measured for small and large blocks using 8 GeV GEANT[64] showers, but there was no adjustment for energy or position of the incident particle. Photon-electron differences were not included. In the current analysis, the correction is a function of the reconstructed position and energy of the cluster and is parameterized separately for

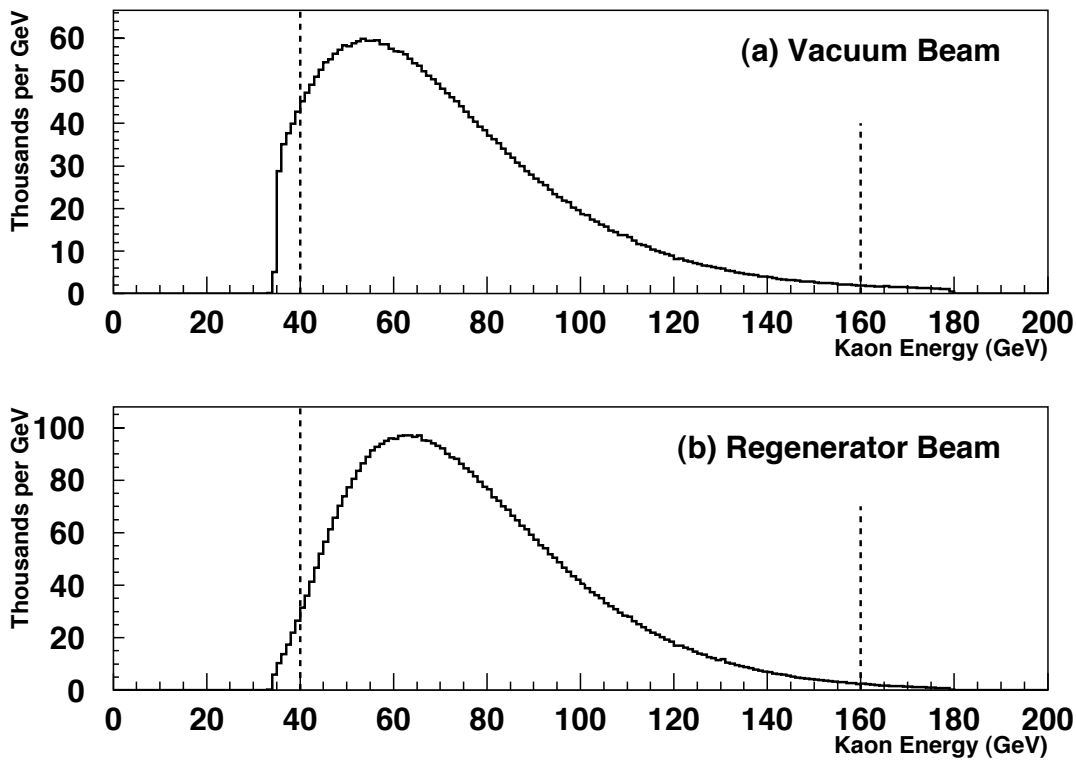

Figure 3.30: $K \to \pi^0\pi^0$ kaon energy distributions for 1999. The dashed lines indicate our cuts.

small and large blocks and for photons and electrons. The effect of energy loss in the wrapping for clusters in the small-large block overlap region is now included.

Uniformity Correction

In the previously published analysis, the uniformity correction was applied at cluster level based on a predicted average longitudinal energy distribution for the whole shower. The uniformity correction is now applied block-by-block. The measured CsI response of each block is convoluted with a GEANT[64] prediction of the longitudinal shower distribution in that block based on the transverse position of that block in the cluster. For the analysis of MC, some generated quantities are used to make

Quantity	Cut Value
Veto Detectors	See Table 3.5
Minimum Photon Energy	$E_\gamma > 3.0$ GeV
Minimum Cluster Separation	mindist > 7.5 cm
Remove Pipe Blocks	smlring2 > 4
Pipefrac	pipefrac < 0.04
Pairing Chi-squared	$\chi^2_{\pi^0} < 50$
Shape Chi-squared	$\chi^2_\gamma < 48$
Reconstructed Kaon Mass	490 MeV/$c^2 < m_{\pi^0\pi^0} <$ 505 MeV/c^2
Ring Number	RING < 110 cm^2
Reconstructed Kaon Z Vertex	110 m $< Z_K <$ 158 m
Reconstructed Kaon Energy	40 GeV $< E_K <$ 160 GeV

Table 3.6: Summary of selection criteria for $K \to \pi^0\pi^0$ decays

sure that we apply the correction only to those blocks for which the longitudinal non-uniformity was simulated.

Final Energy Scale

The final energy scale is applied in the same 10 GeV kaon energy bins used by the fitter for this analysis. In the previously published analysis, the energy scale was measured in energy bins but applied as a third order polynomial function determined by fitting the energy scale required to match the data to Monte Carlo. As a result of the changes to the simulation and reconstruction of clusters, the size and shape of the energy scale adjustment has changed; the required adjustment is smaller and less strongly dependent on kaon energy for low kaon energies. Figure 3.31 shows the final energy scale adjustments used in the previous and current analyses.

In the previously published analysis, decays in the regenerator were not simulated in the Monte Carlo. We used the calculation of the effective regenerator edge for $K \to \pi^0\pi^0$ decays to find the expected difference in the z position of the regenerator edge between data and MC and shifted the data upstream by that distance (6.2 mm) after matching the z distribution at the regenerator between data and MC. In this

analysis we simulate decays in the regenerator, so we adjust the data only by the data-MC difference we measure at the regenerator edge.

Photon Correction

For this analysis, a correction is applied to photon clusters to correct for possible electron-photon differences. The correction is based on photons from $K \to \pi^0\pi^0$ and $K_L \to \pi^0\pi^0\pi^0$ decays. The correction is measured separately for each year in nine regions of the calorimeter.

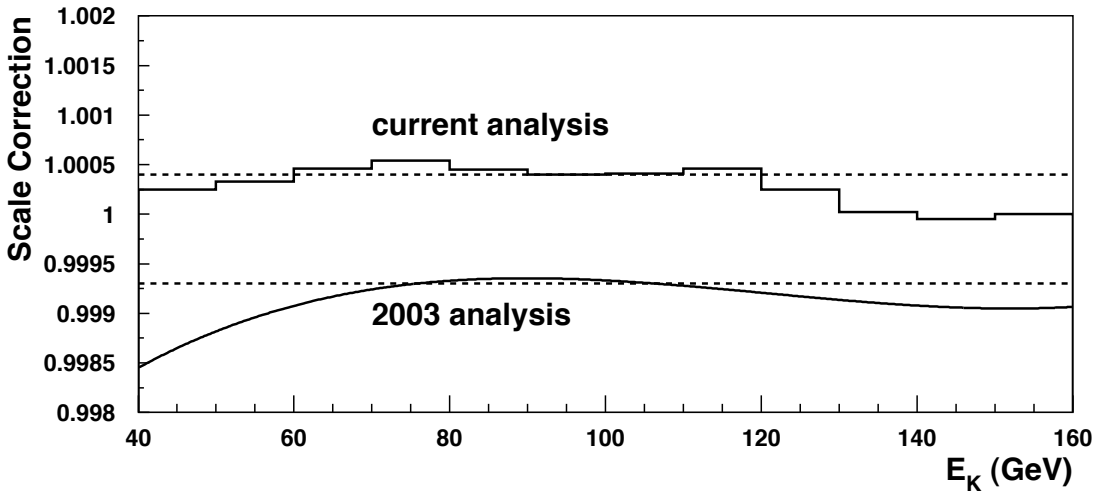

Figure 3.31: Change in the final energy scale adjustment relative to the 2003 analysis. The function is the third order polynomial correction applied to 1997 data in the 2003 analysis and the histogram is the binned correction applied to 1997 data in the current analysis. The dashed lines are the corresponding flat energy scale corrections.

3.2.7 Yields

Table 3.7 contains the number of $K \rightarrow \pi^0\pi^0$ events selected before background subtraction. We have selected over 6 million vacuum beam events and over 10 million regenerator beam events.

Year	Vacuum Beam	Regenerator Beam
1996	772140	1321917
1997	2150865	3689815
1999	3085243	5290092
Total	6008248	10301824

Table 3.7: $\pi^0\pi^0$ event yields before background subtraction

CHAPTER 4
MONTE CARLO SIMULATION

KTeV relies on a Monte Carlo (MC) simulation called KTeVMC to make the acceptance correction and to model backgrounds to the signal modes. The very different K_L and K_S lifetimes lead to very different z vertex distributions and somewhat different energy distributions in the vacuum and regenerator beams. We use the Monte Carlo to determine the detector acceptance as a function of kaon decay vertex and energy including the effects of geometry, detector response, and resolutions. The Monte Carlo simulates kaon generation at the BeO target, propagates the kaon along the beamline to the decay point while tracking its quantum state, simulates the kaon decay, traces the decay products through the detector, and simulates the detector response including the digitization of the detector signals. The geometry of the detector comes from survey measurements and from calibrations based on data. Many aspects of the tracing and detector response are based on GEANT[64] simulations. The effects of accidental activity are included in the simulation by overlaying data events from the accidental trigger onto the simulated events. The Monte Carlo event format is identical to data and the events are reconstructed and analyzed in the same manner as data with very few exceptions. The simulation is extremely detailed and reproduces most features of the data with extraordinary accuracy.

4.1 Kaon Propagation and Decay

The kaon energy spectrum and the relative flux of K^0 and $\bar{K}^0$ states produced at the target are based on a parameterization due to Malensek[66]. The Malensek parameterization is of K^+ and K^- production by 450 GeV protons incident on a beryllium target. We model K^0 and $\bar{K}^0$ production by relating neutral kaon

production to charged kaon production using their quark contents. The energy distribution is tuned to match KTeV $\pi^+\pi^-$ data using a polynomial correction. The production angle distribution is also tuned to match the data beam profiles.

As the kaon propagates down the beamline, its quantum state evolves from the initial K^0 or $\bar{K}^0$ state. KTeVMC uses K_L and K_S as its basis states and calculates the transformation matrix. The matrix is diagonal in vacuum; off-diagonal elements characterize regeneration and are generated as the kaon traverses matter such as the absorbers and the regenerator. The most important source of regeneration in the KTeV beamline is the regenerator. The regeneration amplitude used by KTeVMC for the regenerator has a power-law dependence on kaon energy. We simulate regeneration due to coherent forward scattering only.

As they propagate down the beamline, kaons may be absorbed by or scatter off of the various beamline elements. The primary and slab collimators are treated as perfectly absorbing while scattering in the defining collimators is allowed with a probability given by models which are tuned to data. Scattering in the absorbers is modeled using lead or beryllium scattering probabilities. Scattering in the regenerator is also simulated using models tuned to data; the quantum state of the scattered kaon is changed depending on the effective regeneration amplitude predicted by the model.

The kaon is forced to decay within a specified z range downstream of the target; the z position of each kaon decay is chosen based on the appropriate z distribution for the kaon state including the effects of interference between K_L and K_S. The decay generators for each type of kaon decay include effects that are relevant to the different decay modes. The simulation of $K \to \pi^+\pi^-$ includes radiative corrections due to inner Bremsstrahlung. Direct emission is not simulated. In $K \to \pi^0\pi^0$ decays only the four photon final state is allowed for this analysis. For three-body decays such as $K_L \to \pi^\pm e^\mp \nu$, the appropriate form factor is included. Kaon decays inside the regenerator are simulated.

4.2 Tracing of Decay Products

All decay products except neutrinos are traced through the detector. Particles are traced to the end of the BA except for muons which are traced through to the muon veto detectors. Pions may "punch through" to the muon vetos with a probability of $\sim 10^{-4}$/GeV. Particles are no longer traced when they leave the detector; the user may veto events with missing particles for efficient generation. Charged particles receive a transverse momentum kick from the analyzing magnet; the value of this kick depends on the transverse position of the particle and is based on the zip-track measurement of the magnetic field. Fringe fields between the chambers and inside the vacuum tank are also simulated.

KTeVMC models interactions in the materials of the detector by defining volumes of materials and using GEANT[64] to calculate the multiple scattering angle distribution, the radiation length, the Bremsstrahlung rate, the δ-ray rate, and other information about each material. Charged particles can scatter in the vacuum-window, the helium bags, the drift chambers, the trigger hodoscope, and the steel and will lose energy through ionization as they pass through matter. Electrons can undergo Bremsstrahlung in all materials. Charged pions may decay via $\pi \rightarrow \mu\nu$. Photons can convert to e^+e^- pairs. Secondary particles are also traced through the detector.

4.3 Simulation of the Drift Chambers

As KTeVMC traces each particle through the drift chambers, the hit position at each drift chamber plane is converted into a TDC value. The position resolutions measured in data are used to smear the hit positions and the inverse of the x(t) map is used to convert the smeared hit positions into drift times. Several sources of drift chamber inefficiencies are simulated.

The drift chamber wires have some localized spots of inefficiency due to silicon compounds on the wires. We measure these inefficiencies in 1 cm steps along each wire of each chamber and we measure a profile of the hit inefficiency as a function

of distance from the wire. The average single-hit inefficiency is less than 1%. We use these inefficiency maps in KTeVMC to model the wire inefficiency.

A hit is delayed when the signal from the first drift electron from a track is below threshold. This can lead to a hit-pair with a SOD too high to satisfy the hit-pair requirement. The delayed hit probability is a few percent in the beam region and about 1% over the rest of the drift chamber area. Delayed hits are simulated in KTeVMC by distributing 26 primary drift electrons along the track using a Poisson distribution with an average interval of 340 μm and then generating a composite signal at the sense wire. The drift electrons are summed into a composite signal using a parameterization of the pulse shape for a single drift electron given by:

$$p(t) = \frac{1}{1 + (\frac{t}{t_0})^{\frac{3}{2}}} exp\left(-\frac{t^2}{2\sigma^2}\right). \tag{4.1}$$

The MC threshold is tuned by matching the simulated delayed hit probability to data; we measure the delayed hit probability in data in 1 cm steps along each wire.

If an accidental hit arrives in the in-time window before a signal hit on the same wire, the accidental hit will be used by the tracking algorithm instead of the signal hit. This can lead to a SOD too low to satisfy the hit-pair requirement and occurs in $\sim$0.7% of hit-pairs. Accidentals arriving before the in-time window can also cause inefficiencies because the discriminator has a deadtime of 42 ns during which the wire is 100% inefficient and because large analog pulses may stay above threshold for longer than 42 ns. The variations of the pulse lengths are modeled and tuned to data.

Delta rays produced in the drift chambers cause a low-SOD for 0.5% of hit-pairs. High momentum delta rays are simulated by injecting them into the Monte Carlo and tracing them as we do any particle. Low momentum delta rays are simulated using a GEANT library. The library is based on GEANT4[67] and contains a full description of the drift chamber volumes including the mylar windows and buffer volumes. Pion interactions in the drift chambers are simulated using a GEANT library. The typical loss for a pion track is $\sim$0.6%.

4.4 Simulation of the CsI Calorimeter

KTeVMC simulates the energy deposit of particles in the CsI calorimeter, including a detailed simulation of electromagnetic showers. The digitization and readout of the calorimeter is simulated and some MC specific calibrations are done.

4.4.1 Electromagnetic Shower Simulation

The accurate simulation of electromagnetic showers in the CsI calorimeter is critical to the $K \to \pi^0\pi^0$ analysis. It is important to model not only the average transverse and longitudinal profiles of the showers but to capture the effects of shower-to-shower fluctuations. We must also model details of the calorimeter response such as energy lost in the wrapping around each crystal and the longitudinal non-uniformity of the CsI response. A full GEANT[64] simulation of the shower development of each photon or electron hitting the calorimeter would be ideal, but this would be prohibitively time consuming. Instead, we use a GEANT-based library of photon and electron showers which is binned in energy, incident position, and incident angle to simulate electromagnetic showers in the calorimeter.

To generate the GEANT shower library, we define an array of 13×13 crystals of CsI each of which is 2.5×2.5×50 cm^3. Each crystal is wrapped with mylar which is 12.5 μm thick; the wrapping overlaps and is taped together such that there is an extra 25 μm of wrapping at the top of each crystal. This wrapping is included in the GEANT simulation. The crystals are segmented longitudinally into 10 bins to allow us to simulate the longitudinal response. Photons or electrons are injected immediately upstream of the CsI incident on the central block in the array and the resulting showers are simulated down to photon and electron energies of 50 keV. Showers are generated at six different energies (2 GeV, 4 GeV, 8 GeV, 16 GeV, 32 GeV, and 64 GeV). The position of the incident particles relative to the center of the central block is generated in 325 position bins spread over one octant of the block. The size of these position bins varies from 700 μm at the block center to 200 μm at the edge. Figure 4.1 shows the layout of the position bins. This binning is chosen to match the variation in reconstructed position resolution which

is better for particles incident near the edge of a crystal. We generate position bins covering only one octant of the central block and rotate the showers appropriately to simulate particles incident on the other 7 octants of the block. We generate showers at 9 different angles of incidence for photons and 15 angles of incidence for electrons. Photon showers are generated at 0 mrad, ±5 mrad, ±15 mrad, ±25 mrad, and ±35 mrad in x and y. Electron showers are generated at 0 mrad, ±5 mrad, ±15 mrad, ±25 mrad, ±35 mrad, ±45 mrad, ±65 mrad, and ±85 mrad in x and y. We must simulate higher angles of incidence for electrons since they are bent in the magnet; we need higher angles in both x and y because we rotate the showers into all 8 octants to cover all incident positions in the central crystal. We generate 16 shower libraries, each containing one shower per bin. These libraries are distributed across the nodes of the FNAL farm such that when we generate Monte Carlo which accesses the shower library, each batch of 16 MC generation jobs contains showers from all 16 libraries.

One photon shower library consists of 6 energy bins, 325 position bins, and 81 angle bins for a total of over 150,000 showers. An electron shower library has 225

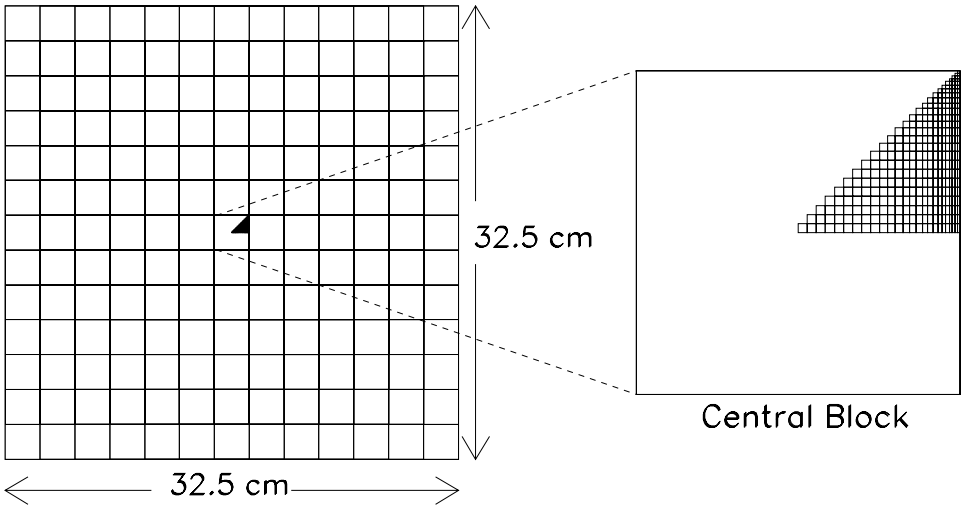

Figure 4.1: Position bins used for shower library generation.

angle bins for a total of over 400,000 showers. During MC generation, the entire shower library is read into memory, so we must pack the showers efficiently. In our shower packing scheme, the 13×13 array is divided into rings of crystals; the kinds of information and the precision used to store it vary with ring. We use more precision to store information about the central blocks as this is where the most energy is deposited. For example, we use 10 bits to store the block energy for the central block and only 5 bits each to store the block energies for the outermost blocks. We store energy deposits in the wrapping and longitudinally segmented energy deposits for the 3 innermost rings (13 innermost blocks) only. In total, each shower is stored using 200 bytes where 64% of that is used for block energies, 10% is used for wrapping energies, and 22% is used for longitudinally segmented energies. The remainder is header information and unused bits. The total sizes of the libraries are 33 Mb and 93 Mb for the photon and electron libraries respectively.

When a photon or electron hits the CsI, a shower is selected from the appropriate shower library. Before choosing the shower, we smear the energy of the incident particle. The energy smearing is tuned by matching the E/p resolution of MC to data using K_{e3} electrons from the calibration sample with all corrections applied. The smearing is determined separately for 1996, 1997, and 1999 and is applied as a polynomial function of energy with separate functions for small and large blocks. For 1996, we apply separate smearing functions for RF phases 1/2 and 3. For showers with energy less than 2 GeV we apply an additional smearing to account for the difference between shower fluctuations at the GEANT shower energy (2 GeV) and at the desired particle energy. This effect is treated appropriately by the MC for higher energy showers by interpolating between energy bins. We also apply a smearing which is designed to simulate the low-side tail in the E/p distribution. Figure 4.2 shows the data and MC resolutions as a function of energy for small blocks in 1999 with only the E/p tail smearing applied; these distributions are used to determine the polynomial smearing function.

We select the energy bin from the shower library by choosing between the two closest energy bins using a logarithmic interpolation. The probability of selecting a shower from each bin varies with the logarithm of the desired energy and the

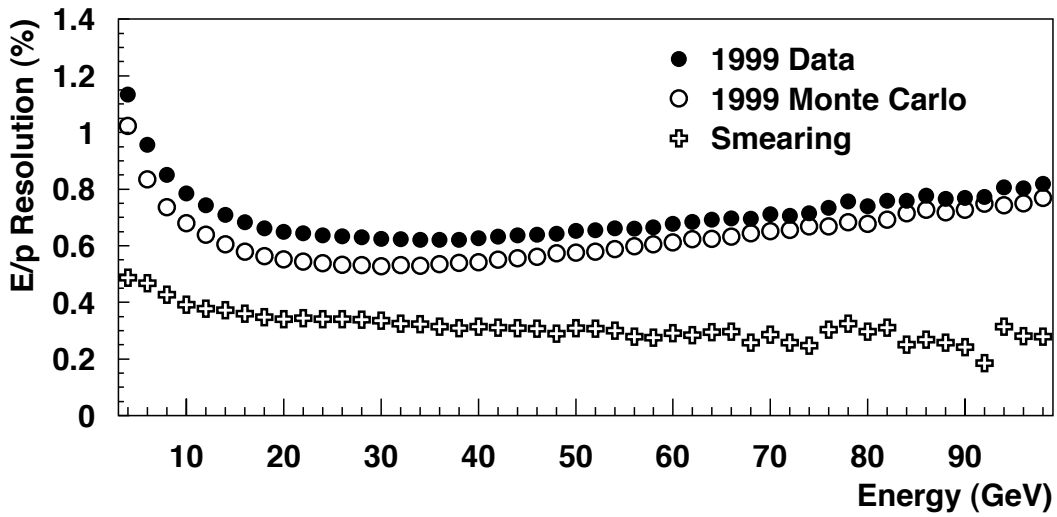

Figure 4.2: E/p resolutions as a function of energy for K_{e3} electrons in small blocks in 1999 data and Monte Carlo before final energy smearing. Both distributions include a small contribution from the momentum resolution which is not subtracted since it will cancel in the difference.

final selection is made using a random number. The selected shower is later scaled block-by-block to the desired energy.

We select the angle bin from the shower library by interpolating linearly between the two closest angle bins. We correct for the difference between the GEANT shower angle and the desired angle by shifting the transverse position of incidence such that the shower maximum will occur at the same position that it would have with the desired position and angle. Figure 4.3 is a cartoon of the geometry involved in shifting the positions. In order to calculate the appropriate position shift, we must know the longitudinal (z) position at which we want to align the showers. This is calculated individually for each particle and is a function of particle type (photon or electron), angle of incidence, position of incidence relative to the block center, and block size (small or large). Since the angles of incidence are less than 100 mrad, we use the small angle approximation to calculate the shifts. Finally, we use the shifted positions to select the position bin.

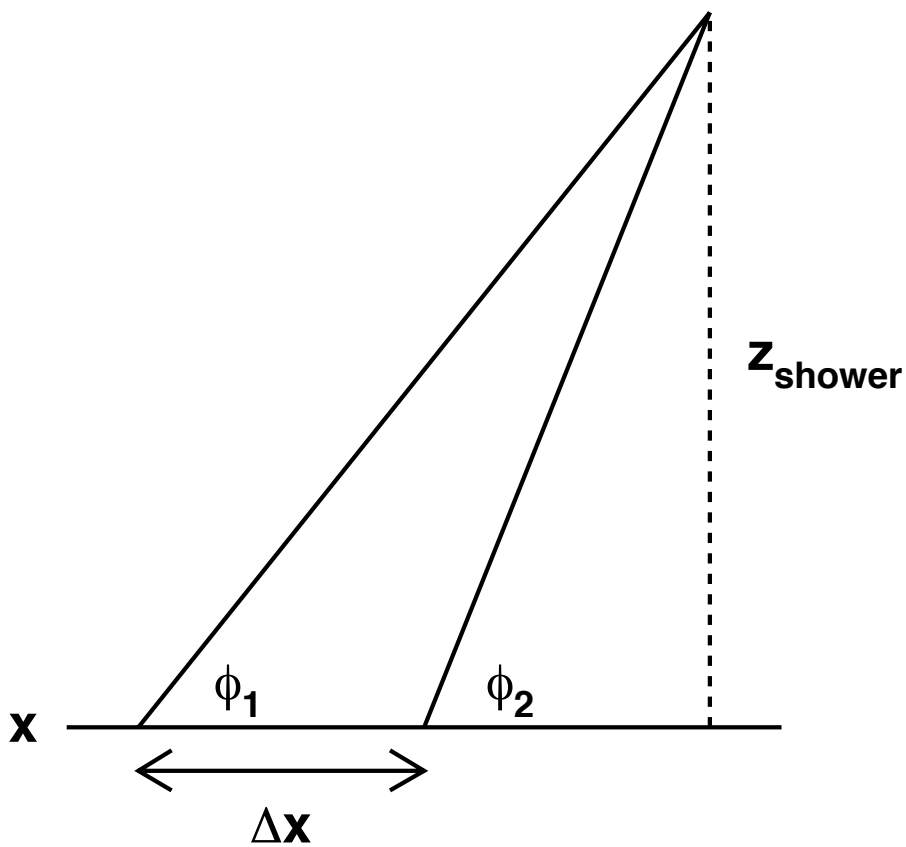

Figure 4.3: Cartoon of position shift to correct for differing incident angles. A shower with incident angle ϕ_1 will reach shower maximum at the same position as a shower with angle ϕ_2 shifted by Δx.

Care must be taken in selecting the angle and position bins to make sure we have rotated the desired angles and positions into the first octant where the GEANT showers are generated (see Figure 4.1). After we have chosen a shower from the library and unpacked the block energies, we rotate the shower back into the desired octant. It is at this point that we scale the block energies using the ratio of the smeared energy of the incident particle to the generated energy of the shower from the library.

Next we convolute the block energies with the measured longitudinal response of the CsI crystals. We use the position of the particle in the KTeV coordinate system to determine on which CsI crystal the particle is incident. The shower from the library will be overlaid on the calorimeter with the central block of the shower on this crystal. For those blocks in the shower for which we have stored longitudinally segmented energies, we scale the energy deposit in each z slice by the normalized longitudinal response for that slice of the particular CsI crystal we are simulating. We use the same response constants that are used by the longitudinal uniformity correction in data. We sum the energies in the ten z slices to find the energy in each block.

The shower library is generated using small blocks only and includes the wrapping around each block. When the particle we wish to simulate deposits energy in the large blocks we simply overlay a shower from the library on that portion of the calorimeter, summing small block energies from the shower when necessary to find the energy deposit in the large blocks. This means that we overestimate the amount of energy lost in the wrapping for large blocks, since we simulate wrapping in the middle of the large blocks which is not really there. Figure 4.4 is a cartoon of this effect. We store the energy deposit in the wrapping on each side of each block as part of the shower library[1]; for wrapping that should not be present we simply add that energy back into the block energy.

In stacking the CsI calorimeter it was necessary to add shims between some rows of crystals. We estimate the energy lost in this dead material by using the energy deposit in the wrapping (which is part of the shower library) and scaling to the size of the shims. We split the energy lost in the shims evenly between the blocks above and below each shim and simply subtract the lost energy from the energy in each block.

We simulate leakage of energy across the beam holes using the same maps that are used for the "sneaky energy" correction in data. We simulate the energy deposited in crystals outside the 13×13 block shower from the shower library using

[1]To save space in the shower library we store wrapping information for only the central 13 blocks in each shower.

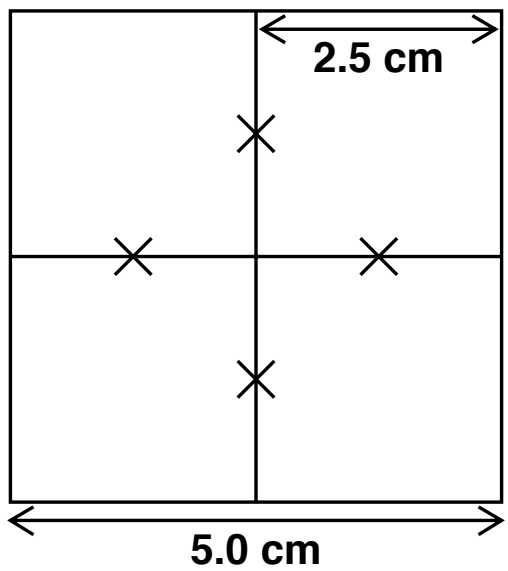

Figure 4.4: Cartoon of extra wrapping in the simulation of large blocks. The Xs mark the wrapping that is simulated in the shower library but is removed in KTeVMC.

a parameterization which is a function of distance from the shower center. The parameterization is based on a GEANT simulation of 31×31 2.5 cm CsI crystals. We simulate energy deposits in a 27×27 array of blocks.

4.4.2 Simulation of Other Particles

Muons incident on the CsI calorimeter deposit energy only in the crystal they hit at the face of the CsI. The energy deposited by a muon is calculated using Bethe-Bloch ionization loss with fluctuations. The energy deposit is convoluted with the longitudinal response of the CsI crystal by dividing the energy evenly among ten z slices and scaling by the normalized longitudinal response for each slice. A correction

which lowers the energy deposit by 6% relative to the Bethe-Block prediction is applied to match the MIP energy scale to data.

Pions with energy greater than 2 GeV may shower hadronically in the calorimeter and are simulated using a GEANT shower library. Showers are selected from the library using the energy and position of the incident particle. The shower library consists of a continuous energy distribution of showers with 4 mm x and y position bins. The showers contain the energy deposits in a 50×50 array of small blocks. It is possible to force all pions to deposit minimum ionizing energy rather than showering; this saves time for Monte Carlo samples which do not require simulation of pion showers. Protons and charged kaons are treated like pions and use the same shower library.

All other particles and minimum ionizing pions deposit 320 MeV or the total energy of the particle (whichever is smaller) into a single CsI crystal determined by the position of incidence.

4.4.3 Digitization and Readout

The energy in each CsI crystal is determined by summing the energy deposit to that crystal from each particle and from the accidental overlay event. The block energies are converted to charges using the Q/E constants measured in the electron calibration. The total charge in each block is divided into time slices using pulse time profiles measured in $K \to \pi^0\pi^0$ data. The charge in each time slice is smeared using photostatistics and digitized using the DPMT calibration constants. As in data, digitized information is written out only if the energy in a given block is above threshold.

4.4.4 Monte Carlo Clustering and Corrections

In general we use the same calibration constants for data and Monte Carlo; we use the DPMT and Q/E calibration constants found in data to generate and analyze Monte Carlo events. To account for the possibility that we have not perfectly simulated the transverse shower shapes, we generate Monte Carlo specific transverse

energy maps and position lookups to be used in the reconstruction of MC events. We use the same procedure to generate these maps as we use for data; we simply use simulated $K \to \pi^0\pi^0$ events rather than data.

For reasons that are not understood, the position resolution of CsI clusters in the Monte Carlo is slightly worse than in data. To match the resolutions, we artificially improve the MC position resolution by 9%. This factor is determined by matching the widths of the $\pi^0\pi^0$ invariant mass peaks between data and Monte Carlo. Reconstructed cluster positions are adjusted in MC events by finding the difference between the reconstructed and generated positions and reducing that difference by 9%. The scaled difference is then added to the generated position to find the "unsmeared" reconstructed position. This has the effect of moving the reconstructed positions 9% closer to the generated position. This is one of the few places where we use generated quantities in the reconstruction of Monte Carlo events.

The longitudinal uniformity correction is applied only to those blocks in which the effect is simulated. We use generated quantities to determine which blocks should have this correction applied. We do not simulate variations in energy response across the face of the crystal, so the intrablock correction is not applied. The phase correction is not applied for 1996 MC. We generate a separate channel-by-channel linearity correction for MC using simulated K_{e3} events which is applied in place of the data correction. We do not simulate time variations in the electronics or CsI response, so the laser correction and spill-by-spill correction are not applied. The photon correction and final energy scale correction are tuned to match data to Monte Carlo so they are not applied to MC events. All other clustering corrections are applied to MC events just as in data.

4.5 Accidental Overlays

As a result of the high flux of kaons and neutrons in the KTeV beam, there can be underlying activity in the detector that is unrelated to kaon decay and is proportional to the instantaneous intensity of the proton beam. The average accidental energy under each CsI cluster is a few MeV and there are roughly 20 extra in-

time drift chamber hits in each event. KTeVMC simulates these effects by using data events from the accidental trigger to add the underlying accidental activity to each generated MC event. The run and spill number for each Monte Carlo event is obtained from the accidental event so that we simulate the run-dependence of accidental activity. In the calorimeter and veto system the energy deposits from accidental events are added to the generated energies channel-by-channel. For the drift chamber simulation, we model the manner in which an accidental hit can cause inefficiencies in the tracking as described briefly in Section 4.3 and detailed in [2].

4.6 Simulation of the Trigger

KTeVMC simulates the level 1, level 2, and level 3 triggers. For the $K \to \pi^+\pi^-$ trigger the most important effect to simulate is the 0.3% level 1 inefficiency due to the scintillator gaps in VV′. The gap sizes and positions are measured in data using the K_{e3} sample. The simulation also includes the drift chamber signals at level 1 and level 2. For the $K \to \pi^0\pi^0$ trigger we use $K_L \to \pi^\pm e^\mp \nu$ decays to determine the Etotal threshold and turn-on width and to measure the HCC threshold for each CsI channel.

4.7 Updates Since 2003

Many improvements and updates have been made to the MC simulation since the previously published result in 2003[50].

4.7.1 Changes to Kaon Propagation and Decay

Kaon Parameters

We have updated τ_L, τ_S, $|\epsilon|$, and m_K. We now use the following values:

- τ_L= 5.09685814 $\times 10^{-8}$ s
- τ_S= 8.96185833 $\times 10^{-11}$ s

- $|\epsilon| = 0.002224$
- $m_K = 497.626$ MeV/c^2

The value of τ_L is the PDG average[51]. The value of τ_S is the KTeV[50] result combined with the NA48[58] result. $|\epsilon|$ is the KTeV measurement from the $|Vus|$ analyses[65]; KLOE and NA48 have reported similar values. m_K is one PDG sigma lower than the PDG[51] value; this value produces better MC agreement with our data.

Decays in Regenerator

In the previously published analysis we did not simulate decays in the regenerator in the Monte Carlo. In the current analysis, decays in the regenertor are simulated.

4.7.2 Changes to Geometry and Tracing

MA Aperture

We have reduced the MA aperture by 50 μm from the measured aperture. This change is well within the systematic errors on the aperture measurement and produces better data-MC agreement in the upstream part of the $K_L \to \pi^0\pi^0\pi^0$ vertex z distribution.

Drift Chamber Sizes

We now use drift chamber sizes and rotations measured in the lab in 2002. The survey of the wire positions used a large coordinate measurement machine with a camera and magnifying lens mounted on the end of a movable arm. The measured drift chamber size is about 0.02% larger than the nominal value from scaling the 6.25 mm cell size. The rotation between DC1 and DC2 is limited to ± 30 μrad.

Interactions with Matter

In the previously published analysis, we did not include the effect of ionization (dE/dx) losses for charged particles in the simulation. In the current analysis, we use GEANT to calculate dE/dx for each volume of material in the decay region and include ionization losses in the simulation. The total dE/dx loss up to the surface of the CsI is ∼4.5 MeV and the loss between the magnet and the CsI is ∼3.5 MeV. This is a very small effect for $K \to \pi^+\pi^-$ decays but becomes important for low-energy electrons used in the calibration of the CsI.

In the previously published analysis, the MC included electron Bremsstrahlung in materials upstream of the analyzing magnet only. In the current analysis, the Bremsstrahlung rate in each volume of material in the detector is calculated by GEANT and included in the simulation.

In the previous analysis, only delta rays produced in a single cell of the drift chambers were considered. KTeVMC now has a full treatment of delta rays in which high momentum delta rays are traced through the detector like any other particle and low momentum delta rays are simulated using a GEANT4[67] library. The new treatment of delta rays improves our prediction of the distribution of extra in-time hits in the drift chambers.

Pion interactions in the drift chambers are now simulated using a GEANT library which contains a list of secondary particles produced by each hadronic interaction. An average of nine secondary particles are produced per interaction. These secondary particles are read in from the shower library and traced through the rest of the detector like any other particle. These hadronic interactions in the drift chamber were not simulated in the previous analysis.

Fringe Fields

Fringe fields from the analysis magnet between the vacuum tank and DC4 have been measured and are now simulated.

Pion Punch Thru

The probability for a pion to punch through the CsI, HA, and filter steel to fire MU2 and MU3 has been measured and implemented in the simulation.

4.7.3 Changes to Detector Response

RC/SA Thresholds

In the previous analysis, veto thresholds were simulated using nominal values. We now measure the RC, SA, and CIA thresholds using using $K_L \to \pi^+\pi^-\pi^0$ decays. The thresholds for these detectors are summarized in Table 4.1.

Detector	Threshold	
	1996/1997	1999
RC6	150 MeV	351 MeV
RC7	150 MeV	172 MeV
RC8	150 MeV	138 MeV
RC9	150 MeV	151 MeV
RC10	150 MeV	143 MeV
SA2	270 MeV	141 MeV
SA3	270 MeV	158 MeV
SA4	270 MeV	222 MeV
CIA	250 MeV	165 MeV

Table 4.1: Veto detector thresholds

Position Resolution of Drift Chambers

The position resolution of the drift chambers is dependent upon position within the cell. In the previous analysis, the resolution was treated as flat across the cell; the position dependence of the resolution is now simulated.

Electromagnetic Shower Library

For this analysis, the GEANT[64] shower library used to simulate photons and electrons in the CsI calorimeter has been improved to simulate the effects of incident

particle angle. The library used for the previous analysis was binned in energy and incident position; the effect of angles was approximated by shifting the incident position based on the angle of incidence. The shower library has now been expanded to include nine angles (-35 mrad to 35 mrad) for photons and 15 angles (-85 mrad to 85 mrad) for electrons. Differences between the library angle and the desired angle are approximated using the same position shifting scheme used previously. A particle energy cutoff of 50 keV has been applied for both photons and electrons in the GEANT[64] shower library generation. A new bit packing scheme for the shower library has been implemented to make the larger shower library small enough to hold in memory. Sixteen separate libraries with one shower per bin have been generated.

Wrapping and Shims

The shower library is generated using small blocks with wrapping; large blocks are simulated by combining four small blocks. This means that, in the simulation, large blocks contain wrapping in the center of the block in both transverse dimensions which is not actually present. A correction is now applied to large blocks in MC generation to replace the energy lost in that extra wrapping. Energy lost in the shims between rows of CsI crystals is now removed.

Transverse Energy Adjustment

In the previous analysis, the transverse distribution of energy in electromagnetic showers did not agree between data and MC, so a correction was applied during MC generation to match the shower profiles. With the new shower library this correction is no longer needed and is not applied.

CsI Energy Tail

The energy smearing in KTeVMC has been changed to better simulate the CsI energy tail. The old smearing was measured using K_{e3} electrons with a cut of

$\chi^2_\gamma < 3.0$. The smearing has been re-measured for $\chi^2_\gamma < 48.0$ which is the cut we use for the $Re(\epsilon'/\epsilon)$ analysis; this provides better agreement with the data.

CsI Threshold for Accidentals

There is a low energy bias in the CsI energy readout of ∼2 MeV per channel. The accidentals have a 2 count readout threshold which results in a zero point energy of ∼9 MeV per cluster. This effect is reduced by an order of magnitude by artificially raising the CsI threshold to 3 counts in MC.

Quality of CsI Simulation

The improvements to the CsI simulation, particularly the improvements to the shower library and the treatment of dead material, represent significant improvements to the $K \to \pi^0\pi^0$ analysis. Figure 4.5 shows the fraction of energy in the seed block relative to the total cluster energy for K_{e3} data compared to the Monte Carlo used in the previously published analysis[50] and the current Monte Carlo. The 2003 MC contains the transverse energy correction which was designed to force data-MC agreement in the transverse shower shapes. The current MC does not need this correction. Figure 4.6 shows the improvement in the data-MC comparison of the fraction of energy in each of the 49 blocks in a small cluster relative to the total cluster energy for K_{e3} electrons. These particular plots are made for 16-32 GeV electrons with incident angles of 20-30 mrad, but the quality of agreement is similar for other energies and angles. The data-MC disagreement improves from up to 15% for the 2003 MC to less than 5% for the current MC.

4.7.4 Changes to Monte Carlo Analysis

Position unsmearing

The position resolution of CsI clusters in the MC is slightly worse than in data. To better match the resolutions, we artificially improve the resolution of the MC by

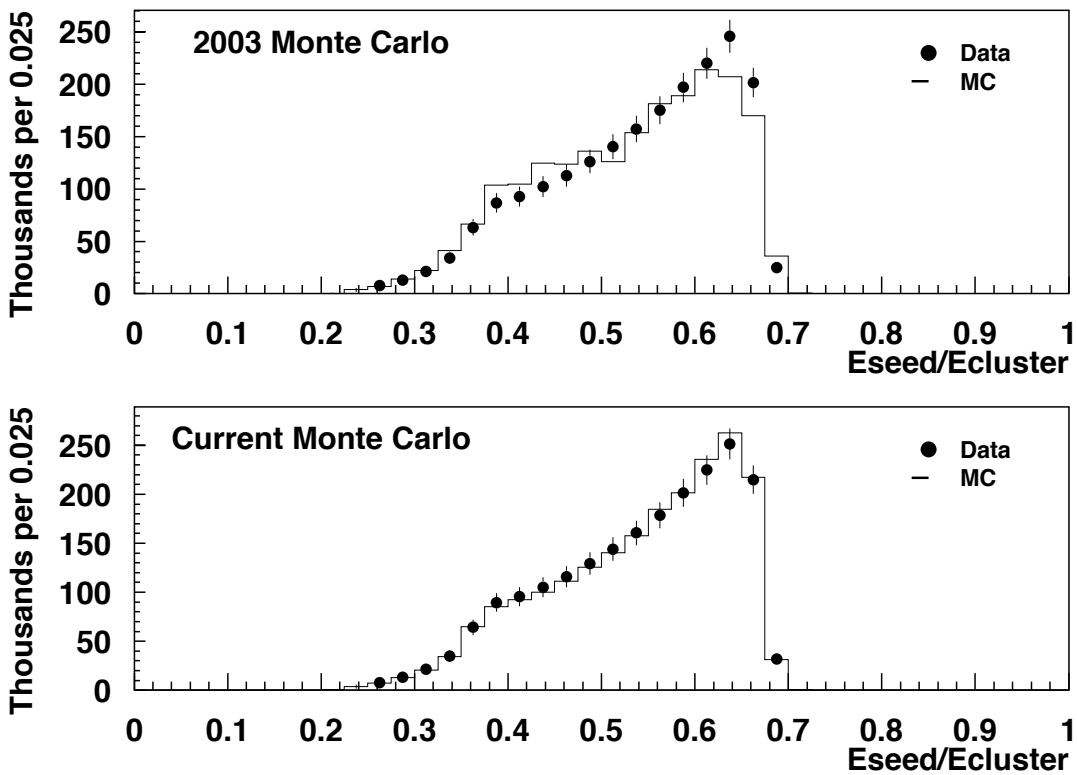

Figure 4.5: Data-MC comparison of fraction of energy in the seed block for small blocks using K_{e3} electrons. The top panel shows the 2003 MC which includes a transverse energy correction. The bottom panel shows the current MC with no correction.

9%. This is done by moving the reconstructed position toward the generated photon position.

4.8 Monte Carlo Samples

Table 4.2 contains a summary of the coherent $K \to \pi^+\pi^-$ and $K \to \pi^0\pi^0$ Monte Carlo event yields used to determine the acceptance for the measurement of $Re(\epsilon'/\epsilon)$. The total error on $Re(\epsilon'/\epsilon)$ due to Monte Carlo statistics is 0.40×10^{-4}. Monte Carlo samples of $K_L \to \pi^\pm e^\mp \nu$ and $K_L \to \pi^0\pi^0\pi^0$ decays are compared to the high statis-

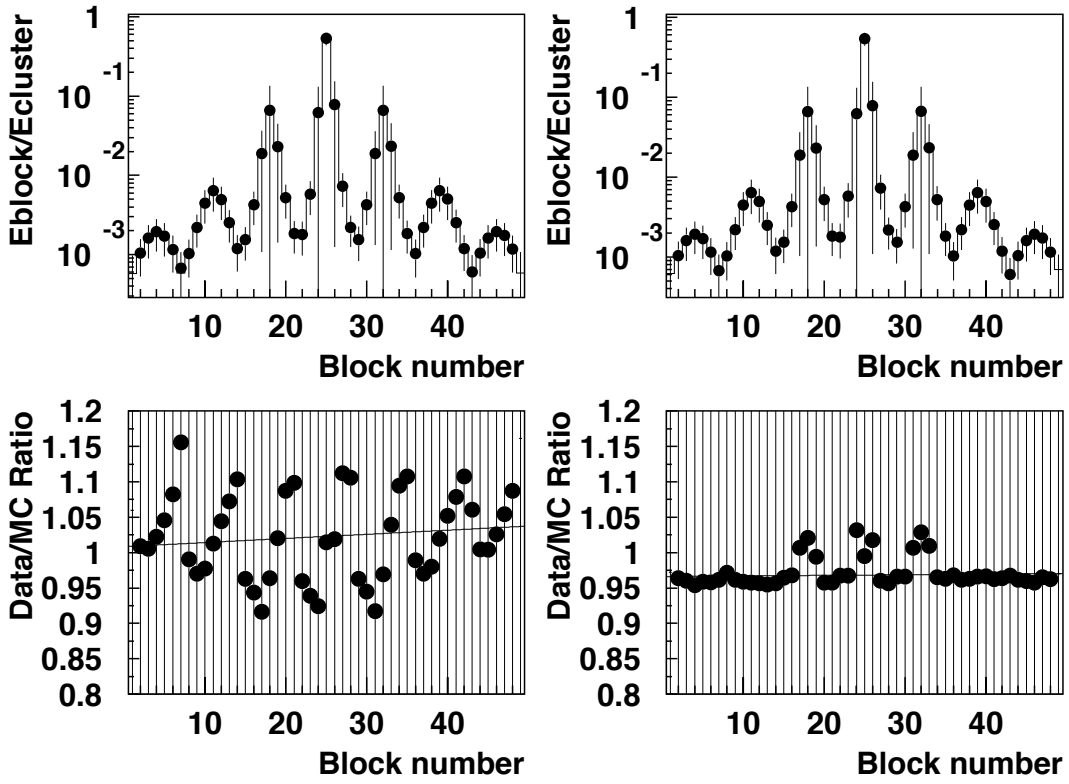

Figure 4.6: Data-MC comparison of fraction of energy in each of the 49 blocks in a small block cluster using K_{e3} electrons. These plots are made using 16-32 GeV electrons with incident angles of 20-30 mrad. The top left panel shows the the data(dots) and MC(histogram) overlay for 2003 Monte Carlo and the bottom left panel shows the data/MC ratio. The top right panel shows the data(dots) and MC(histogram) overlay for current Monte Carlo and the bottom right panel shows the data/MC ratio.

tics data samples in these modes to check the quality of the simulation, particularly the acceptance measurement. KTeVMC is used to generate background samples for all relevant backgrounds; the background simulation is described in detail in Chapter 5.

Year	$K \to \pi^+\pi^-$ Events		$K \to \pi^0\pi^0$ events	
	Vacuum Beam	Regenerator Beam	Vacuum Beam	Regenerator Beam
1996	n/a		10377863	17528188
			14 datasets	
			$\sigma_{stat} = 0.75 \times 10^{-4}$	
1997	72146768	125764960	42332052	71564816
	7 datasets		20 datasets	
	$\sigma_{stat} = 0.28 \times 10^{-4}$		$\sigma_{stat} = 0.37 \times 10^{-4}$	
1999	75944776	132193104	34351084	58119264
	5 datasets		11 datasets	
	$\sigma_{stat} = 0.28 \times 10^{-4}$		$\sigma_{stat} = 0.41 \times 10^{-4}$	
Total	148091544	257958064	87060999	147212268
	$\sigma_{stat} = 0.20 \times 10^{-4}$		$\sigma_{stat} = 0.25 \times 10^{-4}$	

Table 4.2: $K \to \pi^+\pi^-$ and $K \to \pi^0\pi^0$ MC event yields for 1996, 1997, and 1999. A "dataset" refers to the number of data events in our samples.

CHAPTER 5
BACKGROUNDS

Backgrounds to the $K \to \pi\pi$ signal modes are simulated using the Monte Carlo, normalized to the data, and subtracted. As discussed in Section 2.3.2, we use only decays from coherently regenerated kaons in this analysis. Diffractive and inelastic scattering in the regenerator is treated as background. This regenerator scattering background and background from kaons that scatter in the defining collimators are the same for both $K \to \pi^+\pi^-$ and $K \to \pi^0\pi^0$ decays. These backgrounds can be identified using the reconstructed transverse momentum of their decay products in charged mode; this means that the scattering backgrounds are rather small in charged mode and we may use $K \to \pi^+\pi^-$ decays to tune the simulation of scattering backgrounds on which we must rely in neutral mode. The non-$\pi\pi$ backgrounds are present due to the misidentification of high branching-ratio decay modes. The background to $K \to \pi^+\pi^-$ decays comes from $K_L \to \pi^\pm e^\mp \nu$ and $K_L \to \pi^\pm \mu^\mp \nu$ decay modes. The background to $K \to \pi^0\pi^0$ decays comes from $K_L \to \pi^0\pi^0\pi^0$ decays and hadronic production in the regenerator.

5.1 Scattering Backgrounds

5.1.1 Collimator Scattering

Events due to scattering in the defining collimator are identified using $K \to \pi^+\pi^-$ decays with high values of p_T^2 in the vacuum beam. We select $K \to \pi^+\pi^-$ decays using nominal selection criteria with a few exceptions. To select scattered events, we require $p_T^2 > 1000$ MeV^2/c^2; for reference, the requirement for selecting coherent events is $p_T^2 < 250$ MeV^2/c^2. To reduce other backgrounds, we require 493 MeV/c^2 $< \mathrm{m}_{\pi^+\pi^-} <$ 503 MeV/c^2 and E/p < 0.75. The reconstructed kaon

trajectory is projected back to the z position of the defining collimator. Figure 5.1a shows the y vs. x distribution of this projection. The square bands in this plot are from collimator scatters. We define a variable analogous to the RING number, called RINGCOLL, which has a clear collimator scatter peak at 20 cm^2 (see Figure 5.1b). The reconstructed invariant mass distribution (Figure 5.1c) for all events and events outside the RINGCOLL peak shows a flat mass background to the collimator scatters which is suggestive of semileptonic decays. This background level ($\sim$10%) is measured using sidebands of the RINGCOLL distribution in 10 GeV kaon momentum bins and the background is subtracted.

As the Monte Carlo propagates each kaon along the beamline, those kaons that strike the defining collimator are traced through the steel and allowed to scatter back into the beam. A kaon that scatters in the collimator is parameterized to be either pure K_S or K_L. The relative amounts of K_S and K_L are determined using a fit to two-dimensional plots of p_T^2 vs z vertex from the $K \to \pi^+\pi^-$ collimator scattering data sample, a simulation of pure K_L scatters, and a simulation of pure K_S scatters. The K_L scatters tend to be flat in z and peaked towards smaller p_T^2 while the K_S scatters tend to be more upstream with a broader p_T^2 spectrum. About 1/3 of the collimator-scattered kaons hit the MA. The Monte Carlo simulates the 60% probability measured in data for the kaon to "punch through" the MA. Particles that exit the MA are either pure K_S or pure K_L with a K_S to K_L ratio of $\sim$50.

For the $K \to \pi^+\pi^-$ signal mode, the background from collimator scatters is 0.01%. It is small because the p_T^2 cut eliminates most of this background. It is normalized to the high p_T^2 $K \to \pi^+\pi^-$ data sample in which selection criteria have been applied to enhance the level of this background; this sample requires E/p < 0.5 for both pions, both pions must shower in the calorimeter, and the reconstructed kaon momentum must point back to the defining collimator. The efficiency of these cuts is applied to the normalization factor to predict the level of collimator scatters in the coherent $K \to \pi^+\pi^-$ sample. The normalization is done in 10 GeV energy bins.

In the $K \to \pi^0\pi^0$ mode, the collimator scattering background is more significant since we cannot make a cut on p_T^2. We use the collimator scattering Monte Carlo to

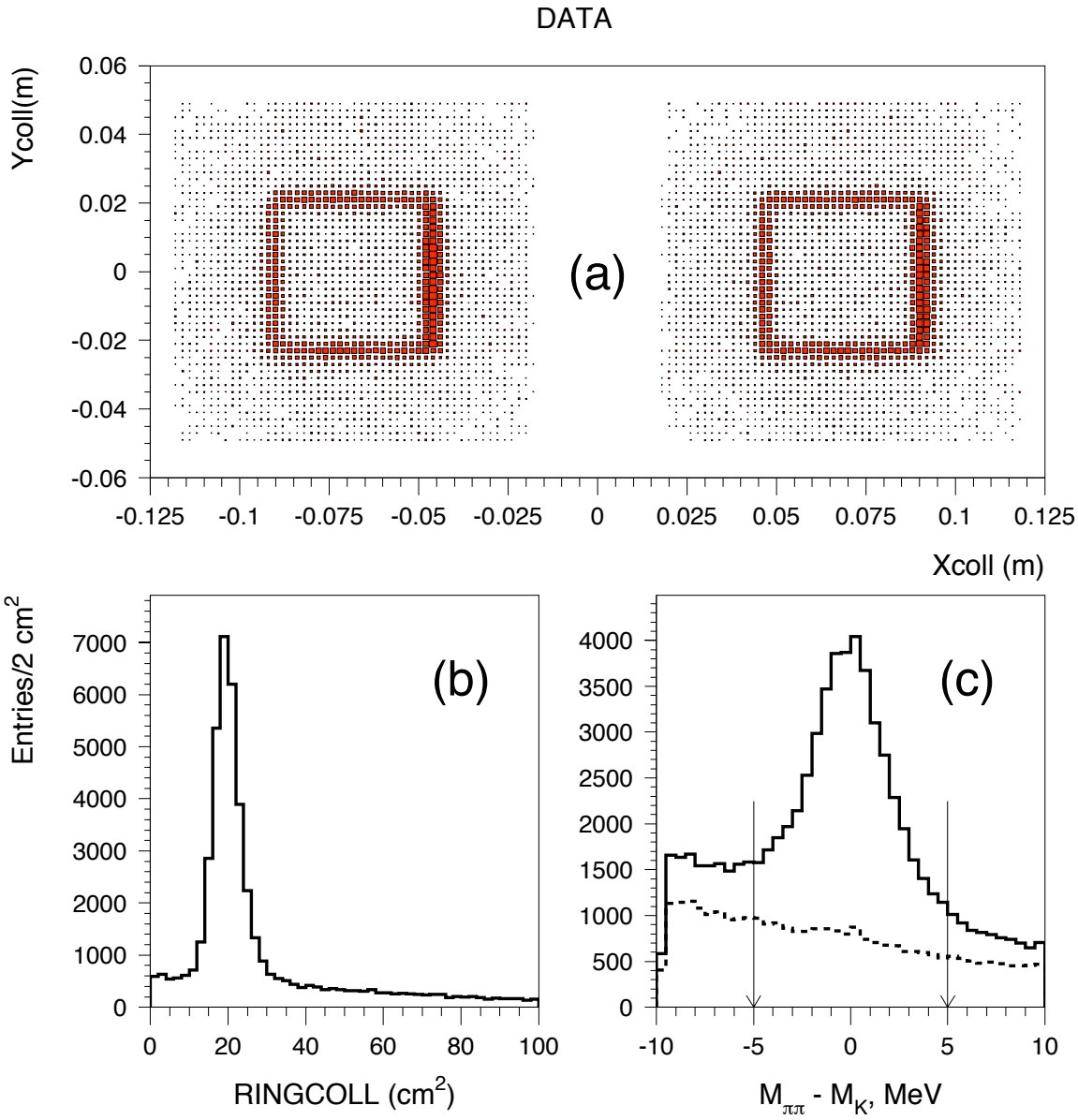

Figure 5.1: Identification of collimator scattering background using high p_T^2 $K \to \pi^+\pi^-$ decays. (a) y vs x distribution of the kaon trajectory projected to the z of the defining collimator. The square bands correspond to the edges of the defining collimators. (b) RINGCOLL variable. The collimator scattering peak is visible at 20 cm^2. (c) Reconstructed $m_{\pi^+\pi^-}$ for all events (solid) and events outside the RINGCOLL peak (dashed). Figure courtesy of R. Kessler[68].

predict the level of collimator scatters in neutral mode; this background is absolutely normalized meaning it is not scaled to the $K \to \pi^0\pi^0$ data in any way. The level of collimator scattering in the $K \to \pi^0\pi^0$ sample is ~0.1% in both beams.

5.1.2 Regenerator Scattering

Regenerator scattering is also characterized using a fit to a high p_T^2 sample of $K \to \pi^+\pi^-$ decays. To select this sample we apply nominal $K \to \pi^+\pi^-$ selection criteria with exceptions to select regenerator scatters and reduce other backgrounds. We require $p_T^2 > 1000\ \mathrm{MeV}^2/\mathrm{c}^2$. We require that the reconstructed kaon trajectory point back to the regenerator by requiring that the projected vertex position be within ± 4 cm of the center of the regenerator beam. We apply tighter veto cuts on in-time clusters in the CsI, vetoing in-time clusters that are > 10 cm from a pion shower, in-time clusters that have $\chi_\gamma^2 < 20$, and in-time clusters with energy > 5 GeV with a seed in the first ring of blocks around the beam hole.

There are a number of backgrounds to the regenerator scattering $K \to \pi^+\pi^-$ sample. Collimator scatters, $K_L \to \pi^\pm e^\mp \nu$ background, and $K_L \to \pi^\pm \mu^\mp \nu$ background are all simulated using KTeVMC. The p_T^2 distribution of each of these backgrounds is normalized to the p_T^2 distribution of the regenerator scattering sample in regions of mass and p_T^2 which enhance each background, and subtracted. Two track "junk" events from hadronic production in the regenerator Pb module are excluded by limiting the fit to events downstream of 0.2 K_S lifetimes. We avoid contamination from the p_T^2 tail of coherent $K \to \pi^+\pi^-$ decays by limiting the fit to $p_T^2 > 2000\ \mathrm{MeV}^2/\mathrm{c}^2$. At this point, the contribution from the coherent tail is less than 4%.

When a kaon scatters in the regenerator, its decay is simulated in the Monte Carlo using a function that is fit to this background subtracted regenerator scattering $K \to \pi^+\pi^-$ sample. The fit function contains several factors that depend on kaon momentum and six individual scattering terms that describe various types of kaon

scattering. The function is

$$\frac{d^3N_{regscat}}{dp_T^2 d\tau dp_K} = M(p_K) \times T(p_K) \times S(p_K) \times \sum_{j=1}^{6} A_j e^{\alpha_j p_T^2} |\hat{\rho}_j e^{\Lambda_S t} + \eta e^{\Lambda_L t}|^2. \tag{5.1}$$

M(p_K) is the Malensek K^0 and $\bar{K}^0$ energy spectrum, T(p_K) is the kaon transmission which includes the measured attenuation in the regenerator beam relative to the vacuum beam and regeneration in the upstream absorber, and S(p_K) is the absorber scatter correction. These p_K dependent factors are shown in Figure 5.2 as a function of kaon momentum. A_j, α_j, $|\hat{\rho}_j|$, and $\phi_{\hat{\rho}_j}$ are the 24 fit parameters, $\Lambda_{S,L}$ = $i m_{S,L}$ - $\frac{1}{2}\Gamma_{S,L}$, and t is the proper time of the decay. The index, j, runs over the six independent scattering terms which correspond to inelastic K_S-like scattering, scattering off lead, single carbon scattering, multiple carbon scattering, scattering off hydrogen, and inelastic K_L-like scattering. There are two additional parameters that are not explicit in Equation 5.1: the momentum dependence of the phase ($\phi_{\hat{\rho}_j}$) and p_T^2 slope (α_j) associated with diffractive scattering from the lead at the downstream edge of the regenerator. Eight of the 26 parameters in Equation 5.1 are fixed using known properties of kaon scattering. An additional 12 parameters are floated to fit the momentum dependence of $N_{regscat}$ in 10 GeV/c bins. The total number of free parameters in the fit is 30.

The α_j parameters describe the exponential p_T^2 dependence of each term in the fit. They are used to distinguish between inelastic and diffractive scattering. The K_S- and K_L-like terms have the broadest p_T^2 distribution ($\alpha^{-1} = 2.4 \times 10^5$ MeV^2/c^2) and are identified with inelastic scattering. The other four terms have much steeper p_T^2 distributions (5000 MeV^2/c^2 $< \alpha^{-1} <$ 70000 MeV^2/c^2) and are associated with diffractive scattering. In the Monte Carlo generation, events are tagged as coming from the inelastic terms or from the diffractive terms; this allows us to separate the normalization of the diffractive and inelastic contributions when we subtract backgrounds from the signal modes.

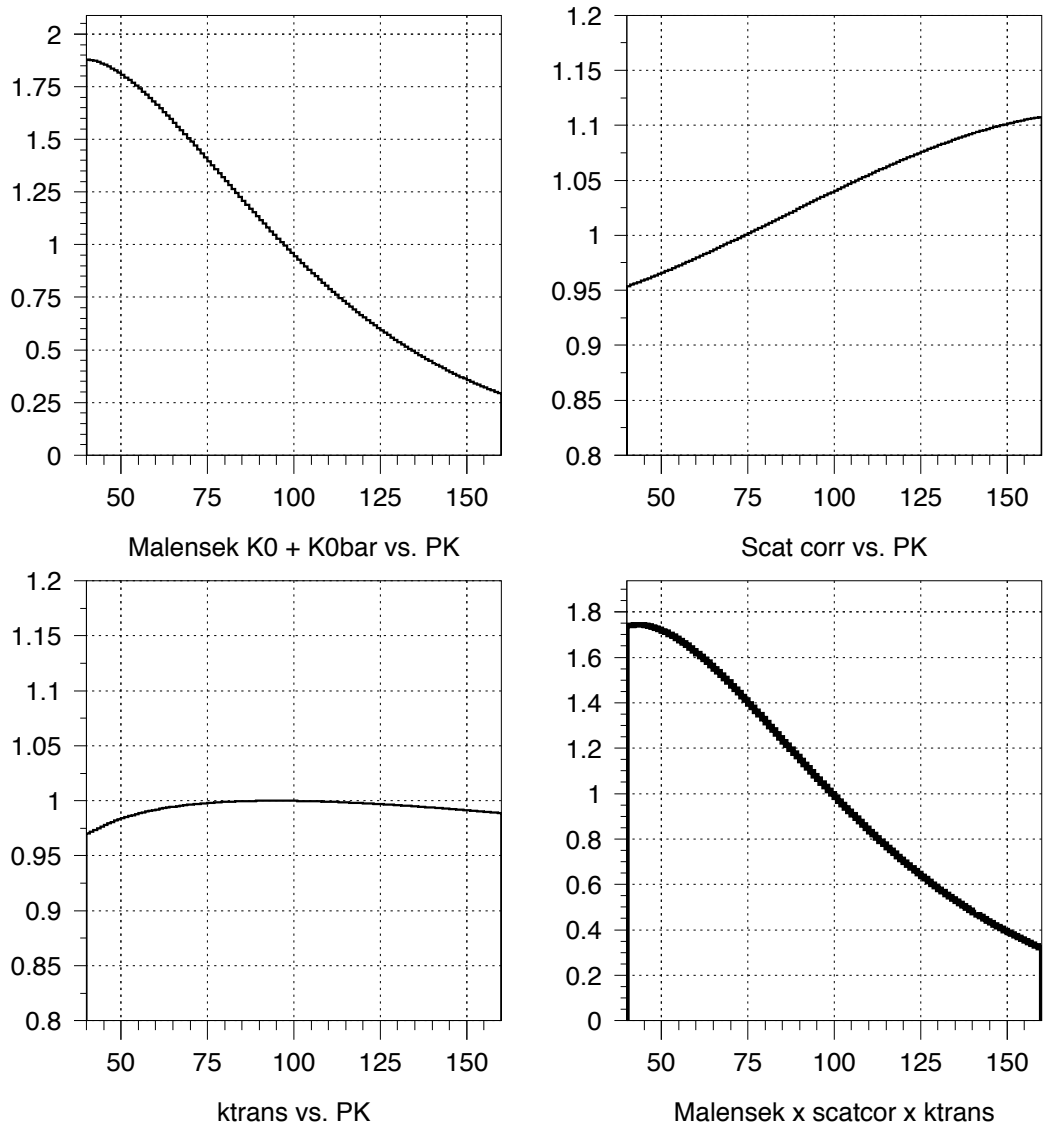

Figure 5.2: p_K dependent factors in the regenerator scattering p_T^2 fit. The bottom right plot shows the product of the three factors.

An overall kaon-momentum correction is applied to force the fit function to match the data in each p_K bin. This "fudge factor" is the ratio of regenerator scattering data to the acceptance corrected p_T^2 fit function and is applied as a polynomial function of kaon momentum. The fudge factor is shown in Figure 5.3.

The normalization of the regenerator scattering background relative to coherent $K \to \pi^+\pi^-$ data is determined by requiring that the ratio of scattered ($p_T^2 >$ 2000 MeV^2/c^2) to coherent ($p_T^2 <$ 250 MeV^2/c^2) $K \to \pi^+\pi^-$ events be the same in data and MC. Coherent data events have collimator scatters and semileptonic backgrounds removed before making this comparison. The scattering level is adjusted in the simulation so that the final background Monte Carlo is absolutely normalized. The level of regenerator scattering in the $K \to \pi^+\pi^-$ sample is ~0.07% in the regenerator beam. There is no regenerator scattering in the vacuum beam.

In the $K \to \pi^0\pi^0$ analysis, the diffractive portion of the regenerator scattering background is absolutely normalized; we subtract the amount predicted by the Monte Carlo. The level of diffractive regenerator scattering in the $K \to \pi^0\pi^0$ sample

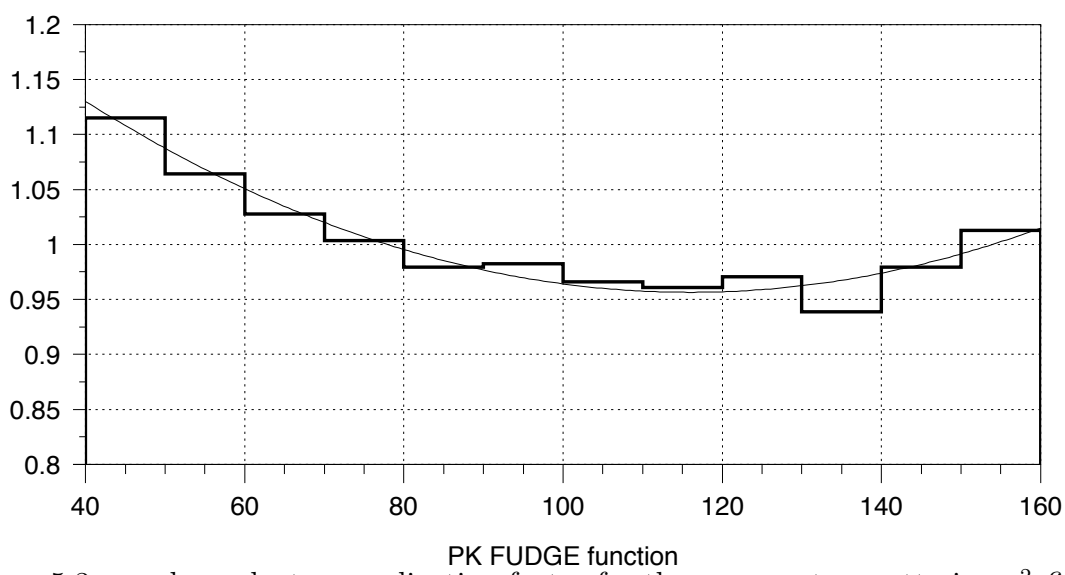

Figure 5.3: p_K dependent normalization factor for the regenerator scattering p_T^2 fit.

is ∼0.13% in the vacuum beam and ∼0.9% in the regenerator beam. The inelastic portion of the background is floated to match the 300 cm^2 < RING < 800 cm^2 tail in the RING distribution between data and MC after subtracting all other backgrounds from the data. This is necessary because of the differing veto requirements between the charged and neutral analyses; we find that the neutral mode veto requirements suppress the inelastic scattering component by 16% relative to the charged mode in 1997 data. Figure 5.4 shows the RING distributions for $K \to \pi^0\pi^0$ data with all other backgrounds subtracted and inelastic regenerator scattering MC in the regenerator beam after normalization of the background. We use only data downstream of the regenerator (z > 125.0 m) to find the normalization in each beam. The level of inelastic regenerator scattering in the $K \to \pi^0\pi^0$ sample is ∼0.13% in the vacuum beam and ∼0.18% in the regenerator beam.

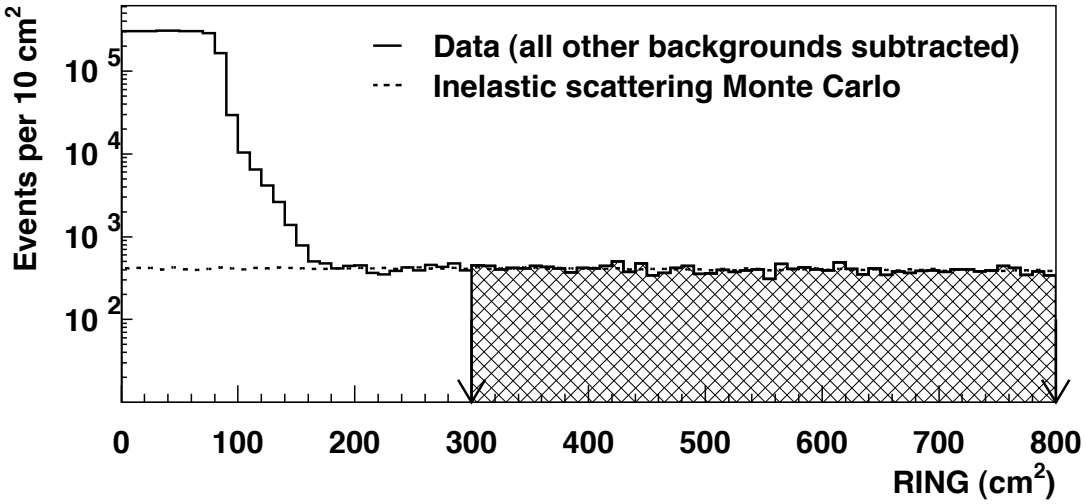

Figure 5.4: RING distributions for $K \to \pi^0\pi^0$ data and inelastic regenerator scattering MC in the regenerator beam after normalization. The data distribution has all other backgrounds subtracted. The hatched region shows the area in which the normalization is performed.

5.2 Non-$\pi\pi$ Background

5.2.1 Backgrounds to $K \to \pi^+\pi^-$ Decays

The non-$\pi\pi$ backgrounds to $K \to \pi^+\pi^-$ are the semileptonic decays $K_L \to \pi^\pm e^\mp \nu$ and $K_L \to \pi^\pm \mu^\mp \nu$. The electron from a K_{e3} decay can "fake" a pion by depositing less than 85% of its energy in the CsI calorimeter. The tail on the electron E/p distribution extends down to E/p of 50%, so this will happen some fraction of the time. A muon from a $K_{\mu 3}$ decay can fake a pion if it fails to fire the muon veto detectors. The muon vetos are extremely efficient and the minimum pion energy cut should be high enough that the muons pass through the filter steel, but there are scattering processes that allow an 8 GeV muon to range out before reaching the muon veto detectors.

The K_{e3} and $K_{\mu 3}$ backgrounds are normalized to the data in p_T^2 and $\mathrm{m}_{\pi^+\pi^-}$ sidebands using data samples with cuts which enhance each background sample. The procedure is the same as the one for collimator scatters; the efficiency of the enhancement cuts is applied to the normalization factor to predict the level of background in the coherent $K \to \pi^+\pi^-$ sample and the normalization is done in 10 GeV energy bins. To enhance $K_L \to \pi^\pm e^\mp \nu$ background we require the maximum E/p > 0.75 and we require both particles to shower in the calorimeter. To enhance the $K_L \to \pi^\pm \mu^\mp \nu$ background we require both particles to be minimum ionizing in the calorimeter. Figure 5.5 shows the mass and p_T^2 sidebands used to perform the normalization.

There is a small background due to hadronic production in the regenerator. We consider hadronic production of K* and Δ resonances via K_L + N $\to$ $K_S{}^*$ + x and n + N $\to$ Δ + X. For $K_S{}^*$ decays both the $K_S{}^* \to \mathrm{K}^\pm\pi^\mp$ and the $K_S{}^* \to \pi^0 K_S$, $K_S \to \pi^+\pi^-$ decay modes are simulated. The $K_S{}^* \to \pi^0 K_S$ background is normalized using the p_T^2 sideband in the regenerator beam. The $K_S{}^* \to \mathrm{K}^\pm\pi^\mp$ and $\Delta \to \mathrm{p}^\pm\pi^\mp$ backgrounds are normalized using mass sidebands in the regenerator beam using events with a z vertex at the regenerator edge. The two modes are separated using the asymmetry of the momentum distribution of the decay products.

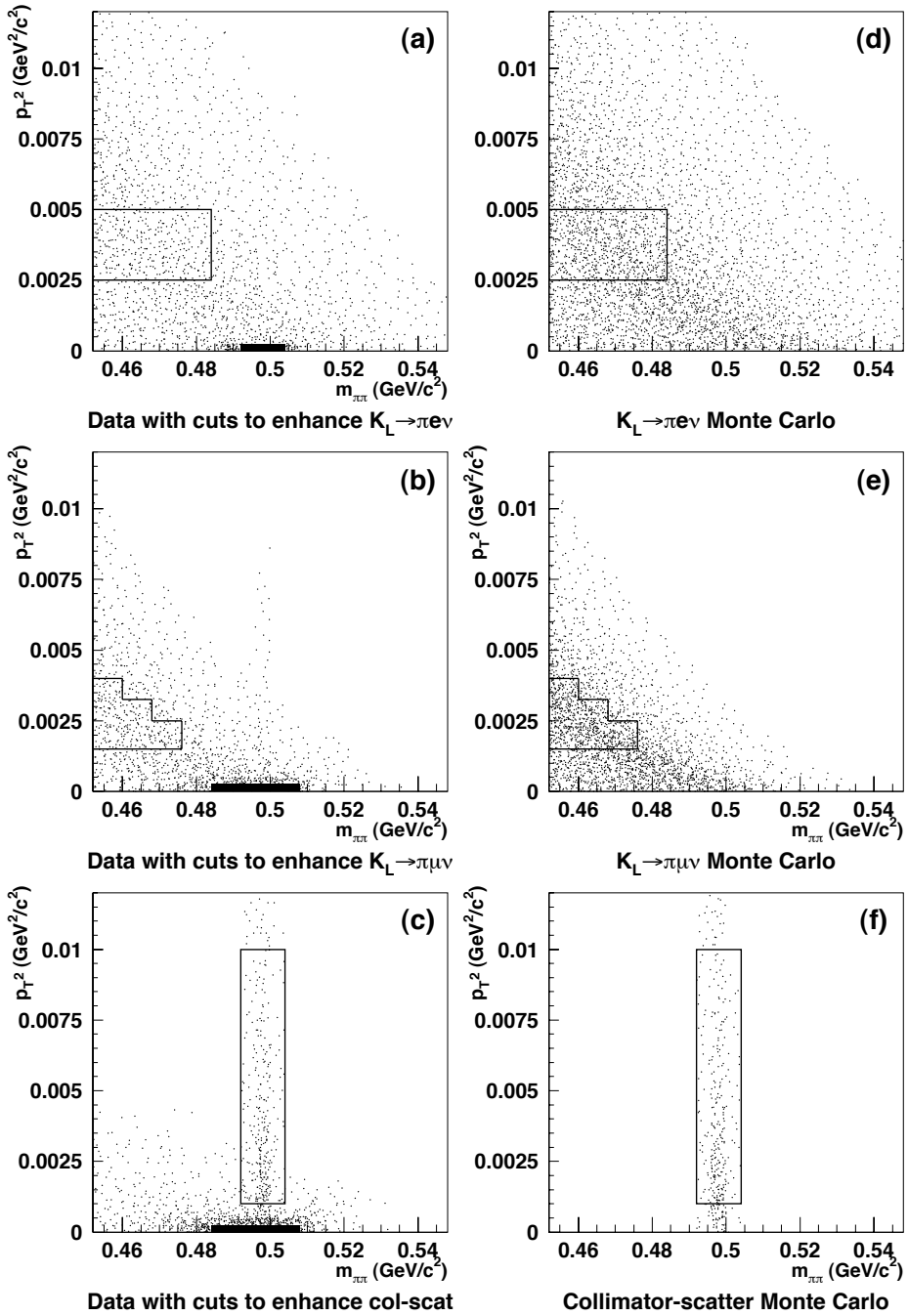

Figure 5.5: Distributions used to normalize the background contributions in the vacuum beam $\pi^+\pi^-$ sample. Panels (a), (b), and (c) show the distributions of p_T^2 vs. $m_{\pi^+\pi^-}$ for the data with extra cuts to enhance $K_L \to \pi^\pm e^\mp \nu$, $K_L \to \pi^\pm \mu^\mp \nu$, and collimator scatter events respectively. Panels (d), (e), and (f) show the same distributions for the Monte Carlo predictions of these backgrounds. The outlined regions show the sideband areas used to normalize the Monte Carlo prediction to data. Figure courtesy of J. Graham[2].

The level of hadronic production background in the $K \to \pi^+\pi^-$ sample is less than 0.001% and is not subtracted.

5.2.2 Backgrounds to $K \to \pi^0\pi^0$ Decays

The main source of background to the $K \to \pi^0\pi^0$ signal mode is $K_L \to \pi^0\pi^0\pi^0$ decays in which two photons escape the detector or merge with the remaining photons in the calorimeter. $K_L \to \pi^0\pi^0\pi^0$ decays are simulated using KTeVMC and are normalized to data using sidebands in the $\pi^0\pi^0$ invariant mass distribution. Though mispairings (events in which the photons are incorrectly paired by the reconstruction) are present in both data and Monte Carlo and not treated as background for the $K \to \pi^0\pi^0$ analysis, we must remove mispaired events from the invariant mass distribution in data before using the mass sidebands to normalize the $3\pi^0$ background. The level of the mispairing background is measured in Monte Carlo using generated quantities to select events in which we have chosen the wrong pairing. The fraction of events with mispaired photons is 0.007%. Figure 5.6 shows the $K \to \pi^0\pi^0$ invariant mass distributions for data with mispairings subtracted and $K_L \to \pi^0\pi^0\pi^0$ MC in the vacuum beam after normalization of the background. The sideband regions used for normalization (460 MeV/c^2 $< \mathrm{m}_{\pi^0\pi^0} <$ 480 MeV/c^2 and 520 MeV/c^2 $< \mathrm{m}_{\pi^0\pi^0} <$ 540 MeV/c^2) are indicated on the plot. We use only events with reconstructed z vertices in the range 140 m $< z <$ 158 m to normalize the $3\pi^0$ background because we need to be well away from regenerator backgrounds. For this reason, it is particularly important that our simulation of the z vertex distribution in the $K_L \to \pi^0\pi^0\pi^0$ background be accurate. Figure 5.7 shows the z vertex distributions for data and $3\pi^0$ background MC in the mass sidebands used for normalization. The level of $K_L \to \pi^0\pi^0\pi^0$ background to $K \to \pi^0\pi^0$ signal is 0.2%-0.4% in the vacuum beam and ∼0.1% in the regenerator beam. The variation in background level is due to varying veto requirements among the three data samples.

Background due to hadronic production in the regenerator lead module is simulated by KTeVMC and normalized to data using sidebands in the $\pi^0\pi^0$ invariant

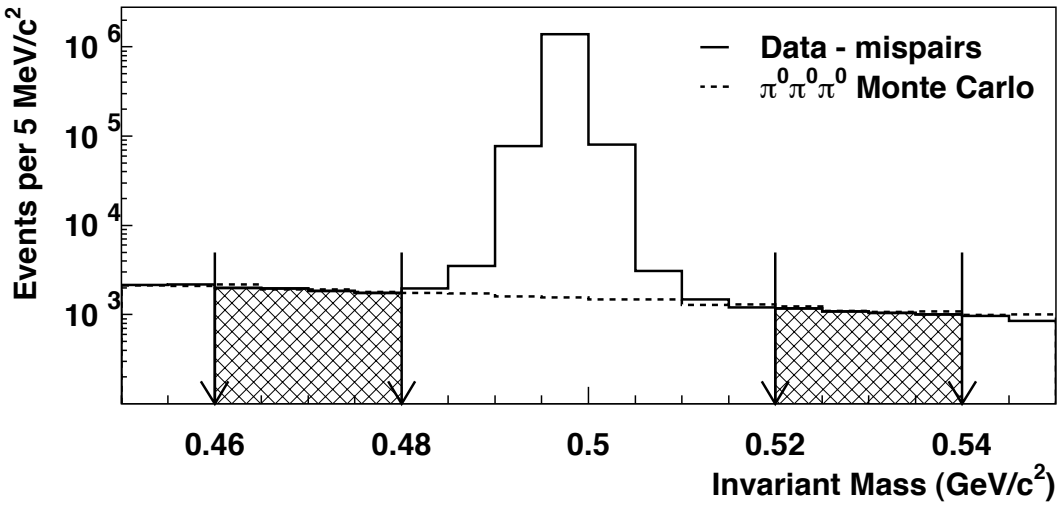

Figure 5.6: Invariant mass distributions for $K \to \pi^0\pi^0$ data and $3\pi^0$ background MC in the vacuum beam after normalization. The data distribution has mispairings subtracted. The hatched regions show the areas used for normalization.

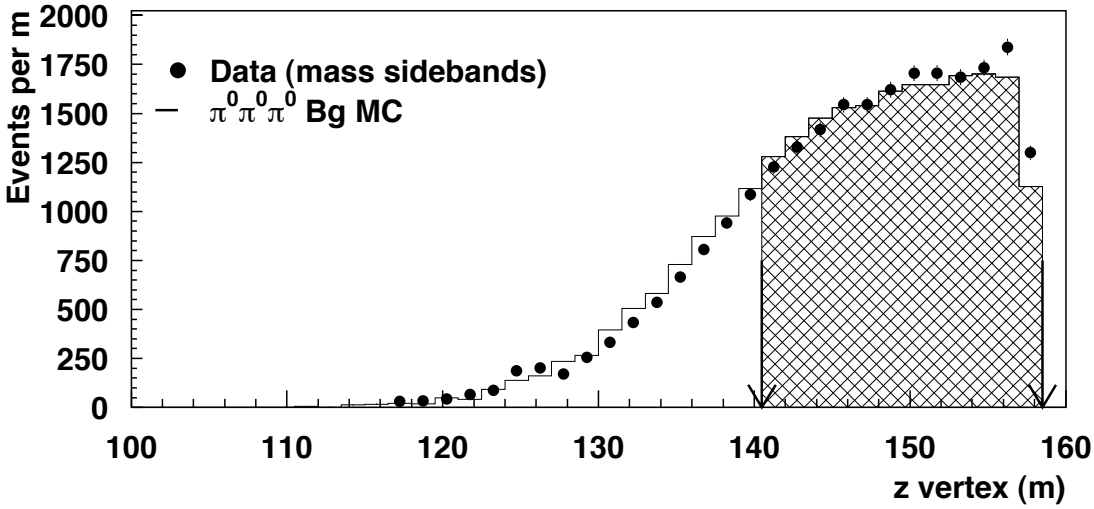

Figure 5.7: z vertex distributions for mass sidebands in $K \to \pi^0\pi^0$ data and $K_L \to \pi^0\pi^0\pi^0$ background MC. The hatched region shows the area used for normalization.

mass distribution. The mass sidebands are the same as those used for the $3\pi^0$ background normalization. We use events with a reconstructed z vertex in the range 125 m $< z <$ 130 m. Before normalizing the background we subtract mispairs and $3\pi^0$ background from the data distribution. The level of background to the $K \to \pi^0\pi^0$ signal from hadronic production in the regenerator is 0.001% in the vacuum beam and 0.007% in the regenerator beam. We also consider the possibility of backgrounds due to $K_L \to \pi^0\gamma\gamma$ and $\Xi^0 \to \Lambda\pi^0$, $\Lambda \to \mathrm{n}\pi^0$. These backgrounds are extremely small and are ignored.

5.3 Updates Since 2003

The background prediction and subtraction procedure is largely unchanged from the previous analysis[50]. There are, however, several improvements to the determination of the $K \to \pi^+\pi^-$ background. The K_{e3} and $K_{\mu3}$ components of the background are now normalized separately using information from the CsI calorimeter to separate the samples. For the $K_{\mu3}$ background, the momentum dependent probability of a muon firing the muon vetos is determined in data and explicitly included in the background determination. Additional backgrounds due to hadronic production of K^* and Δ resonances in the regenerator beam are now considered.

5.4 Summary of Background Levels and Event Yields

The total background level is ∼0.1% for $K \to \pi^+\pi^-$ and ∼1% for $K \to \pi^0\pi^0$.

The largest sources of background to the $K \to \pi^+\pi^-$ mode are the semileptonic decays in the vacuum beam and regenerator scattering in the regenerator beam. Figures 5.8 and 5.9 show the p_T^2 and $\mathrm{m}_{\pi^+\pi^-}$ distributions for $K \to \pi^+\pi^-$ data and all backgrounds. Table 5.1 contains a summary of the background fractions for the 1997 and 1999 $K \to \pi^+\pi^-$ samples. Table 5.2 contains the final number of events in the $K \to \pi^+\pi^-$ samples after background subtraction.

The largest sources of background to the $K \to \pi^0\pi^0$ mode are $K_L \to \pi^0\pi^0\pi^0$ decays in the vacuum beam and regenerator diffractive scattering in the regenerator

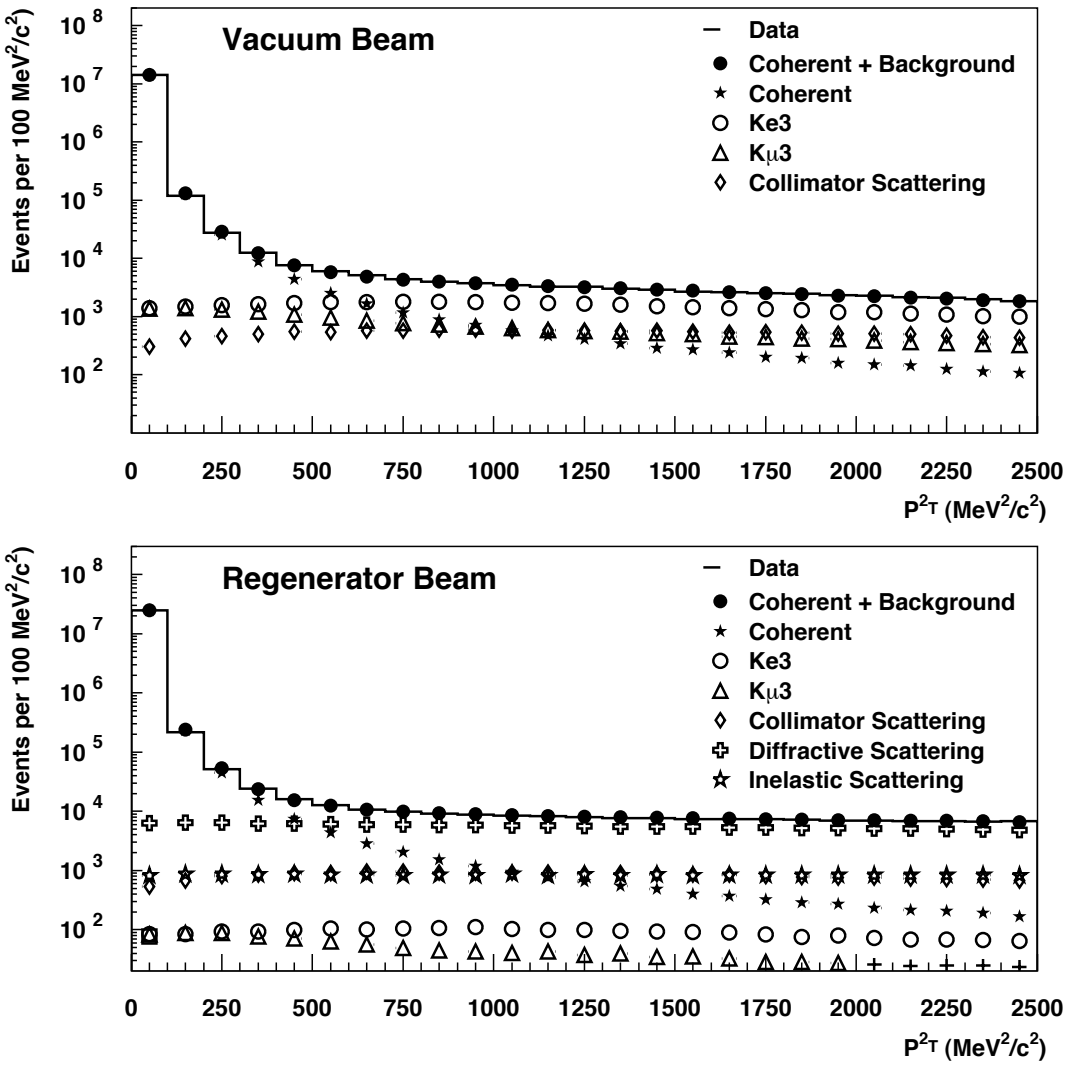

Figure 5.8: p_T^2 distributions for $K \to \pi^+\pi^-$ and all backgrounds.

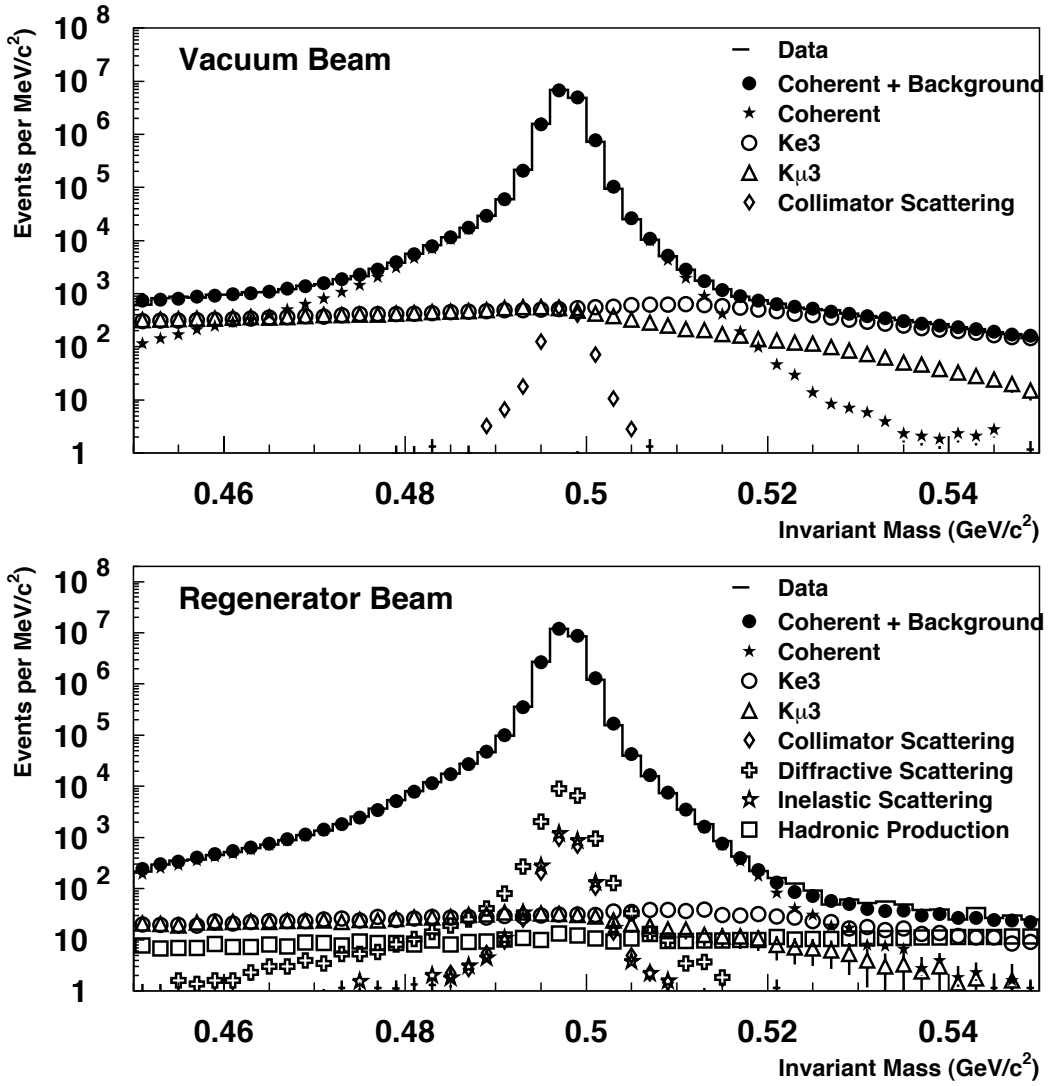

Figure 5.9: Invariant mass distributions for $K \to \pi^+\pi^-$ and all backgrounds.

Source	Vacuum Beam 1997	Vacuum Beam 1999	Regenerator Beam 1997	Regenerator Beam 1999
Regenerator Scattering	—	—	0.073%	0.075%
Collimator Scattering	0.009%	0.008%	0.009%	0.008%
$K_L \to \pi^{\pm} e^{\mp} \nu$	0.032%	0.032%	0.001%	0.001%
$K_L \to \pi^{\pm} \mu^{\mp} \nu$	0.034%	0.030%	0.001%	0.001%
Total Background	0.074%	0.070%	0.083%	0.085%

Table 5.1: Summary of $K \to \pi^+\pi^-$ background levels

Year	Vacuum Beam	Regenerator Beam
1997	10668660	18578930
1999	14438581	25095278
Total	25107242	43674208

Table 5.2: $\pi^+\pi^-$ event yields after background subtraction

beam. Figures 5.10 and 5.11 show the RING and $m_{\pi^0\pi^0}$ distributions for $K \to \pi^0\pi^0$ data and all backgrounds. Table 5.3 contains a summary of the background fractions for the 1996, 1997, and 1999 $K \to \pi^0\pi^0$ samples. The variation in the level of $K_L \to \pi^0\pi^0\pi^0$ background among the years for neutral mode is due to the varying trigger thresholds and veto cuts. Table 5.4 contains the final number of events in the $K \to \pi^0\pi^0$ samples after background subtraction.

Source	Vacuum Beam 1996	Vacuum Beam 1997	Vacuum Beam 1999	Regenerator Beam 1996	Regenerator Beam 1997	Regenerator Beam 1999
Inelastic Scattering	0.153%	0.132%	0.128%	0.214%	0.186%	0.175%
Diffractive Scattering	0.135%	0.128%	0.130%	0.893%	0.906%	0.906%
Collimator Scattering	0.102%	0.122%	0.120%	0.081%	0.093%	0.091%
$K_L \to \pi^0\pi^0\pi^0$	0.444%	0.220%	0.301%	0.015%	0.006%	0.012%
Photon Mispairing	0.007%	0.007%	0.008%	0.007%	0.008%	0.007%
Hadronic Production	0.002%	0.001%	—	0.007%	0.007%	0.007%
Total Background	0.835%	0.603%	0.678%	1.209%	1.197%	1.190%

Table 5.3: Summary of $K \to \pi^0\pi^0$ background levels. Note that photon mispairing is not subtracted from the data and is not included in the total background sum.

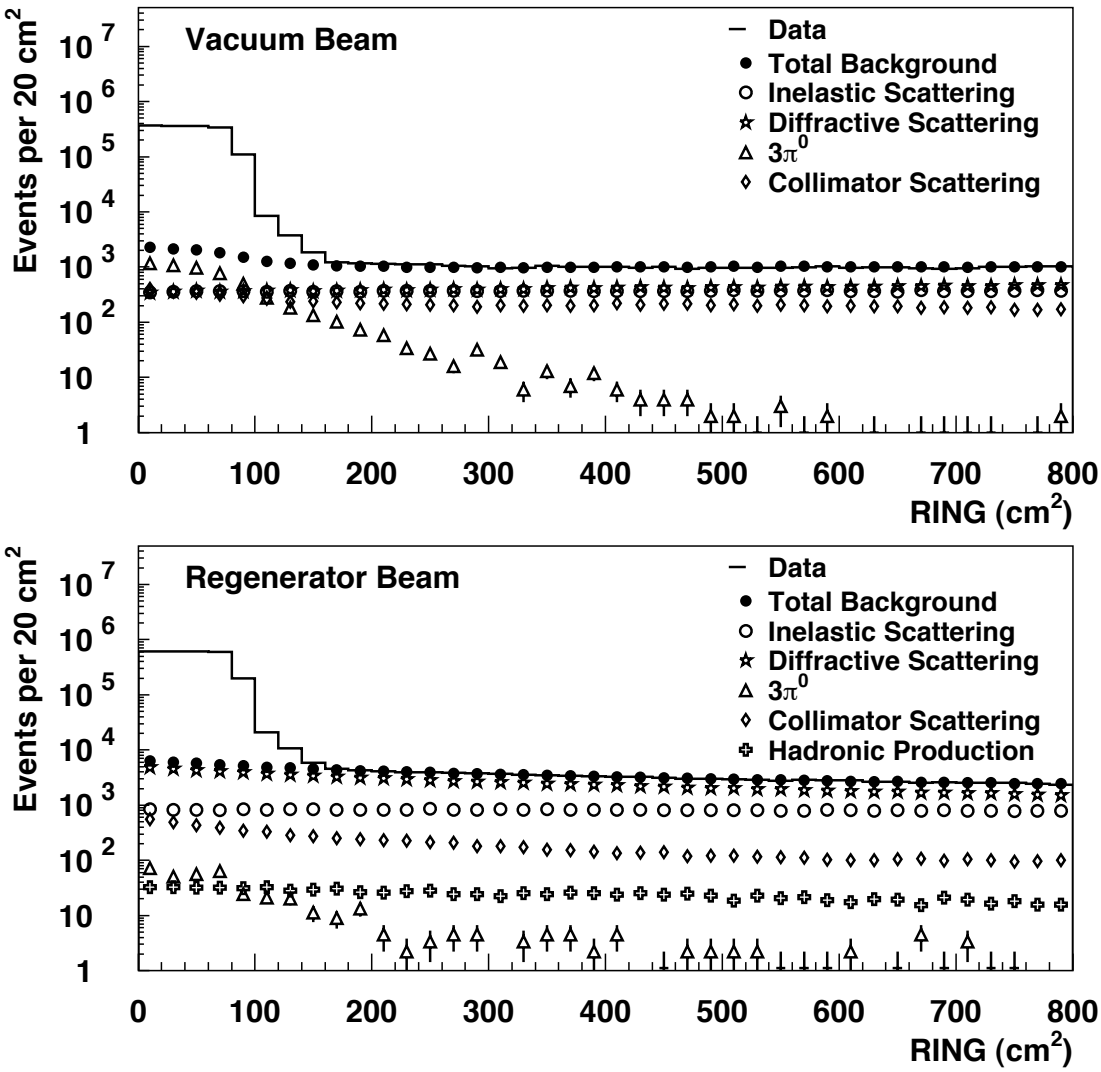

Figure 5.10: RING distributions for $K \to \pi^0\pi^0$ and all backgrounds.

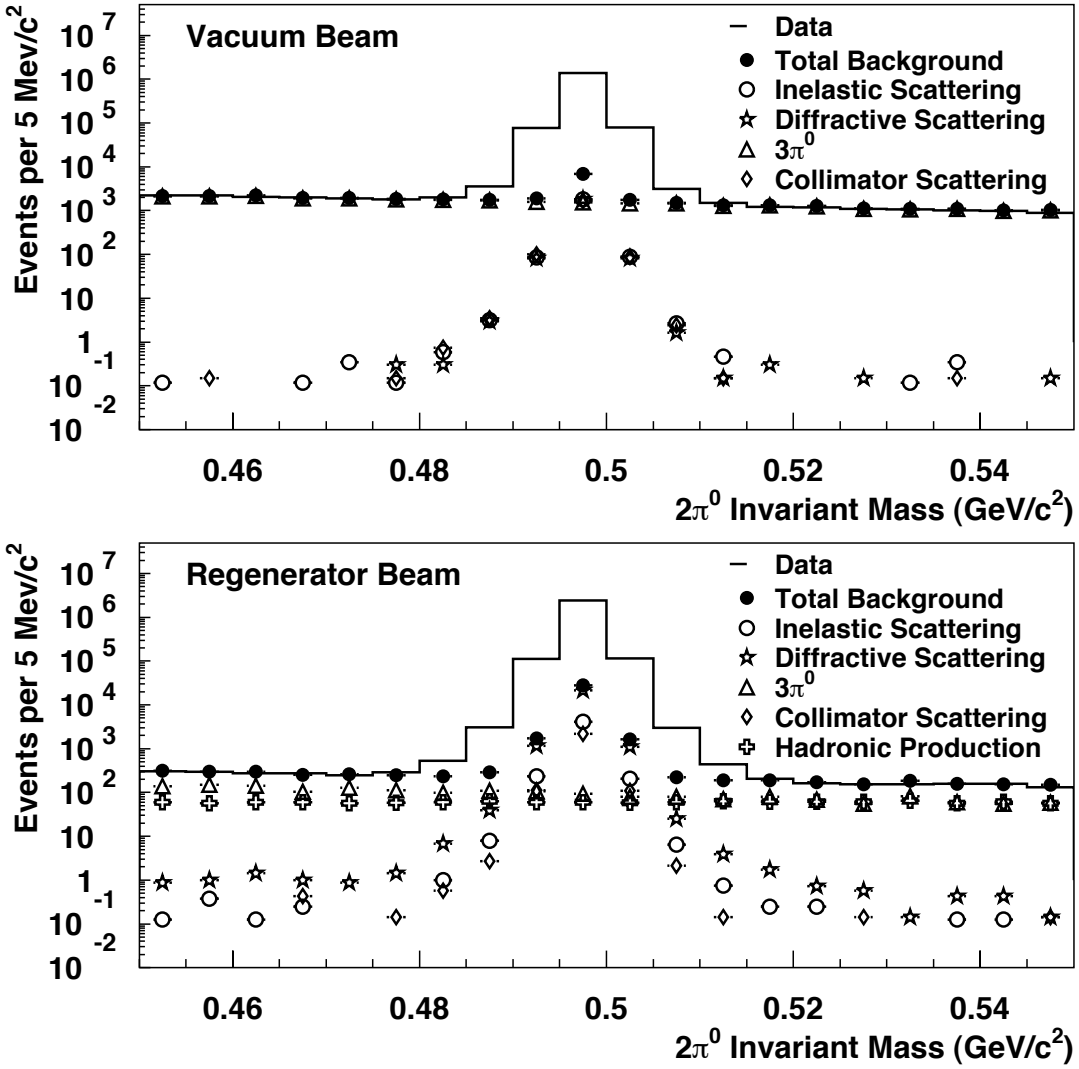

Figure 5.11: Invariant mass distributions for $K \to \pi^0\pi^0$ and all backgrounds.

Year	Vacuum Beam	Regenerator Beam
1996	765746	1306122
1997	2137983	3646166
1999	3064469	5227887
Total	5968198	10180175

Table 5.4: $\pi^0\pi^0$ event yields after background subtraction

CHAPTER 6
EXTRACTING PHYSICS PARAMETERS

We measure $Re(\epsilon'/\epsilon)$, Δm, τ_S, ϕ_{+-}, and $\Delta\phi$ using the background subtracted event samples and the Monte Carlo simulation described in the preceding chapters. We use the Monte Carlo simulation to correct for detector acceptance and a fitting program to extract the physics parameters. The fits for the different physics parameters are binned differently, have different free parameters, and make different assumptions about CPT symmetry.

6.1 Acceptance Correction

The very different K_L and K_S lifetimes lead to very different z vertex distributions in the vacuum and regenerator beams. This causes a difference between the average acceptance for decays in the two beams. We use the Monte Carlo to determine the acceptance separately for $K \to \pi^+\pi^-$ and $K \to \pi^0\pi^0$ decays in the vacuum and regenerator beams. We perform the acceptance correction in bins of momentum and z vertex. Using small acceptance bins decreases our sensitivity to mismatches between data and MC in the overall p_K and z_K distributions; the important factor is that the data/MC ratio does not vary greatly within an acceptance bin. The acceptance is measured in 2 GeV/c bins in p_K in both beams. In the regenerator beam we use 2 m acceptance bins because the z vertex distribution is dependent upon the kaon sector parameters and is therefore affected by the parameters which are used as inputs to the MC simulation. In the vacuum beam we use one 48 m acceptance bin since the decay vertex distribution does not depend on the kaon parameters for which we are fitting. The acceptance is simply defined as the ratio of the number of reconstructed MC events to the number of generated MC events

in each acceptance bin. Figure 6.1 shows the acceptance as a function of z for the whole momentum range 40 GeV/c $<$ p_K $<$ 160 GeV/c.

The acceptance correction shifts the measured value of $Re(\epsilon'/\epsilon)$ by $\sim 85\times10^{-4}$ relative to a naive double ratio of event yields. Of this, about 85% of the correction is due to the geometry of the detector and the remaining correction comes from the details of the detector response and resolution.

6.2 The Fitter

For pure K_L and K_S beams, the event yields and acceptances would be sufficient to determine $Re(\epsilon'/\epsilon)$. However, the regenerator beam contains a coherent K_S-K_L mixture and there is a target-K_S component in both beams. A fitting program is required to properly treat the interference effects between K_L and K_S. The fitter uses a simulation similar to KTeVMC to calculate kaon decay distributions using the kaon sector parameters and a regeneration model. The Monte Carlo acceptance is used to scale these distributions to produce a "prediction function" for the number

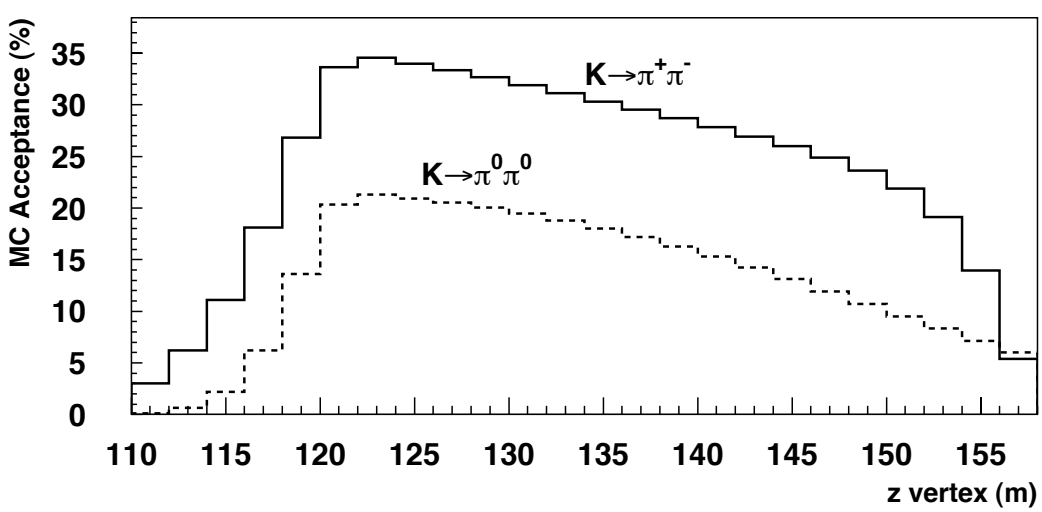

Figure 6.1: MC acceptance as a function of z vertex for $K \to \pi^+\pi^-$ and $K \to \pi^0\pi^0$.

of events expected in each (p_K,z) bin. The prediction function is compared to the number of observed events and the floated parameters are varied to minimize the χ^2 of this comparison.

As discussed above, the acceptance is calculated in small p_K and z bins. The prediction function is also calculated in p_K and z bins; the binning depends on which fit is being performed. For $Re(\epsilon'/\epsilon)$ we are ultimately measuring numbers of events, so we perform the fit in a single z bin. For the measurement of Δm, τ_S, ϕ_{+-}, and $\Delta\phi$ we are measuring the shape of the decay distribution in the regenerator beam, so the fit is binned in z. All fits are performed in twelve 10 GeV/c momentum bins in both beams and in a single z bin in the vacuum beam.

The prediction function includes a full propagation of the kaon state from the target up to the decay point; it is similar to the simulation in the Monte Carlo (see Chapter 4). The decay region begins with the effective regenerator edge to account for decays inside the regenerator. The calculation depends on kaon parameters such as Δm and τ_S which may be fixed or floated in the fit. The prediction function includes the effects of the target-K_S component in the beam; these effects are not included in the following discussion.

For a pure K_L beam, the number of $K \to \pi\pi$ decays is

$$N^{\pi\pi}_{p,z} \propto \mathcal{F}(p)|\eta|^2 e^{-t/\tau_L}, \tag{6.1}$$

where t = m_K(z-z_{reg})/p is the measured proper time relative to the regenerator edge, $\eta = \eta_{+-}$ or η_{00} for charged or neutral decays, $\mathcal{F}$(p) is the kaon flux, and τ_L is the K_L lifetime. The decay distribution in the vacuum beam is determined by τ_L and the total event yield is proportional to $|\eta|^2$ and the kaon flux.

For a pure K_L beam incident on the KTeV regenerator, the number of $K \to \pi\pi$ decays downstream of the regenerator is

$$N^{\pi\pi}_{p,z} \propto \mathcal{F}_R(p)T_{reg}(p)\ \left[|\rho(p)|^2 e^{-t/\tau_S} + |\eta|^2 e^{-t/\tau_L} + 2|\rho||\eta|cos(\Delta m t + \phi_\rho - \phi_\eta)e^{-t/\tau_{avg}}\right], \tag{6.2}$$

where $\phi_\eta = \arg(\eta)$, $|\rho|$ and ϕ_ρ are the magnitude and phase of the coherent regeneration amplitude, $1/\tau_{avg} \equiv (1/\tau_S + 1/\tau_L)/2$, $\mathcal{F}_R$(p) is the kaon flux upstream of the regenerator, and T_{reg}(p) is the kaon flux transmission through the regenerator. Figure 6.2 shows the effect of the interference term on the decay vertex distribution in the regenerator beam.

In those fits that assume CPT symmetry, we force ϕ_{+-} and ϕ_{00} to be equal to the superweak phase:

$$\phi_\eta = \phi_{SW} = tan^{-1}(2\Delta m/\Delta\Gamma). \tag{6.3}$$

The PDG[51] value for ϕ_{SW} is $(43.51 \pm 0.05)^\circ$. We test CPT symmetry by allowing ϕ_η to float in some fits.

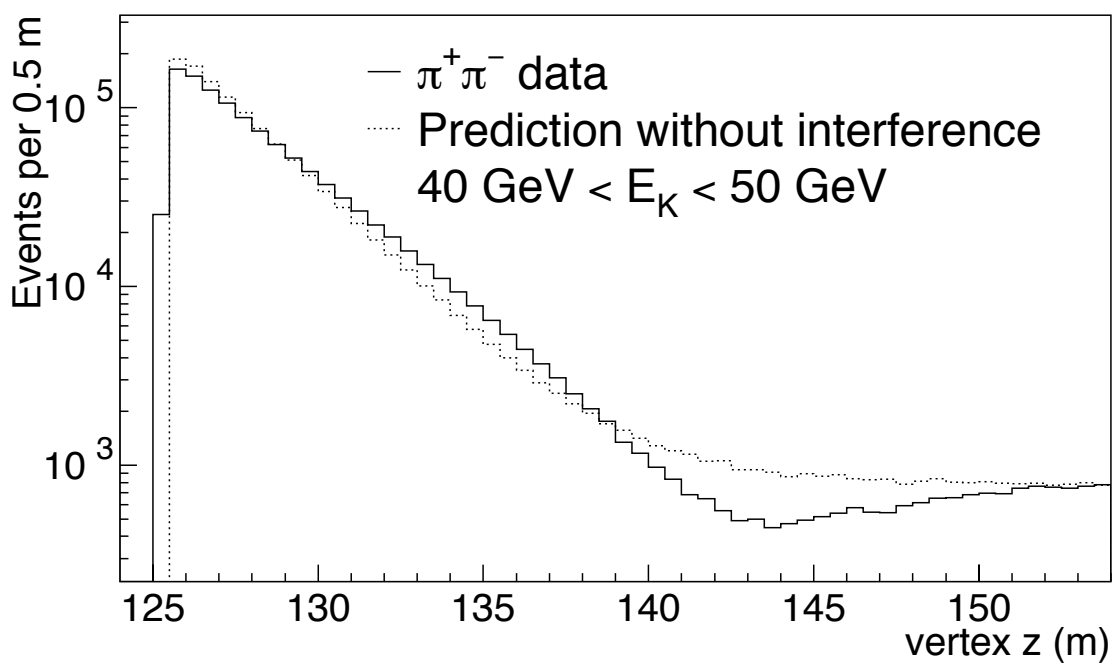

Figure 6.2: K_L-K_S interference downstream of the regenerator. $K \to \pi^+\pi^-$ data and MC z decay distributions downstream of the regenerator are plotted. The dashed histogram is MC without the interference term that is proportional to $2|\rho||\eta|$ in Equation 6.2.

The average vacuum to regenerator kaon flux ratio ($\mathcal{F}/\mathcal{F}_R$) and the average regenerator transmission (T_{reg}) cancel in the $Re(\epsilon'/\epsilon)$ fit but we need to know the momentum dependence of ($\mathcal{F}/\mathcal{F}_R\mathrm{T}_{reg}$). We measure this quantity using the vacuum to regenerator ratio of $K_L \to \pi^+\pi^-\pi^0$ decays. We find that the ratio is 7.8% at the average kaon momentum of 61.5 GeV and has a momentum slope of (-3.47 $\pm$ 0.16)$\times$ 10^{-5}(GeV/c)$^{-1}$ between 40 and 160 GeV/c. This variation is mostly due to the momentum variation of the regenerator transmission.

The regeneration amplitude is related to the difference between the forward kaon-nucleon scattering amplitudes for K^0 and $\bar{K}^0$.

$$\rho = i\pi N L f_- g(L) \tag{6.4}$$

where

$$f_- \equiv \hbar \frac{f(0) - \bar{f}(0)}{\mathrm{p}}, \tag{6.5}$$

N is the number density of nuclei, L is the length of the regenerator, g(L) is a geometric correction for the time evolution of regenerated K_S relative to K_L as they travel through the regenerator, and f(0) and $\bar{f}(0)$ are the forward scattering amplitudes for K^0 and $\bar{K}^0$ respectively.

Regge theory[69] predicts that the magnitude of f_- should vary with kaon momentum as a power law for an isoscalar target and kaon momenta in the KTeV energy range. We express this dependence with respect to the average kaon momentum in KTeV, 70 GeV/c:

$$|f_-(p)| = |f_-(70\ \mathrm{GeV}/c)| \left(\frac{\mathrm{p}}{70\ \mathrm{GeV/c}}\right)^{\alpha}. \tag{6.6}$$

We allow the values of $|f_-(70\ \mathrm{GeV}/c)|$ and α for plastic scintillator (the material making up the bulk of the regenerator) to float in the fitter. We use fixed values of $|f_-(70\ \mathrm{GeV}/c)|$ and α for the lead at the end of the regenerator and the beryllium and lead in the absorbers. Figure 6.3 shows a power law fit to $|f_-(\mathrm{p})|$ using KTeV $K \to \pi^+\pi^-$ data.

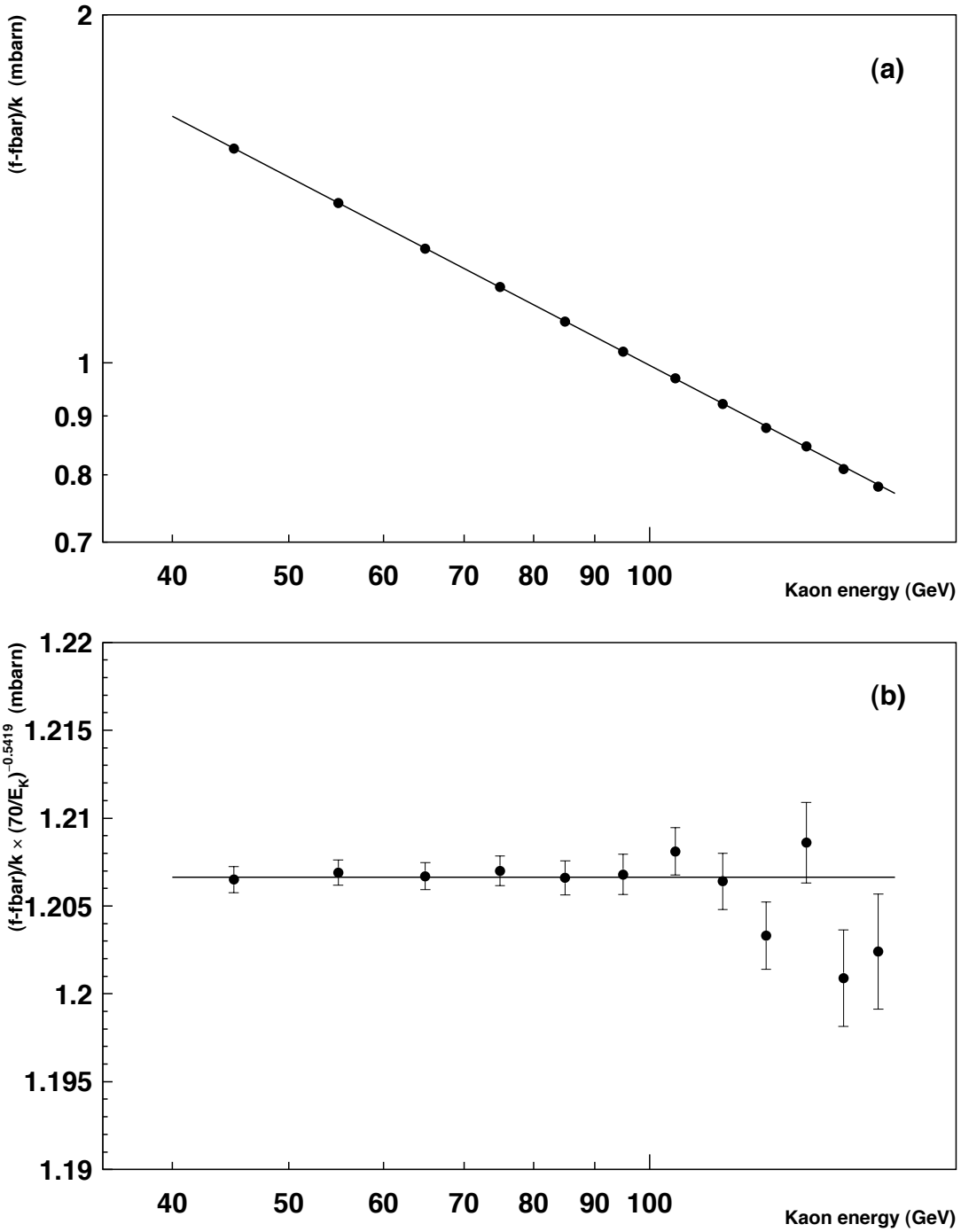

Figure 6.3: Power law fit to f_- using KTeV $K \to \pi^+\pi^-$ data. Figure courtesy of J. Graham[2].

The complex phase of f_- can be determined from its momentum dependence through an integral dispersion relation, with the requirement that the forward scattering amplitudes be analytic functions. For a pure power law momentum dependence, this analyticity requirement yields a constant phase:

$$\phi_f = -\frac{\pi}{2}(2+\alpha). \tag{6.7}$$

We must correct the regeneration amplitude described by the power law because of nuclear screening effects in the regenerator. The correction affects both the power law and the phase. The correction maps the pure power law described above to a phenomenological variable related to the momentum dependence of Regge ω exchange. The screening correction results in a 10% correction to α; most of the screening effect comes from elastic screening.

The number of events in each (p,z) bin calculated using Equations 6.1 and 6.2, is corrected for acceptance to determine the number of predicted events in each bin. The number of predicted events, $\mathrm{P}^{\pi\pi}_{p,z}$, is compared to the number of data events in each fit bit bin using a χ^2:

$$\chi^2 = \sum_i \frac{(N_i - P_i)^2}{\sigma^2_{N_i} + \sigma^2_{P_i}}, \tag{6.8}$$

where N_i is the number of data events and P_i is the number of predicted events. The χ^2 is minimized using MINUIT[70] with the entire process of kaon propagation, acceptance correction, and χ^2 calculation iterated until a minimum χ^2 is found.

6.3 Fits

6.3.1 $Re(\epsilon'/\epsilon)$ Fit

The $Re(\epsilon'/\epsilon)$ fit has 48 measured inputs: the observed numbers of $K \to \pi^+\pi^-$ and $K \to \pi^0\pi^0$ decays in each beam, binned in twelve 10 GeV/c momentum bins. The fit is not binned in z; each momentum bin contains the entire yield from z = 110-158 m. The free parameters in the fit are the kaon fluxes for $K \to \pi^+\pi^-$ and $K \to \pi^0\pi^0$ in each momentum bin, the regeneration parameters $|f_-(70\ \mathrm{GeV}/c)|$ and α, and

$Re(\epsilon'/\epsilon)$. We assume CPT by forcing the the phases ϕ_{+-} and ϕ_{00} to be equal to the superweak phase. The values of Δm and τ_S are fixed to $\Delta m = 5262.0 \times 10^6\ \hbar s^{-1}$ and $\tau_S = 89.645 \times 10^{-12}$ s. The fit has 21 degrees of freedom. For the full dataset, we find

$$\begin{aligned} Re(\epsilon'/\epsilon) &= (18.87 \pm 1.14) \times 10^{-4} \\ |f_-(70\ \mathrm{GeV}/c)| &= (1.1779 \pm 0.0002)\ \mathrm{mbarns} \\ \alpha &= -0.5381 \pm 0.0005 \\ \chi^2/\mathrm{dof} &= 22.9/21, \end{aligned} \tag{6.9}$$

where the errors reflect the statistical uncertainty only.

6.3.2 Δm and τ_S Fits

The fits for Δm and τ_S are performed separately for the $K \to \pi^+\pi^-$ and $K \to \pi^0\pi^0$ data. The fits are binned in twelve 10 GeV/c momentum bins in each beam, one z bin in the vacuum beam, and seventeen 2 m z bins in the regenerator beam. The free parameters are the kaon flux in each of the twelve momentum bins, the regeneration parameters $|f_-(70\ \mathrm{GeV}/c)|$ and α, a z-shift parameter which is different for the charged and neutral fits, Δm, and τ_S. The z-shift parameter is floated to allow for resolution effects in z which could affect the shape of the z distribution near the regenerator. CPT is assumed by dynamically setting ϕ_η equal to the superweak phase using the floated values of Δm and τ_S. The fits have 199 degrees of freedom.

Fit to $K \to \pi^+\pi^-$ Data

For the charged mode fit, we float the charged effective regenerator edge. For the full $K \to \pi^+\pi^-$ dataset, we find

$$\begin{aligned}
\Delta m &= (5269.0 \pm 4.1) \times 10^6\ \hbar\text{s}^{-1} \\
\tau_S &= (89.620 \pm 0.020) \times 10^{-12}\ \text{s} \\
|f_-(70\ \text{GeV}/c)| &= (1.1755 \pm 0.0003)\ \text{mbarns} \\
\alpha &= -0.5376 \pm 0.0005 \\
\text{z-shift} &= (-2.52 \pm 0.26)\ \text{mm} \\
\chi^2/\text{dof} &= 198.8/199
\end{aligned} \tag{6.10}$$

where the errors reflect the statistical uncertainty.

Fit to $K \to \pi^0\pi^0$ Data

For the neutral mode fit, the z-shift parameter we float is the effective regenerator edge which we have calculated to be 6.2 ± 0.1 mm upstream of the physical regenerator edge. Using the full $K \to \pi^0\pi^0$ dataset, we find

$$\begin{aligned}
\Delta m &= (5257.6 \pm 8.2) \times 10^6\ \hbar\text{s}^{-1} \\
\tau_S &= (89.667 \pm 0.039) \times 10^{-12}\ \text{s} \\
|f_-(70\ \text{GeV}/c)| &= (1.1829 \pm 0.0005)\ \text{mbarns} \\
\alpha &= -0.5378 \pm 0.0011 \\
\text{z-shift} &= (-3.84 \pm 0.56)\ \text{mm} \\
\chi^2/\text{dof} &= 226.5/199
\end{aligned} \tag{6.11}$$

where the errors reflect the statistical uncertainty.

6.3.3 CPT Fits

ϕ_{+-} Fits

The fit for ϕ_{+-} is performed on the $K \to \pi^+\pi^-$ sample only. It is similar to the fit for Δm and τ_S except that the CPT assumption is removed and ϕ_{+-} is a free parameter. There are large correlations between Δm, τ_S, and ϕ_{+-}; for this reason the statistical errors on Δm and τ_S are much larger in this fit than in the fit which assumes CPT. There are 198 degrees of freedom in this fit. Using the full $K \to \pi^+\pi^-$ dataset, we find

$$\begin{aligned}
\phi_{+-} &= (44.09 \pm 0.46)^\circ \\
\Delta m &= (5290.2 \pm 15.0) \times 10^6\ \hbar\mathrm{s}^{-1} \\
\tau_S &= (89.553 \pm 0.049) \times 10^{-12}\ \mathrm{s} \\
|f_-(70\ \mathrm{GeV}/c)| &= (1.1771 \pm 0.0011)\ \mathrm{mbarns} \\
\alpha &= -0.5375 \pm 0.0005 \\
\text{z-shift} &= (-2.30 \pm 0.30)\ \mathrm{mm} \\
\chi^2/\mathrm{dof} &= 196.8/198
\end{aligned} \tag{6.12}$$

where the errors reflect the statistical uncertainty.

We also fit the deviation from the superweak phase, ϕ_{+-} - ϕ_{SW}, which is a direct test of CPT symmetry. This fit is the same as the fit for ϕ_{+-} except that the value of ϕ_{SW} is computed dynamically using the floated values of Δm and τ_S. Using the

full $K \to \pi^+\pi^-$ dataset, we find

$$\begin{aligned}
\phi_{+-} - \phi_{SW} &= (0.59 \pm 0.40)^\circ \\
\Delta m &= (5290.2 \pm 14.9) \times 10^6\ \hbar \mathrm{s}^{-1} \\
\tau_S &= (89.553 \pm 0.049) \times 10^{-12}\ \mathrm{s} \\
|f_-(70\ \mathrm{GeV}/c)| &= (1.1771 \pm 0.0011)\ \mathrm{mbarns} \\
\alpha &= -0.5375 \pm 0.0005 \\
\text{z-shift} &= (-2.30 \pm 0.30)\ \mathrm{mm} \\
\chi^2/\mathrm{dof} &= 196.8/198
\end{aligned} \tag{6.13}$$

where the errors reflect the statistical uncertainty.

$\Delta\phi$ Fit

The fit for $\Delta\phi$ is similar to the fit for Δm and τ_S except that it is a simultaneous fit to the $K \to \pi^+\pi^-$ and $K \to \pi^0\pi^0$ data and the CPT assumption is removed. The fit is binned in twelve 10 GeV/c momentum bins in each beam, one z bin in the vacuum beam, and seventeen 2 m z bins in the regenerator beam. The free parameters are the charged and neutral kaon fluxes in each of the twelve momentum bins, the regeneration parameters $|f_-(70\ \mathrm{GeV}/c)|$ and α, the charged and neutral z-shift parameters, Δm, τ_S, ϕ_{+-}, $Re(\epsilon'/\epsilon)$, and $Im(\epsilon'/\epsilon)$. There is a correlation between the real and imaginary parts of ϵ'/ϵ; the statistical uncertainty on $Re(\epsilon'/\epsilon)$ is therefore increased relative to the nominal fit for $Re(\epsilon'/\epsilon)$ in which $Im(\epsilon'/\epsilon)$ is

fixed at zero. Using the full dataset, we find

$$
\begin{aligned}
Im(\epsilon'/\epsilon) &= (-16.97 \pm 9.25) \times 10^{-4} \\
Re(\epsilon'/\epsilon) &= (20.43 \pm 1.37) \times 10^{-4} \\
\Delta m &= (5279.7 \pm 13.7) \times 10^{6}\ \hbar \mathrm{s}^{-1} \\
\tau_S &= (89.586 \pm 0.043) \times 10^{-12}\ \mathrm{s} \\
|f_-(70\ \mathrm{GeV}/c)| &= (1.1793 \pm 0.0010)\ \mathrm{mbarns} \\
\alpha &= -0.5378 \pm 0.0005 \\
\phi_{+-} &= (43.89 \pm 0.41)^\circ \\
\text{neutral z-shift} &= (-3.53 \pm 0.54)\ \mathrm{mm} \\
\text{charged z-stretch} &= (-1.72 \pm 0.30)\ \mathrm{mm} \\
\chi^2/\mathrm{dof} &= 425.6/399
\end{aligned}
\tag{6.14}
$$

where the errors reflect the statistical uncertainty.

CHAPTER 7
SYSTEMATIC STUDIES

In general, we study the systematic uncertainties in $Re(\epsilon'/\epsilon)$ by adjusting some aspect of the analysis and measuring the change in $Re(\epsilon'/\epsilon)$ associated with that adjustment. When assigning systematic errors, we typically deal with the statistical uncertainties on the change in $Re(\epsilon'/\epsilon)$ in the following manner. We estimate a potential shift, $s \pm \sigma_s$ where s is the shift in $Re(\epsilon'/\epsilon)$ and σ_s is the statistical uncertainty on that shift. We convert the shift to a symmetric systematic error, Δ_s, such that the range [-Δ_s,+Δ_s] includes 68.3 % of the area of a Gaussian with means s and width σ_s:

$$\frac{1}{\sigma_s\sqrt{2\pi}}\int_{-\Delta_s}^{+\Delta_s} dx\ exp\left[-\frac{(x-s)^2}{2\sigma_s^2}\right] = 0.683. \tag{7.1}$$

Note that $\Delta_s = \sigma_s$ when $s = 0$. This procedure is not followed for every systematic error, but is used frequently in the evaluation of systematic uncertainties.

7.1 Acceptance Correction

We use the Monte Carlo simulation binned in momentum and z to determine the acceptance of the detector in each beam. We evaluate the quality of this simulation by comparing energy reweighted z vertex distributions in the vacuum beam between data and Monte Carlo. We use the same 10 GeV/c momentum bins used in the fitter and weight the number of MC events in each bin so that the data and MC kaon momentum distributions agree. We compare the z distributions for data and MC by fitting a line to the data/MC ratio as a function of z. We call the slope of this line, s, the acceptance "z-slope" and use it to evaluate the systematic error on $Re(\epsilon'/\epsilon)$.

A z-slope affects the value of $Re(\epsilon'/\epsilon)$ by producing a bias between the regenerator and vacuum beams because of the very different z vertex distributions in the two

beams. A good approximation of the bias on $Re(\epsilon'/\epsilon)$ is $s\Delta z/6$ where Δz is the difference of the mean z values for the vacuum and regenerator beam z vertex distributions. The factor of 6 converts the bias on the vacuum-regenerator beam ratio to a bias on $Re(\epsilon'/\epsilon)$. $\Delta z = 5.6$ m for the $K \to \pi^+\pi^-$ sample and $\Delta z = 7.2$ m for the $K \to \pi^0\pi^0$ sample. We use Equation 7.1 to convert the measured bias on $Re(\epsilon'/\epsilon)$ to a systematic uncertainty on $Re(\epsilon'/\epsilon)$.

We use $K \to \pi^+\pi^-$ decays to measure the z-slope in charged mode. We fit for the slope over the entire decay region 110 m $< z <$ 158 m. We find a 2.7σ slope in 1997 and no slope in 1999. Figure 7.1 shows the $K \to \pi^+\pi^-$ vacuum beam data/MC ratio for each year. The combined dataset has slope $s = (-0.34 \pm 0.20) \times 10^{-4}$/m, shown in Figure 7.2, which converts to a systematic error on $Re(\epsilon'/\epsilon)$ of $\pm 0.41 \times 10^{-4}$.

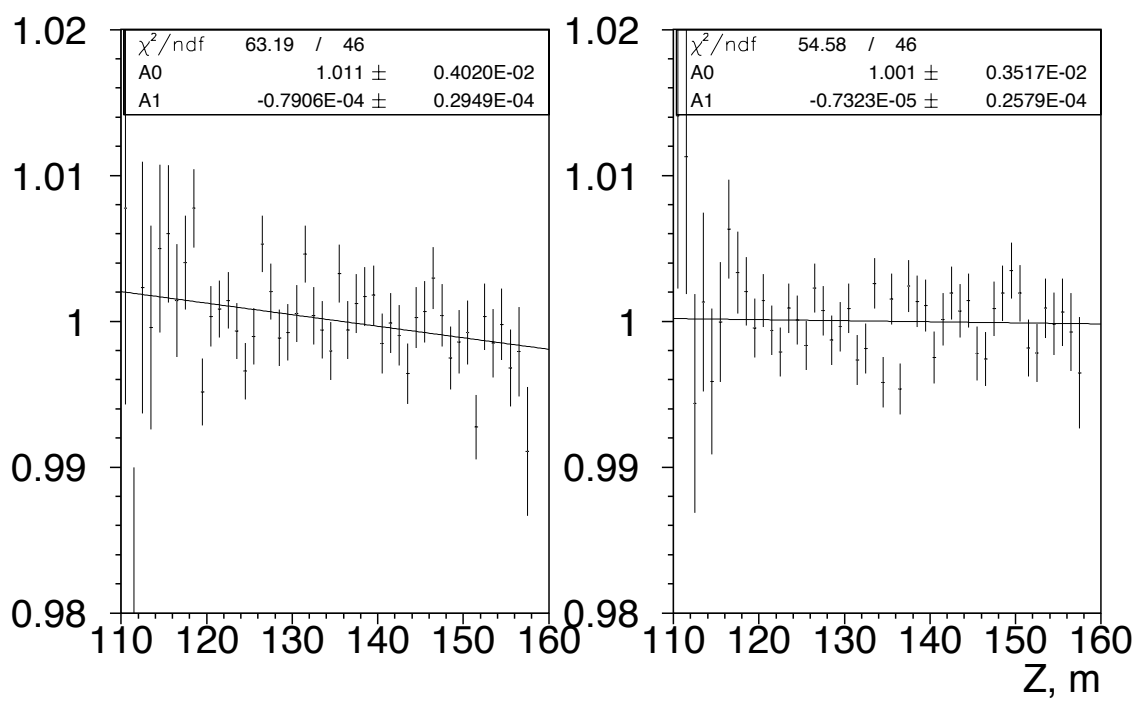

Figure 7.1: Data/MC ratio of z distribution for $K \to \pi^+\pi^-$ decays from 1997 (left) and 1999(right). The z-slopes are parameter A1 in the fits.

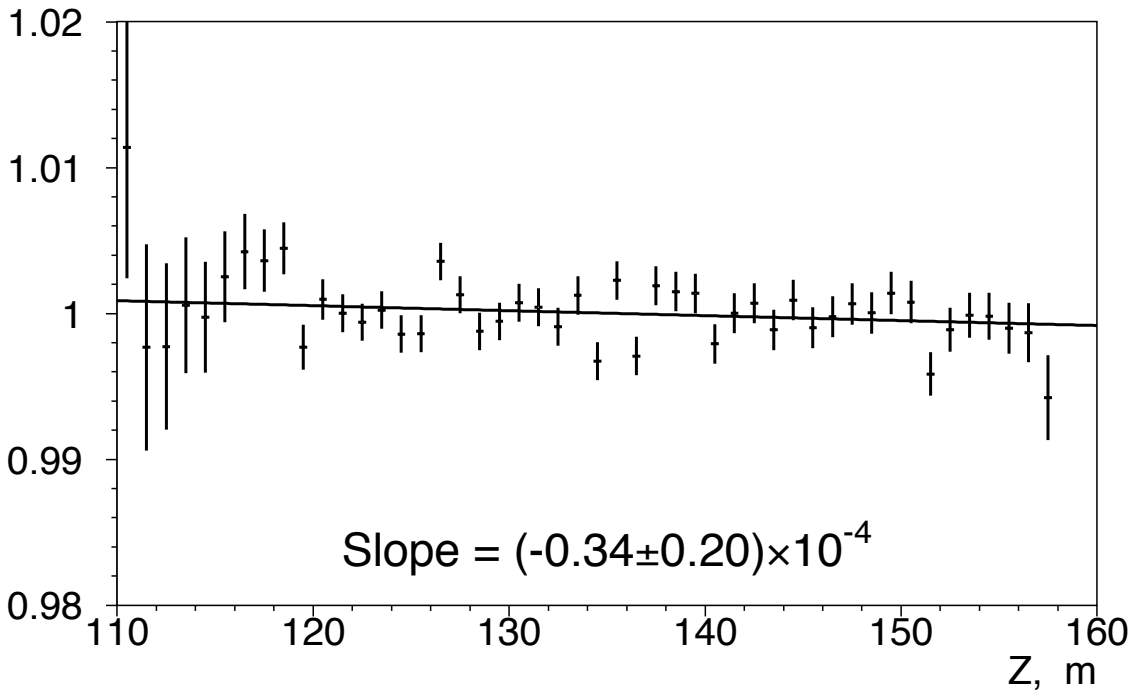

Figure 7.2: Data/MC ratio of z distribution for $K \to \pi^+\pi^-$ decays from the full dataset.

As a test of the upstream region, we fit for $Re(\epsilon'/\epsilon)$ excluding the region upstream of the MA ($z < 122.5$ m) for $K \to \pi^+\pi^-$ data only. Making this cut changes the average z vertex in the vacuum beam by +2.5 m. For a given z-slope, s_z, we expect a change in $Re(\epsilon'/\epsilon)$ of $2.5/6 s_z$ due to the change in average z vertex. We correct the change in $Re(\epsilon'/\epsilon)$ by this expected change and take the remaining difference as the systematic on $Re(\epsilon'/\epsilon)$ due to acceptance in the region upstream of the MA. Table 7.1 summarizes the measured and expected changes in $Re(\epsilon'/\epsilon)$ with this cut for the two years. The total systematic uncertainty in $Re(\epsilon'/\epsilon)$ associated with the acceptance upstream of the MA is $\pm 0.40 \times 10^{-4}$.

We use the high statistics $K_L \to \pi^0\pi^0\pi^0$ decay mode to measure the z-slope in neutral mode. This mode has the same type of particles in the final state as $K \to \pi^0\pi^0$ and is more sensitive than $\pi^0\pi^0$ to potential problems in the reconstruction due

Year	$\Delta Re(\epsilon'/\epsilon)$ ($\times 10^{-4}$)	Expected $\Delta Re(\epsilon'/\epsilon)$ ($\times 10^{-4}$)	Error on $Re(\epsilon'/\epsilon)$ ($\times 10^{-4}$)
1997	-0.35 ± 0.33	-0.33	±0.33
1999	-0.40 ± 0.24	-0.03	±0.48
1997+1999	-0.41 ± 0.18	-0.10	±0.40

Table 7.1: Summary of systematic errors due to acceptance upstream of the MA

to close clusters, energy leakage at the CsI edges, and low photon energies. We fit for the slope over the entire decay region 110 m $< z <$ 158 m. The individual z-slopes for 1996, 1997, and 1999 are shown in Figure 7.3. The z-slope for the full combined $K_L \to \pi^0\pi^0\pi^0$ vacuum beam data sample is shown in Figure 7.4. The slope is (0.33 ± 0.14)$\times 10^{-4}$/m; the associated systematic error on $Re(\epsilon'/\epsilon)$ is $\pm 0.48\times 10^{-4}$.

We check the z-slope in $K \to \pi^0\pi^0$ decays and find that the results are consistent with those from $K_L \to \pi^0\pi^0\pi^0$ decays. Figure 7.5 shows the individual z-slopes for 1996, 1997, and 1999 for vacuum beam $K \to \pi^0\pi^0$ decays. None of the $K \to \pi^0\pi^0$ z-slopes are significant at the 2σ level. The z-slope for the full combined $K \to \pi^0\pi^0$ vacuum beam data sample, shown in Figure 7.6, is (0.77 ± 0.39)$\times 10^{-4}$/m.

7.2 $K \to \pi^+\pi^-$ Systematics

7.2.1 Trigger

Level 1 and Level 2 Trigger

We measure the level 1 and level 2 trigger inefficiencies using $K_L \to \pi^\pm e^\mp \nu$ decays from trigger 5 and trigger 3, respectively. We calculate the bias on $Re(\epsilon'/\epsilon)$ using the the change in the single ratio. We find no significant bias in level 1 or level 2 [1] so we take the statistical error on the measurement of the bias to be the systematic error in $Re(\epsilon'/\epsilon)$. The error in $Re(\epsilon'/\epsilon)$ from the level 1 and level 2 trigger is $\pm 0.2\times 10^{-4}$.

[1] The bias is measured using data from 1997 and 1999 for level 1. For level 2, only the 1997 bias is measured. During 1999 data taking, the level 2 trigger was monitored closely so we believe that the 1999 bias can not be greater than the 1997 bias.

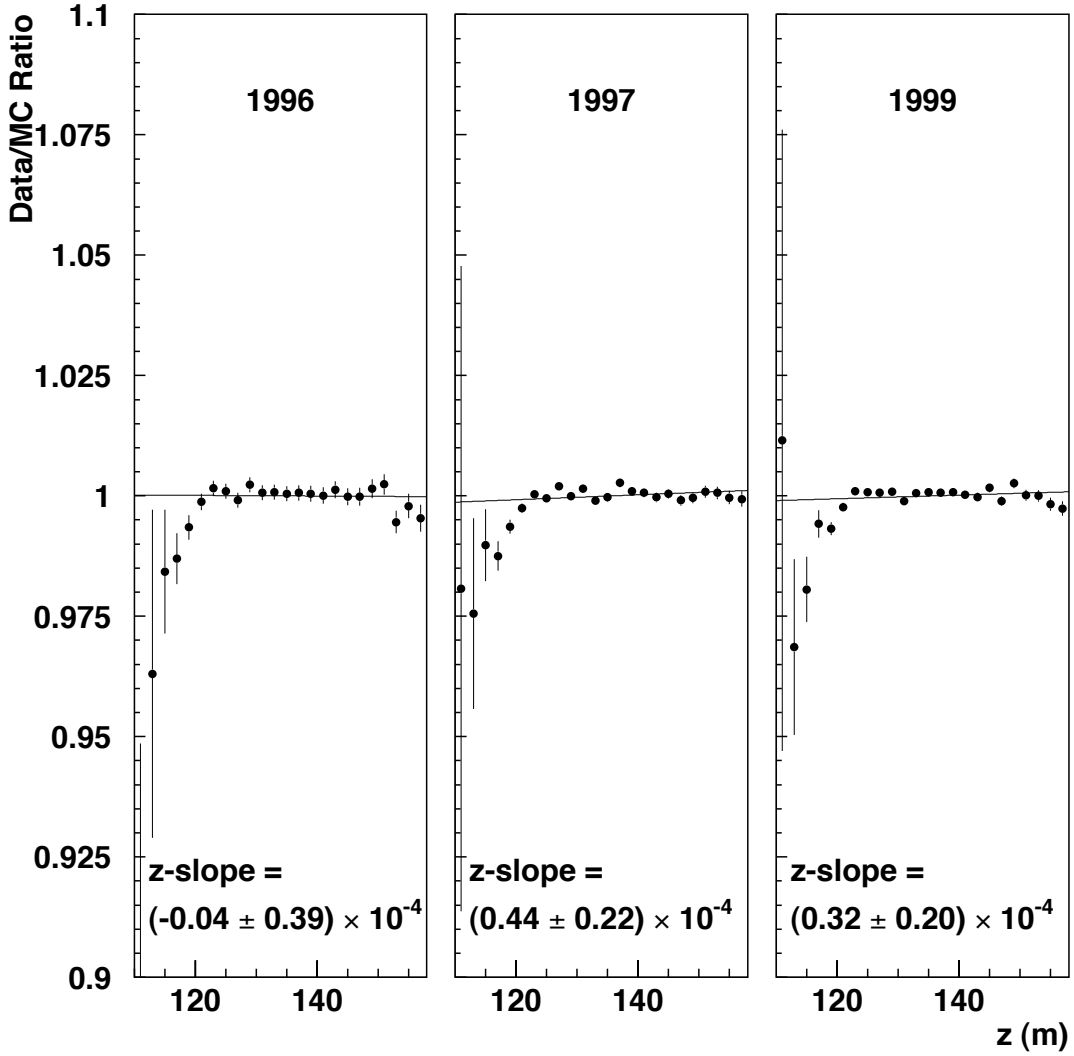

Figure 7.3: Data/MC ratio of z distributions for $K_L \to \pi^0\pi^0\pi^0$ decays from 1996 (left), 1997 (center), and 1999 (right). The individual z-slopes for each year are noted on the plot.

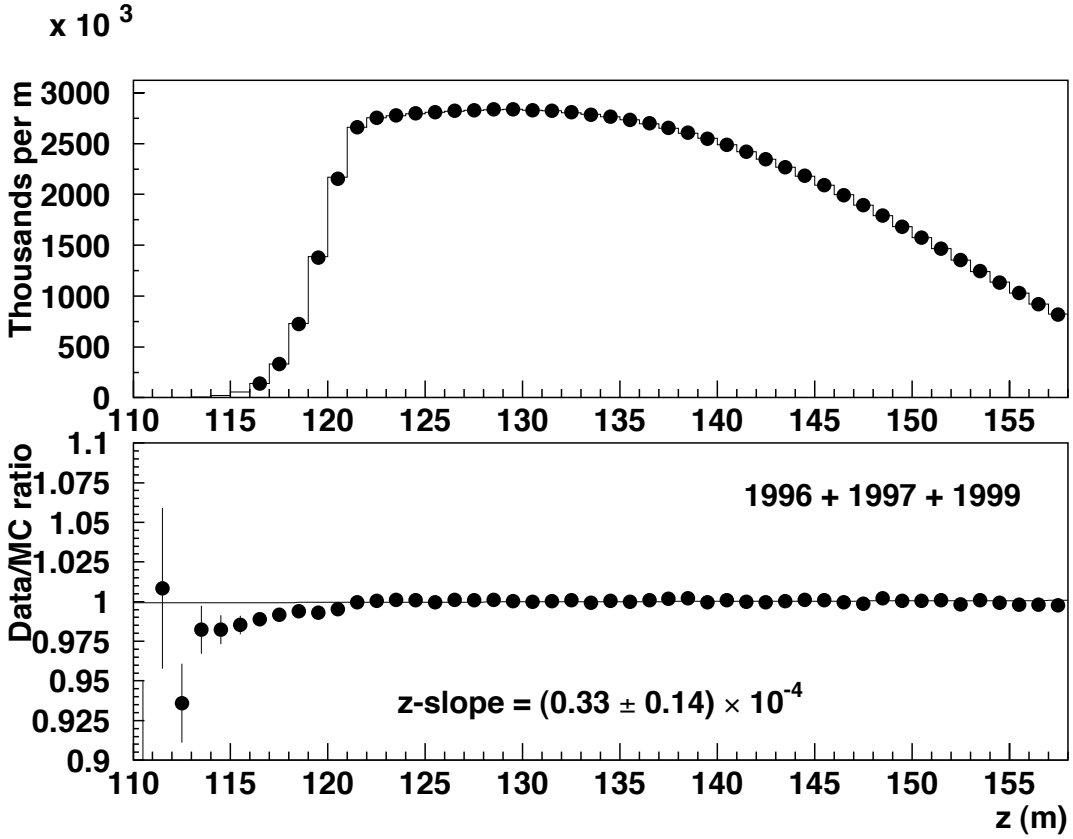

Figure 7.4: Data-MC comparison of z distributions for $K_L \to \pi^0\pi^0\pi^0$ decays from the full 1996 + 1997 + 1999 data sample. The top plot shows the data (dots) and MC (histogram) overlay. The bottom plot shows the data/MC ratio. The z-slope is noted on the plot.

Level 3 Trigger

We measure the level 3 trigger inefficiency using trigger 1 random accepts; this prescaled subset of the $K \to \pi^+\pi^-$ trigger has no level 3 requirement. This sample is analyzed using the full offline analysis; those events which pass all cuts but do not have the level 3 tag bit set represent the inefficiency. Five runs from 1999 with large sporadic level 3 losses are excluded from the data sample. The bias on $Re(\epsilon'/\epsilon)$ is calculated using the change in the single ratio and is used to correct $Re(\epsilon'/\epsilon)$. We crosscheck the combined L2 and L3 inefficiency using trigger 3 which is a version of

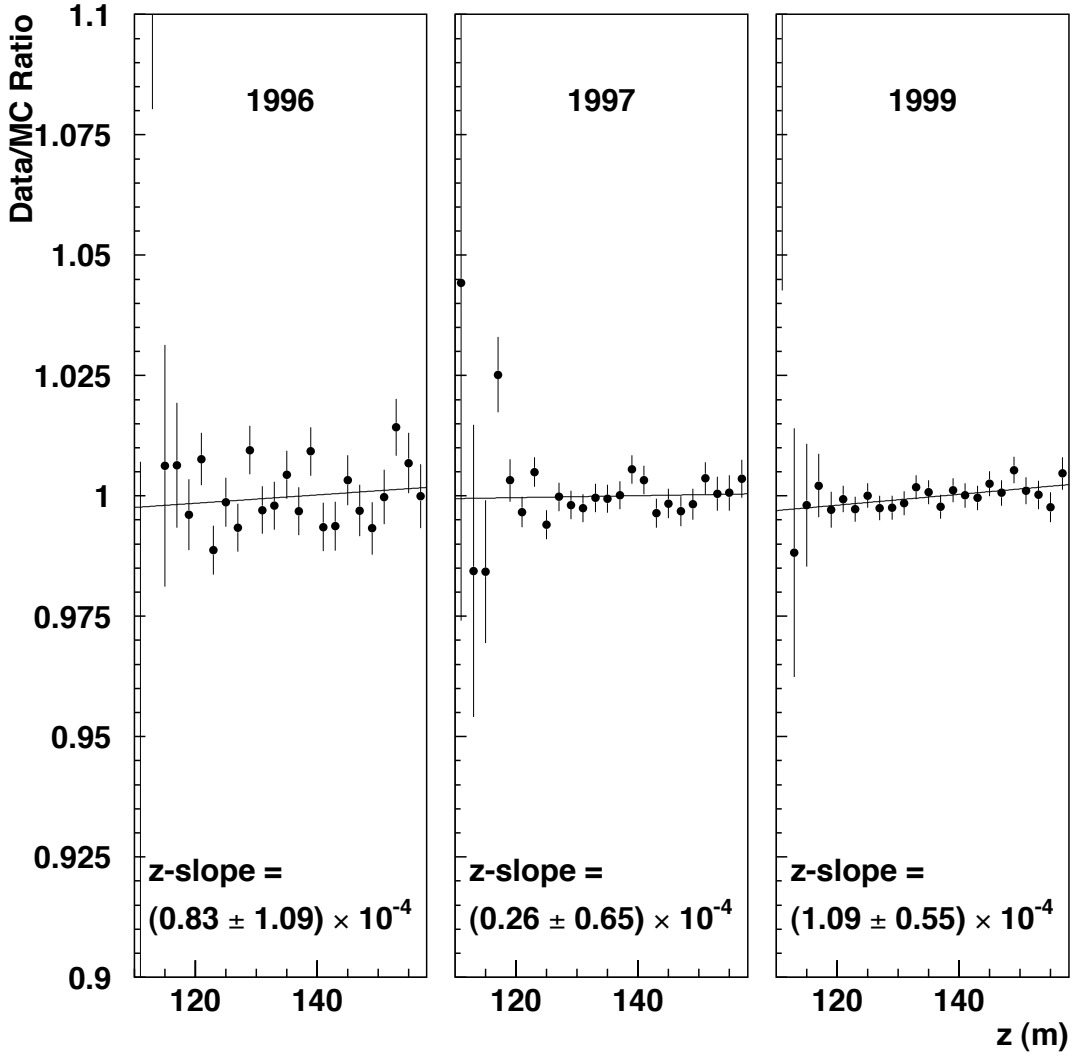

Figure 7.5: Data/MC ratio of z distributions for $K \to \pi^0\pi^0$ decays from 1996 (left), 1997 (center), and 1999 (right). The individual z-slopes for each year are noted on the plot.

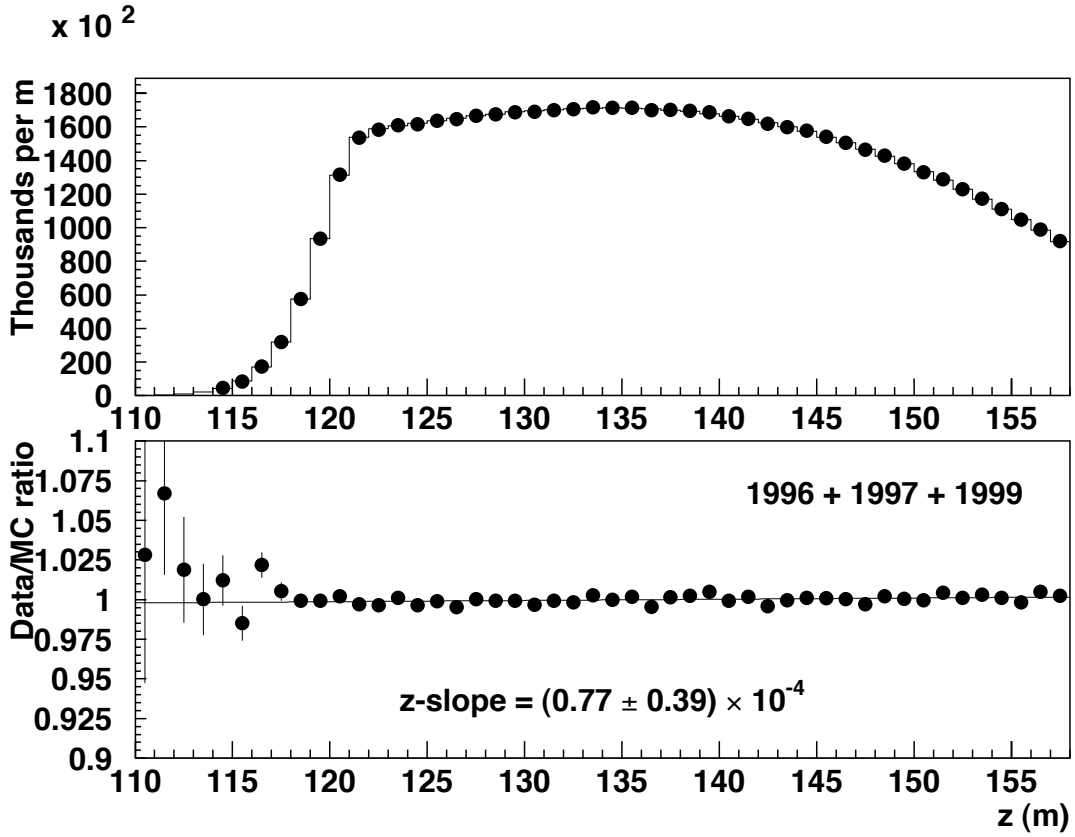

Figure 7.6: Data-MC comparison of z distributions for $K \to \pi^0\pi^0$ decays from the full 1996 + 1997 + 1999 data sample. The top plot shows the data (dots) and MC (histogram) overlay. The bottom plot shows the data/MC ratio. The z-slope is noted on the plot.

the $K \to \pi^+\pi^-$ trigger with no level 2 or level 3 requirements. Table 7.2 summarizes the bias on $Re(\epsilon'/\epsilon)$ in each year found in both studies. We take the error on the correction found in the trigger 1 study to be the uncertainty in $Re(\epsilon'/\epsilon)$ from the level 3 trigger inefficiency: $\pm 0.12 \times 10^{-4}$.

7.2.2 Track and Momentum Reconstruction

We estimate the error associated with alignment and calibration of the drift chambers by evaluating the change in $Re(\epsilon'/\epsilon)$ when we vary a number of measured

Trigger	Bias in $Re(\epsilon'/\epsilon)$ ($\times 10^{-4}$)		
	1997	1999	Combined
B01	0.32 ± 0.20	0.28 ± 0.14	0.30 ± 0.12
B03	0.58 ± 0.59	-0.24 ± 0.60	0.12 ± 0.42

Table 7.2: Level 3 bias in $K \to \pi^+\pi^-$ trigger. The bias measured using B01 events is applied as a correction to $Re(\epsilon'/\epsilon)$.

quantities within their errors. We vary the transverse drift chamber offsets and rotations, the non-orthogonality between the x and y wire planes, the z positions of the drift chambers, the the x(t) maps. The x(t) maps are varied in a manner that changes the average SOD value within its uncertainty. From these studies, we assign an uncertainty on $Re(\epsilon'/\epsilon)$ of $\pm 0.20 \times 10^{-4}$.

The energy scale in the $K \to \pi^+\pi^-$ analysis is set by fixing the momentum kick of the magnet using the kaon mass as a constraint. The kaon mass is known to within 0.022 MeV[51]; this uncertainty in the mass corresponds to an uncertainty in $Re(\epsilon'/\epsilon)$ of $\pm 0.10 \times 10^{-4}$.

7.2.3 Cut Variations

We vary our selection criteria around their nominal values to search for potential biases in $Re(\epsilon'/\epsilon)$. In the $K \to \pi^+\pi^-$ analysis we find that the only cut variation with which $Re(\epsilon'/\epsilon)$ shows a significant change is the cut on p_T^2. We vary the p_T^2 cut from 125 MeV^2/c^2 to 1000 MeV^2/c^2. Figure 7.7 shows the change in $Re(\epsilon'/\epsilon)$ as we vary the p_T^2 cut in 1997 and 1999. Based on these variations we assign a systematic uncertainty on $Re(\epsilon'/\epsilon)$ of $\pm 0.10 \times 10^{-4}$.

7.2.4 Drift Chamber Simulation

To measure the systematic uncertainty associated with our simulation of the drift chamber efficiencies, we generate separate sets of Monte Carlo in which scattering, DC maps, and accidental activity are turned off. We find the change in $Re(\epsilon'/\epsilon)$ with each of these changes and take 10% of that change as the systematic error.

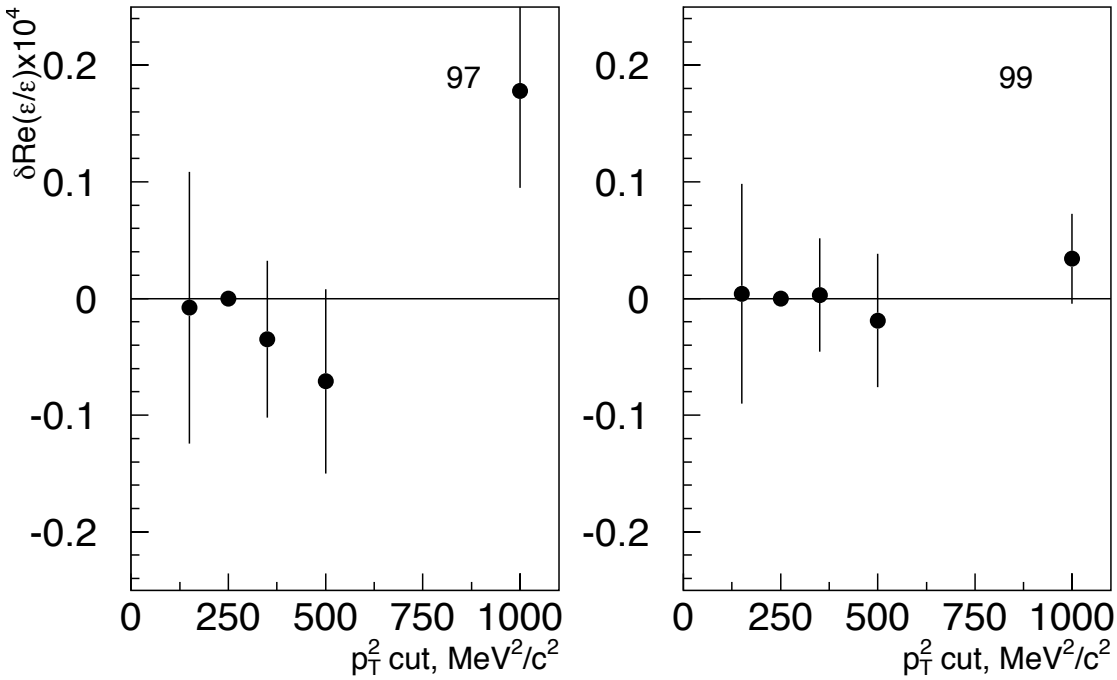

Figure 7.7: Change in $Re(\epsilon'/\epsilon)$ with variation of p_T^2 cut for 1997 (left) and 1999 (right). The nominal requirement is $p_T^2 < 250$ MeV^2/c^2.

Table 7.3 shows the change in $Re(\epsilon'/\epsilon)$ with each change in the simulation for both years. Based on these changes, we assign a systematic uncertainty on $Re(\epsilon'/\epsilon)$ of $\pm 0.15 \times 10^{-4}$ from the modeling of drift chamber efficiency.

Change to MC	Change in $Re(\epsilon'/\epsilon)$ ($\times 10^{-4}$)	
	1997	1999
No scattering in spectrometer	+0.19	-0.55
No DC maps	-0.87	-0.31
No accidental overlays	+0.26	+0.03

Table 7.3: Change in $Re(\epsilon'/\epsilon)$ with changes to DC efficiency simulation

The simulation of drift chamber resolutions is checked by comparing the widths of the SOD distributions between data and Monte Carlo. The MC simulates the resolutions to within 5%; the associated systematic error on $Re(\epsilon'/\epsilon)$ is $\pm 0.15 \times 10^{-4}$.

7.2.5 Backgrounds

The systematic uncertainty in $Re(\epsilon'/\epsilon)$ from backgrounds and background subtraction was evaluated for the 1997 data in the previously published analysis[50]. As the background subtraction procedure has not changed substantially, we do not re-evaluate the systematic for 1997 and we take the same error for 1999.

To evaluate the uncertainty due to backgrounds we vary the background levels $\pm 10\%$; the largest associated variation in $Re(\epsilon'/\epsilon)$ is 0.10×10^{-4}. We check the background enhancement procedure described in Section 5.2.1 by floating the background levels directly without using the enhancement procedure. This changes $Re(\epsilon'/\epsilon)$ by 0.07×10^{-4}. We vary those cuts which are designed to suppress backgrounds and find the change in $Re(\epsilon'/\epsilon)$ with those changes. Loosening the invariant mass cut to 484 MeV/c^2 $< m_{\pi^+\pi^-} <$ 512 MeV/c^2 changes $Re(\epsilon'/\epsilon)$ by (-0.04 $\pm$ 0.04)$\times10^{-4}$. Varying the minimum pion momentum and the E/p cut have no appreciable effect on $Re(\epsilon'/\epsilon)$. We assign a conservative systematic uncertainty on $Re(\epsilon'/\epsilon)$ due to backgrounds of $\pm0.20\times10^{-4}$.

7.2.6 Apertures

The track separation cut forms a limiting inner aperture and depends on the position of each wire within the drift chambers. The wire spacing is known to 20 μm on average. There are variations in the actual wire spacing which are measured in data but are not simulated in the Monte Carlo; to determine the effect of these variations we convolute the track illumination with the wire-cell size to determine the number of events that migrate across the track separation cut in data but not in MC. We find that the bias in $Re(\epsilon'/\epsilon)$ is (-0.16 $\pm$ 0.12)$\times10^{-4}$; the corresponding uncertainty in $Re(\epsilon'/\epsilon)$ is $\pm0.22\times10^{-4}$.

The $\pi^+\pi^-$ effective regenerator edge defines the upstream edge of acceptance in the regenerator beam. As discussed in Section 2.3.2, we find the effective regenerator edge using the energy deposit of a muon passing through the regenerator Pb module, the fraction of energy coming from the last piece of scintillator due to the geometry of the phototube placement on the Pb module, the value of the trigger threshold,

and the value of the offline cut on energy deposit in the Pb module to calculate the probability for two minimum ionizing pions to escape the last piece of scintillator without depositing enough energy to be vetoed. We find the effective regenerator edge to be (1.65 ± 0.4) mm upstream of the physical edge in 1997 and (0.7 ± 0.4) mm upstream of the physical edge in 1999.[2] The error on this measurement comes from varying the trigger threshold and the fraction of energy coming from the last piece of scintillator by ∼15% each. The 0.4 mm uncertainty in the position of the effective regenerator edge leads to an uncertainty in $Re(\epsilon'/\epsilon)$ of $\pm 0.20\times 10^{-4}$.

7.2.7 Summary

The systematic errors on $Re(\epsilon'/\epsilon)$ due to the $K \to \pi^+\pi^-$ analysis are summarized in Table 7.4. For reference, the systematic errors from the 2003 PRD[50] are also included in Table 7.4. Some systematics are evaluated separately for each dataset and then combined as a weighted average, some are evaluated for the combined 1997+1999 dataset, and some are taken to be the same for both years. The total systematic error on $Re(\epsilon'/\epsilon)$ due to the charged analysis is $\pm 0.81\times 10^{-4}$.

7.3 $K \to \pi^0\pi^0$ Systematics

7.3.1 Trigger

Level 1 Trigger

The level 1 trigger requires that the total in-time energy in the CsI be greater than 30 GeV. The offline cut on kaon energy is 40 GeV. We use $K \to \pi^+\pi^-\pi^0$ events from the $K \to \pi^+\pi^-$ trigger to measure the L1 trigger inefficiency. Standard $\pi^+\pi^-\pi^0$ selection criteria are applied with the exceptions that the $\gamma - \pi$ separation cut is relaxed to increase statistics and a cut on CsI timing χ^2 is applied. The L1 inefficiency is the ratio of events with energy greater than 40 GeV for which the

[2]The difference in effective edges is due to different offline cuts on the energy deposit in the Pb module. In 1997 the edge is defined by the trigger threshold. In 1999, a tight offline cut is applied.

Source	Error on $Re(\epsilon'/\epsilon)$ ($\times 10^{-4}$)			
	PRD	1997	1999	Total
L1 and L2 Trigger	0.20	0.20	0.20	0.20
L3 Trigger	0.54	0.20	0.14	0.12
Alignment and Calibration	0.28	0.20		0.20
Momentum scale	0.16	0.10		0.10
p_T^2	0.25	0.10		0.10
DC efficiency modeling	0.37	0.15		0.15
DC resolution modeling	0.15	0.15		0.15
Background	0.20	0.20		0.20
Wire Spacing	0.22	0.22		0.22
Reg Edge	0.20	0.20	0.20	0.20
Acceptance	0.79	0.87	0.25	0.41
Upstream z	—	0.33	0.48	0.40
Monte Carlo Statistics	0.41	0.28	0.28	0.20
Total	1.26	1.12	0.81	0.81

Table 7.4: Summary of systematic uncertainties in $Re(\epsilon'/\epsilon)$ from the $K \to \pi^+\pi^-$ analysis.

Etotal trigger bit is not set to the total number of events with energy is greater than 40 GeV. The majority of the L1 inefficiencies found in the $\pi^+\pi^-\pi^0$ sample have total energies of 40-45 GeV and there are no inefficiencies for energies greater than 60 GeV. The vacuum and regenerator beam event yields differ by ∼10% in the range 40 GeV $< \mathrm{E}_K <$ 60 GeV, so we take 10%/6 of the measured inefficiency as the systematic error on $Re(\epsilon'/\epsilon)$. Table 7.5 summarizes the L1 inefficiencies from $\pi^+\pi^-\pi^0$ and the associated systematic error on $Re(\epsilon'/\epsilon)$ for each year.

Year	Number of Events		L1 Inefficiency	Error on $Re(\epsilon'/\epsilon)$
	Etot > 40 GeV	Fail L1 Trigger	($\times 10^{-4}$)	($\times 10^{-4}$)
1996	242000	12	0.5	0.01
1997	32749	2	0.6	0.01
1999	281587	45	1.6	0.03

Table 7.5: Level 1 inefficiencies in $K \to \pi^0\pi^0$ trigger

It is also possible to measure the L1 inefficiency using $K_L \to \pi^\pm e^\mp \nu$ decays. Both samples are checked for 1996 and 1997 data and yield consistent results, but only

the $K \to \pi^+\pi^-\pi^0$ study is used to set the systematic error. The total systematic uncertainty in $Re(\epsilon'/\epsilon)$ due to the level 1 trigger is $\pm 0.02 \times 10^{-4}$.

Level 2 Trigger

The level 2 trigger inefficiency is measured using $K_L \to \pi^0\pi^0\pi^0$ events from trigger 5, a trigger which requires L1 but makes no L2 or L3 requirements. We reconstruct $3\pi^0$ events using software clusters. The L2 inefficiency is the ratio of the number of events with fewer than 6 HCC bits set to the total number of events passing offline reconstruction in the vacuum beam. The measured inefficiencies above 3 GeV are 2.4%, 0.6%, 0.3%, and 0.77% for 96a, 96bc, 97, and 99, respectively. The inefficiency is very high for the first part of 1996 because HCC matching had not yet been done. The inefficiency increases in 1999 because the HCC thresholds are higher and therefore closer to the minimum cluster energy. The thresholds were not raised intentionally in 1999; we believe that the increase was a side effect of the HCC matching procedure.

$K_L \to \pi^0\pi^0\pi^0$ Monte Carlo simulates the inefficiency quite well. For all years the MC predicts the data inefficiency to within 0.2%. Figure 7.8 shows the inefficiency as a function of minimum cluster energy for data and MC. To estimate how much the thresholds in MC could be wrong, we compare the L2 inefficiency between data and a MC simulation in which the thresholds are raised by 100 MeV. For 1999, we find that the data-MC difference changes from 0.09% to -0.55% or 0.64% per 100 MeV. We conclude that the thresholds are off by less than 15 MeV for 1999. Using the same procedure, we conclude that the thresholds are off by less than 30 MeV for 1996 and 1997.

To determine the systematic error on $Re(\epsilon'/\epsilon)$ from the L2 inefficiency, we measure the bias on the neutral mode single ratio from the L2 trigger. We use $K \to \pi^0\pi^0$ MC to measure the inefficiency in each beam. The bias above 3 GeV is 2.1×10^{-4} for 1996, 0.3×10^{-4} for 1997, and 1.3×10^{-4} for 1999. In all years, the inefficiency is simulated to within 10% so we take 10% of the bias as as systematic error on $Re(\epsilon'/\epsilon)$. To determine the systematic on $Re(\epsilon'/\epsilon)$ from the uncertainty in the HCC

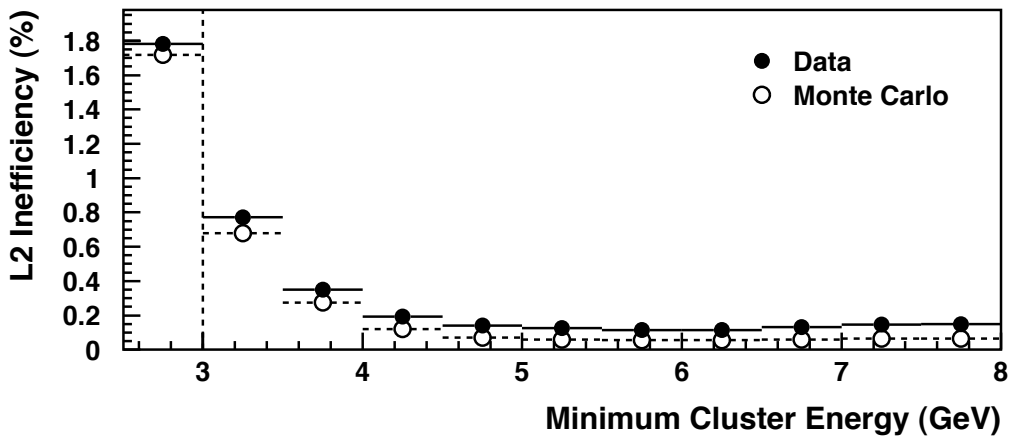

Figure 7.8: L2 inefficiency as a function of minimum cluster energy for data and Monte Carlo. The dashed line indicates the value of our minimum cluster energy requirement.

thresholds, we compare the bias in nominal $K \to \pi^0\pi^0$ MC to the bias in MC with the thresholds changed by the amount we believe they could be wrong. The bias changes by 0.02×10^{-4} in 1996, 0.12×10^{-4} in 1997, and 0.19×10^{-4} in 1999.

The L2 inefficiencies and systematics are summarized in Table 7.6. The total systematic error on $Re(\epsilon'/\epsilon)$ from level 2 is 0.20×10^{-4}, 0.12×10^{-4}, and 0.23×10^{-4} for 1996, 1997, and 1999, respectively.

Year	L2 Inefficiency	Systematic on $Re(\epsilon'/\epsilon)$ ($\times10^{-4}$)		
		L2 Bias	HCC Thresholds	Total
1996	2.4%,0.6%	0.21	0.02	0.21
1997	0.3%	0.03	0.12	0.12
1999	0.8%	0.13	0.19	0.23

Table 7.6: Level 2 inefficiencies in $K \to \pi^0\pi^0$ trigger

Level 3 Trigger

We measure the level 3 trigger inefficiency using trigger 4 random accepts; this subset of the $K \to \pi^0\pi^0$ trigger has no level 3 requirement. We analyze this sample using the full offline $K \to \pi^0\pi^0$ analysis; the inefficiency is the fraction of events passing the offline analysis which do not have the L3 tag bit set. The systematic error on $Re(\epsilon'/\epsilon)$ is calculated using the change in the single ratio and Equation 7.1. The inefficiencies and the associated systematic errors for 1997 and 1999 are summarized in Table 7.7. There were very different level 3 inefficiencies during different run ranges of 1996 so the error calculation for 1996 is more involved.

Year	Fail L3 Trigger		$\frac{1}{6} \mid \frac{\delta V}{V}$ - $\frac{\delta R}{R} \mid$	Error on $Re(\epsilon'/\epsilon)$
	Vac Beam	Reg Beam	$(\times 10^{-4})$	$(\times 10^{-4})$
1997	1/49415	2/82708	0.01 ± 0.04	0.04
1999	0/39305	0/65391	0.0 ± 0.05	0.05

Table 7.7: Level 3 inefficiencies in $K \to \pi^0\pi^0$ trigger

7.3.2 Cut Variations

We study potential systematic errors due to our selection criteria by varying our cuts around the nominal values. We adjust the cut value in data and Monte Carlo as well as our background simulations and repeat the full analysis for each cut value. We do not re-match the energy scale as the data-MC mismatch at the regenerator edge varies by less than 2 mm for all cut variations. We compare the $Re(\epsilon'/\epsilon)$ result for each cut variation to the nominal result, estimating the independent errors by taking the quadrature difference of the error with the nominal error. We assign a systematic error on $Re(\epsilon'/\epsilon)$ in cases where there is a statistically significant shift from the nominal value for reasonable cut variations. In cases where there appears to be a systematic shift in $Re(\epsilon'/\epsilon)$ we use the difference between the nominal result and the loosest cut we have investigated and Equation 7.1 to find the systematic error. Figure 7.9 shows the change in $Re(\epsilon'/\epsilon)$ for many of the cut variations we study.

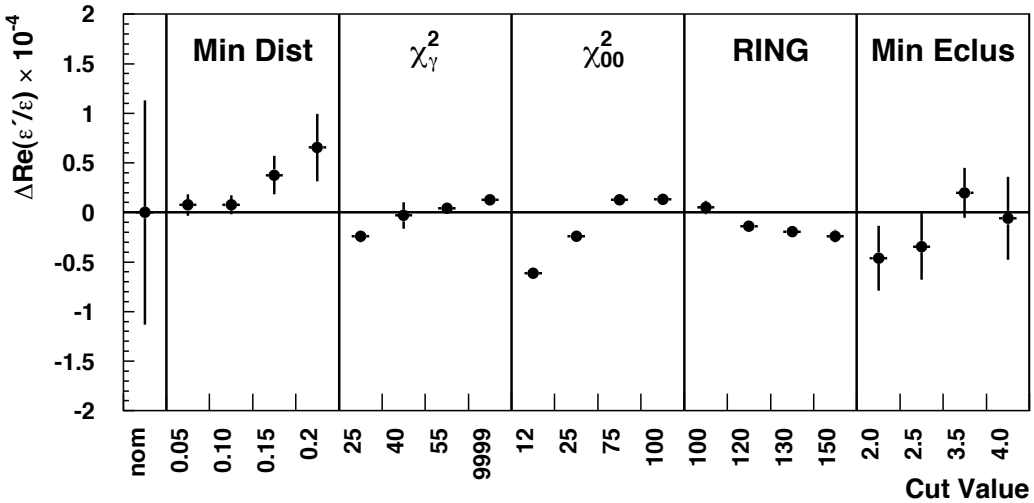

Figure 7.9: Changes in $Re(\epsilon'/\epsilon)$ with variations of selection criteria. The error bar on the nominal point represents the full statistical error on $Re(\epsilon'/\epsilon)$. The independent errors of the other points are estimated by taking the quadrature difference with the nominal statistical error.

We vary the minimum cluster separation cut from 5 cm to 20 cm. There does not appear to be any systematic variation in the vicinity of the nominal cut and the variations with larger cut values are marginally significant so we do not quote any systematic for this cut. Figure 7.10 shows the data-MC comparison for this variable.

We vary the cut on χ^2_γ from 25 to 55 and remove the cut entirely. There is a systematic increase in $Re(\epsilon'/\epsilon)$ as we loosen this cut, so we use the shift associated with removing the cut, $(0.13 \pm 0.05)\times10^{-4}$, to calculate the error on $Re(\epsilon'/\epsilon)$. The uncertainty in $Re(\epsilon'/\epsilon)$ due to the cut on χ^2_γ is $\pm0.15\times10^{-4}$. Figure 7.11 shows the data-MC comparison for this variable.

We vary the cut on $\chi^2_{\pi^0}$ from 12 to 100. We see a significant systematic increase in $Re(\epsilon'/\epsilon)$ as we loosen this cut, so we use the shift associated with loosening the cut to $\chi^2_{\pi^0} < 100$ to find the systematic error. The shift is $(0.13 \pm 0.02)\times10^{-4}$ and

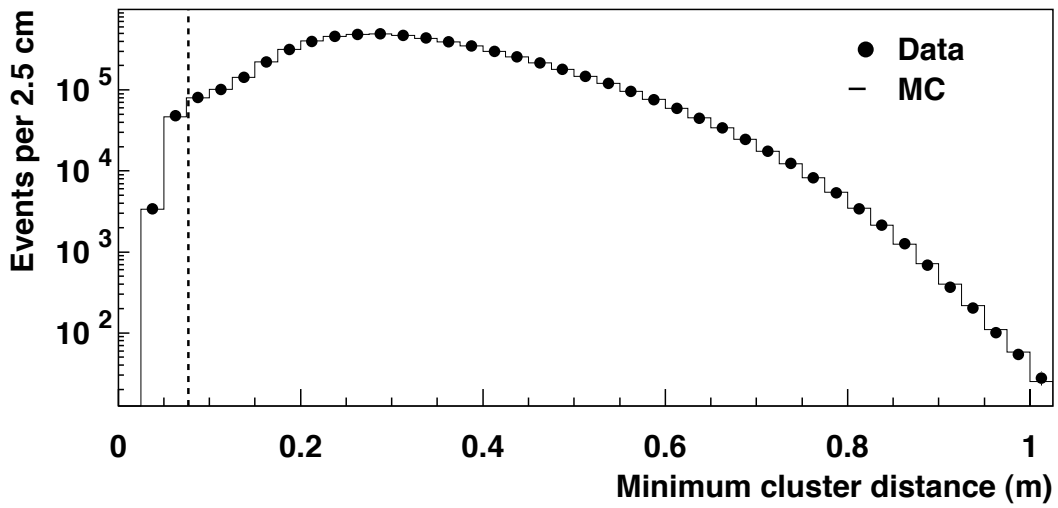

Figure 7.10: Minimum cluster separation for vacuum beam $K \to \pi^0\pi^0$ data and MC. The data is background subtracted. The dashed line indicates the value of our nominal cut.

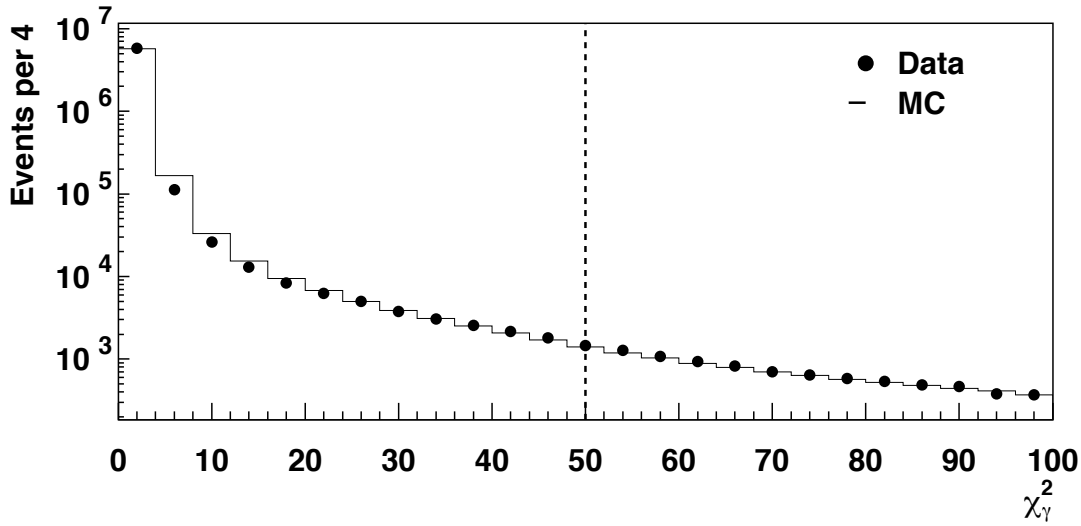

Figure 7.11: χ^2_γ for vacuum beam $K \to \pi^0\pi^0$ data and MC. The data is background subtracted. The dashed line indicates the value of our nominal cut.

the uncertainty in $Re(\epsilon'/\epsilon)$ due to the cut on $\chi^2_{\pi^0}$ is $\pm 0.14\times 10^{-4}$. Figure 7.12 shows the data-MC comparison for this variable.

We vary the RING cut from 100 cm^2 to 150 cm^2. We see a systematic decrease in $Re(\epsilon'/\epsilon)$ as we loosen this cut, so we use the shift associated with loosening the cut to RING $<$ 150 cm^2 to find the systematic error. The shift is (-0.24 $\pm$ 0.06) $\times 10^{-4}$ and the uncertainty in $Re(\epsilon'/\epsilon)$ due to the RING cut is $\pm 0.27\times 10^{-4}$. Figure 7.13 shows the data-MC comparison for this variable.

We vary the minimum cluster energy from 2.0 GeV to 4.0 GeV. We do not see a statistically significant shift in $Re(\epsilon'/\epsilon)$, but the errors are quite large. We believe that accepting minimum cluster energies below 3.0 GeV would be dangerous because the block energies would be close enough to the HCC thresholds that the result would be extremely sensitive to our modeling of these thresholds. For this reason, we are not very concerned about the fact that we are unable to statistically rule out a large systematic variation for a tighter cut. We do not quote any systematic error on $Re(\epsilon'/\epsilon)$ associated with the minimum cluster energy cut. Figure 7.14 shows the

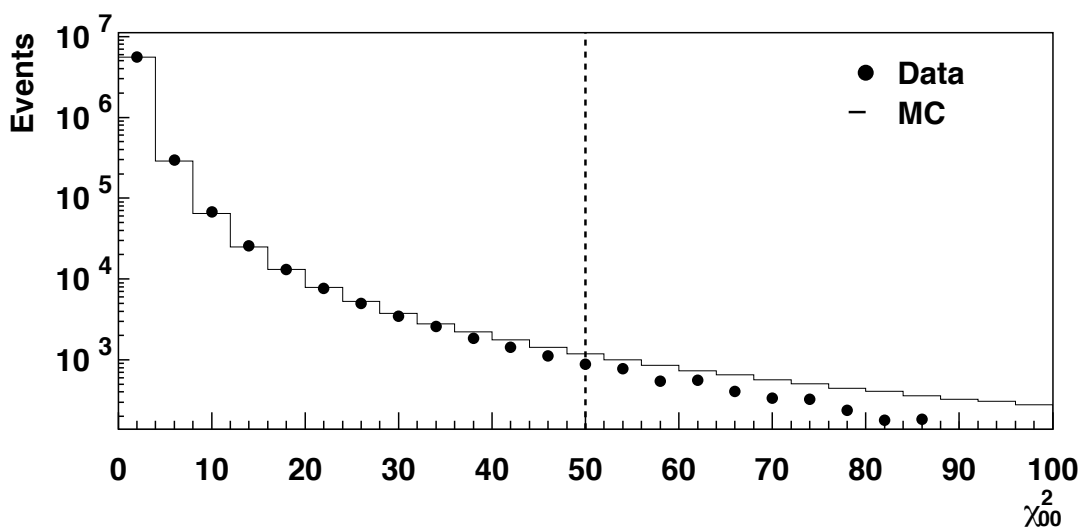

Figure 7.12: $\chi^2_{\pi^0}$ for vacuum beam $K \to \pi^0\pi^0$ data and MC. The data is background subtracted. The dashed line indicates the value of our nominal cut.

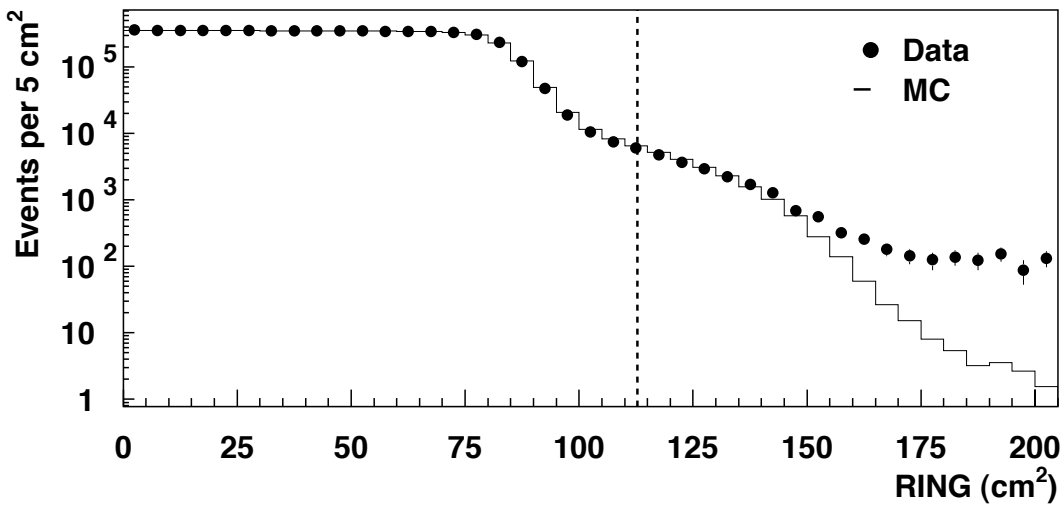

Figure 7.13: RING variable for vacuum beam $K \to \pi^0\pi^0$ data and MC. The data is background subtracted. The dashed line indicates the value of our nominal cut.

data-MC comparison for this variable. We investigate the effect of requiring the maximum cluster energy be less than 60 GeV; we do not see any significant change in $Re(\epsilon'/\epsilon)$ with this additional cut. Figure 7.15 shows the data-MC comparison for cluster energy and energy in the seed block; we do not cut on these variables but the agreement between data and MC gives us confidence in our modeling of cluster energies.

We vary the cut on SMLRING2 from no cut to removing events with a cluster seed within 3 blocks of the beam hole. We do not see a significant shift in $Re(\epsilon'/\epsilon)$ when we remove the cut. As we tighten the cut we rapidly loose statistics; we do not see any statistically significant shift in $Re(\epsilon'/\epsilon)$ as we tighten the cut, but the statistical errors are quite large. We do not quote any systematic error on $Re(\epsilon'/\epsilon)$ associated with the value of this cut.

We add in quadrature the errors associated with each cut variation. The total systematic uncertainty in $Re(\epsilon'/\epsilon)$ associated with our selection criteria is $\pm 0.34 \times 10^{-4}$.

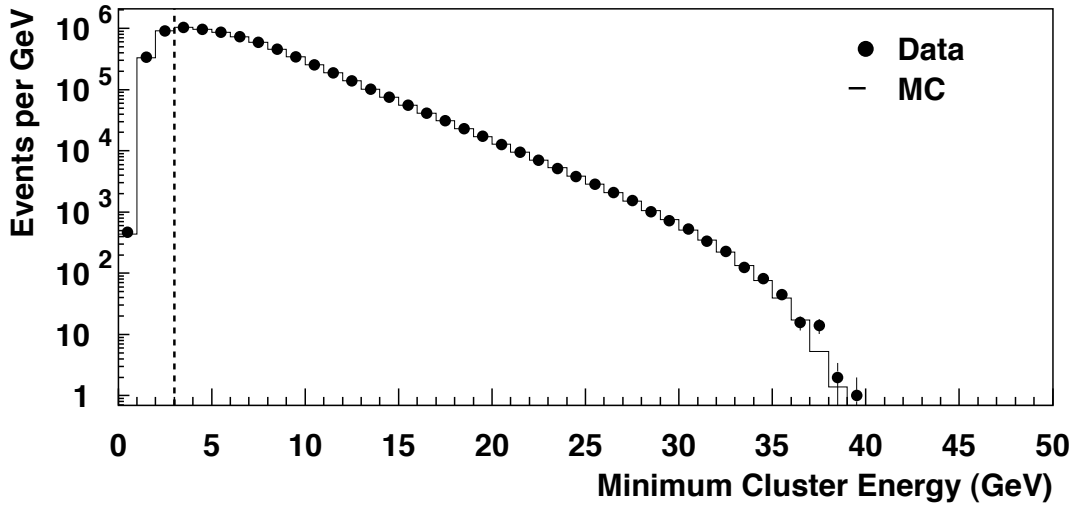

Figure 7.14: Minimum cluster energy for vacuum beam $K \to \pi^0\pi^0$ data and MC. The data is background subtracted. The dashed line indicates the value of our nominal cut.

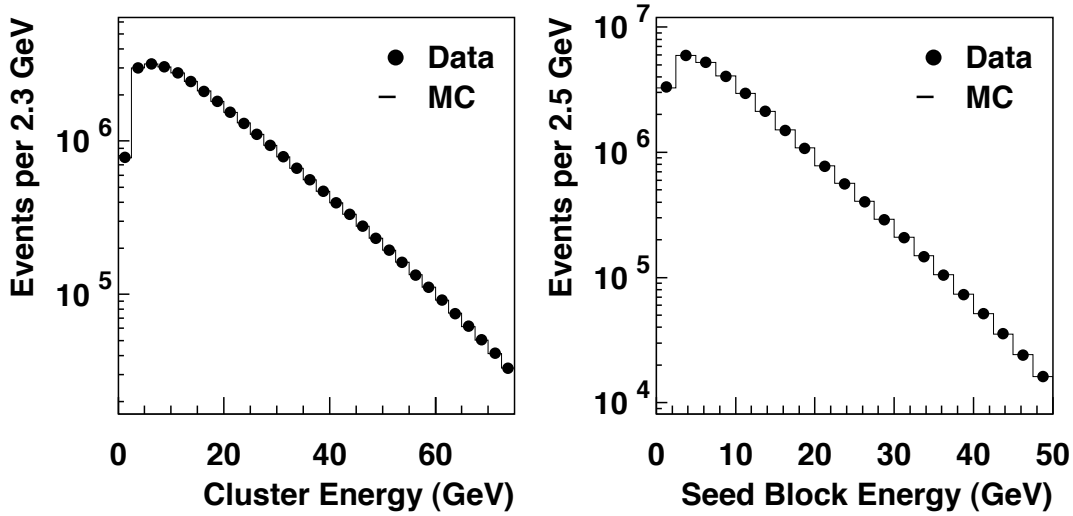

Figure 7.15: Cluster energy (left) and seed block energy (right) for vacuum beam $K \to \pi^0\pi^0$ data and MC. The data is background subtracted. We do not cut on these variables.

7.3.3 Energy Reconstruction

Non-Linearities

We evaluate the systematic due to energy non-linearities by studying the way the reconstructed kaon mass varies with reconstructed kaon energy, kaon z vertex, minimum cluster separation, and incident photon angle. Data-MC comparisons for these distributions from 1999 are shown in Figure 7.16. The data and MC agree very well in all of these distributions so we are confident that energy non-linearities in the analysis are well modeled by the Monte Carlo. To measure any bias due to energy non-linearities, we look for adjustments to the cluster energies that improve the agreement between data and MC in the plot of reconstructed kaon mass vs kaon energy. We find that the distortion which produces the best data-MC agreement is 0.1%/100 GeV for the 1997 and 1999 datasets. The 1996 dataset has slightly larger non-linearities; we find that 0.3%/100 GeV produces the best data-MC agreement for 1996. Figure 7.17 shows the improvement in data-MC agreement with the 0.1%/100 GeV distortion applied to 1999 data. To evaluate the systematic error associated with these non-linearities, we apply the distortion to the data, re-match the regenerator edge to find a new energy scale, subtract the backgrounds, and perform a new fit to see how the distortion affects our fit results. We find that $Re(\epsilon'/\epsilon)$ changes by less than 0.2×10^{-4} for all three distortions; there are also small changes in the data-MC z-slope associated with these distortions. Table 7.8 summarizes the changes we see with the non-linearity distortions. We estimate the systematic error for each dataset to be the change in $Re(\epsilon'/\epsilon)$ with the appropriate distortion applied relative to the nominal result. We combine the errors for the three datasets using a weighted average and find that the systematic uncertainty on $Re(\epsilon'/\epsilon)$ due to energy non-linearities is $\pm0.15\times10^{-4}$.

Energy Scale

As described in Section 3.2.4, we use the sharp edge in the regenerator beam $K \rightarrow \pi^0\pi^0$ z vertex distribution at the regenerator edge to match the energy scale between

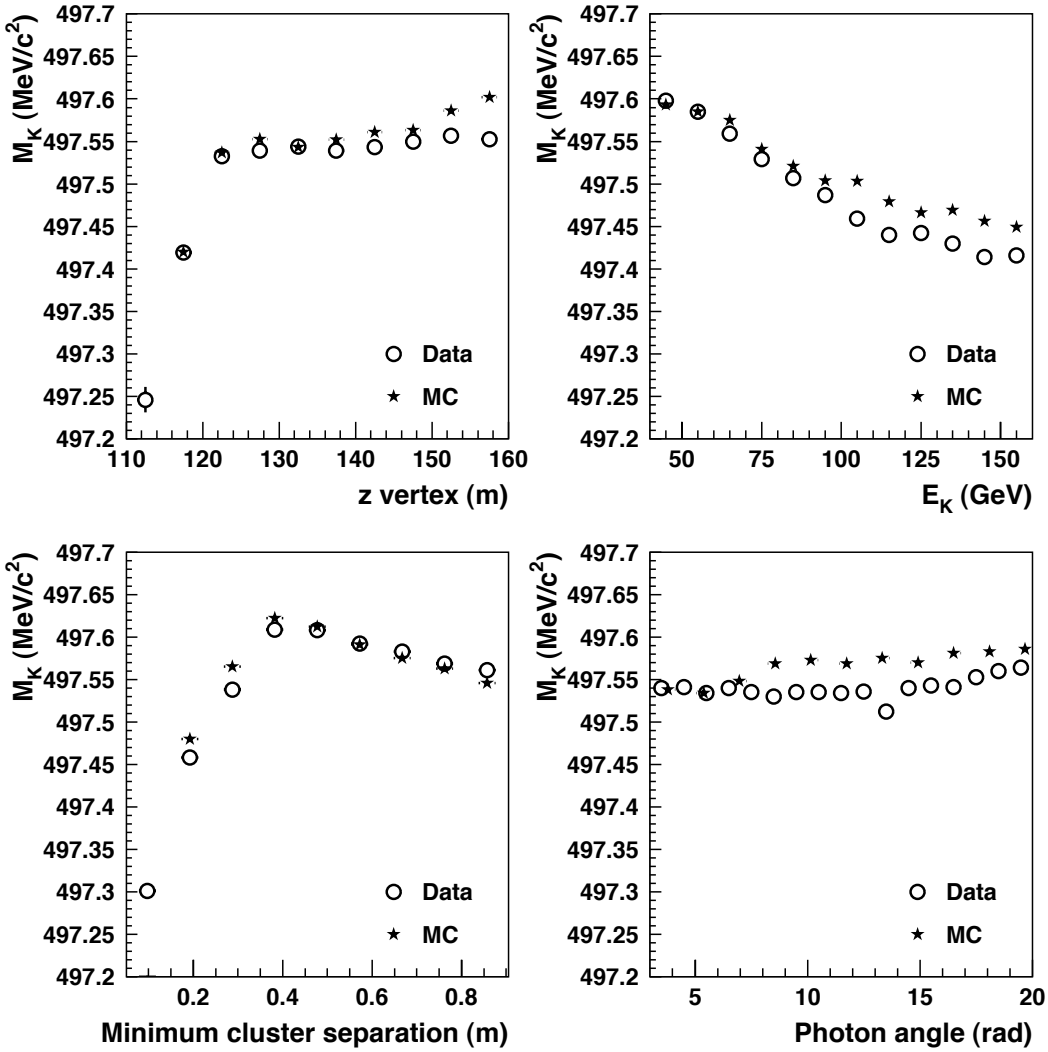

Figure 7.16: Comparisons of M_K vs z_K (top left), E_K (top right), minimum cluster separation (bottom left), and photon angle (bottom right) for 1999 data and MC.

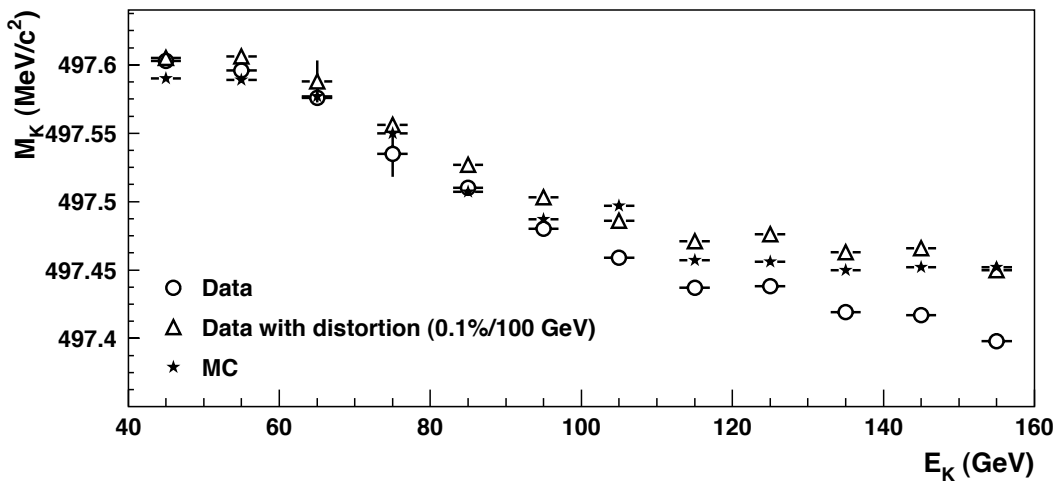

Figure 7.17: Effect of 0.1%/100 GeV distortion on M_K vs E_K for 1999 data.

Year	Non-linearity distortion per 100 GeV	$\Delta Re(\epsilon'/\epsilon)$ $\times 10^{-4}$	Δ z-slope $\times 10^{-4}$	Systematic Error $\times 10^{-4}$
1996	0.3%	-0.1	+0.30	$\pm$ 0.1
1997	0.1%	-0.1	+0.15	$\pm$ 0.1
1999	0.1%	+0.2	+0.22	$\pm$ 0.2

Table 7.8: Summary of energy non-linearity systematic studies

data and Monte Carlo. We know, therefore, that the energy scale matches between data and MC at the regenerator edge, but we must check whether the energy scale remains constant for the full length of the decay volume. Any systematic energy scale difference between data and MC as a function of z vertex leads to uncertainty in the $Re(\epsilon'/\epsilon)$ measurement since the vacuum and regenerator beam are affected differently. We check the energy scale at the downstream end of the decay region by studying the z vertex distribution of $\pi^0\pi^0$ pairs produced by hadronic interactions in the vacuum window in data and MC. We call this sample "vacuum window junk." To verify that this type of production has a comparable energy scale to $K \to \pi^0\pi^0$, we also study the z vertex distribution of hadronic $\pi^0\pi^0$ pairs produced in the regenerator or "regenerator junk." We check the 4-photon energy, individual

photon energy, and photon angle distributions in each of these samples to verify that they are comparable to $K \to \pi^0\pi^0$ decays.

To select the regenerator junk sample, we require the reconstructed $\pi^0\pi^0$ mass to be in the kaon mass sidebands, we do not apply a cut on RING number, we apply tight cuts on χ^2_γ and $\chi^2_{\pi^0}$ to reduce contamination from non-photons, and we remove any event with extra in-time clusters. We find that the total 4-photon energy in regenerator junk events is ∼20 GeV higher than in regenerator beam $K \to \pi^0\pi^0$ decays in the region 123 m $< z <$ 128 m, but for a given range of total energy the individual cluster energy and angle distributions agree well between the two samples.

To compare z vertex distributions between data and Monte Carlo for regenerator junk, we study the average production point for junk events. The hadronic interactions which produce the regenerator junk may occur in the lead or the scintillator of the regenerator; we vary the ratio of production cross-sections in lead and scintillator by 25% to bound the uncertainty in the production cross-sections and find that the average production point varies from 5.4-13.8 mm upstream of the end of the regenerator. In Monte Carlo, we simulate junk events produced 5.2 mm upstream of the end of the regenerator. We correct for differences in the mean production point before comparing the z vertex distributions between data and MC. The z vertex distributions of regenerator junk events for data and MC are shown in 7.18.

We compare the Gaussian z vertex distributions of regenerator junk events between data and MC by sliding the distributions past each other and using the KS test. The data-MC differences for each year are summarized in Table 7.9 and the average shift is plotted in Figure 7.20. Data and MC are generally in good agreement, though we see a 2.7 statistical σ difference between data and MC in 1997.

The actual z position of the vacuum window is measured to within 1 mm using charged two-track events produced in the vacuum window. We select $\pi^0\pi^0$ vacuum window junk events using the same criteria as for regenerator junk except that we require the z vertex to be near the vacuum window. We find that in the range 153 m $< z <$ 158 m, the 4-photon energy, individual cluster energy, and individual

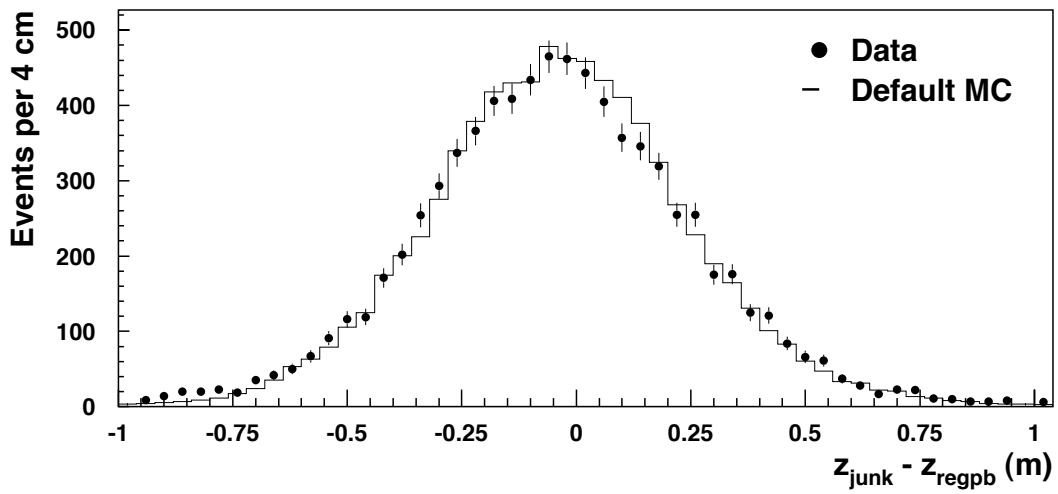

Figure 7.18: z vertex distributions of $\pi^0\pi^0$ pairs produced hadronically in the regenerator for 1999 data and MC.

cluster angle distributions agree well between $K \to \pi^0\pi^0$ decays and vacuum window junk.

The z distribution of vacuum window junk is not as simple as that of regenerator junk because the vacuum window junk is produced by four separate sources; the vacuum window, DC1, and two helium bags surrounding DC1. The production of vacuum window junk in each of these sources is simulated separately and a fit is used to determine the relative contribution of each material and to find the data-MC z vertex shift. Figure 7.19 shows the z vertex distributions of vacuum window junk before and after the shift is applied for 1999 data and MC. The z shifts measured for each year are summarized in Table 7.9 and are plotted in Figure 7.20.

We see a significant mismatch between data and MC in the vacuum window junk z distributions for all years. We evaluate the associated systematic error on $Re(\epsilon'/\epsilon)$ by applying a linearly varying energy scale distortion to data such that no adjustment is made at the regenerator edge and the z shift at the vacuum window is that measured by the vacuum window junk. The average energy scale distor-

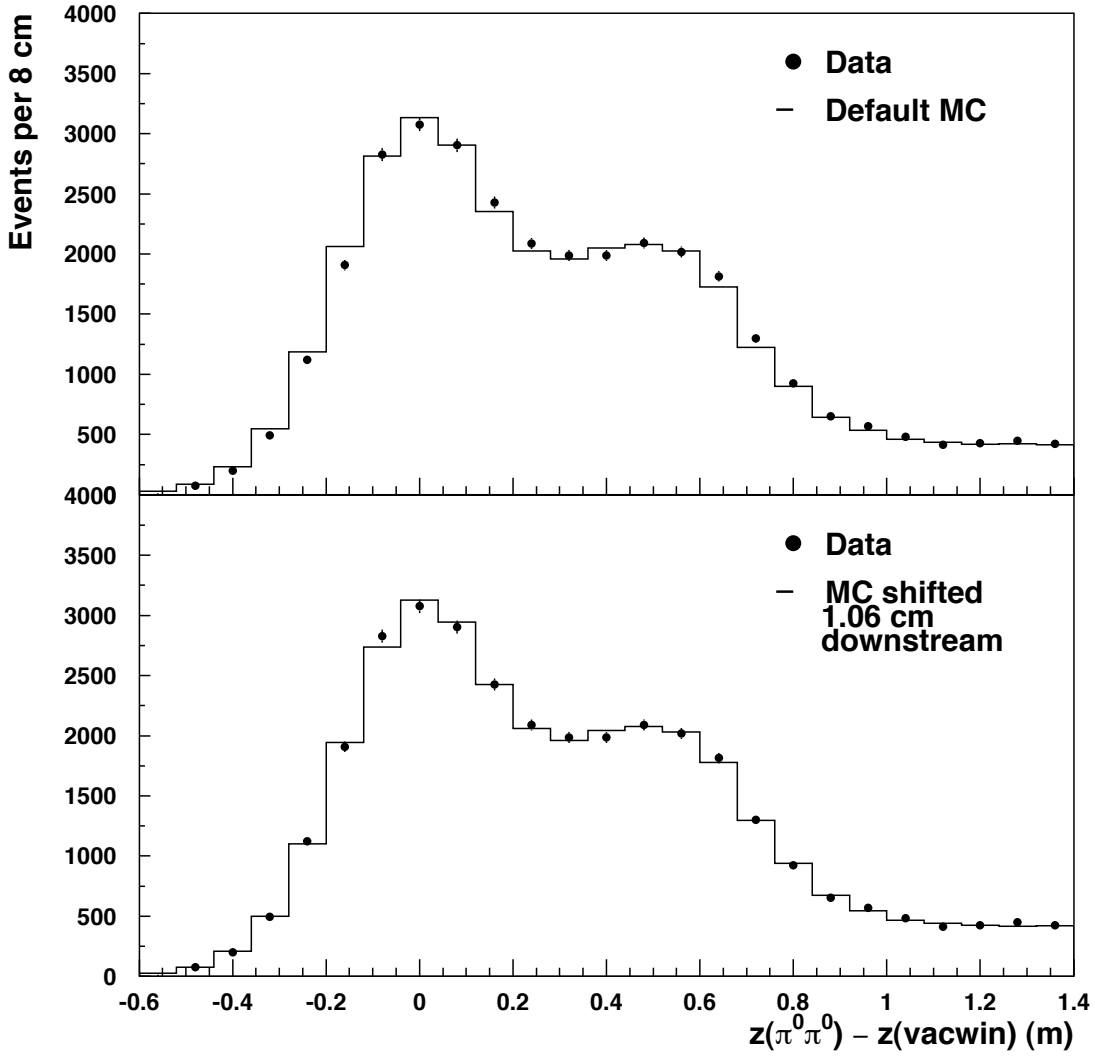

Figure 7.19: z vertex distributions of $\pi^0\pi^0$ pairs produced hadronically in the vacuum window for 1999 data and MC. The top plot shows data and nominal MC. The bottom plot shows data and MC that is shifted 1.06 cm downstream to match the data.

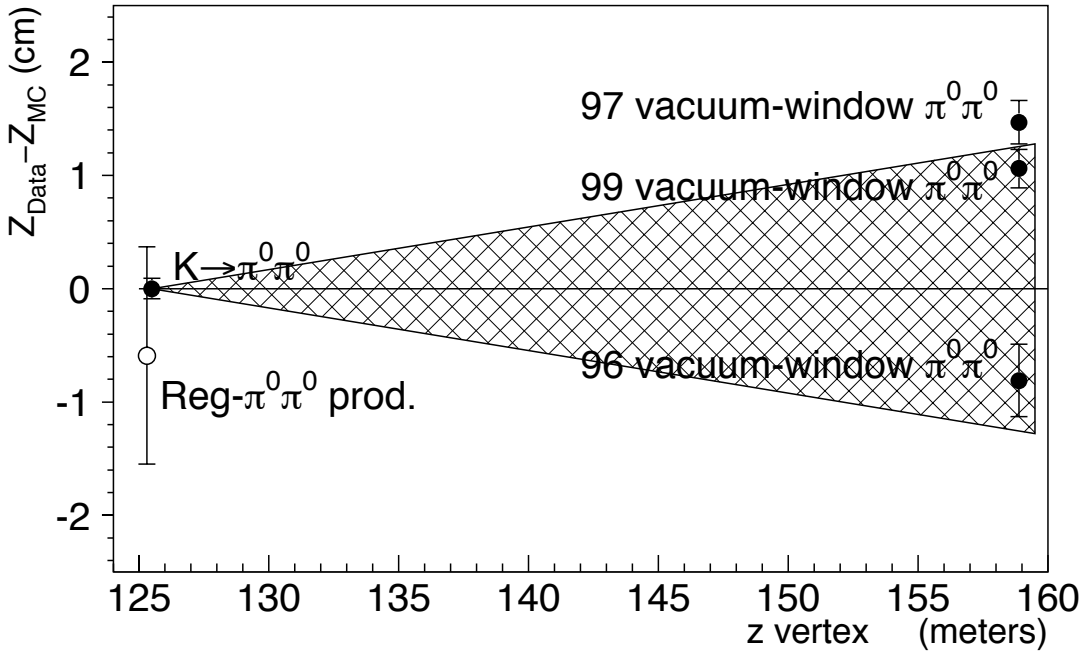

Figure 7.20: Energy scale tests at the regenerator and vacuum window. The difference between the reconstructed z positions for data and MC is plotted for the $K \to \pi^0\pi^0$, regenerator junk, and vacuum window junk samples. The solid point at the regenerator edge is the $K \to \pi^0\pi^0$ sample; there is no difference between data and MC by construction. The open point at the regenerator edge is the average shift of the regenerator junk samples for all three years. This point includes a systematic error in addition to the statistical error quoted in Table 7.9. The points at the vacuum window are the shifts for the vacuum window junk for each year separately. The hatched region shows the range of data-MC shifts covered by the total systematic uncertainty from the energy scale.

tion we apply is shown by the hatched region in Figure 7.20. We rule out energy scale distortions that vary non-linearly as a function of z vertex as they introduce data-MC discrepancies in other distributions. The changes in $Re(\epsilon'/\epsilon)$ with the distortion applied for each year are summarized in Table 7.9. The weighted average of these errors is 0.65×10^{-4}; we take this as the systematic error on $Re(\epsilon'/\epsilon)$ due to uncertainties in the $K \to \pi^0\pi^0$ energy scale.

Year	Regenerator Junk z_{data} - z_{MC} (cm)	Vacuum Window Junk z_{data} - z_{MC} (cm)	Error on $Re(\epsilon'/\epsilon)$ ($\times 10^{-4}$)
1996	0.24 ± 0.75	-0.81 ± 0.32	0.45
1997	-1.24 ± 0.46	1.47 ± 0.19	0.82
1999	-0.35 ± 0.42	1.06 ± 0.17	0.59
Average	-0.59 ± 0.48	0.97 ± 0.20	0.65

Table 7.9: Data-MC z shifts for hadronic $\pi^0\pi^0$ production in the regenerator and vacuum window.

Position Reconstruction

The systematic on $Re(\epsilon'/\epsilon)$ due to the position reconstruction is measured using K_{e3} electrons. We measure the difference between the reconstructed cluster position and the track position extrapolated to shower mean as a function of distance from the center of the seed block. The bias on $Re(\epsilon'/\epsilon)$ is determined using MC in which the track-cluster difference has been corrected using a parameterization. This study was performed for the previously published analysis and has not been repeated for the current analysis. The error on $Re(\epsilon'/\epsilon)$ due to the position reconstruction is $\pm 0.35 \times 10^{-4}$.

7.3.4 Backgrounds

The systematic uncertainty in $Re(\epsilon'/\epsilon)$ from backgrounds and background subtraction was evaluated for the 1996 and 1997 data in the previously published analysis[50]. As the background subtraction procedure is unchanged and the systematic error is rather conservative, we do not re-evaluate the systematics for 1996 and 1997; we take the error for 1999 to be the same as for 1997.

The error on $Re(\epsilon'/\epsilon)$ due to backgrounds in the $K \to \pi^0\pi^0$ analysis is dominated by the uncertainty due to regenerator scatters. The level of regenerator scattering depends on the p_T^2 acceptance, backgrounds to the $K \to \pi^+\pi^-$ analysis and details of the $\pi^+\pi^-$ reconstruction, the p_T^2 fit procedure and quality, and the veto differences between charged and neutral mode.

We use high p_T^2 $K \to \pi^+\pi^-$ decays to characterize regenerator scattering, so the p_T^2 acceptance and the $K \to \pi^+\pi^-$ analysis and backgrounds affect the measured level of regenerator scattering in $K \to \pi^0\pi^0$ decays. We compare the p_T^2 distributions in data and MC using $K_L \to \pi^+\pi^-\pi^0$ decays; we find that the data and MC agree to with 0.49 GeV^{-2}. The corresponding uncertainty in $Re(\epsilon'/\epsilon)$ is 0.4×10^{-4}. We check the effect of backgrounds to $K \to \pi^+\pi^-$ by varying the amount of collimator scatters, semi-leptonic background, and coherent tail by 15%, 20%, and 50%, respectively. We obtain the systematic uncertainty in $Re(\epsilon'/\epsilon)$ by summing in quadrature the changes in $Re(\epsilon'/\epsilon)$ associated with these variations. We vary the cuts on maximum energy deposit in the regenerator and the ring counters and the cut on extra clusters in the CsI in the $K \to \pi^+\pi^-$ analysis. We also break the $K \to \pi^+\pi^-$ data into subsets such as time periods and inbends/outbends. The largest change is associated with varying the cut on energy deposit in the regenerator. We assign a systematic error on $Re(\epsilon'/\epsilon)$ of 0.75×10^{-4} based on the largest change in $Re(\epsilon'/\epsilon)$ seen in these variations.

We measure the uncertainty on $Re(\epsilon'/\epsilon)$ due to the p_T^2 fitting procedure by varying fitting parameters such as bin size and kinematic region of the fit. Most variations have no effect. The largest change in $Re(\epsilon'/\epsilon)$, 0.3×10^{-4}, is associated with changing the p_T^2 binning; we assign an uncertainty of 0.3×10^{-4} as the uncertainty on $Re(\epsilon'/\epsilon)$ due to the fitting procedure. The quality of the p_T^2 fit is evaluated by comparing $K \to \pi^+\pi^-$ data to the fit in the 40 GeV to 160 GeV energy range. The fit agrees with the data to within 2.5%. The effect on $Re(\epsilon'/\epsilon)$ of a 2.5% variation in the overall normalization of the regenerator scattering background is 0.4×10^{-4}; we take this value as the systematic error on $Re(\epsilon'/\epsilon)$ due to the p_T^2 fit quality.

The $K \to \pi^+\pi^-$ and $K \to \pi^0\pi^0$ analyses have different veto requirements which leads to different levels of inelastic regenerator scattering backgrounds. The veto requirements do not affect the diffractive scattering background because secondary particles are not produced. In the $K \to \pi^0\pi^0$ analysis, the background level due to diffractive scattering is taken directly from the simulation but the normalization of the inelastic scattering background is floated using sidebands of the RING variable. We study the effect of normalizing the full diffractive + inelastic scattering background using RING sidebands and find that the change in $Re(\epsilon'/\epsilon)$ relative to

the nominal procedure is 0.3×10^{-4}. We assign this change as the uncertainty on $Re(\epsilon'/\epsilon)$ due to differing veto requirements between the $K \to \pi^+\pi^-$ and $K \to \pi^0\pi^0$ analyses.

The uncertainty in the normalization of collimator scatters is conservatively approximated to be 15%. The associated systematic uncertainty in $Re(\epsilon'/\epsilon)$ is 0.1×10^{-4}. The uncertainty in the normalization of the $K_L \to \pi^0\pi^0\pi^0$ background is measured by comparing the nominal background subtraction procedure (in which $3\pi^0$ background MC is normalized to mass sidebands) to a procedure in which the background level is found using data mass sidebands only. The change in $Re(\epsilon'/\epsilon)$, 0.06×10^{-4}, is taken as the systematic uncertainty in $Re(\epsilon'/\epsilon)$ due to the $K_L \to \pi^0\pi^0\pi^0$ background. We evaluate the systematic error due to hadronic production backgrounds by checking the effect on $Re(\epsilon'/\epsilon)$ of not subtracting these backgrounds. The error on $Re(\epsilon'/\epsilon)$ is 0.05×10^{-4}. The systematic error due to the other misreconstructed backgrounds which are not subtracted ($K_L \to \pi^0\gamma\gamma$ and $\Xi^0 \to \Lambda\pi^0$, $\Lambda \to n\pi^0$) is taken to be 0.1×10^{-4}.

Table 7.10 summarizes the systematic uncertainties in $Re(\epsilon'/\epsilon)$ due to backgrounds and background subtraction in the 1997 $K \to \pi^0\pi^0$ analysis. The total error for 1997 is 1.06×10^{-4}.

Background Source	Systematic Uncertainty on $Re(\epsilon'/\epsilon)$ ($\times10^{-4}$)
Regenerator Scatters:	
p_T^2 Acceptance	0.40
$K \to \pi^+\pi^-$ Backgrounds	0.20
$K \to \pi^+\pi^-$ Analysis	0.75
p_T^2 Fit Procedure	0.30
p_T^2 Fit Quality	0.40
Veto Differences	0.30
Collimator Scatters	0.10
$K_L \to \pi^0\pi^0\pi^0$ Background	0.06
Hadronic Production Backgrounds	0.05
Unsubtracted Backgrounds	0.10
Total	1.06

Table 7.10: Systematic errors due to backgrounds in the $K \to \pi^0\pi^0$ analysis.

7.3.5 Apertures

There are five apertures which define the $K \to \pi^0\pi^0$ acceptance. The CsI inner and outer apertures are defined by cuts which remove events with a seed block in the first ring of crystals around the beam holes or the outermost ring of crystals in the calorimeter. The inner aperture is measured by comparing the transverse positions of tracks from $K_L \to \pi^\pm e^\mp \nu$ decays extrapolated to the CsI with the associated cluster positions measured by the calorimeter. The uncertainty on the inner aperture is $\sim$100μm; the associated uncertainty in $Re(\epsilon'/\epsilon)$ is $\pm 0.42\times 10^{-4}$. The size of the CsI calorimeter is determined by surveys and is known to within 1 mm; the associated uncertainty in $Re(\epsilon'/\epsilon)$ is $\pm 0.15\times 10^{-4}$. The upstream aperture in the vacuum beam is defined by the MA. The MA effective size and location are measured with 100 μm precision using $K_L \to \pi^\pm e^\mp \nu$ decays. The uncertainty on $Re(\epsilon'/\epsilon)$ due to the 100 μm uncertainty in the MA aperture is $\pm 0.18\times 10^{-4}$. The upstream edge in the regenerator beam is defined by the effective regenerator edge which we calculate with an uncertainty of $\pm$0.1 mm; the associated uncertainty on $Re(\epsilon'/\epsilon)$ is $\pm 0.04\times 10^{-4}$. Finally, the requirement that photons be separated by at least 7.5 cm at the CsI creates an effective inner aperture. The effect of varying this cut is shown in section 7.3.2; we do not assign any systematic uncertainty associated with this cut. The total uncertainty in $Re(\epsilon'/\epsilon)$ due to apertures in the $K \to \pi^0\pi^0$ analysis is $\pm 0.48\times 10^{-4}$.

7.3.6 Summary

The systematic errors on $Re(\epsilon'/\epsilon)$ due to the $K \to \pi^0\pi^0$ analysis are summarized in Table 7.11. For reference, the systematic errors from the 2003 PRD[50] are also included in Table 7.11. Some systematics are evaluated separately for each dataset and then combined as a weighted average, some are evaluated for the combined 1996+1997+1999 dataset, and some are taken to be the same for all years. The total systematic error on $Re(\epsilon'/\epsilon)$ due to the neutral analysis is 1.55×10^{-4}.

Source	Error on $Re(\epsilon'/\epsilon)$ ($\times 10^{-4}$)				
	PRD	1996	1997	1999	Total
L1 Trigger	0.10	0.01	0.01	0.03	0.02
L2 Trigger	0.13	0.20	0.12	0.23	0.19
L3 Trigger	0.08	0.20	0.04	0.05	0.07
Ring Number	0.24	0.27			0.27
Pairing χ^2	0.20	0.14			0.14
Shape χ^2	0.20	0.15			0.15
Energy Nonlinearity	0.66	0.10	0.10	0.20	0.15
Energy Scale	1.27	0.45	0.82	0.59	0.65
Position Reconstruction	0.35	0.35			0.35
Background	1.07	1.14	1.06		1.07
CsI Inner Aperture	0.42	0.42			0.42
MA Aperture	0.18	0.18			0.18
Reg Edge	0.04	0.04			0.04
CsI Size	0.15	0.15			0.15
Acceptance	0.39	0.48			0.48
MC Statistics	0.40	0.75	0.37	0.41	0.25
Total	2.01	1.69	1.63	1.56	1.55

Table 7.11: Summary of systematic uncertainties in $Re(\epsilon'/\epsilon)$ from the $K \to \pi^0\pi^0$ analysis. For errors which are evaluated individually for each year, the individual errors are listed in columns and the total is the weighted average of the individual errors. For those errors which are evaluated for the full dataset or taken to be the same for all years, only one number is listed.

7.4 Fitter Systematics

Uncertainties from the fitting procedure are mainly related to regenerator properties and the dependence of the result on external parameters. The uncertainty on the momentum dependence of the regenerator transmission corresponds to a 0.08×10^{-4} uncertainty in $Re(\epsilon'/\epsilon)$. The sensitivity to our simulation of target-K_S is checked by floating the $K^0/\bar{K}^0$ flux ratio in the fit. This changes the target-K_S component by $(2.5 \pm 1.6)\%$ of itself; the associated systematic error on $Re(\epsilon'/\epsilon)$ is $\pm0.12\times10^{-4}$. The uncertainty in $Re(\epsilon'/\epsilon)$ due to the values of Δm and τ_S used in the fit is 0.11×10^{-4}. There are uncertainties due to the analyticity relation and screening models used to predict the regeneration phase. We estimate the systematic error from the ana-

lyticity assumption by allowing ϕ_ρ to deviate 0.25° from analyticity; the associated change in $Re(\epsilon'/\epsilon)$ is 0.07×10^{-4}. We vary the screening models in the fit and find that $Re(\epsilon'/\epsilon)$ varies by $\pm0.15\times10^{-4}$. The fit uses the same K_L/K_S flux ratio in both charged and neutral decay modes. Since the 1996 $K \to \pi^0\pi^0$ data has no corresponding $K \to \pi^+\pi^-$ data, it is possible that there could be differences in the flux ratio between the two years which do not cancel in the fit. We assign an uncertainty in $Re(\epsilon'/\epsilon)$ of $\pm0.03\times10^{-4}$ from this possibility. The value of τ_L used by the fitter is $(5.114 \pm 0.021)\times10^{-8}$ s[51]; the uncertainty in $Re(\epsilon'/\epsilon)$ due to the uncertainty in this measurement is 0.01×10^{-4}. The systematic uncertainties in $Re(\epsilon'/\epsilon)$ from the fitting procedure are summarized in Table 7.12. The total systematic uncertainty in $Re(\epsilon'/\epsilon)$ from fitting is $\pm0.25\times10^{-4}$.

Source	Error on $Re(\epsilon'/\epsilon)$ ($\times10^{-4}$)
Regenerator transmission	0.08
Target-K_S	0.12
Δm and τ_S	0.11
Regenerator screening	0.15
ϕ_ρ (analyticity)	0.07
1996 K_S/K_L flux ratio	0.03
τ_L	0.01
Total	0.25

Table 7.12: Summary of systematic uncertainties in $Re(\epsilon'/\epsilon)$ from the fitting procedure.

7.5 Changes Relative to 2003 Analysis

Upstream Z Vertex

The systematic error on $Re(\epsilon'/\epsilon)$ in the previously published analysis did not include any extra contribution from uncertainty in the acceptance upstream of the MA. The study and additional systematic error are added for the current analysis.

Drift Chamber Modeling Efficiency

The method used to estimate the error on $Re(\epsilon'/\epsilon)$ from the simulation of drift chamber inefficiencies has changed. In the previously published analysis, a large number of small adjustments were made to the Monte Carlo to evaluate the simulation of inefficiencies. In the current analysis, we make large changes by turning off the simulation of various affects and take the error to be 10% of the change in $Re(\epsilon'/\epsilon)$. The simulation of drift chamber efficiencies has been improved since the previous analysis through more detailed treatments of interactions in the drift chambers; this results in a reduction of the uncertainty in $Re(\epsilon'/\epsilon)$.

$K \to \pi^0\pi^0$ Level 1 Trigger

In the previously published analysis we took 1/6 of the measured L1 inefficiency as the systematic error on $Re(\epsilon'/\epsilon)$. As the beam yields in the energy range where there are inefficiencies present (40-60 GeV) differ by only 10%, this overestimated the error on $Re(\epsilon'/\epsilon)$ significantly. In the current analysis, we take the error to be 1/6 of the bias in the single ratio, or 10%/6 of the inefficiency, which reduces the error estimates by a factor of ten.

Energy Non-Linearities

We evaluate the systematic due to energy non-linearities by studying the way the reconstructed kaon mass varies with reconstructed kaon energy, kaon z vertex, minimum cluster separation, and incident photon angle. In the 2003 PRD there were significant data-MC differences in the way the kaon mass varied so a number of distortions were applied to the data to better match the data-MC distributions. These distortions included a non-linearity of the type we have applied, a non-linearity with an offset, an adjustment to shower positions to account for differences in shower depth, and an energy correction for close clusters.

In the current analysis the data-MC distributions match quite well and a simple non-linearity is enough to match all four distributions, so fewer distortions are inves-

tigated. The distortion we must apply to match data to MC is only 0.1%/100 GeV for the 1997 and 1999 data samples; we required a 0.7%/100 GeV distortion in the previous analysis for 1997 data to match only the M_K vs E_K and z_K distributions. The total systematic error due to energy non-linearities is therefore substantially smaller than in the previous analysis. This reduction is attributed to improvements in the simulation of showers in the CsI, improvements to the out-of-cone and longitudinal uniformity corrections, and the addition of the photon correction.

Energy Scale

The systematic error on $Re(\epsilon'/\epsilon)$ due to uncertainties in the energy scale is reduced considerably with respect to the previously published analysis. The method for evaluating this error is unchanged. The improvement in data-MC agreement is attributed to improvements in the $K \to \pi^0\pi^0$ analysis, especially the simulation of showers in the CsI and the out-of-cone correction.

7.6 Summary of Systematic Errors for $Re(\epsilon'/\epsilon)$

The systematic uncertainties in $Re(\epsilon'/\epsilon)$ from the $K \to \pi^+\pi^-$ and $K \to \pi^0\pi^0$ analyses are summarized in Table 7.13. The total systematic uncertainty in $Re(\epsilon'/\epsilon)$ is $\pm 1.77 \times 10^{-4}$. The $K \to \pi^+\pi^-$ analysis, the $K \to \pi^0\pi^0$ analysis, and the fitting procedure contribute 21%, 77%, and 2% of the uncertainty, respectively.

7.7 Systematic Errors for Kaon Sector Parameters

The systematic errors for Δm, τ_S, ϕ_{+-}, and $\Delta\phi$ are evaluated using the same methods used for $Re(\epsilon'/\epsilon)$. The systematic errors on each of these parameters from the $K \to \pi^+\pi^-$ analysis, the $K \to \pi^0\pi^0$ analysis, and fitting are summarized in Table 7.14. The fitting errors are common to the $K \to \pi^+\pi^-$ and $K \to \pi^0\pi^0$ analyses. To combine the charged and neutral results for Δm and τ_S we take an average weighted by the statistical uncertainty and the independent parts of the systematic uncertainty.

Source	Error on $Re(\epsilon'/\epsilon)$ ($\times 10^{-4}$)	
	$K \to \pi^+\pi^-$	$K \to \pi^0\pi^0$
Trigger	0.23	0.20
CsI cluster reconstruction	—	0.75
Track reconstruction	0.22	—
Selection efficiency	0.23	0.34
Apertures	0.30	0.48
Acceptance	0.57	0.48
Backgrounds	0.20	1.07
MC statistics	0.20	0.25
Total	0.81	1.55
Fitting	0.25	
Total	1.77	

Table 7.13: Summary of systematic uncertainties in $Re(\epsilon'/\epsilon)$. See Tables 7.4 and 7.11 for more details on the errors from the $K \to \pi^+\pi^-$ and $K \to \pi^0\pi^0$ analyses, respectively.

Source	Error in: Δm ($\times 10^6$ $\hbar$s^{-1})	τ_S ($\times 10^{-12}$ s)	ϕ_{+-} ($^\circ$)	$\Delta\phi$ ($^\circ$)
$K \to \pi^+\pi^-$ Analysis:				
Trigger	0.2	0.004	0.10	0.02
Track Reconstruction	0.6	0.007	0.08	0.04
Selection Efficiency	1.1	0.002	0.13	0.02
Apertures	2.0	0.011	0.33	0.08
Background	2.0	0.002	0.01	0.01
Acceptance	0.2	0.014	0.06	0.05
MC Statistics	1.5	0.007	0.16	0.03
Fitting:				
Regenerator Transmission	4.6	0.012	0.05	0.00
Other Fitting Errors	8.8	0.040	0.80	0.02
$K \to \pi^+\pi^-$ Total	10.5	0.047	0.90	0.11
$K \to \pi^0\pi^0$ Analysis:				
Trigger	0.4	0.014	—	0.03
CsI Reconstruction:				
Energy nonlinearity	1.3	0.010	—	0.03
Energy scale	3.1	0.041	—	0.17
Selection efficiency	2.2	0.022	—	0.06
Apertures	2.2	0.040	—	0.14
Acceptance	2.5	0.037		0.06
MC Statistics	2.2	0.011	—	0.04
Fitting:				
Regenerator Transmission	2.1	0.041	—	0.03
Other Fitting Errors	8.8	0.040	—	0.03
$K \to \pi^0\pi^0$ Total	10.7	0.094	—	0.25
Combined Total (incl. σ_{stat})	10.5	0.050	—	0.31

Table 7.14: Systematic uncertainties in kaon parameters

CHAPTER 8
RESULTS

8.1 ϵ'/ϵ Results

The fit result from Section 6.3.1 is corrected by $+0.3\times10^{-4}$ to remove the bias in the charged mode level 3 trigger as discussed in Section 7.2.1. The statistical error is the data error only; the error from Monte Carlo statistics is included in the systematic error. The final KTeV measurement of $Re(\epsilon'/\epsilon)$ including data from 1996, 1997, and 1999 is:

$$\begin{aligned} Re(\epsilon'/\epsilon) &= [19.2 \pm 1.1(stat) \pm 1.8(syst)] \times 10^{-4} \\ &= (19.2 \pm 2.1) \times 10^{-4}. \end{aligned} \tag{8.1}$$

For comparison with previous KTeV publications[22, 50], we also present the results using 1996, 1997, and 1999 data separately in Table 8.1. Note that this comparison is not exact since we use the 1997 $K \to \pi^+\pi^-$ sample for both "1996" and "1997"; these results are intended only for comparison of the 1996 and 1997 $K \to \pi^0\pi^0$ samples.

8.1.1 ϵ'/ϵ Crosschecks

We crosscheck our result by breaking the data into subsets and checking the consistency of the $Re(\epsilon'/\epsilon)$ result in the various subsets. To check for any time dependence, we break the data into 11 run ranges with roughly equal statistics. There are five run ranges in 1997 and six in 1999. Since the 1996 $K \to \pi^0\pi^0$ data does not have any corresponding $K \to \pi^+\pi^-$ data, we combine it with the neutral mode data in

Year	$K \to \pi^0\pi^0$ sample	$K \to \pi^+\pi^-$ sample	$Re(\epsilon'/\epsilon)$ $\times 10^{-4}$
1996	1996	1997	$20.8 \pm 2.8 \pm 2.0$ $= 20.8 \pm 3.4$
1997	1997	1997	$18.9 \pm 1.7 \pm 2.0$ $= 18.9 \pm 2.6$
1999	1999	1999	$19.0 \pm 1.4 \pm 1.8$ $= 19.0 \pm 2.3$

Table 8.1: $Re(\epsilon'/\epsilon)$ results by year. Note that the "1996" and "1997" results use the same $K \to \pi^+\pi^-$ data and are intended only to compare the $K \to \pi^0\pi^0$ samples.

the first 1997 run range. The $Re(\epsilon'/\epsilon)$ result for each run range is shown in Figure 8.1. We find consistent results in all of the run ranges.

In 1999 we took data at high and low intensity so we are able to check for any dependence of $Re(\epsilon'/\epsilon)$ on beam intensity using the 1999 data. Figure 8.2 shows the $Re(\epsilon'/\epsilon)$ result for SEM $< 5 \times 10^{12}$ and SEM $> 5 \times 10^{12}$. The low intensity sample

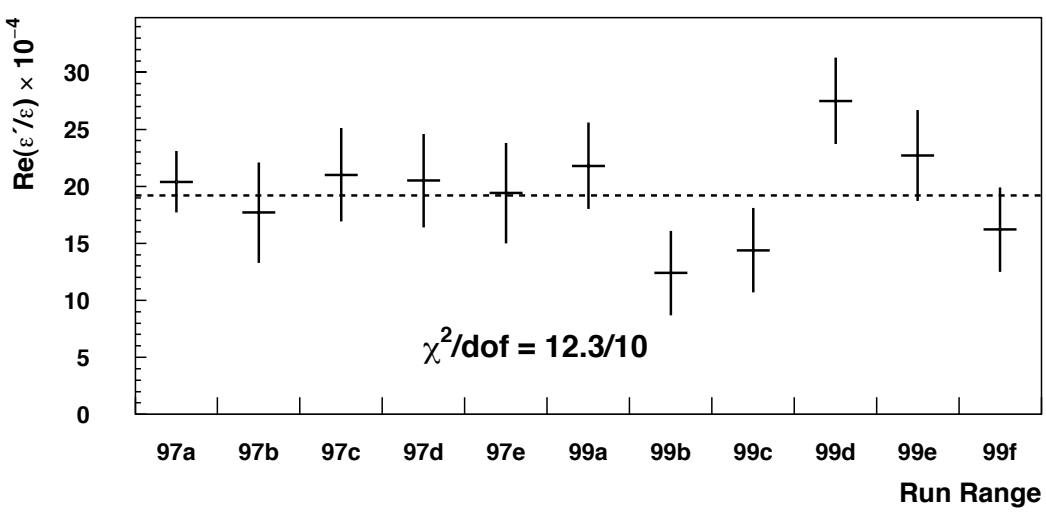

Figure 8.1: $Re(\epsilon'/\epsilon)$ in subsets of the data sample. Each point is statistically independent. The dashed line indicates the value of $Re(\epsilon'/\epsilon)$ for the full data sample. The 97a run range includes the 1996 $K \to \pi^0\pi^0$ data.

has an average SEM of 4×10^{12} and the high intensity sample has an average SEM of 6.5×10^{12}. We break the data in half based on regenerator position; Figure 8.2 also shows the value of $Re(\epsilon'/\epsilon)$ for each regenerator position. In these comparisons, each data point is statistically independent. All of these comparisons show good agreement.

There are several crosschecks of the $K \to \pi^+\pi^-$ sample for which we do not break up the $K \to \pi^0\pi^0$ sample. We break the $K \to \pi^+\pi^-$ sample in half based on the polarity of the analysis magnet and whether the tracks bend inward or outward in the magnet. In each of these cases, the $K \to \pi^0\pi^0$ sample is common to both data points and the errors are estimated by the difference between the subset error and the nominal error in quadrature. Figure 8.2 shows the $Re(\epsilon'/\epsilon)$ results for each of these subsets; they all show good agreement. The fit results for track inbends and outbends are both larger than the nominal result; in this case the regeneration parameter, α, has changed in each fit to allow the higher values of $Re(\epsilon'/\epsilon)$.

We check for dependence on kaon momentum by breaking the data into twelve 10 GeV/c momentum bins. In these fits, we fix the power-law dependence of the regeneration amplitude to the value found in the nominal fit (α = -0.53810). The free parameters are $Re(\epsilon'/\epsilon)$, $|f_-(70\text{ GeV}/c)|$, and the charged and neutral kaon fluxes. Figure 8.3 shows the values of $Re(\epsilon'/\epsilon)$ and $|f_-(70\text{ GeV}/c)|$ for these fits. We see no evidence for dependence of the $Re(\epsilon'/\epsilon)$ result on kaon momentum.

8.2 Kaon Sector Parameter Results

The measurements of Δm and τ_S using the $K \to \pi^+\pi^-$ dataset are:

$$\begin{aligned} \Delta m &= [5269.0 \pm 3.8(stat) \pm 10.5(syst)]\times10^6\ \hbar\text{s}^{-1} \qquad (8.2) \\ &= (5269.0 \pm 11.2)\times10^6\ \hbar\text{s}^{-1} \\ \tau_S &= [89.620 \pm 0.019(stat) \pm 0.047(syst)]\times10^{-12}\ \text{s} \qquad (8.3) \\ &= (89.620 \pm 0.051)\times10^{-12}\ \text{s}. \end{aligned}$$

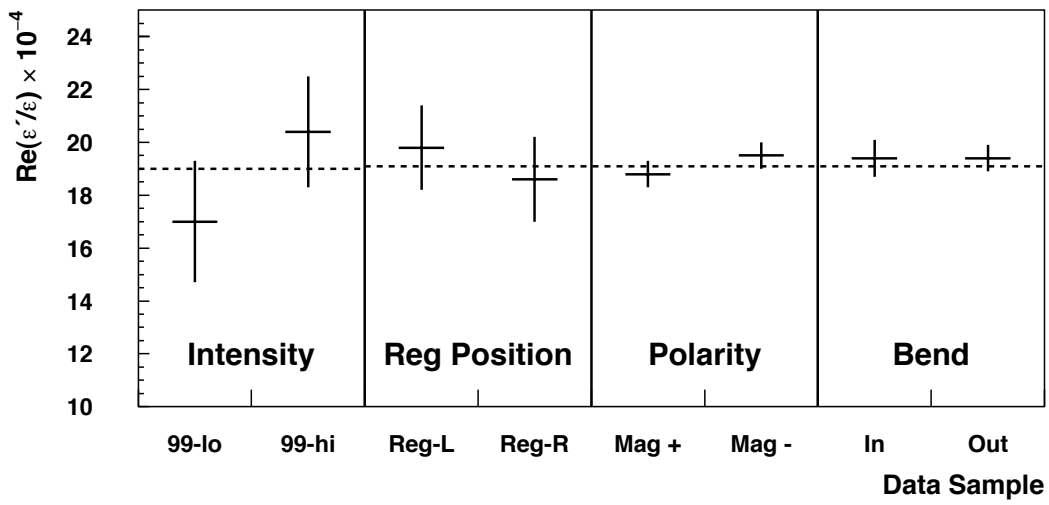

Figure 8.2: $Re(\epsilon'/\epsilon)$ consistency with beam intensity, regenerator position, magnet polarity, and track bend. The low intensity sample has an average SEM of 4×10^{12} and the high intensity sample has an average SEM of 6.5×10^{12}. These subsets are for the 1999 data only. Reg-left and reg-right refer to the position of the regenerator beam in the detector. These subsets are for the full data sample. Mag+ and Mag- are the magnet polarity and in/out are the bend of the two tracks in the magnet. In each of these subsets the $K \to \pi^0\pi^0$ sample is common to both fits; the errors are estimated by taking the quadrature difference with the error for the full dataset. The dashed lines indicate the value of $Re(\epsilon'/\epsilon)$ in the appropriate full data sample.

The measurements of Δm and τ_S using the $K \to \pi^0\pi^0$ dataset are:

$$\begin{aligned} \Delta m &= [5257.6 \pm 7.9(stat) \pm 10.7(syst)]\times10^6\ \hbar\mathrm{s}^{-1} && (8.4) \\ &= (5257.6 \pm 13.3)\times10^6\ \hbar\mathrm{s}^{-1} \\ \tau_S &= [89.667 \pm 0.037(stat) \pm 0.094(syst)]\times10^{-12}\ \mathrm{s} && (8.5) \\ &= (89.667 \pm 0.101)\times10^{-12}\ \mathrm{s}. \end{aligned}$$

We combine the $K \to \pi^+\pi^-$ and $K \to \pi^0\pi^0$ measurements of Δm and τ_S weighted by the statistical uncertainty and the independent part of the systematic

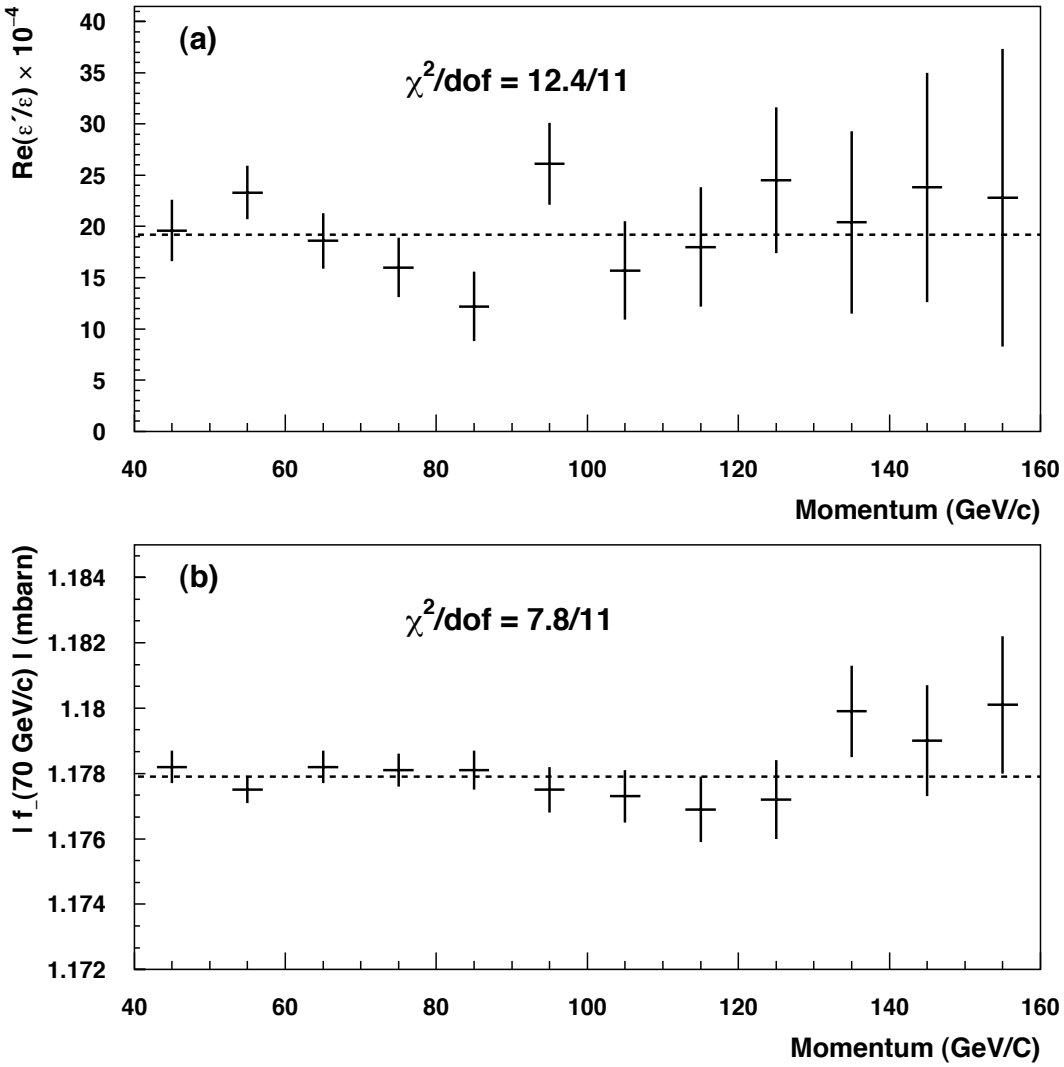

Figure 8.3: (a) $Re(\epsilon'/\epsilon)$ and (b) $|f_-(70\ \mathrm{GeV}/c)|$ in 10 GeV/c momentum bins. The dashed line indicates the value for the full data sample.

uncertainty. The combined results are:

$$\begin{aligned} \Delta m &= (5265 \pm 11)\times 10^{6}\ \hbar s^{-1} \\ \tau_S &= (89.62 \pm 0.05)\times 10^{-12}\ \text{s.} \end{aligned} \tag{8.6}$$

The measurements of ϕ_{+-} and $\phi_{+-} - \phi_{SW}$ using the $K \to \pi^+\pi^-$ dataset are:

$$\begin{aligned} \phi_{+-} &= [44.09 \pm 0.43(stat) \pm 0.90(syst)]^\circ \\ &= (44.09 \pm 1.00)^\circ \end{aligned} \tag{8.7}$$

$$\begin{aligned} \phi_{+-} - \phi_{SW} &= [0.59 \pm 0.38(stat) \pm 0.78(syst)]^\circ \\ &= (0.59 \pm 0.87)^\circ \end{aligned} \tag{8.8}$$

The measurement of $Im(\epsilon'/\epsilon)$ and the corresponding value of $\Delta\phi$ using the full KTeV dataset are:

$$\begin{aligned} Im(\epsilon'/\epsilon) &= [-17.0 \pm 8.8(stat) \pm 15.7(syst)] \times 10^{-4} \\ &= (-17.0 \pm 18.0) \times 10^{-4} \end{aligned} \tag{8.9}$$

$$\begin{aligned} \Delta\phi &= [0.29 \pm 0.15(stat) \pm 0.27(syst)]^\circ \\ &= (0.29 \pm 0.31)^\circ. \end{aligned} \tag{8.10}$$

The results for the kaon sector parameters using the full 1996, 1997, and 1999 KTeV datasets are summarized in Table 8.2.

8.2.1 Kaon Sector Parameter Crosschecks

We perform the same crosschecks for the Δm, τ_S, ϕ_{+-}, and $\Delta\phi$ measurements that are described above for $Re(\epsilon'/\epsilon)$. The plots of these crosschecks may be found in appendix A. Figures A.1-A.6 show the results for the kaon sector parameters broken into run ranges. In the fits for Δm and τ_S using the $K \to \pi^0\pi^0$ data we keep the 1996 data separate from 1997a, so there are twelve run ranges rather than eleven. We do not see any evidence for run dependence of the results. Figures A.7-A.12

Parameter	Dataset Used	Result
Δm	$K \to \pi^+\pi^-$	$(5269.0 \pm 11.2)\times 10^6\ \hbar s^{-1}$
	$K \to \pi^0\pi^0$	$(5257.6 \pm 13.3)\times 10^6\ \hbar s^{-1}$
	weighted average	$(5265 \pm 11)\times 10^6\ \hbar s^{-1}$
τ_S	$K \to \pi^+\pi^-$	$(89.620 \pm 0.051)\times 10^{-12}$ s
	$K \to \pi^0\pi^0$	$(89.677 \pm 0.101)\times 10^{-12}$ s
	weighted average	$(89.62 \pm 0.05)\times 10^{-12}$ s
ϕ_{+-}	$K \to \pi^+\pi^-$	$(44.09 \pm 1.00)^\circ$
$\phi_{+-} - \phi_{SW}$	$K \to \pi^+\pi^-$	$(0.59 \pm 0.87)^\circ$
$\Delta\phi$	$K \to \pi^+\pi^-$ and $K \to \pi^0\pi^0$	$(0.29 \pm 0.31)^\circ$

Table 8.2: Summary of kaon sector parameter results. The weighted average is the result of combining the results from $K \to \pi^+\pi^-$ and $K \to \pi^0\pi^0$ weighted by the statistical and independent parts of the systematic uncertainty.

show the results for the kaon sector parameter fits with the data set split in half in various ways. None of these crosschecks show any signs of a bias.

We check the kaon sector parameters for dependence on momentum by dividing the dataset into momentum bins. These plots are also found in appendix A. Some of the z-binned fits do not have enough statistics at high momenta for the fits to converge, so we either combine data or stop fitting at higher momenta. For the Δm and τ_S fits to the $K \to \pi^+\pi^-$ data, we stop fitting above 110 GeV/c. For the Δm and τ_S fits to the $K \to \pi^0\pi^0$ data, we combine data with kaon momenta from 90-160 GeV/c in a single bin. For the $\Delta\phi$ fits, we stop fitting above 120 GeV/c. Figures A.13 - A.18 show the results for the kaon sector parameters in momentum bins. We see no evidence for dependence on kaon momentum in these fits.

8.3 Comparison to Other Measurements

Combining results from E731[21], NA31[20], and NA48[49] with the final KTeV result presented here, the new world average is:

$$Re(\epsilon'/\epsilon) = (16.8 \pm 1.4) \times 10^{-4}. \tag{8.11}$$

The probability for this average is 13%. Figure 8.4 compares the four measurements and the new world average.

Combining the new KTeV results with the other results included in the PDG 2006[51] averages, the new world averages for Δm and τ_S are:

$$\begin{aligned} \Delta m &= (5277 \pm 9) \times 10^6\ \hbar \mathrm{s}^{-1} \\ \tau_S &= (89.59 \pm 0.04) \times 10^{-12}\ \mathrm{s} \end{aligned} \tag{8.12}$$

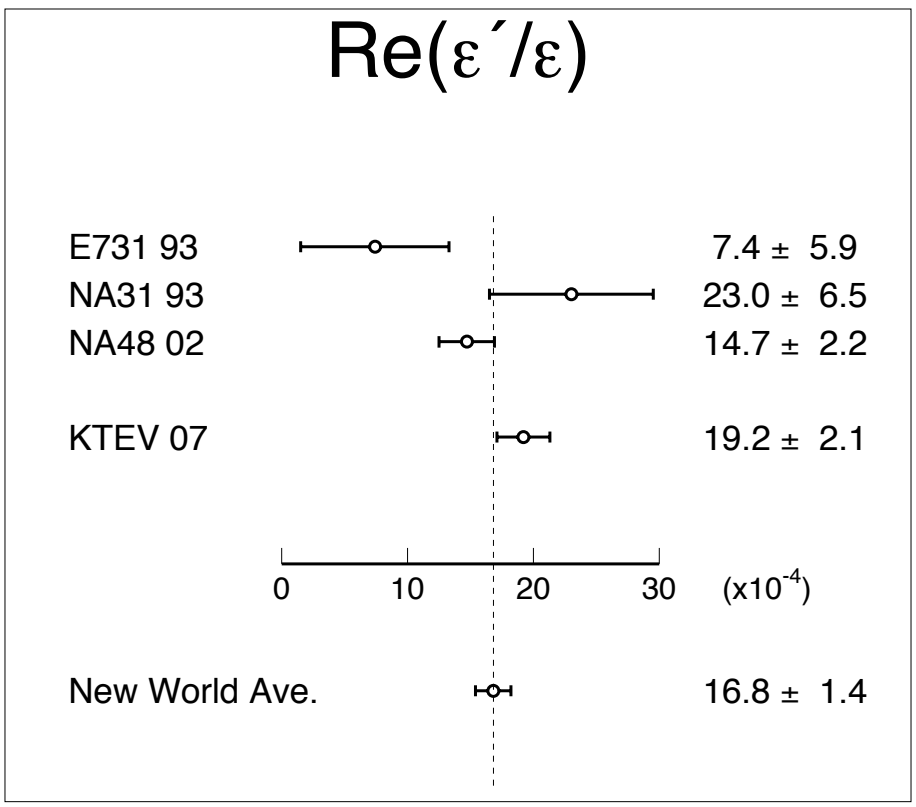

Figure 8.4: New world average for $Re(\epsilon'/\epsilon)$ combining results from E731[21], NA31[20], NA48[49], and KTeV.

Figures 8.5 and 8.6 compare the previous measurements to the current measurement and the new world average.

Figures 8.7 and 8.5 compare the new KTeV results for ϕ_{+-} and $\Delta\phi$ presented here to the previous measurements.

8.4 Conclusions

The primary goal of this analysis is the precision measurement of parameters related to direct CP violation and CPT symmetry in the neutral kaon system.

We measure the direct CP violation parameter $Re(\epsilon'/\epsilon) = (19.2 \pm 2.1)\times10^{-4}$. This is the final KTeV measurement of $Re(\epsilon'/\epsilon)$ using data from 1996, 1997, and 1999. The systematic error associated with this measurement, particularly in the analysis of $K \to \pi^0\pi^0$ decays, is significantly reduced relative to previous KTeV measurements. The final results from NA48 and KTeV differ by only 1.5σ and together provide a precise measurement of the level of direct CP violation in the neutral kaon system. This measurement may be used as a test of the Standard Model and beyond once theoretical predictions of $Re(\epsilon'/\epsilon)$ are improved using lattice QCD.

We measure the kaon sector parameters, $\Delta m = (5265 \pm 11)\times10^6\ \hbar s^{-1}$ and $\tau_S = (89.62 \pm 0.05)\times10^{-12}$ s. The errors associated with these measurements have also been reduced. The KTeV measurement of Δm is in good agreement with measurements from the 1990s, and the KTeV measurement of τ_S agrees well with previous measurements.

We measure $\phi_{+-} - \phi_{SW}$ and $\Delta\phi$ as tests of CPT symmetry. Both measurements are consistent with previous measurements and with CPT symmetry.

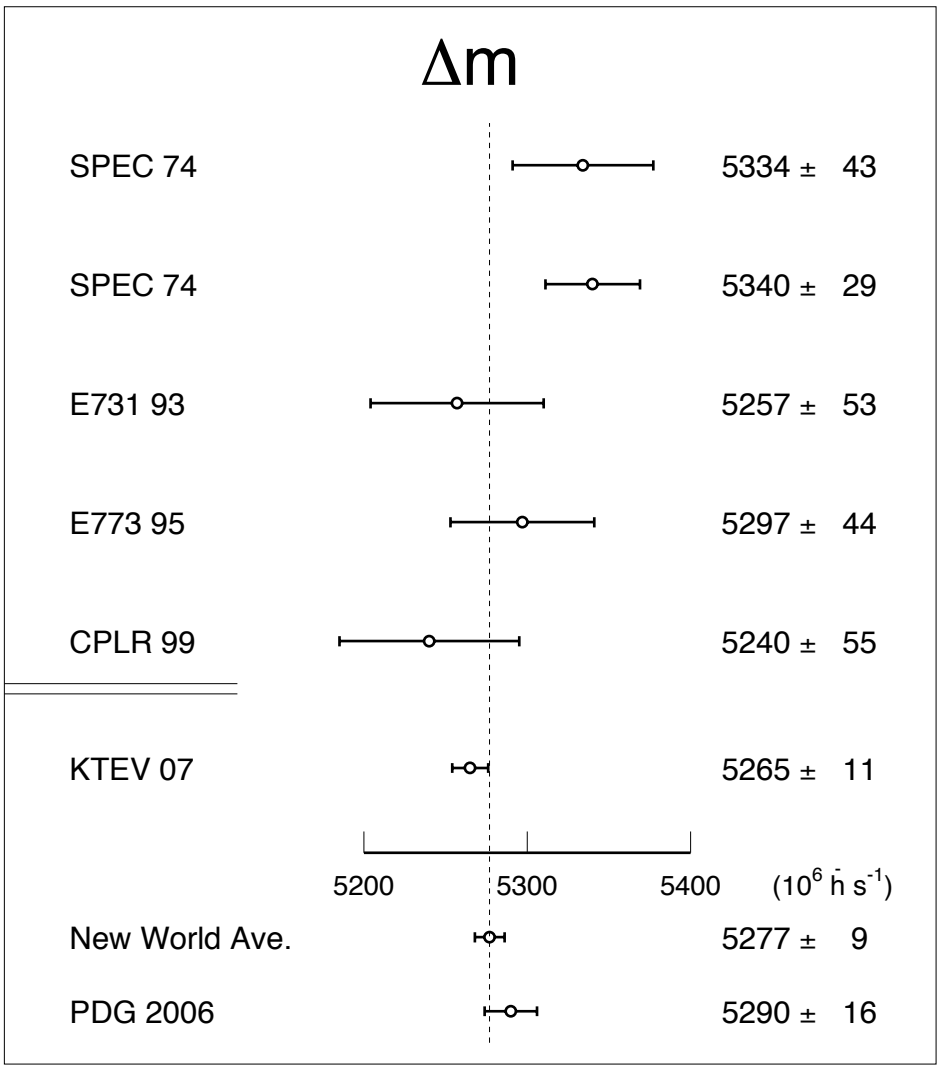

Figure 8.5: New world average for Δm combining results from SPEC74[53, 54], E731[55], E773[52], and CPLR[56], and KTeV.

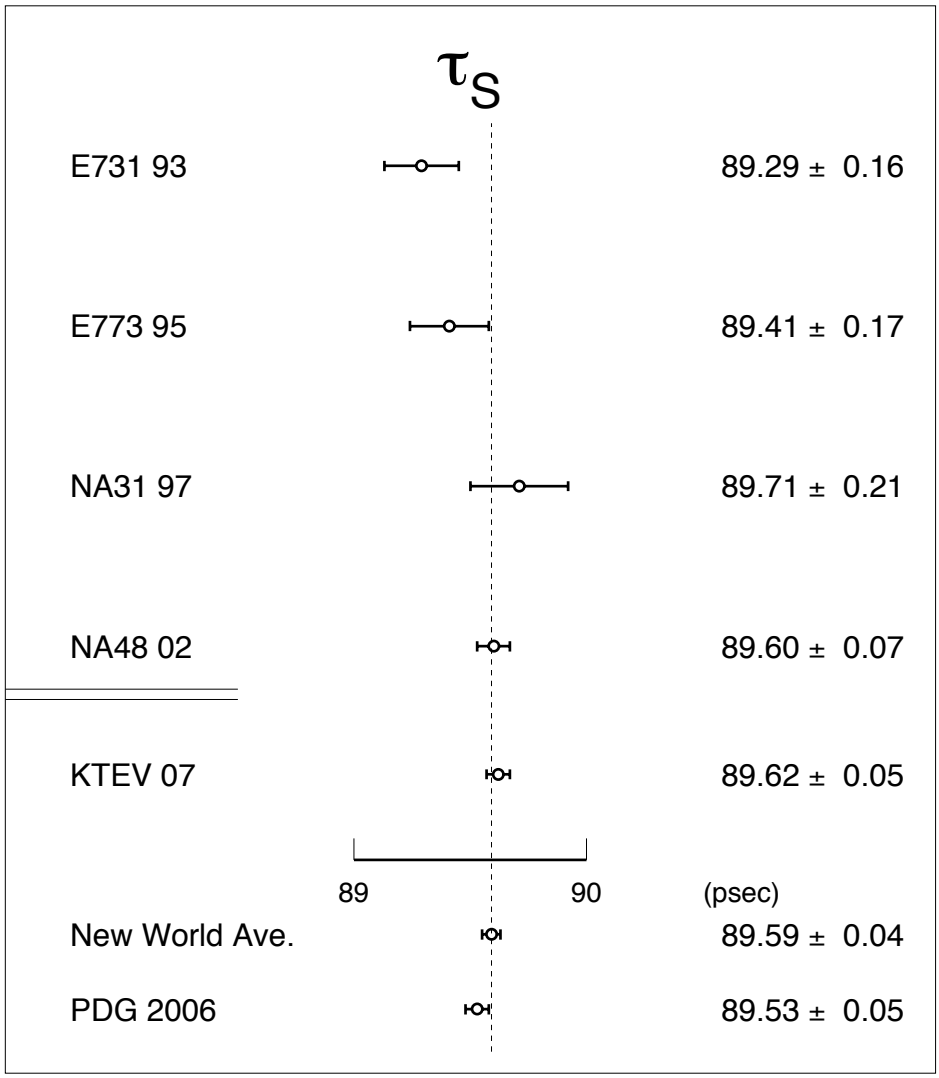

Figure 8.6: New world average for τ_S combining results from E731[55], E773[52], NA31[57], NA48[58], and KTeV.

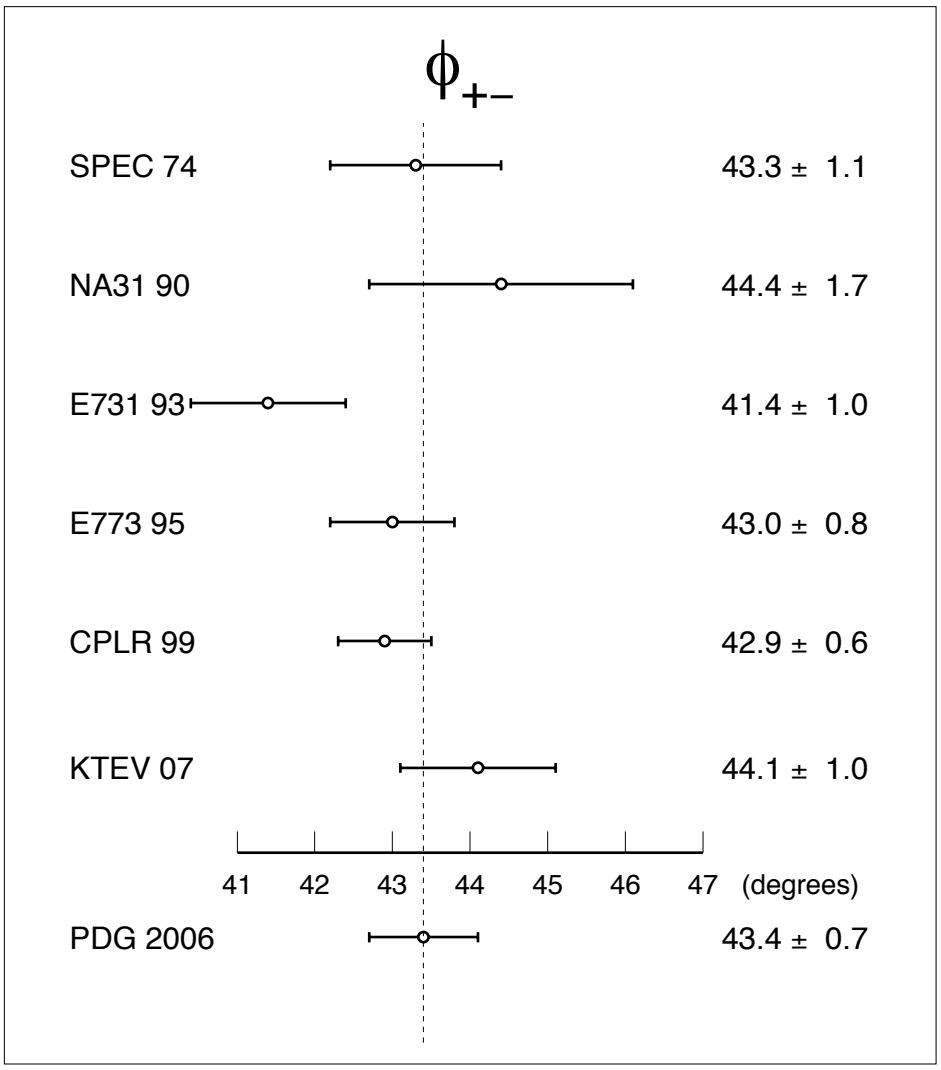

Figure 8.7: Comparison of ϕ_{+-} to previous results. References are [52–56]. In the PDG fit, experimental results are adjusted using their reported correlations with Δm and τ_S to use the PDG values of Δm and τ_S. The results shown in this plot for previous measurements of ϕ_{+-} include the PDG correction.

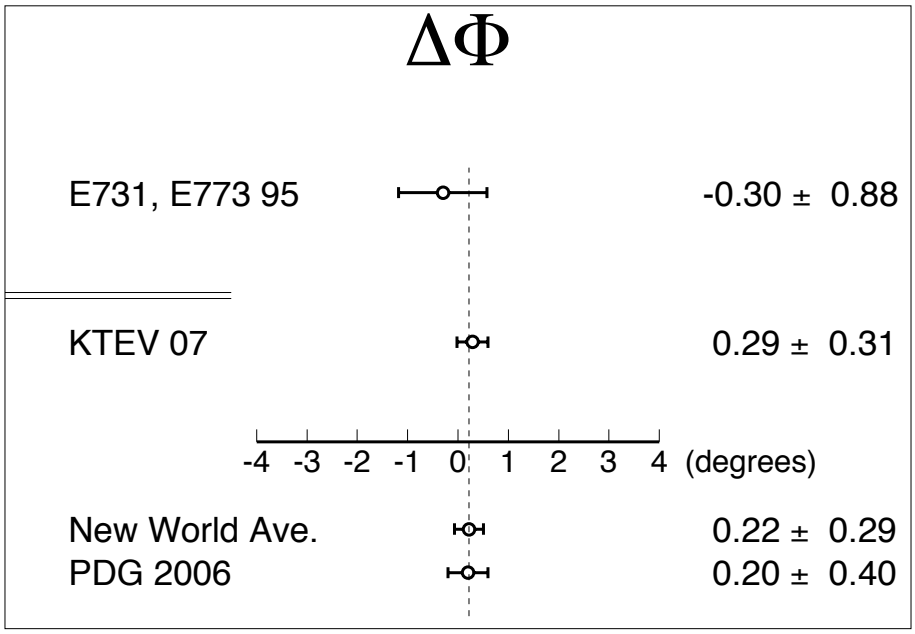

Figure 8.8: Comparison of $\Delta\phi$ to the previous combined result from E731 and E773[52].

APPENDIX A
FIGURES FOR KAON SECTOR PARAMETER CROSSCHECKS

This appendix contains plots showing the crosschecks for the kaon sector parameter results. We show the results for Δm and τ_S in charged and neutral mode, ϕ_{+-}, and $\Delta\phi$ as a function of run range, broken in half in a variety of ways, and as a function of kaon momentum. These crosschecks are discussed in the text in Section 8.2.1.

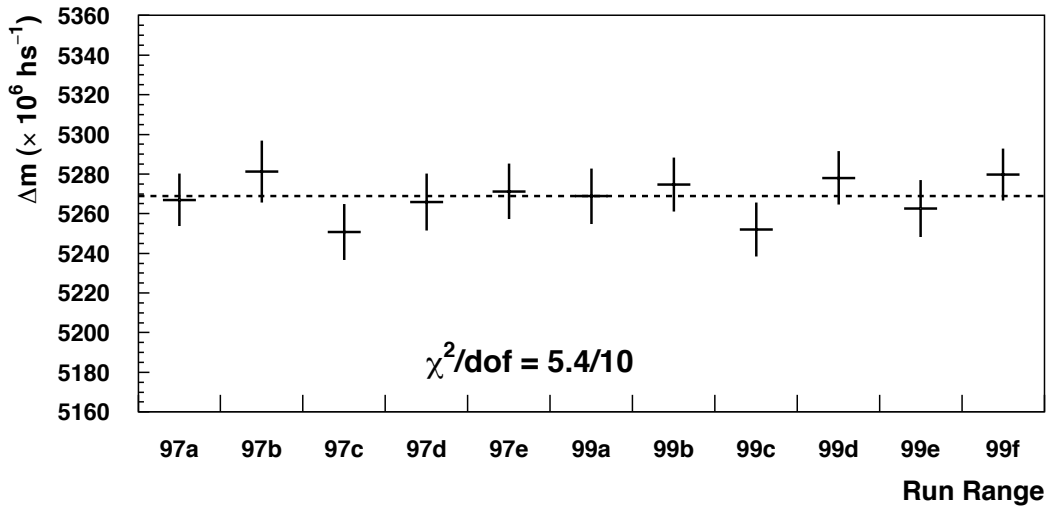

Figure A.1: Δm in subsets of the $K \to \pi^+\pi^-$ data sample. Each point is statistically independent. The dashed line indicates the value of Δm for the full data sample.

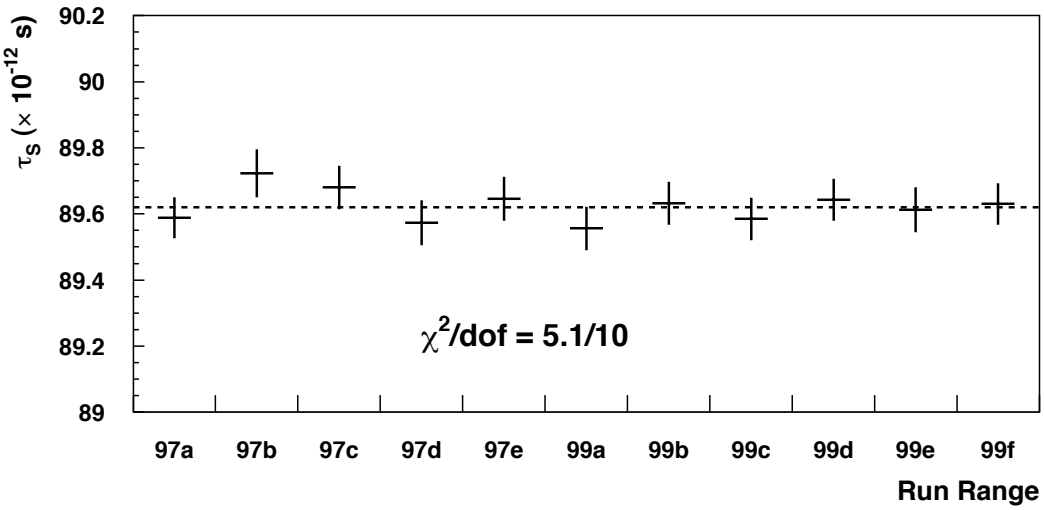

Figure A.2: τ_S in subsets of the $K \to \pi^+\pi^-$ data sample. Each point is statistically independent. The dashed line indicates the value of τ_S for the full data sample.

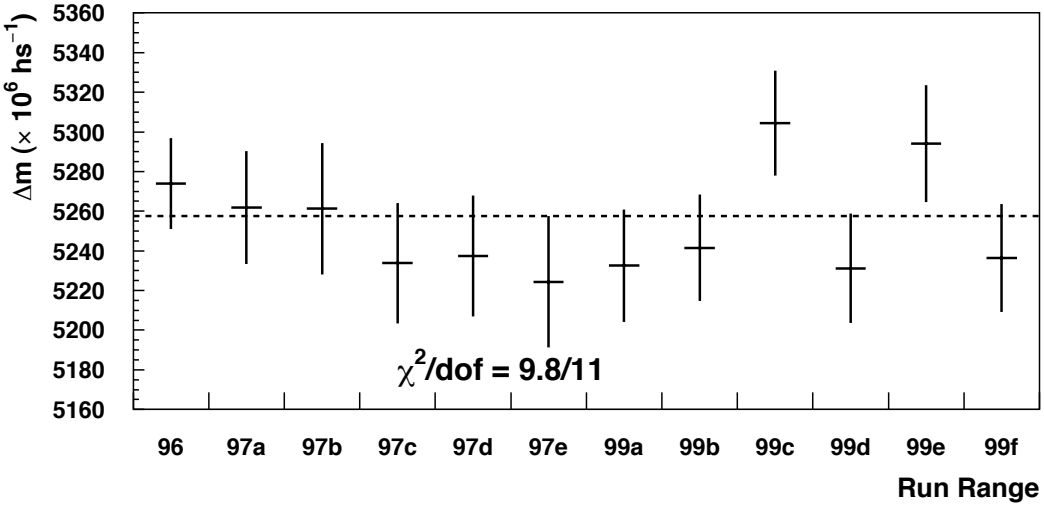

Figure A.3: Δm in subsets of the $K \to \pi^0\pi^0$ data sample. Each point is statistically independent. The dashed line indicates the value of Δm for the full data sample.

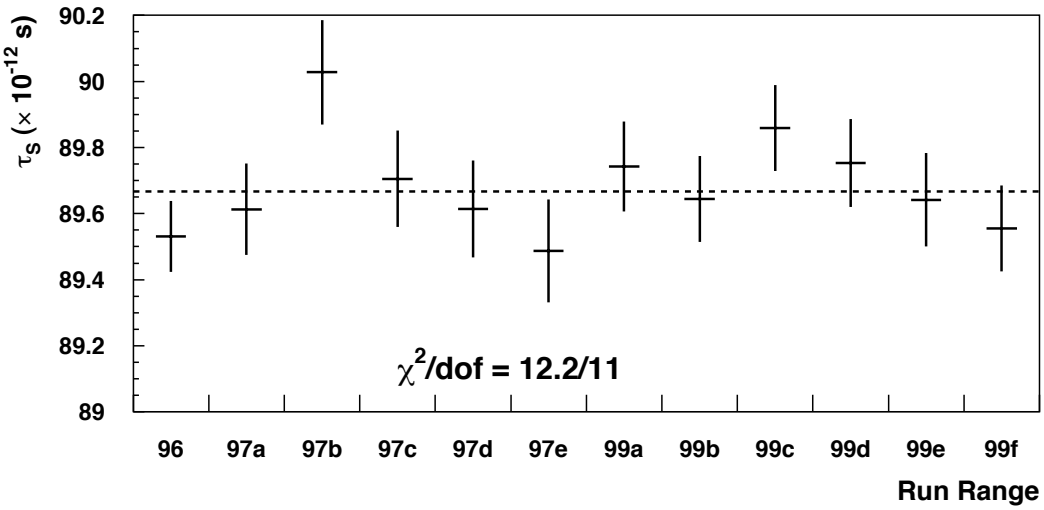

Figure A.4: τ_S in subsets of the $K \to \pi^0\pi^0$ data sample. Each point is statistically independent. The dashed line indicates the value of τ_S for the full data sample.

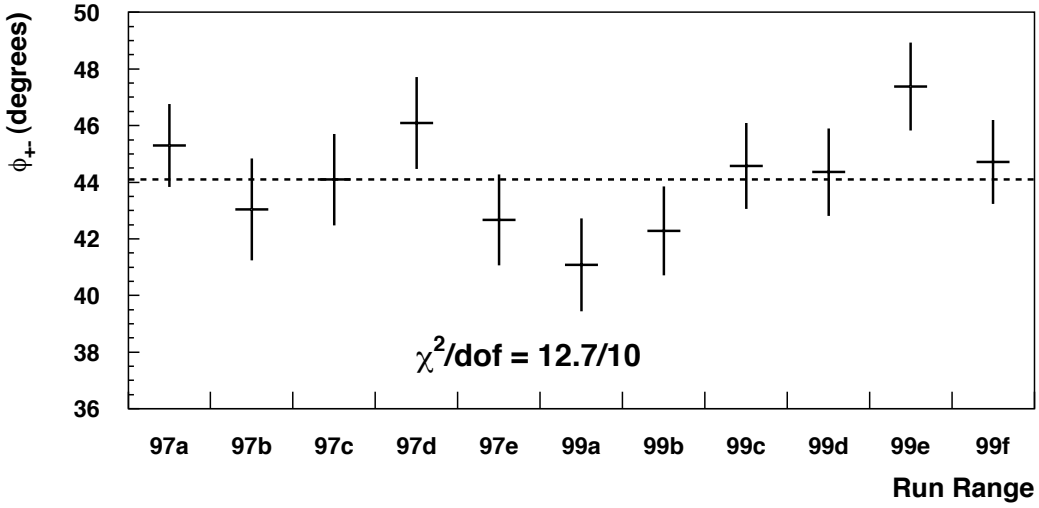

Figure A.5: ϕ_{+-} in subsets of the $K \to \pi^+\pi^-$ data sample. Each point is statistically independent. The dashed line indicates the value of ϕ_{+-} for the full data sample.

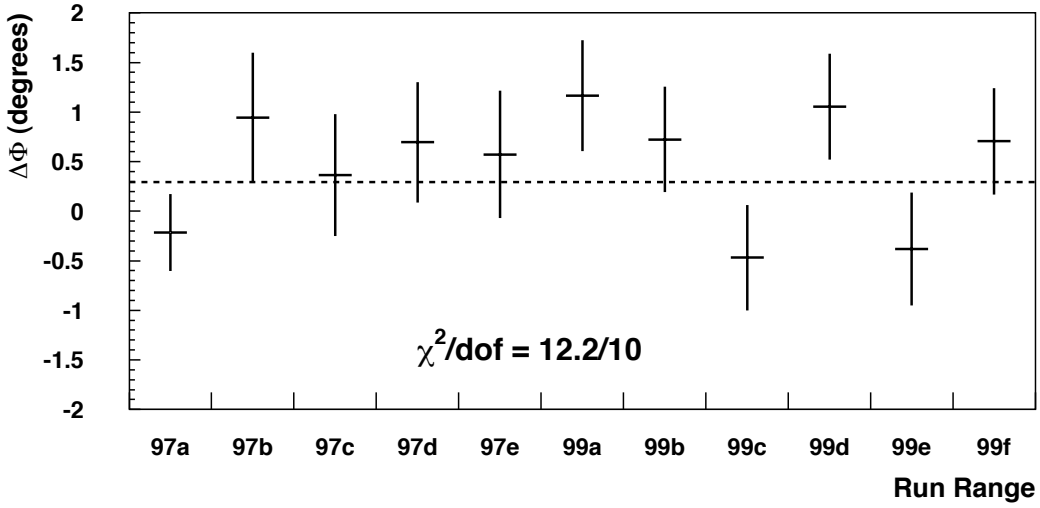

Figure A.6: $\Delta\phi$ in subsets of the data sample. Each point is statistically independent. The dashed line indicates the value of $\Delta\phi$ for the full data sample. The 97a run range includes the 1996 $K \to \pi^0\pi^0$ data.

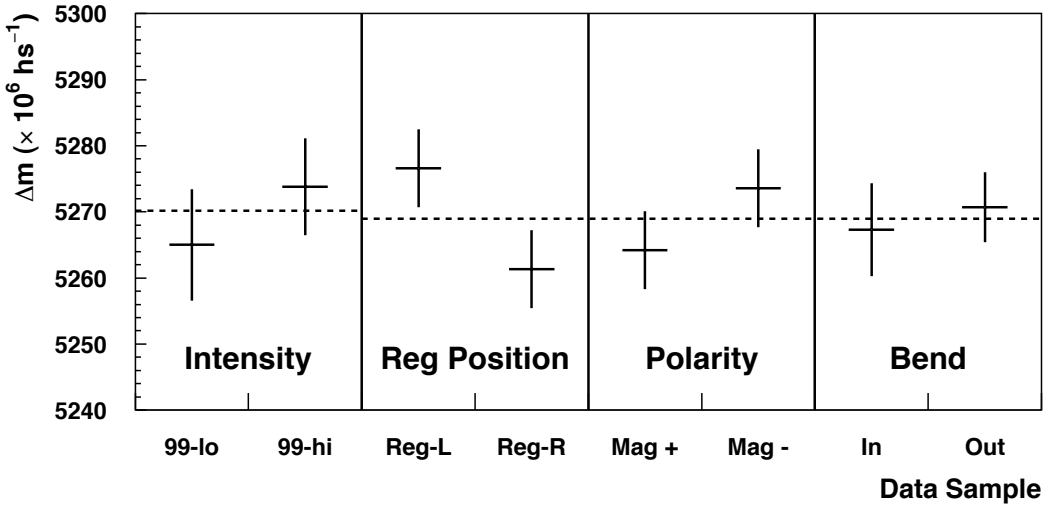

Figure A.7: Δm consistency with beam intensity, regenerator position, magnet polarity, and track bend for the $K \to \pi^+\pi^-$ sample. The low intensity sample has an average SEM of $4{\times}10^{12}$ and the high intensity sample has an average SEM of $6.5{\times}10^{12}$. These subsets are for the 1999 data only. Reg-left and reg-right refer to the position of the regenerator beam in the detector. Mag+ and Mag- are the magnet polarity and in/out are the bend of the two tracks in the magnet. These subsets are for the full data sample. The dashed lines indicate the value of Δm in the appropriate full data sample.

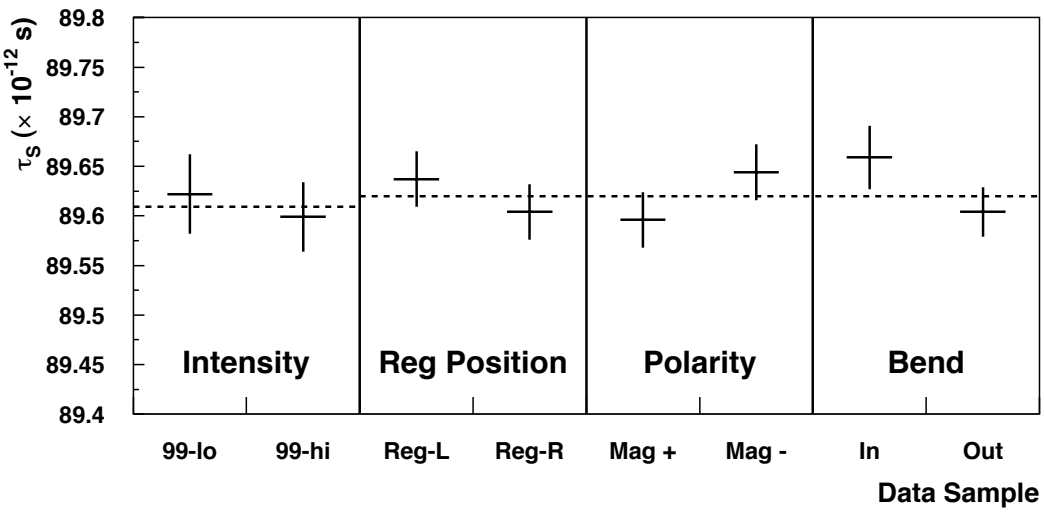

Figure A.8: τ_S consistency with beam intensity, regenerator position, magnet polarity, and track bend for the $K \to \pi^+\pi^-$ sample. The low intensity sample has an average SEM of 4×10^{12} and the high intensity sample has an average SEM of 6.5×10^{12}. These subsets are for the 1999 data only. Reg-left and reg-right refer to the position of the regenerator beam in the detector. Mag+ and Mag- are the magnet polarity and in/out are the bend of the two tracks in the magnet. These subsets are for the full data sample. The dashed lines indicate the value of τ_S in the appropriate full data sample.

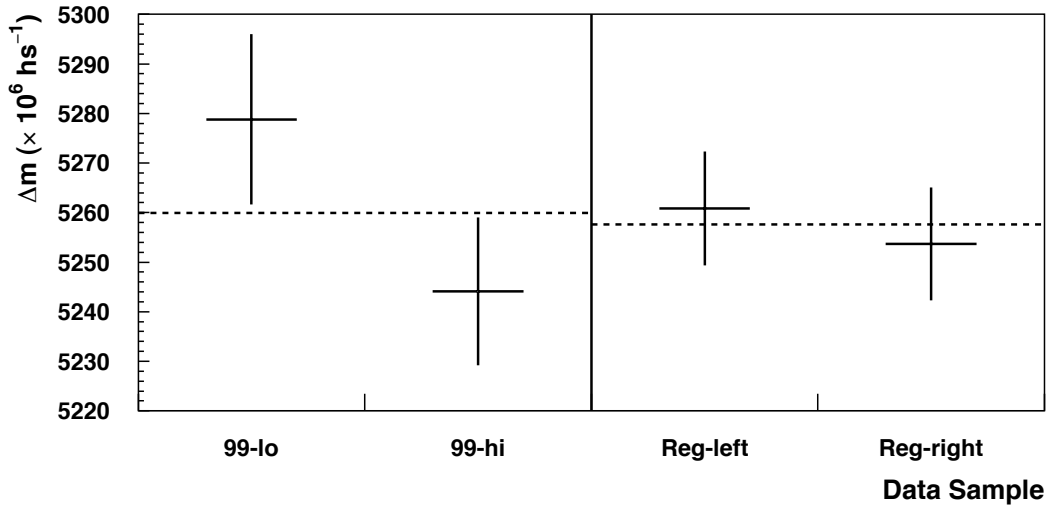

Figure A.9: Δm consistency with beam intensity and regenerator position for the $K \to \pi^0\pi^0$ sample. The low intensity sample has an average SEM of $4{\times}10^{12}$ and the high intensity sample has an average SEM of $6.5{\times}10^{12}$. These subsets are for the 1999 data only. Reg-left and reg-right refer to the position of the regenerator beam in the detector. These subsets are for the full data sample. The dashed lines indicate the value of Δm in the appropriate full data sample.

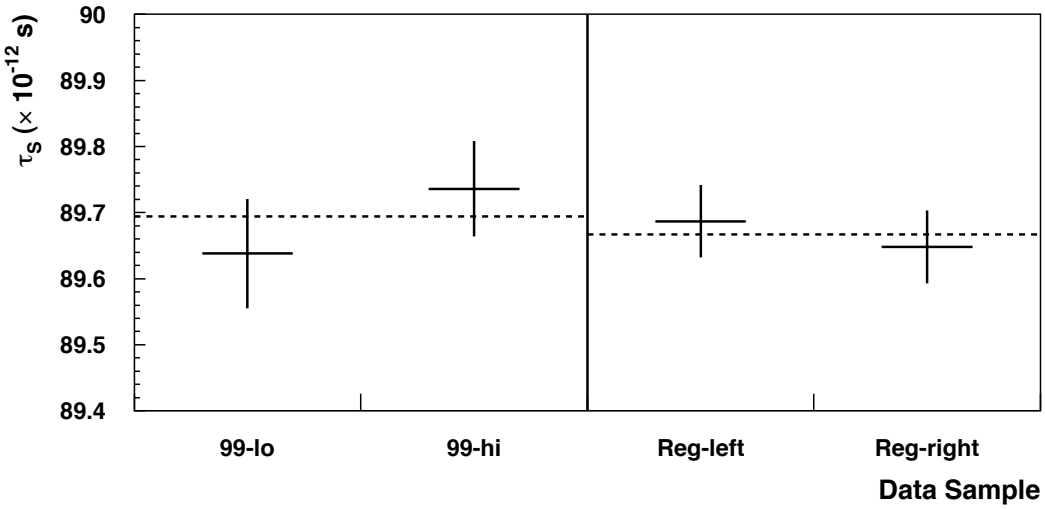

Figure A.10: τ_S consistency with beam intensity and regenerator position for the $K \to \pi^0\pi^0$ sample. The low intensity sample has an average SEM of 4×10^{12} and the high intensity sample has an average SEM of 6.5×10^{12}. These subsets are for the 1999 data only. Reg-left and reg-right refer to the position of the regenerator beam in the detector. These subsets are for the full data sample. The dashed lines indicate the value of τ_S in the appropriate full data sample.

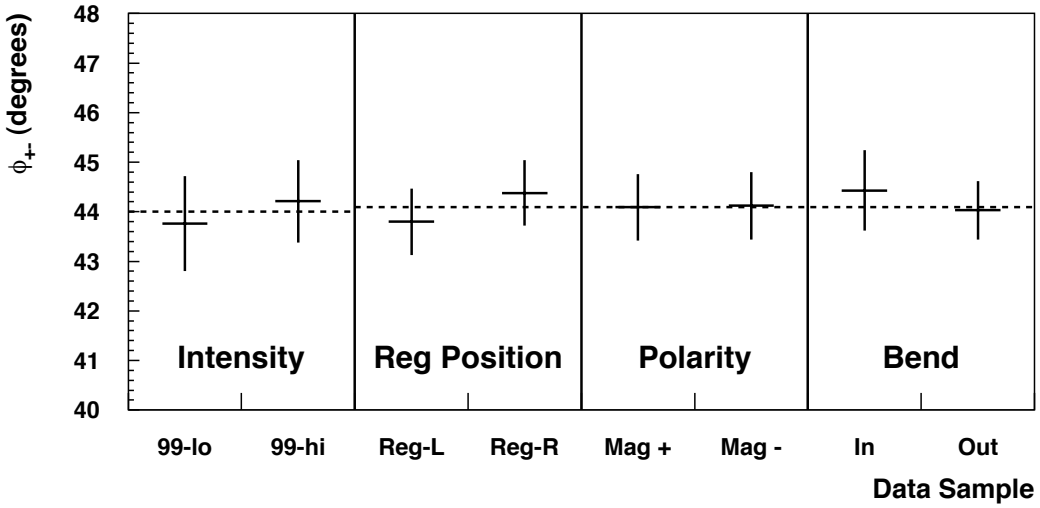

Figure A.11: ϕ_{+-} consistency with beam intensity, regenerator position, magnet polarity, and track bend. The low intensity sample has an average SEM of 4×10^{12} and the high intensity sample has an average SEM of 6.5×10^{12}. These subsets are for the 1999 data only. Reg-left and reg-right refer to the position of the regenerator beam in the detector. Mag+ and Mag- are the magnet polarity and in/out are the bend of the two tracks in the magnet. These subsets are for the full data sample. The dashed lines indicate the value of ϕ_{+-} in the appropriate full data sample.

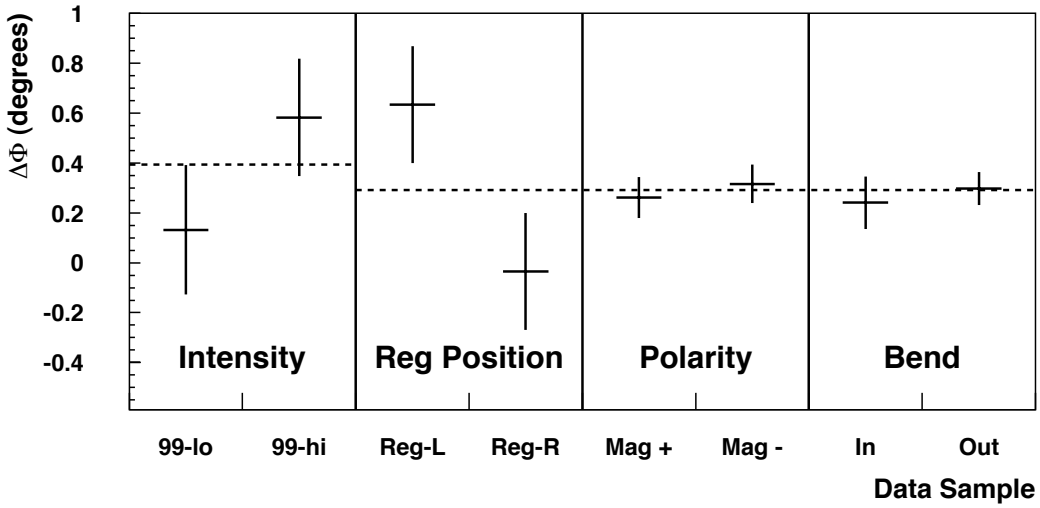

Figure A.12: $\Delta\phi$ consistency with beam intensity, regenerator position, magnet polarity, and track bend. The low intensity sample has an average SEM of 4×10^{12} and the high intensity sample has an average SEM of 6.5×10^{12}. These subsets are for the 1999 data only. Reg-left and reg-right refer to the position of the regenerator beam in the detector. These subsets are for the full data sample. Mag+ and Mag- are the magnet polarity and in/out are the bend of the two tracks in the magnet. In each of these subsets the $K \to \pi^0\pi^0$ sample is common to both fits; the errors are estimated by taking the quadrature difference with the error for the full dataset. The dashed lines indicate the value of $\Delta\phi$ in the appropriate full data sample.

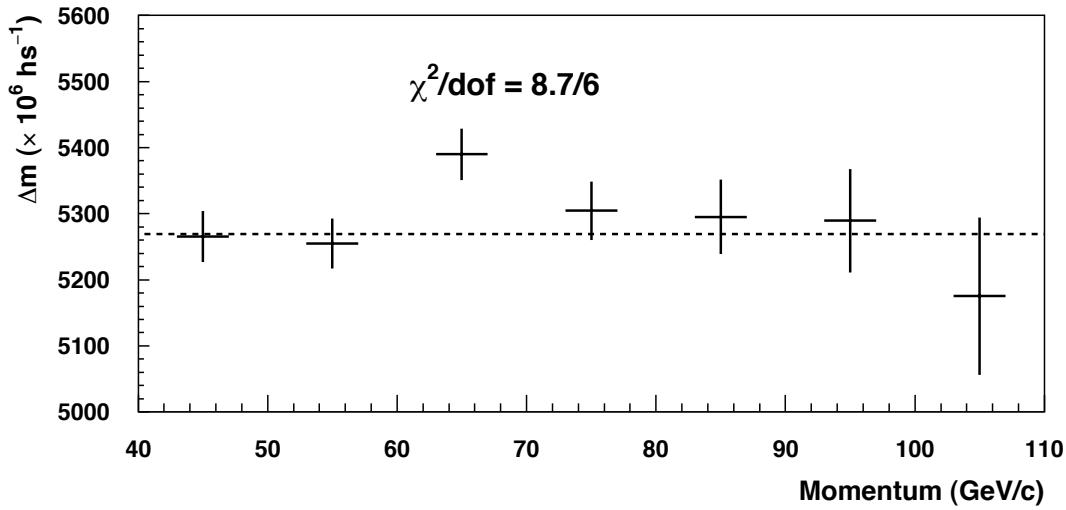

Figure A.13: Δm in 10 GeV/c momentum bins using the $K \to \pi^+\pi^-$ sample. Note that there are no fits above 110 GeV/c. The dashed line indicates the value for the full data sample.

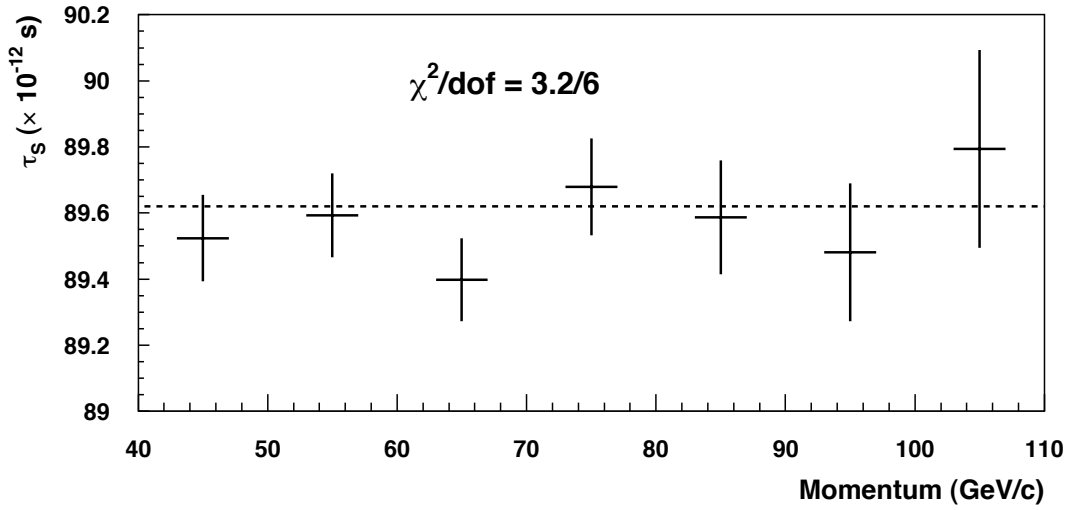

Figure A.14: τ_S in 10 GeV/c momentum bins using the $K \to \pi^+\pi^-$ sample. Note that there are no fits above 110 GeV/c. The dashed line indicates the value for the full data sample.

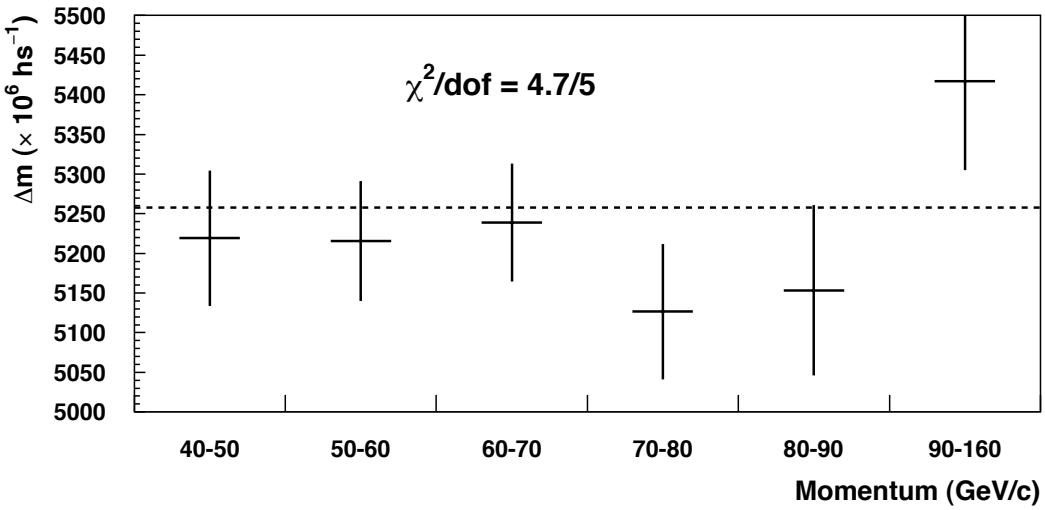

Figure A.15: Δm in momentum bins using the $K \to \pi^0\pi^0$ sample. The first five data points are 10 GeV/c momentum bins. The last bin is 90-160 GeV/c. The dashed line indicates the value for the full data sample.

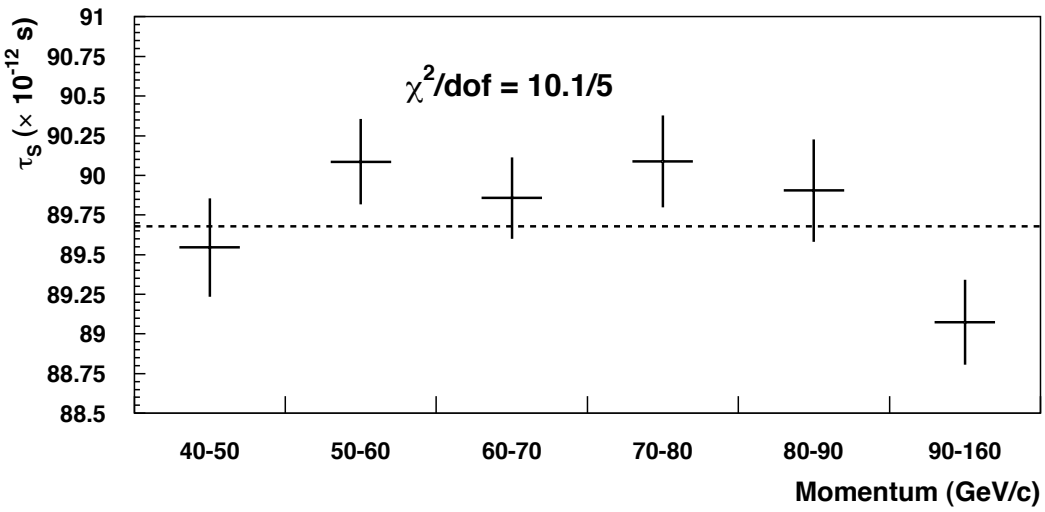

Figure A.16: τ_S in momentum bins using the $K \to \pi^0\pi^0$ sample. The first five data points are 10 GeV/c momentum bins. The last bin is 90-160 GeV/c. The dashed line indicates the value for the full data sample.

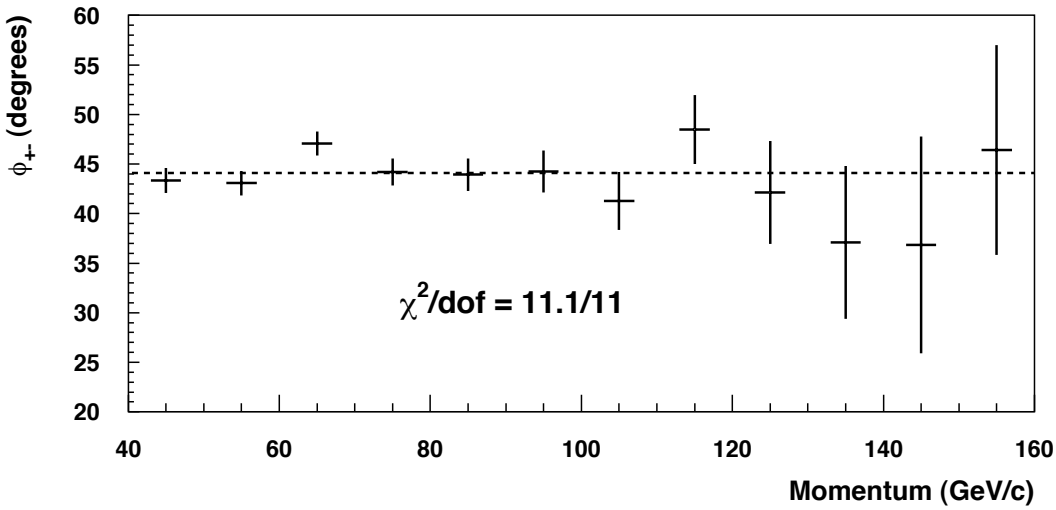

Figure A.17: ϕ_{+-} in 10 GeV/c momentum bins. The dashed line indicates the value for the full data sample.

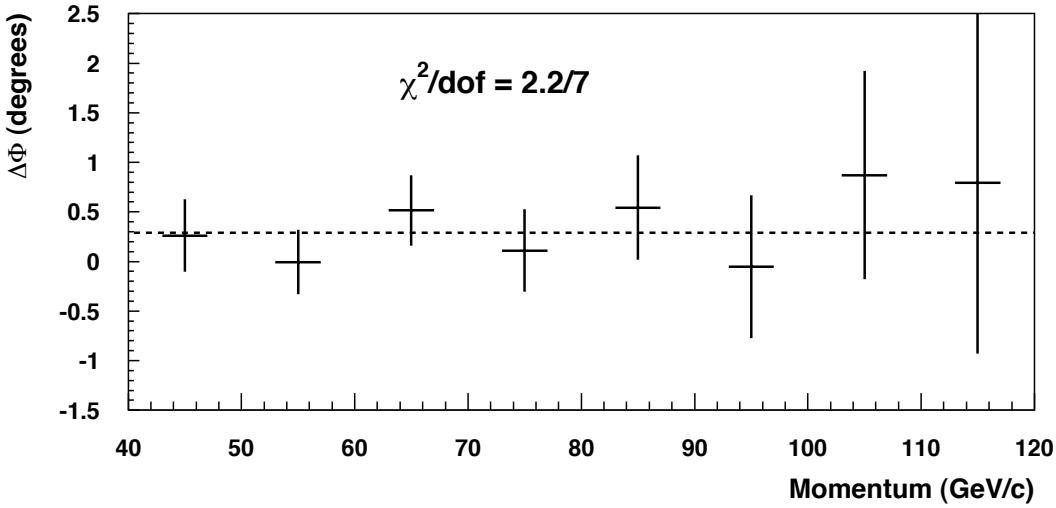

Figure A.18: $\Delta\phi$ in 10 GeV/c momentum bins. Note that there are no fits above 120 GeV/c. The dashed line indicates the value for the full data sample.

REFERENCES

[1] V. Prasad, Ph.D. thesis (The University of Chicago, June, 2002).

[2] J. Graham, Ph.D. thesis (The University of Chicago, December, 2001).

[3] Merriam-Webster's Collegiate Dictionary. 10th ed. 1993.

[4] E. Noether, *Nachr. Gesellschaft. Wiss. Gttingen*, 37-44 (1918).

[5] J. Schwinger, *Phys. Rev.* **91**, 713 (1953).

[6] J. Schwinger, *Phys. Rev.* **94**, 1362 (1954).

[7] G. Lüders, *Kgl. Danske Videnskab Selskab., Matt-fys. Medd.* **28**, 1 (1954).

[8] W. Pauli, *Niels Bohr and the Development of Physics*, Pergamon Press, Elmsford, NY, 1955.

[9] R. Dalitz, *Phys. Rev.* **94**, 1046 (1954).

[10] T. D. Lee and C. N. Yang, *Phys. Rev.* **104**, 254 (1956).

[11] C. S. Wu *et al.*, *Phys. Rev.* **105**, 1413 (1957).

[12] R. L. Garwin, L. M. Lederman, and M. Weinrich, *Phys. Rev.* **105**, 1415 (1957).

[13] J. I. Friedman and V. L. Telegdi, *Phys. Rev.* **105**, 1681 (1957).

[14] J. H. Christenson, J. W. Cronin, V. L. Fitch, and R. Turlay, *Phys. Rev. Lett.* **13**, 138 (1964).

[15] V. L. Fitch, R. F. Roth, J. S. Russ, and W. Vernon, *Phys. Rev. Lett.* **15**, 73 (1965).

[16] M. Banner, J. W. Cronin, J. K. Liu, and J. E. Pilcher, *Phys. Rev. Lett.* **21**, 1103 (1968).

[17] I. A. Budagov *et al.*, *Phys. Lett. B* **28**, 215 (1968).

[18] M. Kobayashi and T. Maskawa, *Prog. Theor. Phys.* **49**, 652 (1973).

[19] L. Wolfenstein, *Phys. Rev. Lett.* **51**, 1945 (1983).

[20] G. D. Barr *et al.*, *Phys. Lett.* **B317**, 233 (1993).

[21] L. K. Gibbons *et al.*, *Phys. Rev. Lett.* **70**, 1203 (1993).

[22] A. Alavi-Harati *et al.*, *Phys. Rev. Lett.* **83**, 22 (1999).

[23] V. Fanti *et al.*, *Phys. Lett.* **B465**, 335-348 (1999).

[24] A. Sakharov, *JETP Lett.* **91B**, 24 (1967).

[25] A. Cohen. CP violation and the origins of matter. Prepared for 27th SLAC Summer Institute on Particle Physics: CP Violation in and Beyond the Standard Model (SSI 99), Stanford, California, 7-16 Jul 1999.

[26] R. Belušević, *Neutral Kaons*, Springer-Verlag, Berlin, 1999.

[27] R. Sachs, *The Physics of Time Reversal*, The University of Chicago Press, Chicago and London, 1987.

[28] S. Bertolini, J. O. Eeg, and M. Fabbrichesi, *Rev. Mod. Phys.* **72**, 65-93 (2000).

[29] A. Buras *et al.*, *Nucl. Phys.* **B370**, 69-104 (1992).

[30] A. Buras *et al.*, *Nucl. Phys.* **B400**, 75-102 (1993).

[31] A. Buras *et al.*, *Nucl. Phys.* **B400**, 37-74 (1993).

[32] A. Buras *et al.*, *Nucl. Phys.* **B408**, 209-285 (1993).

[33] M. Ciuchini *et al.*, *Phys. Lett.* **B301**, 263-271 (1993).

[34] M. Ciuchini *et al.*, *Nucl. Phys.* **B415**, 403-462 (1994).

[35] S. Bertolini. Theory Status of ϵ'/ϵ. Invited talk at the Int. Workshop on Heavy Quarks and Leptons, Vietri sul Mare, Italy, May 27 - June 1, 2002.

[36] M Ciuchini, *Nucl. Phys. Proc. Suppl.* **59**, 149 (1997).

[37] S. Bertolini *et al.*, *Nucl. Phys.* **B514**, 93 (1998).

[38] A. Buras, in *Probing the Standard Model of Particle Interactions*, edited by F. Davids and R. Gupta, (Elevier, Holland, 1999).

[39] M. Ciuchini *et al.*, in *Kaon Physics*, (Chicago, Illinois, 1999).

[40] A. A. Belkov *et al.*, "Phenomenological Analysis of ϵ'/ϵ within an Effective Chiral Lagrangian Approach at $\mathcal{O}(p^6)$", Preprint hep-ph/9907335, 1999.

[41] J. Bijnens and J. Prades, *JHEP* **06**, 035 (2000).

[42] T. Hambye *et al.*, *Nucl. Phys.* **B564**, 391 (2000).

[43] E Pallante, A. Pich, and I. Scimemi, *Nucl. Phys.* **B617**, 441-474 (2001).

[44] Y.-L. Wu, *Phys. Rev. D* **64**, 016001 (2001).

[45] S. Narison, *Nucl. Phys.* **B593**, 3 (2001).

[46] M. Sanchez, Ph.D. thesis (Universidad de Granada, October, 2003).

[47] A. Pich, in *Proceedings of the 32nd International Conference on High-Energy Physics (ICHEP 04)*, (Beijing, China, Aug 2004).

[48] W. Ochs, πN *Newsletter* **3**, 25-42 (1991).

[49] G. Unal, in *Proceedings of 31st International Conference on High Energy Physics (ICHEP 2002)*, (Amsterdam, The Netherlands, July 2002).

[50] A. Alavi-Harati *et al.*, *Phys. Rev. D* **67**, 012005 (2003).

[51] W.-M. Yao *et al.*, *Journal of Physics G* **33**, 1+ (2006).

[52] B. Schwingenheuer *et al.*, *Phys. Rev. Lett.* **74**, 4376 (1995).

[53] S. Gjesdal *et al.*, *Phys. Lett.* **52B**, 113 (1974).

[54] C. Geweniger *et al.*, *Phys. Lett.* **52B**, 108 (1974).

[55] L. Gibbons *et al.*, *Phys. Rev. Lett.* **70**, 1199 (1993).

[56] A. Apostolakis *et al.*, *Phys. Lett.* **B473**, 186 (1999).

[57] L. Bertanza *et al.*, *Z. Phys.* **C73**, 629 (1997).

[58] A. Lai *et al.*, *Phys. Lett.* **B537**, 28 (2002).

[59] R. Carosi *et al.*, *Phys. Lett.* **B237**, 303 (1990).

[60] P. Shawhan, Ph.D. thesis (The University of Chicago, December, 1999).

[61] B. Quinn, Ph.D. thesis (The University of Chicago, June, 2000).

[62] K. Hanagaki, Status of Photon Veto, KTeV Internal, KTEV-0408, 1997.

[63] E. Cheu *et al.*, Proposal to continue the study of direct CP violation and rare decay processes in KTeV in 1999., FERMILAB PROPOSAL, 0799, 1997.

[64] R. Brun *et al.* Computer code GEANT 3.21, CERN, Geneva, 1994.

[65] T. Alexopoulos *et al.*, *Phys. Rev. Lett.* **93**, 181802 (2004).

[66] A. J. Malensek, 1981. Fermilab Reports FN-341, FN-341A (errata).

[67] S. Agostinelli *et al.*, *Nucl. Instrum. Meth.* **A506**, 250-303 (2003).

[68] R. Kessler, Collimator Scatters for the 1997 Data Set, KTeV Internal, , 2000.

[69] F. Gilman, *Phys. Rev.* **171**, 1453 (1968).

[70] F. James and M. Roos, Computer code MINUIT, CERN, Geneva, 1994.